Tracking and vertex reconstruction with the $\overline{\text{P}}$ANDA Micro-Vertex-Detector

Dissertation

zur
Erlangung des Doktorgrades (Dr. rer. nat.)
der
Mathematisch-Naturwissenschaftlichen Fakultät
der
Rheinischen Friedrich-Wilhelms-Universität Bonn

vorgelegt von

M. Sc. Simone Bianco

aus
Torino (Italien)

Bonn, 2013

Angefertigt mit Genehmigung der Mathematisch-Naturwissenschaftlichen Fakultät
der Rheinischen Friedrich-Wilhelms-Universität Bonn

1. Gutachter: Prof. Dr. Kai-Thomas Brinkmann
2. Gutachter: Prof. Dr. Ulrike Thoma

Tag der Promotion: 16.07.2013
Erscheinungsjahr: 2013

Zusammenfassung

$\overline{\text{P}}$ANDA, eines der Experimente am zukünftigen Beschleunigerzentrum FAIR in Darmstadt, wird Kollisionen eines Antiprotonenstrahls mit verschiedenen feststehenden Targets untersuchen. Der Schwerpunkt liegt dabei auf dem Studium der starken Wechselwirkung im Energiebereich des Charm-Quarks. Das Hochpräzisionsexperiment wird Charmonium-Zustände, Open-Charm-Mesonen und Charm-Baryonen untersuchen.
Zur Bestimmung der Teilchenimpulse und der Rekonstruktion der Zerfallsvertices sind die Spurdetektoren von herausragender Bedeutung. Gerade bei kurzlebigen Zuständen wird der innerste der Spurdetektoren, der Micro-Vertex-Detektor (MVD), wichtige Informationen liefern.
In dieser Arbeit werden verschiedene Monte-Carlo-Studien zur räumlichen Abdeckung und zum Vertexrekonstruktionsvermögen des MVD gezeigt. Basierend auf der implementierten Detektorgeometrie wird dazu der MVD in verschiedenen Fällen simuliert, die mit den späteren Betriebsmodi des $\overline{\text{P}}$ANDA Detektors vergleichbar sind.
Monte-Carlo-Simulationen für Testaufbauten der MVD-Sensoren an unterschiedlichen Beschleunigern werden gezeigt und die derart gemachten Vorhersagen mit den experimentell gewonnenen Daten verglichen.
Anhand der Reaktion $\bar{\text{p}}\text{p} \rightarrow \Lambda_\text{c}\overline{\Lambda}_\text{c}$ wird das Rekonstruktionsvermögen des $\overline{\text{P}}$ANDA Experiments aufgezeigt und zusätzlich das Signal-zu-Untergrund-Verhältnis für diesen Zerfallskanal analysiert.

Abstract

$\overline{\text{P}}$ANDA is one of the experiments which will be installed at the FAIR facility in Darmstadt. It will study the collisions of an antiproton beam with different fixed targets.
The main focus of the experiment will be on strong interactions at the energy regime corresponding to the charm quark region. Charmonium states, open-charm mesons and charmed baryons will be studied with a high precision experiment.
The tracking detectors will play an important role allowing for a precise reconstruction of particles momenta and decay vertices. In particular, in the case of short-lived particles, the contribution of the Micro-Vertex-Detector (MVD), which is the innermost tracker of the experiment, will be crucial.
Detailed Monte-Carlo studies based on an implementation of the detector geometry will be presented analyzing the coverage and vertex reconstruction performance of the MVD in different physics scenarios compatible with the $\overline{\text{P}}$ANDA operational modes.
Experimental results obtained with MVD prototype sensors at different particle accelerators will be shown comparing the observations with predictions from Monte-Carlo simulations of the setups.
An analysis of the potential reconstruction performance of the $\overline{\text{P}}$ANDA experiment for the $\overline{\text{p}}\text{p} \rightarrow \Lambda_\text{c}\overline{\Lambda}_\text{c}$ reaction will be presented together with a study of the signal to background significance for the selected decay pattern.

Disclaimer

Some of the results shown in this thesis were already published in articles, conference proceedings and in the Technical Design Report of the $\overline{\mathrm{P}}$ANDA Micro-Vertex-Detector (in the chapter concerning simulations and in the appendix about beam tests).
These publications are always cited as references in the text when the subjects of a section are compatible with what was already published.

Contents

CHAPTER 1

The physics program of the $\overline{\text{P}}$ANDA experiment

The study of strong interaction at intermediate energies such as the ones available at $\overline{\text{P}}$ANDA ($\sqrt{s} = 2.25$–5.47 GeV) is one of the key researches devoted to the understanding of hadronic matter. While at high energies, where the asymptotic freedom applies [1], the interaction between quarks and gluons can be well described by perturbative quantum chromodynamics calculations, the interpretation of strong interaction at lower energies still lacks a unique theoretical framework allowing to get comprehensive predictions. At this regime confinement plays a significant role, since the interaction does not only undergo between the constituents partons, but between whole hadrons. Precise measurements in this sector are fundamental to compare different theoretical approaches and to proceed in the understanding of the interactions.

Formation experiments give the opportunity to measure the mass values, the resonance widths and the line shapes of resonances more precisely than it is possible in production experiments (see figure 1.1). In formation experiments the knowledge about the initial state can be used to scan a resonance changing the energy available in the center of mass. Since the state is formed directly at the primary interaction, it is possible to control the energy available in the initial state. For example in order to study a charmonium state the beam momenta can be modified scanning the energy range around the peak value corresponding to the resonance under study. The parameters of the resonance can therefore be derived measuring the formation rate of such state as a function of the initial center of mass energy. The resolution of the reconstructed parameters depends therefore not only on the performance of the detectors, but also on the determination of the energy available in the initial state, which derives from the control of the beam momentum.

Antiproton proton collisions are particularly suited for such studies since the coherent annihilation of the three valence quarks in the protons with the three antiquarks of the antiproton can form directly $q\bar{q}$ states. On the contrary e^+e^- annihilations, which provide a cleaner measurement environment, can only form states with photon-like quantum numbers ($J^{PC} = 1^{--}$), therefore only some of the quarkonia states can be investigated directly with this method.

The $\overline{\text{P}}$ANDA experiment will study the annihilation of an antiproton beam on a fixed target. In this case in order to control the energy available at the initial state, the antiproton momentum can be adjusted. A high resolution operation mode of the accelerator will allow to study

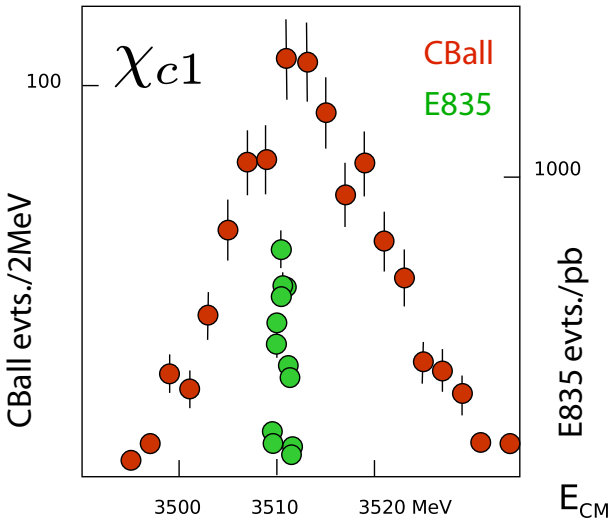

Figure 1.1: Comparison of the χ_c1 invariant mass resolution obtained in formation (E385) and in production (Crystal Ball) experiments [2]. The E835 data set refers to the exclusive measurement of the reaction $\bar{p}p \to \chi_{c1} \to \gamma J/\psi \to \gamma e^+e^-$ [3]. The Crystal Ball data show the inclusive measurement of the χ_{c1} invariant mass in the reaction $e^+e^- \to \gamma\chi_{c1} \to \gamma\gamma J/\psi \to \gamma\gamma e^+e^-$ [4].

charmonium states controlling the beam momentum with a precision down to $\delta p/p \sim 10^{-5}$.

Charmonium and open charm precision spectroscopy will not be the only focus of the experiment. Other topics such as the search for exotic states (hybrids, glueballs, tetra-quarks), a better determination of the nucleon form factors, in medium hadron modifications and hypernuclei will be covered by the $\overline{\text{P}}$ANDA physics program.

1.1 Strong interaction

The experiments of the last decades have proven the validity of quantum field theories both as descriptive and as predictive tools in particle physics. The quantum electrodynamic theory (QED) was extensively tested and found to be extremely predictive (see [5], [6] and [7]).

The description of strong interaction as a quantum field theory consists in the quantum chromodynamics (QCD): it is a non abelian relativistic quantum field theory in which quarks and gluons interact with each other on the base of their color charges. Being a non abelian theory, the gluons, which are the mediators of the strong interaction, do carry color charge and can therefore self-interact. Only color singlet states have been observed so far. The QCD theory is described by the following lagrangian density:

$$\mathcal{L} = -\frac{1}{4} G_a^{\mu\nu} G^a_{\mu\nu} + \sum_f \bar{q}_f \left[i\gamma^\mu D_\mu - m_f \right] q_f \tag{1.1}$$

where the gluonic tensor is defined as:

$$G_a^{\mu\nu} = \partial^\mu A_a^\nu - \partial^\nu A_a^\mu + g f_a^{bc} A_b^\mu A_c^\nu \tag{1.2}$$

and the covariant derivative as:

$$D^\mu = \partial^\mu - i\frac{g}{2} A_a^\mu \lambda^a \tag{1.3}$$

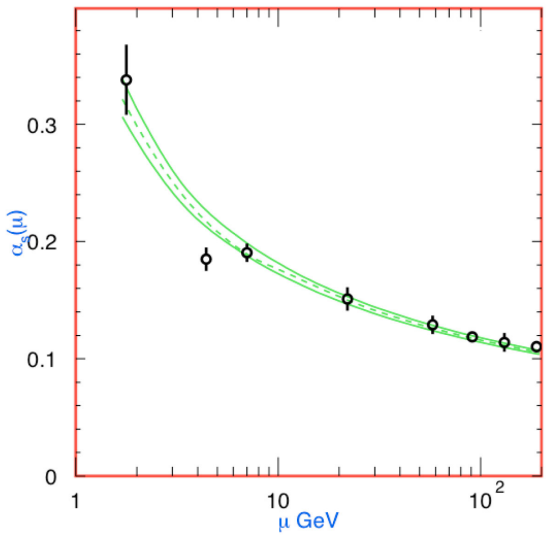

Figure 1.2: The coupling constant α_s as a function of the energy scale μ [13].

The sum over f in equation 1.1 is meant over the available flavors (in the energy region of the $\overline{\text{P}}$ANDA experiment these flavors will be up, down, strange and charm), g relates to the strong coupling constant as $\alpha_s\left(k^2\right) = \frac{g_s^2\left(k^2\right)}{4\pi}$, A_a^μ is the field of a gluon with color quantum number a (a = 1, ..., 8), λ^a are the Gell-Mann matrices and f_a^{bc} are the structure constants of the group (SU(3)). The QCD Lagrangian allows a perturbative treatment at high energies, where the running coupling constant α_s is small enough ($\alpha_s(M_{Z^0}^2) \sim 0.1180$ [8]). The QCD has already been tested at the perturbative regime in several experiments and it appears to be the right theory to describe the strong interaction at high energy scales (see [9], [10], [11] and [12]). Nevertheless at lower scales the coupling constant α_s grows (see figure 1.2), therefore the perturbative methods can no longer be applied.

1.1.1 Non-perturbative approaches to strong interaction

Different theoretical approaches have been developed to tackle the strong interaction at low energies. They can be divided in two main categories: the lattice QCD (LQCD) methods and the effective field theories (EFT).

Lattice Quantum Chromo Dynamics

LQCD consists in a method to study the motion equations of the QCD Lagrangian discretizing the space-time into a four-dimensional lattice and solving numerically the equations with large scale simulations [14]. In order to simplify the calculations a Wick rotation ($t \rightarrow -i\tau$) and some boundary conditions can be applied in order to write the partition function Z of the ensemble as similar as possible to a Feynman's path integral:

$$Z = \int \mathcal{D}\varphi\,(x,\tau)\, e^{-S_E[\varphi(x,\tau)]}$$

where $\mathcal{D}\varphi$ is the differential in the φ field considered in terms of Feynman's integrals and S_E is the Euclidean action. The lattice step size (**a**) acts as a regulator for infra-red divergencies, the limit

for **a** going to zero allows to extrapolate at the end of the calculation results for the continuum. In the past decades several simplifications were adopted to reduce the amount of calculations required: quenched approaches neglecting the sea-quarks were used, frameworks with only two light quark flavors were chosen and light quarks were considered as static sources of color. In the last years the improvement in computing capabilities and in the LQCD approaches allowed to reduce the effects of most of these simplifications.

In LQCD the SU(3) matrices represent link functions connecting sites on the lattice. Closed paths on the lattice are of particular interest since the trace of the ordered product of the matrices ($P_{\square}$) realizing that path is gauge invariant. The simplest possible closed loop is a "square" of side 1 **a** and is referred to as the *plaquette*. LQCD has been able to calculate the mass of some of the open-charm and open-bottom mesons, as well as the ones of charmonium and bottomonium states [15]. Predictions about the glueballs (bound states of two gluons) spectrum have been produced by LQCD (see figure 1.4). Even if the widths of such states are not precisely calculated (and therefore measuring them could be difficult in case of wide overlapping resonances), these studies allow anyway to know the energy regions where to look for glueball candidates. LQCD can also be useful for $\overline{\text{P}}$ANDA in the interpretation of the studies of the proton form factor which will be performed analyzing the reaction $\bar{p}p \rightarrow e^+e^-$.

Effective Field Theories

Effective Field Theories (EFTs) represent a different strategy to study the strong interaction at specific regimes: a scale separation is performed integrating out the degrees of freedom related for example to high energies. The obtained theory is matched to the full QCD comparing the predictions for some observables in the two theories. An example is the Non-Relativistic QCD theory in which heavy quarks are considered to be non-relativistic [16]. In the case of $\overline{\text{P}}$ANDA the contributions from top and bottom quarks can be integrated out, while the charm dynamics can be described with non relativistic fields. Gluon dynamics can be partially removed from this theory depending on the velocity of the heavy quarks (or charm quark in the case of the $\overline{\text{P}}$ANDA experiment). These theories can provide a simpler input to lattice calculations. EFT with hadronic degrees of freedom have been developed to describe the properties of classes of mesons and baryons. In particular within the $\overline{\text{P}}$ANDA physics program these theories can be adopted to study the open-charm spectrum, hypernuclear dynamics and light baryons (such as for example the ones with double strangeness) [17].

Another approach within the set of EFTs is the chiral perturbation theory (ChPT) which is based on the partial chiral symmetry (vanishing quark masses) of the QCD Lagrangian [18]. Quark masses are finite, but compared with the hadronic scales the light quarks can be approximated as massless degenerate states and therefore ChPT can be applied. This theory is based on hadronic degrees of freedom at low energies and implies a spontaneous breaking of a higher chiral symmetry. The Goldstone boson in such framework should be massless. Since for the QCD Lagrangian the chiral symmetry is approximate and not exact, the Goldstone boson can be identified with the pion, which has a much smaller mass than all the other hadrons. ChPT has been able to predict open-charm resonances close respectively to the DK and D^*K thresholds, which are extremely close to the empirical masses of the $D^*_{s0}(2317)$ and $D^*_{s1}(2460)$ [19]. ChPT is a powerful tool to study possible exotic states in the open-charm sector: studies demonstrated that prediction for exotic states can be made, especially on the effect on the invariant mass distributions for the πD and ηD^* channels [20]. It is therefore really important to measure such spectra with high accuracy in order to validate the theoretical predictions.

1.2 Hadron spectroscopy

Charmonium spectroscopy

The charmonium spectrum has been investigated by several experiments in the last decades: from the "November revolution" at SLAC and BNL [21], to the more recent discoveries of the B-factories. Eight states were discovered in the so-called "below $D\overline{D}$ region", corresponding to energies smaller than the one required to form a couple of open-charmed ground state mesons. Some of these states (such as for example the J/ψ or the $\psi(2S)$) have been measured precisely and their masses are known with an error of about ten keV.

However, this is not the case for all the spectrum below threshold. Especially the singlet states (such as the η_c) still have ambiguities in the determination of their masses and widths (for example the error on the mass of the η_c is 1.3 MeV, the one on the total width 4 MeV [22]). Figure 1.3 shows a summary of the measured charmonium states, the theoretical predictions and the newly measured states which allow for an interpretation as charmonium-like states. The spectrum above the $D\overline{D}$ threshold is much more dense, tens of states have been measured.

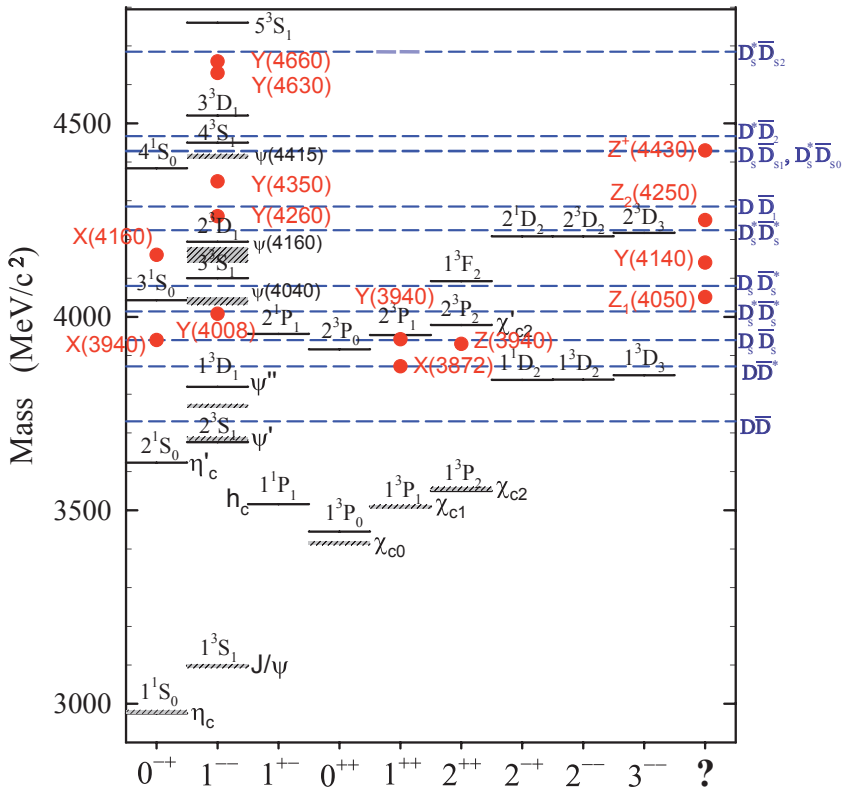

Figure 1.3: States of the charmonium spectrum with quantum numbers assignment [23]. Experimental measurements results are shown with a shaded line, while a solid black line corresponds to theoretical predictions [24]. The red dots represent states with a possible charmonium interpretation (in these cases the most probable quantum number assignment is shown). The states placed in the last column do not fit any standard quantum number assignment and are considered to be exotic.

Several new states were measured in the last years at the B-factories (X(3872), Y(4260), ...), which mainly decay into charmonium states (mostly J/ψ and $\psi(2S)$). They can be interpreted as charmonium-like states, but since their masses are close to production thresholds they can also

be considered as molecular bound states [25]. For example the X(3872) has been interpreted both as a molecular state close to the $D\overline{D}^*$ [26] and as a multi-quark state [27].

Open-charm

$\overline{\text{P}}$ANDA will perform studies in the open charm sector as well. The possibility of measuring precisely the width of such states will allow to investigate their nature: further experimental inputs are especially needed for an interpretation of the D_s spectrum in order to evaluate the different theoretical interpretations proposed. For example so far the $D^*_{s0}(2317)$, whose mass is just below the DK threshold, only has upper limits of a few of MeV on its widths. Simulations showed that $\overline{\text{P}}$ANDA can contribute reaching resolutions in the order of 0.1 MeV on the width of such states [28].

Heavy baryons

The study of the excited baryons spectrum is one of the main goals of non perturbative QCD [29]. The most consistent amount of collected data refers to the nucleon sector but the agreement with quark model predictions is quite poor: the measured states do not fit with the foreseen masses and several predicted resonances have not yet been observed [13]. Several explanations have been formulated including the possibility of a quark-diquark structure of the baryons, which would then limit the number of degrees of freedom and therefore the number of possible states. The status about strange and charmed baryons is more confused because the additional flavor content adds a degree of freedom. $\overline{\text{P}}$ANDA can contribute in this sector studying the baryon antibaryon pairs produced in the final state by inelastic antiproton proton interactions [30]. The cross section for such final states is similar to that relative to the annihilation into mesons at the energies of $\overline{\text{P}}$ANDA [17]. Additionally the $\overline{\text{P}}$ANDA setup offers a nearly 4π acceptance, a comprehensive set of detectors for particle identification and a precise tracking system which allows to reconstruct displaced decay vertices. Furthermore several reactions such as $\overline{p}p \to \overline{\Lambda}_c\Lambda_c, \overline{\Sigma}_c\Sigma_c$ have never been experimentally measured. The cross section for the $\overline{\Lambda}_c\Lambda_c$ final state has been predicted to reach values up to 0.2 µb [31]. The contribution of the tracking systems will be crucial for the reconstruction of the decays of charmed baryons into charged particles due to their short lifetimes and to the displaced vertices of some of their decay modes (for example the ones including some Λ or $\overline{\Lambda}$).

Search for exotic states: hybrids and glueballs

The presence of gluons in the QCD adds to the quark model spectrum new possible types of particles. Hybrids are possible resonances including a quark and an antiquark, bounded by a gluon. The gluonic degree of freedom of such states, which can be interpreted as a vibration of the flux-tube confining the resonance, can influence the quantum number of the hybrid [17]. The typical interpretation consists in considering the case of a single gluon contributing with $J^P = 1^{+-}$ to the quantum number of the quark antiquark bound state. Eight of such states are predicted combining a gluon excitation with S-wave mesons, three of them with exotic quantum numbers which cannot be assumed by standard $q\overline{q}$ pairs. So far the best evidences of possible hybrid states have come from experiments studying antiproton proton annihilations. Two particles with the exotic quantum numbers $J^{PC} = 1^{-+}$ were measured at the LEAR facility: the $\pi_1(1400)$ [32] and the $\pi_1(1600)$ [33]. Hybrids in the charmonium sector are predicted with masses between 3 and 5 GeV/c^2. In this region, due to the lower density of resonances it should

be easier to measure and identify them. All the theoretical models foresee the lightest hybrid charmonium state to have a $J^{PC} = 1^{-+}$ assignment with a mass of about 4.2-4.4 GeV/c^2 [17]. These hybrids are supposed to be not too wide resonances, being below the open-charm decay threshold. The formation mechanism only allows to generate non-exotic states, therefore to look for exotic hybrids production measurements will be performed at the highest beam momentum. Another possible type of hadrons predicted by LQCD are the so-called *glueballs*, which consist of

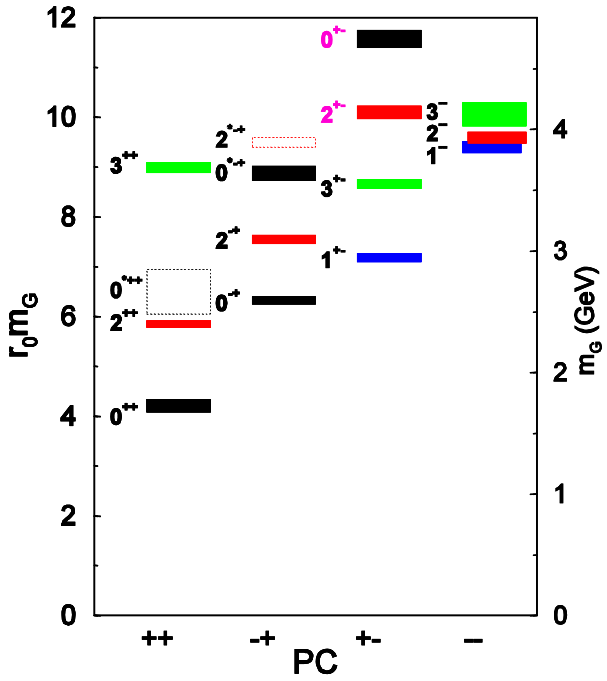

Figure 1.4: Spectrum of the LQCD prediction for the glueballs classified according to the quantum numbers assignment [27].

bound states of gluons without any quark contribution. LQCD calculations predicted more than ten glueballs, most of them in the mass region accessible at $\overline{\text{P}}$ANDA (see figure 1.4) and with widths in the order of 0.1 GeV/c^2. This would make the measurements of such states possible at the $\overline{\text{P}}$ANDA experiment. Glueballs with exotic numbers (the so-called oddballs) cannot mix with mesons and should be therefore easier to measure, due to their narrower width. LQCD studies foresee the lightest oddball to have a mass of ∼4.2 GeV/c^2 and $J^{PC} = 2^{+-}$ [34] [35]. Glueballs can be measured both at production and at formation experiments. The most probable decay channels are $\varphi\varphi - \varphi\eta$ for light glueballs and $J/\psi\varphi - J/\psi\eta$ for the heavier ones. Oddballs over the open-charm decay threshold will be much more difficult to measure because of the many more open decay modes and the consequent larger widths.

1.3 Hadrons in matter

The properties of hadrons in nuclear matter have been investigated both experimentally and theoretically. Mass values of the hadrons can be modified by the medium they are created in. This effect can be referred to differences in the chiral symmetry breaking due to the finite value density [36]. Widths of hadrons are predicted to become larger with the presence of a medium, since new decay channels become available. These effects are foreseen to be more evident for particles at rest or with low momenta.

Predictions have been made for the in medium modifications of open-charm and charmonium states, which will be experimentally accessible at the $\overline{\text{P}}$ANDA experiment. In particular a $D\overline{D}$ mass splitting of about 100 MeV/c^2 is foreseen [37], with the average $D\overline{D}$ mass being about 50 MeV/c^2 lower then in vacuum. In particular an estimate was made for a 50 MeV/c^2 D^+D^- mass splitting.

Another sector where $\overline{\text{P}}$ANDA can contribute to the exploration of in medium hadron modifications is the measurement of the J/ψ in medium dissociation cross section [38], which has been so far determined without clarifying its momentum dependance [39] [40]. The dissociation cross sections of J/ψ and other charmonium states is crucial for quark gluon plasma (QGP) [41] studies as well. One of the manifestations of a QGP state consists in the dissociation of charmonium states due to the screening of the strong interaction confining term. In order to disentangle the QGP "thermal" contribution to a decreasing number of charmonium states able to leave a fireball candidate, the hadronic dissociation cross section of the states under study must be known, as well as counterbalancing charmonium regeneration mechanisms [42].

1.4 Nucleon structure

$\overline{\text{P}}$ANDA will offer the possibility to probe the nucleon structure with different measurements. The generalized parton distributions (GPDs) framework [43] has been used to describe lepton scattering experiments. Recent studies allowed to describe in terms of GPDs the reactions $\overline{p}p \to \gamma\gamma/\pi^0\gamma$, which at the $\overline{\text{P}}$ANDA energy regime could be treated with handbag models [44] [45]. Measurements of Drell-Yan reactions such as $\overline{p}p \to l^+l^- + X$ where l represents the lepton family, will allow to investigate the quark transverse momentum distributions as well as the spectral function of quarks bound in nucleons [46]. The reconstruction of $\overline{p}p \to l^+l^-$ $(l = e, \mu)$ processes at $\overline{\text{P}}$ANDA enables to study the form factors of the proton in a wide time-like transferred momentum range, up to $q^2 \simeq 28$ $(\text{GeV/c})^2$. In particular complementing the measurements performed at the Tevatron by the E760 and by the E835 experiments [47], it will be possible to determine separately both G_E and G_M. So far the statistical sample collected by previous experiments has not been sufficient to determine both independently in this transferred momentum range, the actual results were achieved assuming $|G_E| = |G_M|$ [48].

1.5 Hypernuclear studies

Hypernuclear physics focuses on the study of hyperons bound into nuclei in which they substitute a nucleon. A single hyperon in a nucleus can occupy a large variety of nuclear states, since it is not limited by the Pauli exclusion principle. Hyper-nuclei are therefore a useful tool to study the nuclear structure. Hyperon properties can be studied as well, investigating the differences with the free case [49].

Different mechanisms can be used to generate hypernuclei: kaon beams colliding on targets (for example this is done at the J-PARC facility [50]), soft kaons produced by the decay of a resonance stopping in thin targets (for example at the DAFNE facility [51] the K^-s from the reaction $e^+e^- \to \varphi \to K^+K^-$ were used to generate hypernuclei studied with the FINUDA experiment [52]), other strange hadrons from particle decays implanted in nuclear targets.

The strategy at $\overline{\text{P}}$ANDA consists in using the $\overline{p}p \to \Xi^-\overline{\Xi}^+$ reaction. A dedicated configuration of the experimental setup will be used to perform measurements in the hypernuclear sector (see 2.7). The Ξ^-s will be stopped in a secondary target composed of interleaved layers of silicon detectors

and absorbing materials where double-Λ hypernuclei can be formed. The silicon detectors will allow to reconstruct the production vertex of the hypernuclei. An array of high purity germanium detector will measure the γ-rays produced by the de-excitation of the hypernuclei. Simulations were performed with a 3 GeV/c beam momentum, using available measurements and theoretical predictions for the cross sections involved [53]. The $\overline{\mathrm{p}}\mathrm{p} \to \Xi^-\overline{\Xi}^+$ cross section for a 3 GeV/c beam momentum is expected to be 2 μb [31]. The $\Xi^-\mathrm{p} \to \Lambda\Lambda$ conversion probability is estimated to be about 5%.

Bibliography

[1] H. D. Politzer. Reliable Perturbative Results for Strong Interactions? *Phys. Rev. Lett.*, 30:1346–1349, 1973. http://link.aps.org/doi/10.1103/PhysRevLett.30.1346.

[2] M. Pelizäus. Prospects for Panda: Charmonium Spectroscopy. *Presentation.* http://www-panda.gsi.de/db/talksDB/MP14-071017_Pelizaeus_071020.pdf.

[3] M. Andreotti et al. Measurement of the resonance parameters of the $\chi_1(1^3\mathrm{P}_1)$ and $\chi_2(1^3\mathrm{P}_2)$ states of charmonium formed in antiproton-proton annihilations. *Nucl. Phys. B*, 717(12):34 – 47, 2005. 10.1016/j.nuclphysb.2005.03.042.

[4] Gaiser et al. Charmonium spectroscopy from inclusive ψ' and J/ψ radiative decays. *Phys. Rev. D*, 34:711–721, 1986. http://link.aps.org/doi/10.1103/PhysRevD.34.711.

[5] L3 Collaboration. Hard-Photon Production and Tests of QED at LEP. *Phys. Lett. B 475:198-205*, 2000. arXiv:hep-ex/0002036.

[6] The ALEPH Collaboration, the DELPHI Collaboration, the L3 Collaboration, the OPAL Collaboration, the SLD Collaboration, the LEP Electroweak Working Group, the SLD electroweak, heavy flavour groups. Precision Electroweak Measurements on the Z Resonance. *Phys. Rept. 427:257-454*, 2006. arXiv:hep-ex/0509008.

[7] The DELPHI Collaboration. Determination of the $\mathrm{e}^+\mathrm{e}^- \to \gamma\gamma(\gamma)$ cross-section at LEP 2. *Eur. Phys. J. C37:405-419*, 2004. arXiv:hep-ex/0409058.

[8] M. Bleicher et al. Consistent Measurements of α_s from Precise Oriented Event Shape Distributions. Technical report, 2000. arXiv:hep-ex/0002026.

[9] S. Bethke, J.E. Pilcher. Tests of perturbative QCD at LEP. 1992. http://hdl.handle.net/10068/277893.

[10] S. Bethke. QCD Tests at $\mathrm{e}^+\mathrm{e}^-$ Colliders. 1997. arXiv:hep-ex/9710030.

[11] S. Bethke, M.L. Mangano, P. Nason. QCD in $\mathrm{e}^+\mathrm{e}^-$ collisions at 2 TeV. 1996. arXiv:hep-ph/9604332.

[12] S. Bethke. QCD Studies at LEP. arXiv:hep-ex/0406058.

[13] W. M. Yao et al. Review of Particle Physics. *J. Phys.*, G 33:1, 2006.

[14] R. Gupta. Introduction to Lattice QCD. 1998. arXiv:hep-lat/9807028.

[15] G. Bali et al. Spectra of heavy-light and heavy-heavy mesons containing charm quarks, including higher spin states for $\mathrm{N_f} = 2 + 1$. arXiv:1108.6147 [hep-lat].

[16] J. Soto. Overview of Non-Relativistic QCD. *Eur. Phys. J. A31:705-710*, 2007. arXiv:nucl-th/0611055.

[17] $\overline{\text{P}}$ANDA Collaboration. Physics Performance Report for $\overline{\text{P}}$ANDA: Strong Interaction Studies with Antiprotons. 2009. arXiv:0903.3905 [hep-ex].

[18] V. Koch. Introduction to Chiral Symmetry. 1995. arXiv:nucl-th/9512029.

[19] M. F. M. Lutz, E. E. Kolomeitsev. Chiral dynamics for exotic open-charm resonances. arXiv:hep-ph/0406015.

[20] T. Hilger, B. Kampfer. Chiral symmetry and open-charm mesons. arXiv:0904.3491 [nucl-th], 2009.

[21] A. Khare. The November J/ψ Revolution: Twenty-Five Years Later. *Curr. Sci. 77 (1999) 1210.* arXiv:hep-ph/9910468.

[22] J. Beringer et al. (Particle Data Group). PR D86, 010001 (2012). http://pdg.lbl.gov.

[23] P. Gianotti. Results and perspectives in hadron spectroscopy. *Physica Scripta*, 2012(T150):014014, 2012. http://stacks.iop.org/1402-4896/2012/i=T150/a=014014.

[24] S. Godfrey, N. Isgur. Mesons in a relativized quark model with chromodynamics. *Phys. Rev. D*, 32:189–231, Jul 1985. http://link.aps.org/doi/10.1103/PhysRevD.32.189.

[25] N. A. Törnqvist. Possible large deuteronlike meson-meson states bound by pions. *Phys. Rev. Lett.*, 67:556–559, 1991. http://link.aps.org/doi/10.1103/PhysRevLett.67.556.

[26] Nils A. Törnqvist. Isospin breaking of the narrow charmonium state of Belle at 3872 MeV as a deuson. *Phys. Lett. B 590:209-215*, 2004. 10.1016/j.physletb.2004.03.077.

[27] E. Klempt, A. Zaitsev. Glueballs, hybrids, multiquarks: Experimental facts versus QCD inspired concepts. *Phys. Rep.*, 454(1 - 4):1 – 202, 2007. http://dx.doi.org/10.1016/j.physrep.2007.07.006.

[28] M. C. Mertens. Determination of the $D^*_{s0}(2317)$ width with the $\overline{\text{P}}$ANDA detector. *Hyperfine Interactions*, 209:111–115, 2012. http://dx.doi.org/10.1007/s10751-012-0565-z.

[29] E. Klempt, J.-M. Richard. Baryon spectroscopy. *Rev. Mod. Phys. 82:1095-1153*, 2010. arXiv:0901.2055 [hep-ph].

[30] A. Khodjamirian, Ch. Klein, Th. Mannel, and Y.-M. Wang. How much charm can $\overline{\text{P}}$ANDA produce? *Eur. Phys. J. A* , 48:1–12, 2012. 10.1140/epja/i2012-12031-8.

[31] A. B. Kaidalov and P. E. Volkovitsky. Binary reactions in $\bar{\text{p}}$p collisions at intermediate energies. *Zeitschrift für Physik C Particles and Fields*, 63:517–524, 1994. http://dx.doi.org/10.1007/BF01580332.

[32] Crystal Barrel Collaboration. Exotic $\eta\pi$ state in $\bar{\text{p}}$d annihilation at rest into $\pi^-\pi^0\eta p_{\text{spectator}}$. doi: 10.1016/S0370-2693(98)00123-3.

[33] Crystal Barrel Collaboration, J. Reinnarth. Evidence for an exotic partial wave in $\pi\eta$'. doi: 10.1016/S0375-9474(01)01186-1.

[34] C. J. Morningstar, M. Peardon. The glueball spectrum from an anisotropic lattice study. *Phys. Rev. D*, 60:034509, 1999. arXiv:hep-lat/9901004v2.

[35] E. Gregory et al. Towards the glueball spectrum from unquenched lattice QCD. arXiv:1208.1858 [hep-lat].

[36] U. Mosel. Hadrons in Medium – Theory meets Experiment. 2008. arXiv:0801.4970 [hep-ph].

[37] A. Sibirtsev, K. Tsushima, A. W. Thomas. On Studying Charm in Nuclei through Antiproton Annihilation. arXiv:nucl-th/9904016.

[38] A. Sibirtsev, K. Tsushima, K. Saito, A. W. Thomas. Novel features of J/ψ dissociation in matter. 2000. arXiv:nucl-th/9904015.

[39] B. Alessandro et al. J/psi and psi-prime production and their normal nuclear absorption in proton-nucleus collisions at 400-GeV. *Eur. Phys. J.* , C48:329, 2006. http://dx.doi.org/10.1140/epjc/s10052-006-0079-4.

[40] B. Alessandro et al. Charmonium production and nuclear absorption in p-A interactions at 450 GeV. oai:cds.cern.ch:644496. *Eur. Phys. J. C*, 33(CERN-EP-2003-037):31–40. 16 p, Jun 2003.

[41] M. Gyulassy. The QGP Discovered at RHIC. 2004. arXiv:nucl-th/0403032.

[42] T. Matsui, H. Satz. J/ψ suppression by quark-gluon plasma formation. *Phys. Lett. B178 (1986) 416*. doi: 10.1016/0370-2693(86)91404-8.

[43] Xiangdong Ji. Generalized parton distributions. *Annu. Rev. Nucl. Part. Sci. 2004. 54:413–50*. doi: 10.1146/annurev.nucl.54.070103.181302.

[44] M. Diehl, Th. Feldmann, R. Jakob, P. Kroll. Linking parton distributions to form factors and Compton scattering. *Eur. Phys. J. C - Particles and Fields*, 8:409–434, 1999. 10.1007/s100529901100.

[45] A.V. Radyushkin. Nonforward parton densities and soft mechanism for form-factors and wide angle Compton scattering in QCD. *Phys. Rev.* , D 58:114008, 1998. http://dx.doi.org/10.1103/PhysRevD.58.114008.

[46] O. Linnyk, K. Gallmeister, S. Leupold, U. Mosel. Prediction for the transverse momentum distribution of Drell-Yan dileptons at GSI-PANDA. *Phys. Rev. D 73:037502*, 2006. arXiv:hep-ph/0506134.

[47] The E760/E835 experiments. http://www.e835.to.infn.it/.

[48] M. Sudol. Feasibility studies of the time-like proton electromagnetic form factor measurements with PANDA at FAIR. arXiv:0907.4478 [nucl-ex].

[49] J. Pochodzalla, A. Botvina, A. Sanchez Lorente. Studies of Hyperons and Antihyperons in Nuclei. *PoS BORMIO2010: 033,2010*. arXiv:1101.3181 [nucl-ex].

[50] T. Nagae. Hypernuclear and strangeness physics program at J-PARC. *Pramana*, 75:207–214, 2010. http://dx.doi.org/10.1007/s12043-010-0109-5.

[51] The LNF DAFNE Home Page. http://www.lnf.infn.it/acceleratori/.

[52] P. Gianotti. The FINUDA apparatus and its physics. *Nucl. Phys. B - Proceedings Supplements*, 78(1–3):145 – 150, 1999. http://dx.doi.org/10.1016/S0920-5632(99)00537-X.

[53] Y. Hirata, Y. Nara, A. Ohnishi, T. Harada, J. Randrup. Quantum fluctuation effects on hyperfragment formation from Ξ^- absorption at rest on ^{12}C. *Prog. Theor. Phys. 102 (1999) 89-119.* arXiv:nucl-th/9711063.

CHAPTER 2

The $\overline{\text{P}}$ANDA experiment

The $\overline{\text{P}}$ANDA experiment [1] is one of the key projects of the FAIR facility [2] which is under construction in Darmstadt (Germany). $\overline{\text{P}}$ANDA will perform precision measurements analyzing the final state particles produced by collisions between a beam of antiprotons and different fixed targets.

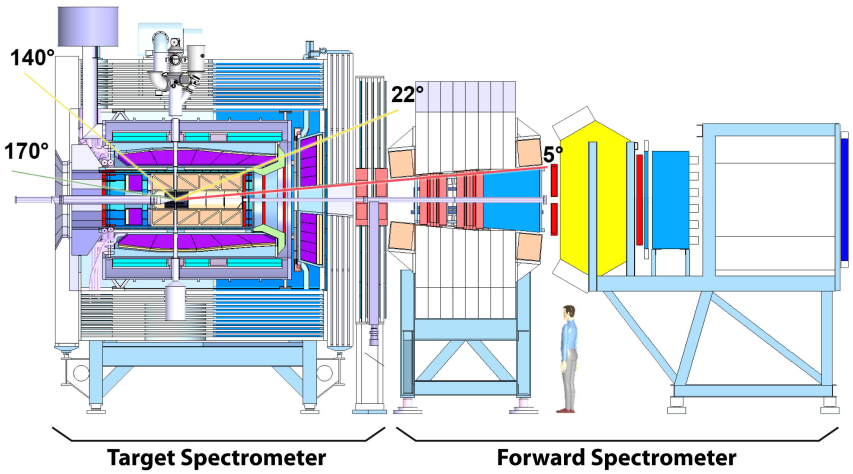

Figure 2.1: Side view of the whole $\overline{\text{P}}$ANDA experimental setup.

The experimental setup is composed of two main parts:

- the target spectrometer which surrounds the interaction region and is permeated by a 2T solenoidal magnetic field;
- the forward spectrometer which measures particles flying at small polar angle in the forward direction and sits downstream from a 2T · m dipole magnet.

2.1 The antiproton beam

The FAIR facility will consist of several accelerators offering the possibility to investigate different branches of the physics research (see figure 2.2). $\overline{\text{P}}$ANDA will mostly focus on hadron physics (as described in the previous chapter), but other experiments will cover fields such as nuclear matter physics, nuclear structure, astrophysics, quark gloun plasmas. The FAIR accelerators will be able to cast beams of protons and heavier ions. The protons are initially accelerated by

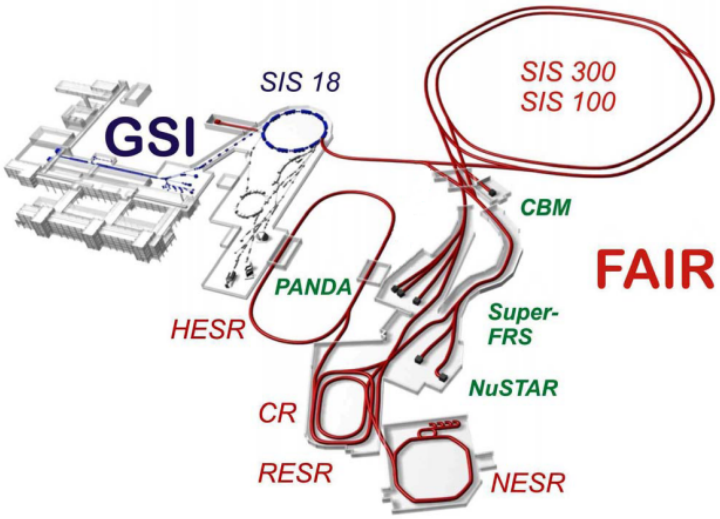

Figure 2.2: Scheme of the accelerators available at the FAIR facility showing the sites of the main experiments [3].

a dedicated proton LINAC [4] up to a energy of 70 MeV which is necessary for the injection in the SIS-100 synchrotron [5]. The SIS-100 accelerates the proton beam up to an energy of 29 GeV. These protons can be collided on a production target [6] in order to create antiprotons. The properties of such a production target must be optimized to reach a compromise between antiproton production probability, collection efficiency, heat dissipation and magnetic rigidity. The antiproton production cross section grows with the proton energy. However with higher energies the produced antiprotons have higher momenta: it is then more difficult to collect them and to bend them toward the following elements. Therefore 29 GeV protons are preferable for this purpose to the 90 GeV available at the SIS-300. The production target itself is a crucial component in order to maximize the final antiproton beam intensity. The antiproton production yield grows with thicker targets as long as the absorption of the produced antiprotons does not dominate the process. The optimal length for the target is a compromise between these two aspects. Materials with higher densities are preferable because they allow to use thinner targets, therefore improving the efficiency of the collection of the produced antiprotons. Nevertheless, materials with high atomic numbers have a low heat capacity and absorb a higher fraction of the secondary cascades generated by the primary proton interaction. Therefore they cannot be used otherwise the target could be melted by the heat produced by the collision of intense beams. The optimal compromise was found to be an 11 cm long target realized with copper or nickel, which leads to a yield of 2×10^{-5} antiprotons per primary proton, with the SIS bunches typically consisting of 2.5×10^{13} protons. The 3 GeV antiprotons produced at the production target are piped to the High Energy Storage Ring (HESR) [7], which acts both as a storage ring and as an accelerator (see figure 2.3). The HESR prepares the final beam used for $\overline{\text{P}}$ANDA with momenta between 1.5 GeV/c and 15 GeV/c depending on the physics requirements. The HESR

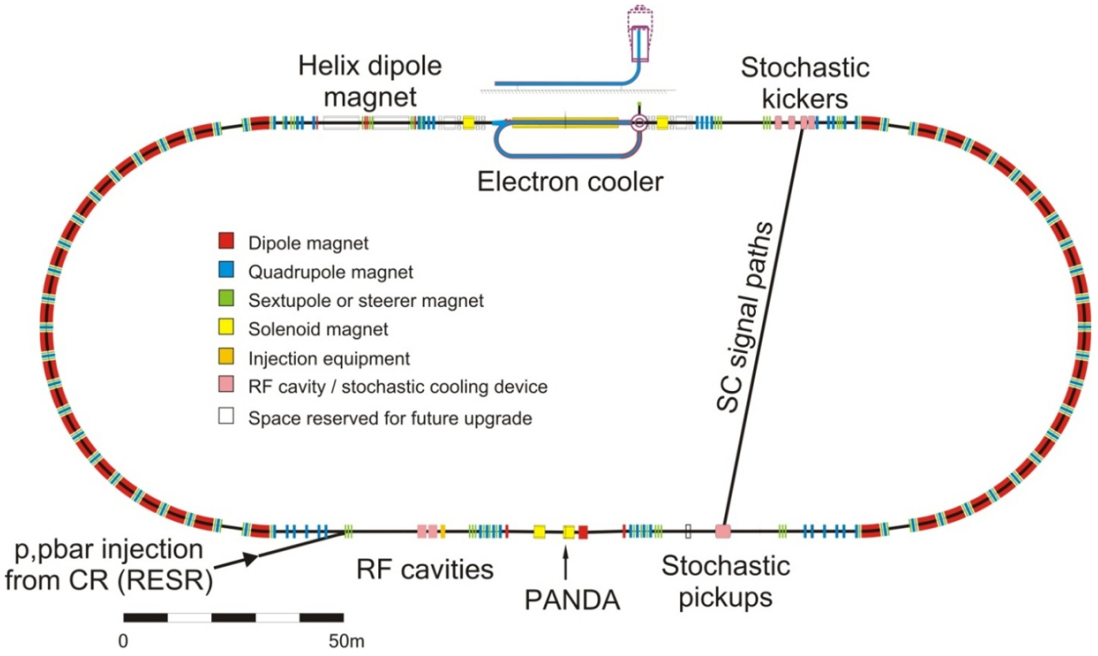

Figure 2.3: Structure of the HESR used to store and accelerate antiprotons [3].

has two operation modes:

- the high intensity mode where the highest luminosity of $2 \cdot 10^{32}\,\mathrm{cm^{-2}s^{-1}}$ can be achieved with 15 GeV/c antiprotons and a beam momentum resolution of $\delta p/p \sim 10^{-4}$;
- the high resolution mode in which the beam momentum is know with a better precision ($\delta p/p \sim 10^{-5}$) and the maximum luminosity is one order of magnitude lower. In this operational mode a maximum beam momentum of 8.9 GeV/c can be achieved.

Stochastic cooling is used in the high luminosity mode, while an electron cooler can be used for beam momenta up to 8.9 GeV/c in the high resolution mode.

2.2 The target for the $\overline{P}$ANDA experiment

$\overline{P}$ANDA is a fixed target experiment and will mostly focus on the collisions of antiprotons on protons. Two different technical solutions have been developed to provide the experiment with a target able to fulfill the requirements of the physics program [8]. Both options are compatible with the mechanical structure of the detectors and of the solenoidal magnet. The aim of studying rare processes requires $\overline{P}$ANDA to achieve luminosities up to $2 \cdot 10^{32}$ $\mathrm{cm^{-2}s^{-1}}$. This implies the necessity of high target densities. The goal of both technical options is to reach an effective target density of $4 \cdot 10^{15}$ hydrogen atoms per square centimeter.

2.2.1 The cluster jet target

The cluster jet technique [9] consists in producing frozen hydrogen clusters with an expansion of a pre-cooled gas injected into the vacuum. The gas passes through a nozzle realizing an adiabatic cooling and forms a supersonic beam of clusters. Typical hydrogen clusters consist of

$10^3 - 10^6$ molecules, therefore they are not influenced by the scattering with residual gases. This is important since it allows a cluster jet to travel for several meters without significant changes in the beam direction and size. A prototype with the dimensions necessary to serve the $\overline{P}$ANDA experiment was built and could achieve a target density of $1.6 \cdot 10^{15}$ atoms/cm^2. Higher numbers can be obtained with further improvements. The cluster jet target allows to modify the density during the operation, this feature can be used to compensate the beam intensity loss during an HESR cycle in order to maintain the luminosity as much stable as possible. With this kind of target the density is well homogeneous along the stream and there is no time structure. Heavier gases can be used producing for example clusters of H_2, D_2, O_2, N_2, Ne, Ar, Kr and Xe. In this case the required initial gas temperature is higher, therefore the are no technological limitations to the usage of this target system to study collisions with heavier nuclei.

2.2.2 The pellets target

This technology [9] consists in injecting through a nozzle a cryogenic gas in a chamber. The chamber is filled with gas of the same element at conditions close to its triple point. The nozzle is regulated by a piezoelectric transducer which breaks the flow into a series of drops. A capillary is then injecting these drops into vacuum. During this last operation the temperature of the drops decreases of a few degrees due to surface evaporation, reaching a temperature below the triple point. In this way the drops become frozen pellets which can be used as targets. The pellets targets have two main advantages as compared to the cluster jet ones: it is possible to reach higher target densities and each pellet can be tracked allowing a better reconstruction of the interaction point. The main disadvantage consists in the stochastic time structure of the density. Large thickness variations appear in a time scale from 10 µs to some ms. This is mostly due to the spread in the speed at which the pellets are injected into vacuum. A speed fluctuation of less the a per mille is necessary to suppress the stochastic fluctuation in time.

2.3 The experimental conditions

The luminosity aimed at $\overline{P}$ANDA is $2 \cdot 10^{32}\text{cm}^{-2}\text{s}^{-\text{s}}$. The beam intensity will not be constant: within an injection cycle it decays exponentially due to the beam-target interactions, which consist mainly of hadronic interactions, single Coulomb scatterings and energy straggling. The loss of particles due to intra-beam interaction are negligible as compared to the previously cited effects. The beam loss rate can be parametrized as $R_{loss} = \tau^{-1} = f_0 \cdot n_t \cdot \sigma_{tot}$ [9], where f_0 is the antiprotons revolution frequency, n_t is the effective target density (atoms/surface), σ_{tot} is the total interaction cross section and τ is the mean beam lifetime. If the density of the target is constant then the luminosity decreases within an injection cycle. The cluster jet target offers the possibility to modify the density within an injection cycle: this allows to tune the density in order to keep the luminosity as much stable as possible.

The two scenarios are summarized in figure 2.4. In order to maximize the average luminosity the antiprotons still present in the ring at the end of a cycle can be kept in the storage ring, restoring the initial momentum and mixing them with the newly injected particles. To reach this purpose the beam structure along the ring will not be homogenous, an empty bucket corresponding to 10% of the orbit length will be left for the injection of new particles. This means that in a situation with constant luminosity the average luminosity will correspond to 90% of the instantaneous one.

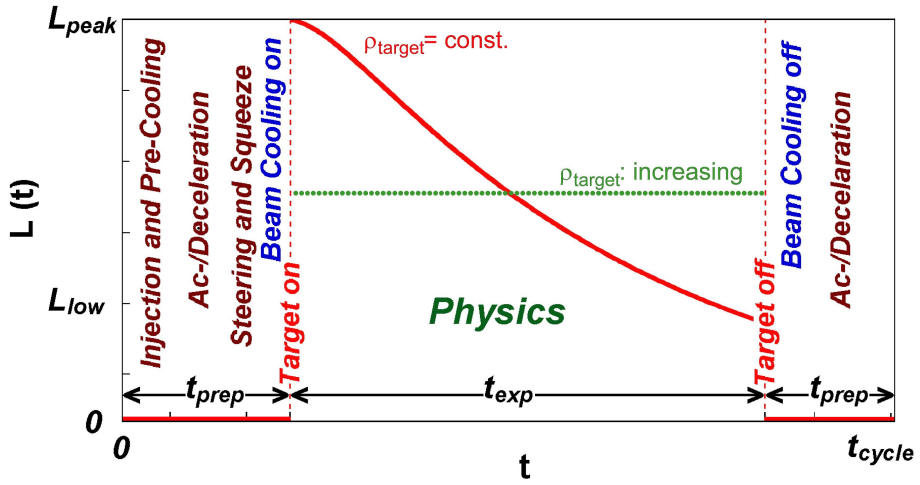

Figure 2.4: Structure of the luminosity trend between two consecutive antiprotons injections. The red line refers to a scenario with a fixed target density, while the green dash line refers to the possibility of compensating the lower beam intensity with a higher target density [3].

According to the notation of figure 2.4 the average luminosity can be formulated as [9]:

$$\overline{L} = N_{\overline{p},0} \cdot f_0 \cdot n_t \cdot \frac{\tau \left[1 - e^{-t_{exp}/\tau}\right]}{t_{exp} + t_{prep}}$$

where $N_{\overline{p},0}$ is the initial number of particles injected in the ring.

Beam momentum (GeV/c)	1.5	9	15
σ_0 (mbarn)	100	57	51
Cluster jet target			
Target density $\left(\text{atoms/cm}^2\right)$	$8 \cdot 10^{14}$		
t_{prep} (s)	120	140	290
t_{cycle} (s)	1280	2980	4750
τ (s)	∼5920	∼29560	∼35550
Max. Luminosity $\left(\text{cm}^{-2}\text{s}^{-1}\right)$	$0.29 \cdot 10^{32}$	$0.38 \cdot 10^{32}$	$0.37 \cdot 10^{32}$
Pellet target			
Target density $\left(\text{atoms/cm}^2\right)$	$4 \cdot 10^{15}$		
t_{prep} (s)	120	140	290
t_{cycle} (s)	4820	1400	2230
τ (s)	∼1540	∼6000	∼7100
Max. Luminosity $\left(\text{cm}^{-2}\text{s}^{-1}\right)$	$0.53 \cdot 10^{32}$	$1.69 \cdot 10^{32}$	$1.59 \cdot 10^{32}$

Table 2.1: Estimates of the cycle properties at different momenta with the two hydrogen options [10].

Table 2.1 summarizes the performance achievable at the HESR with different beam momenta and target configurations. It was previously mentioned that the pellet target density can suffer

from stochastic fluctuations on short time scales. In order to prevent this the distance between consequent pellets must be monitored as well as their trajectories. The ratio between the peak and the average luminosity is a function of the pellet size: in order to prevent the instantaneous luminosity to exceed $10^{33}\text{cm}^{-2}\text{s}^{-1}$ which would create pile-ups in the detectors the pellet size must be kept below 20 µm [10].

2.4 Target Spectrometer

The target spectrometer surrounds the interaction point with an onion shell-like configuration of different detectors. Its three main geometrical parts (forward end cap, barrel and backward end cap) allow to cover polar angles between $5-10°$ and $170°$. The barrel part (which covers the polar range between $22°$ and $140°$) is equipped with trackers, particle identification detectors, an electromagnetic calorimeter and muon detectors (see figure 2.5). The whole target spectrom-

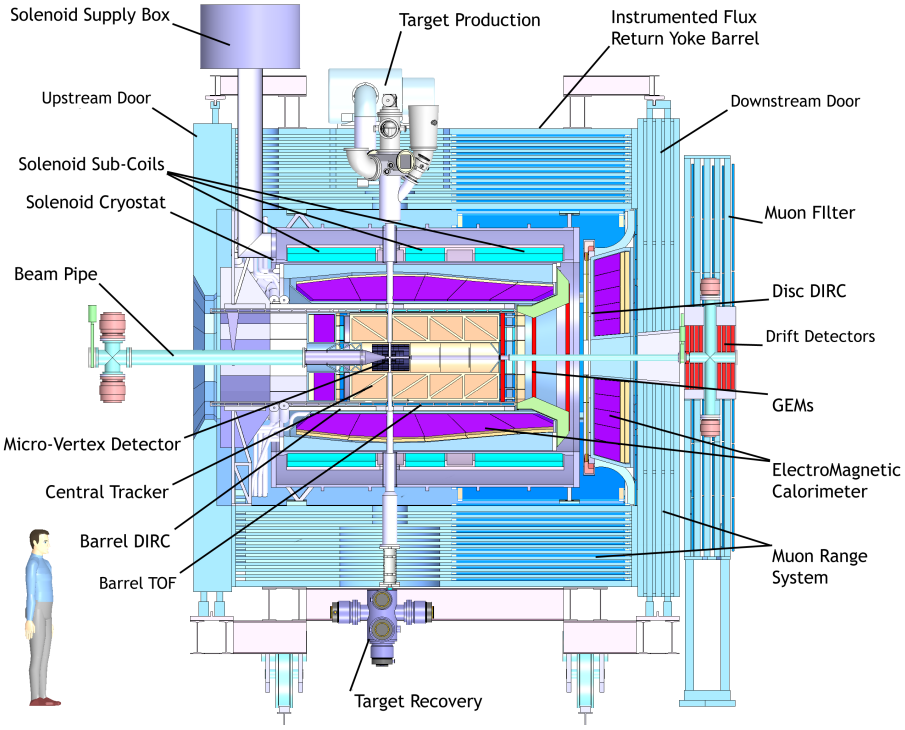

Figure 2.5: Side view of the target spectrometer.

eter is permeated by a 2T solenoidal magnetic field which allows the reconstruction of tracks corresponding to charged particles. The onion shell-like structure of the spectrometer develops around the beam pipe axis. Cut outs in both the detectors and the magnets are implemented to allow the insertion of the target pipes and its necessary infrastructure.

2.4.1 Tracking

The track reconstruction for charged particles is realized in the target spectrometer with the combination of three detectors: the Micro-Vertex-Detector close to the interaction point surrounded by the Straw Tube Tracker, with three Gas Electron Multiplier disks in the forward direction.

The Micro-Vertex-Detector

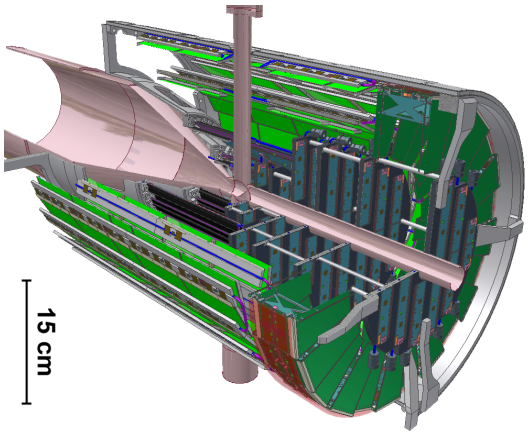

Figure 2.6: A cut-out of the MVD seen from downstream [3].

The Micro-Vertex-Detector (MVD) [3] is the innermost detector of $\overline{\text{P}}$ANDA.

It is designed to measure hit points generated by charged particles as close as possible to the interaction point.

The MVD will contribute to the vertex and momentum reconstruction in combination with the other tracking detectors. One of its most important goals is to reconstruct the decays of short-lived particles (such as for example open-charm mesons and short-lived heavy baryons) distinguishing the secondary vertices from the primary interaction point.

Since this is the innermost detector the flux of particles will be maximum, therefore the detector is designed to deal with high rates and to have the necessary radiation hardness. The detector will be equipped with both silicon pixel and silicon strip sensors. A more detailed description of the geometry and of the performances of the MVD can be found in the next chapters.

The Straw Tube Tracker

The Straw Tube Tracker (STT) [10] is the central tracker of the experiment. A straw tube is a drift chamber with cylindrical geometry: an aluminized mylar tube with a diameter of 10 mm and a thickness of 27 µm is filled with a mixture of gases and acts as a cathode.

A 20 µm thick gold plated tungsten wire positioned along the axis of the mylar tube is used as anode. The gas used to fill the tubes of the $\overline{\text{P}}$ANDA STT will be a mixture of Ar and CO_2, this last one used as a quencher.

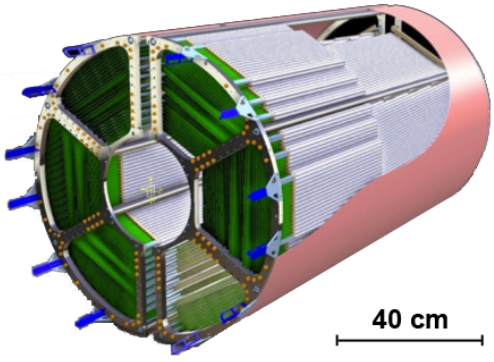

Figure 2.7: The Straw Tube Tracker seen from upstream [10].

The STT consists of 27 layers of 150 cm long tubes: most of the layers lay parallel to the beam axis, while 8 skew layers are positioned with a stereo angle of $\pm 2.9^\circ$ with respect to the other tubes. In total 4636 straw tubes are foreseen to equip the STT. The drift time in each tube allows to measure a radial distance from the anodic wire. This results in a position resolution in the transverse (x-y) plane better than 150 µm. The longitudinal coordinate (parallel z axis) is determined matching the hits measured by the skew layers. This allows to reach a longitudinal position resolution of about 3 mm.

The GEM Stations

Gas Electron Multiplier (GEM) [11] foils will be used to equip forward disks necessary to complement the geometrical coverage of the STT. Three disks will be positioned respectively 1.1, 1.4 and 1.9 m downstream from the interaction point to cover polar angles below 22°. A disk consists of two planes, each of them foreseeing two projections. Each disk will then have four projections, which allow to resolve ambiguities when several hits are measured on one plane. All the three disks have an internal radius of 2.5 cm, while the external radii grow proceeding along the beam axis: respectively the first disk has an external radius of 45 cm, the second one of 56 cm and the last one of 74 cm.

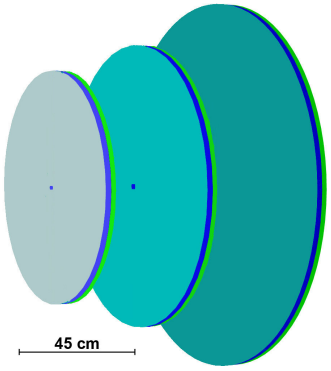

Figure 2.8: The GEM stations.

2.4.2 Particle identification

The target spectrometer foresees three detectors aiming to provide most of the information required to perform efficiently particle identification in the $\overline{P}ANDA$ experimental regime. A barrel detector based on the Detection of Internally Reflected Cherenkov (DIRC) [12] light will cover the polar angle range between 22° and 140°. Slabs realized with fused silica featuring a radial thickness of 1.7 cm will be disposed along a barrel at radial distances of about 50 cm from the beam axis. Lenses will focus the produced Cherenkov light toward micro-channel plate photomultipliers positioned in the backward region of the experiment. These photomultipliers were chosen since they can efficiently work in a magnetic field as the one of the target spectrometer. A similar concept is applied to the forward region: a 2 cm thick fused silica disk with a radius of 110 cm is positioned upstream from the barrel DIRC covering polar angles between 5° and 22°. In this case the light will be focused toward the outer radius of the disk where photomultipliers will be placed along a rim. The whole DIRC detector including both the barrel part and the forward disk is illustrated in figure 2.9a. The third detector used for particle identification is a

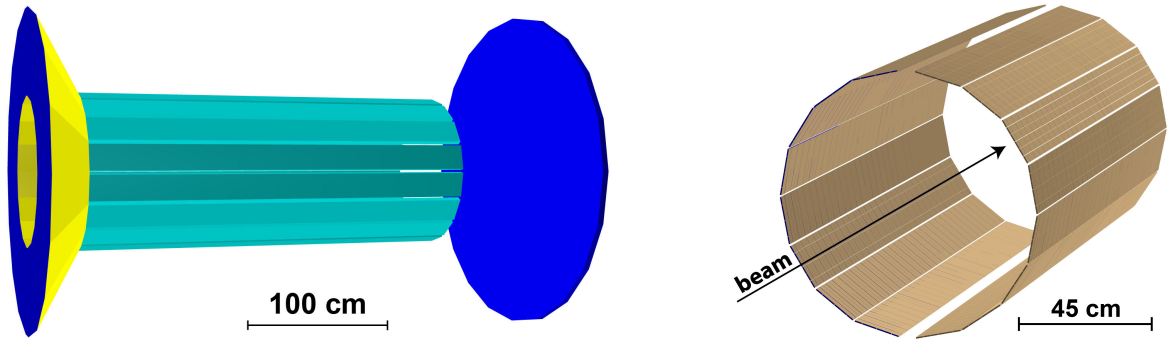

(a) The barrel part and the forward end cap of the DIRC.

(b) The Scintillator Tile Barrel.

Figure 2.9: The detectors of the target spectrometer used for particle identification.

scintillator tile barrel [13] which is meant to identify slow particles with large initial polar angles. This detector will be realized with 5760 scintillator tiles disposed in a barrel configuration just outside the DIRC volume (see figure 2.9b). Each tile will be read-out with two silicon photo-

multipliers, providing a fast signal with a time resolution of about 100 ps. The time of flight information can be therefore used to identify different particle species at low momenta. The fast signal provided by this detector might be also useful as a seed for fast pattern recognitions and trigger algorithms.

2.4.3 Electromagnetic calorimetry

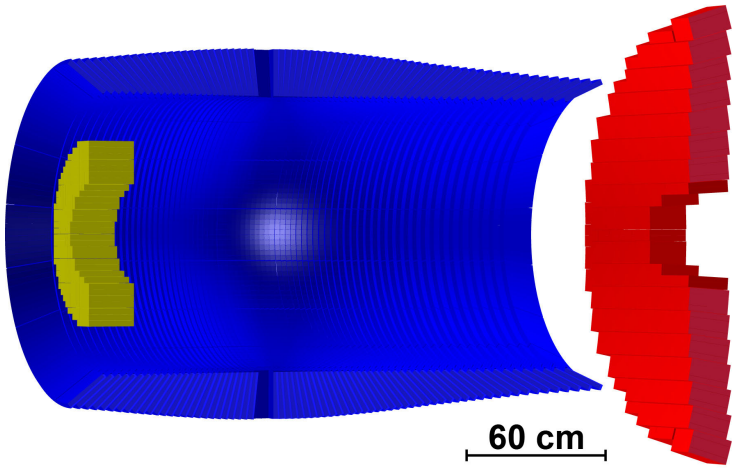

Figure 2.10: Lateral section of the electromagnetic calorimeter. The barrel part is drawn in blue, the forward end cap in red and the backward end cap in green.

The electromagnetic calorimeters (EMC) [14] will be used at $\overline{\text{P}}$ANDA to measure neutral particles (such as π^0 and photons), leptons and hadrons. The EMC can also complement the particle identification information provided by the DIRC and the TOF detectors. This contribution will be especially powerful in distinguishing electrons from charged pions.

Several requirements must be satisfied by the material chosen to realize the crystals: the calorimeter must be compact, it is required to have a % level energy resolution, due to the high rates its response must be fast and the crystal needs to have an appropriate radiation hardness. All these consideration led to the choice of lead tungstate ($PbWO_4$) [15], which has short radiation length (8.8 mm) and Moliere radius (2.19 cm). The crystal will be 20 cm long, corresponding to about 22 radiation lengths: this allows to keep most of the electromagnetic showers within a compact volume. The EMC will operate at a temperature of –25 °C to improve the light yield as compared with that one achievable at room temperature (an improvement of a factor 4 is expected).

The EMC is composed of three parts. The barrel calorimeter covers the region around the TOF tiles with an inner radius of 57 cm. It consists of 11360 crystals read out with radiation hard avalanche photo diodes. The forward end cap is composed of 3600 crystals, which are read out with vacuum photo-triodes. Both for the barrel and for the forward end cap tapered crystals will be used. The position and the direction of each crystal have been optimized in order to point toward the region around the primary vertex, where most of the particles will come from. In order to cover large polar angle up to 170° a backward end cap consisting of 592 parallelepiped crystals will be positioned upstream from the end of the barrel calorimeter. Figure 2.10 shows a vertical section of the three detectors: from left to right the backward end cap, the barrel calorimeter and the forward end cap can be observed.

2.4.4 The muon detector

The muon detector [16] is the most external detector of the target spectrometer. It makes use of Mini Drift Tubes (MDT), which are drift tubes with a central anodic wire. These tubes can directly measure one of the two coordinates along a detector plane. A series of pads disposed along the length of the tubes allows to measure the induced signals and, therefore, to reconstruct the longitudinal coordinate as well. Due to the necessity of distinguishing muons from other particles, the active components of this detector are interleaved with the iron layers of the magnet return yoke with a granularity of 3 cm. The position of each detecting plane and the number of interleaved stages are optimized to maximize the efficiency of the muon recognition. The detector is composed by two main parts: the barrel and the forward end cap. A bilayer composed of two consecutive detector planes is positioned before the first yoke layer. It is aimed to help the back propagation of muon tracks toward the primary interaction point and to facilitate the overall muon tracking. Downstream from the end cap a muon filter is positioned, which is mechanically identical to the end cap. The purpose of this filter is double: it improves the detection of muons at intermediate angles since it increases the thickness of the available absorbers and at the same time it shields the solenoidal magnetic field allowing a better separation between the target and the forward spectrometers.

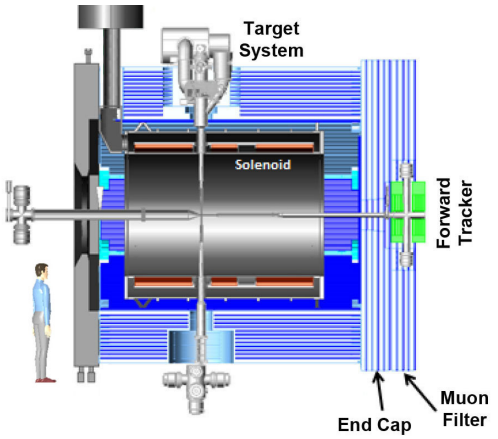

Figure 2.11: Cross section showing the interleaved layers of the magnet yoke and the MDT [16].

2.4.5 The solenoidal magnet

The superconducting solenoid [17] is designed to provide a homogeneous 2T magnetic field to the target spectrometer. The geometry foresees a warm bore with a 1.9 m diameter. The insertion of the vertical target pipe requires the solenoid to be split leaving a hole with 100 mm diameter. The solenoid is therefore divided in three parts which are tuned to provide a uniform field compensating the effect of the target pipe hole. The return yoke is used in combination with the MDTs to detect muons with polar angles below 70°. The optimization of the geometry of the coil and of the return yoke takes into account the occupancy of the detectors and connected infrastructures, the maximum magnetic field tolerable from some components (for example the DIRC photomultipliers) and the need for a highly homogeneous field. In particular the magnet is designed to keep the field variations below a 2% in all the volume occupied by the MVD and the STT. Figure 2.12 shows the superconducting coil on the left and the integration of the whole magnet with the target spectrometer on the right.

2.5 Forward spectrometer

The forward spectrometer will be used to measure particles with polar angles below 5° in the vertical direction and 10° in the horizontal plane. Both charged and neutral particles will be measured with trackers, a calorimeter, muon detectors and detectors suited for particle

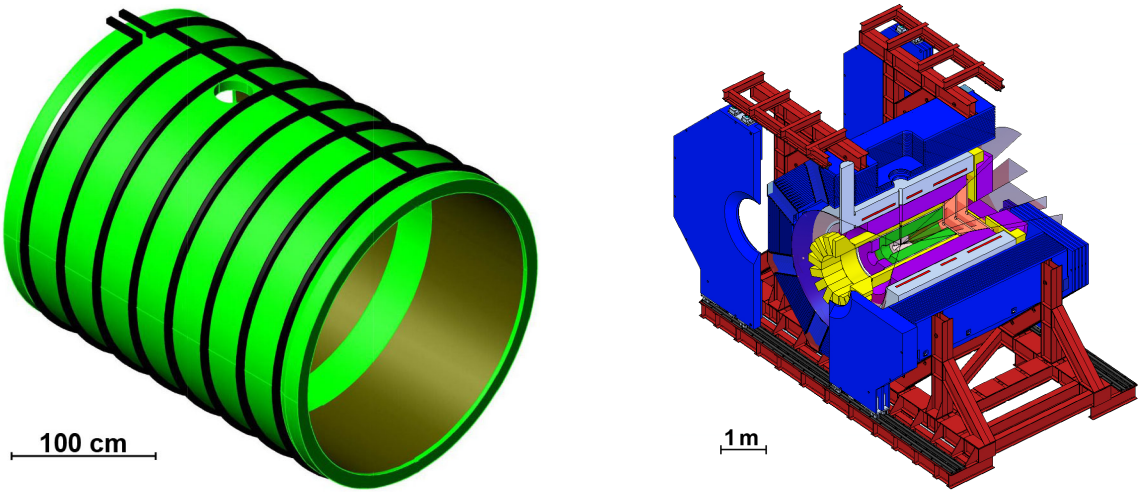

Figure 2.12: The solenoidal magnet on the left and a clipped view from upstream of the yoke integrated with the target spectrometer [17].

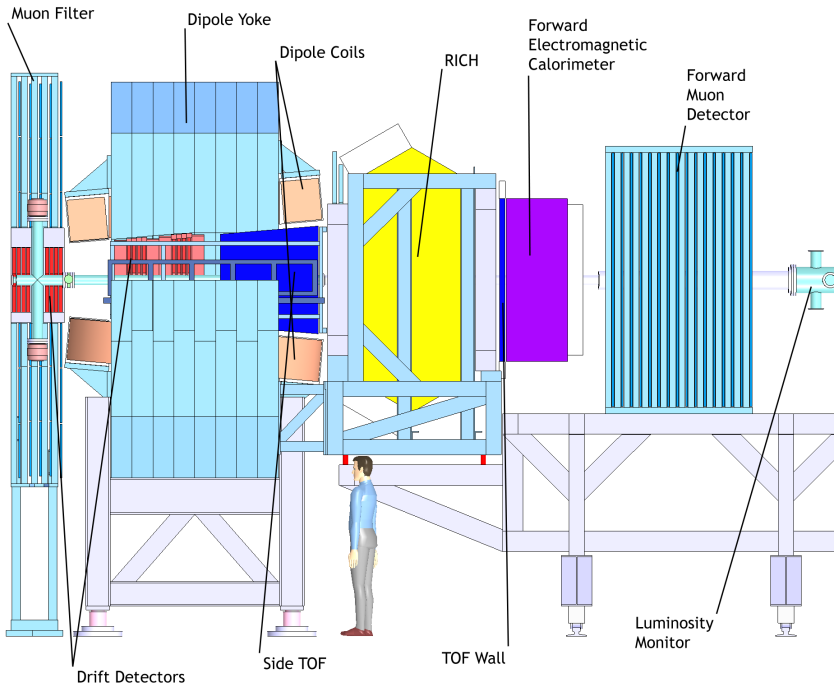

Figure 2.13: The forward spectrometer.

identification. A dipole positioned before the forward spectrometer allows to analyze charged particles. Figure 2.13 shows a side view of the full forward spectrometer.

2.5.1 The forward straw tubes

Straw tubes with a planar disposition will be used to track charged particles at small angles. Three different sets of planes will be positioned respectively before, in the middle and after the dipole magnet. Each set will consist of two individual detector, each composed of four STT

planes. Two of these planes will be equipped with vertical tubes, the remaining two planes will have a stereo angle of a few degrees to allow the reconstruction of the vertical coordinate. This system will perform the measurement of the deflection of charged particles and, therefore, reconstruct their momenta. The whole set of straw tube planes is illustrated in figure 2.14.

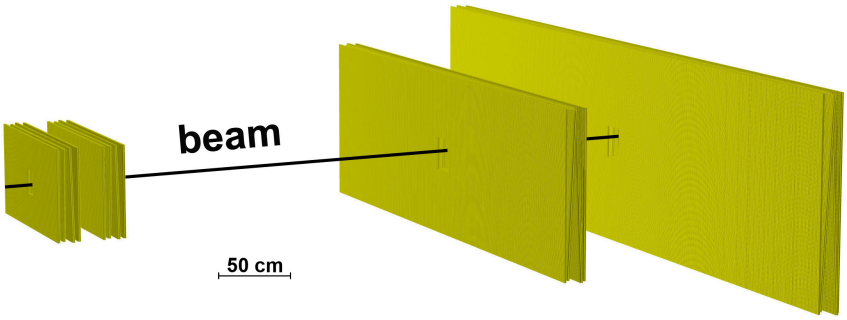

Figure 2.14: The forward straw tube trackers.

2.5.2 The Shashlik calorimeter

A Shashlik calorimeter [18] is used to detect photons and electrons in the forward region. This system is realized with scintillators alternated with lead layers. Optical fibers going through the length of the calorimeter are used to propagate the light toward some photomultipliers positioned at the back side. The calorimeter will be equipped with modules subdivided in four smaller units (55×55 mm^2) in order to improve the spacial resolution. Figure 2.15 shows the

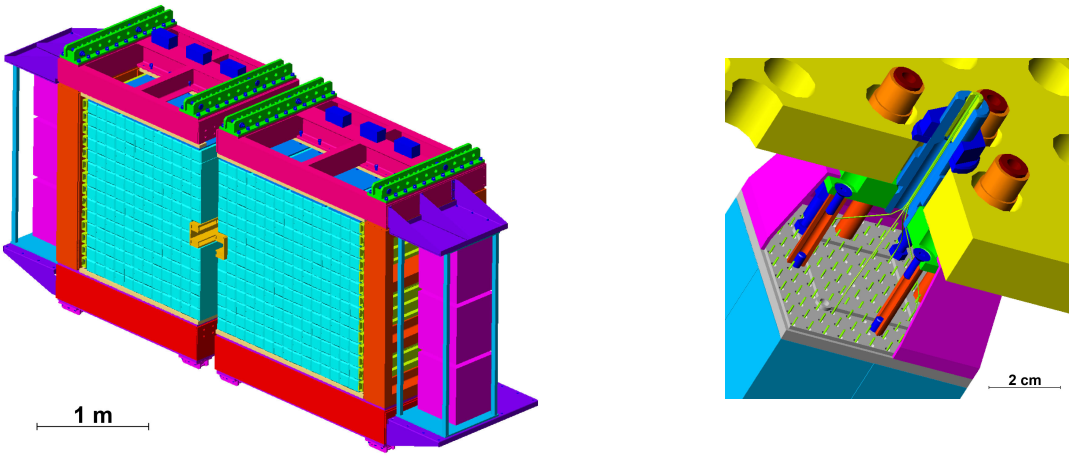

Figure 2.15: The forward Shashlik calorimeter: the whole geometry is shown on the left, a detail of the backside of one module is visible on the right [18].

geometry of the calorimeter on the left. The figure on the right exemplifies the backside of one module with the optical fibers routed toward the photomultipliers. The whole calorimeter will consist of 351 modules. They will be 68 cm long, which corresponds to twenty radiation lengths. An energy resolution of approximately $4\%/\sqrt{E}$ is expected to be achieved.

2.5.3 Particle identification

Particle identification will be realized with two detectors in the forward spectrometer: a ring imaging Cherenkov detector (RICH) and a time of flight (TOF) wall. The RICH will be based on two radiators with different refraction indices: silica aerogel (n=1.0304) and C_4F_{10} (n=1.00137). This will allow to have a good separation power for pions, kaons and protons in a wide momentum range. The TOF wall realized with plastic scintillator slabs read out from both sides by phototubes (see figure 2.16) will be positioned 7 m downstream from the interaction point. It will serve as a stop counter with a time resolution of about 50 ps. This detector will help in distinguishing pions from kaons and kaon from protons up to momenta of several GeV/c. An additional scintillator detector will be positioned within the dipole to measure soft particles which do no reach the following detectors of the forward spectrometer.

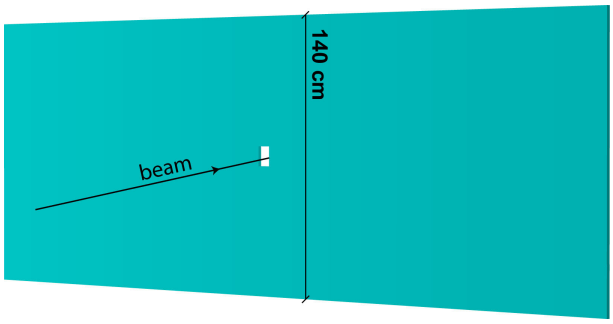

Figure 2.16: The forward time of flight wall.

2.5.4 The muon detector

A muon detector based on the MDT of the target spectrometer will be positioned 9 m downstream from the target (it will be the last detector along the beam line). Due to the high momentum of the particles reaching the end of the spectrometer the thickness of the absorbing layers has been set to 6 cm in order to be able to select muons from pions. This detector can also perform a low resolution hadron calorimetry for particles stopping within its volume.

2.5.5 The dipole

The forward spectrometer is based on the dipole magnet [17] which will allow to analyze high momentum charged particles. This magnet will provide a $2\mathrm{T} \cdot \mathrm{m}$ bending power which corresponds to a deflection of approximately 2° for the 15 GeV/c beam which will be compensated by magnets positioned downstream. The design of the dipole represents a compromise between space occupancy and power consumption. A longer dipole would be easier to build and cheaper to run, but the angular acceptance of the following detectors would be sensibly reduced with increasing distances. On the other side a short dipole with such a wide transverse opening would require intense fields. The final design of a 2.5 m long dipole is a compromise between these two competing requirements.

2.6 The luminosity detector

The physical process chosen to determine the luminosity at $\overline{P}$ANDA is the elastic scattering of the antiproton beam with the protons of the target. Due to the presence of the beam pipe and to the strong solenoidal magnetic filed it is not possible to measure the soft recoiling protons at polar angles close to 90°. It is anyway sufficient to measure the elastic scattering in the region of interference between the Coulombian and the nuclear contribution in order to deduce the absolute luminosity. This can be done at $\overline{P}$ANDA measuring at the end of the spectrometer the high momentum antiprotons which undergo a small angle elastic scattering. For example a 15 GeV/c antiproton interacting elastically in the interference region will have a deflection angle of about 3 mrad. This angle grows for smaller beam momenta reaching approximately 25 mrad for a 1.5 GeV/c beam momentum. The luminosity detector [19] will be therefore positioned in the most forward part of the $\overline{P}$ANDA experiment at 10 m from the interaction point. Four sensor planes will be placed in vacuum to minimize the effect of multiple scattering on the antiprotons before they reach the luminosity detector. MAPS sensors [20] will be adopted to cope with the high intensity of particles fluxing these regions.

2.7 The detectors for hypernuclear physics

The physics program of $\overline{P}$ANDA includes the study of hypernuclei with an alternative setup. The hypernuclear program will make use of a dedicated setup in the innermost region of the experiment. A secondary target will positioned instead of the MVD: it will consist in a series of alternated absorbers and silicon strip sensors. Heavy hyperons can stop in one of the absorber layers, thus enabling the possible generation of single or double-Λ hypernuclei. A precision γ-spectroscopy of the de-excitation of the excited hypernuclei will be performed with a dedicated array of high purity germanium detectors [21].

Bibliography

[1] $\overline{P}$ANDA Collaboration. Technical Progress Report for: $\overline{P}$ANDA. http://www-panda.gsi.de/archive/public/panda_tpr.pdf.

[2] Jürgen Eschke. International Facility for Antiproton and Ion Research (FAIR) at GSI, Darmstadt. *J. Phys. G: Nucl. Part. Phys.*, 31(S967), 2005. stacks.iop.org/JPhysG/31/S967.

[3] $\overline{P}$ANDA Collaboration. Technical Design Report for the: $\overline{P}$ANDA Micro Vertex Detector. 2011. arXiv:1207.6581.

[4] G. Clemente et al. The FAIR proton LINAC: the first LINAC based on a room temperature CH-DTL. *Proceedings of HB2010, Morschach, Switzerland*, MOPD26, 2010.

[5] P. J. Spiller. The FAIR Synchrotrons SIS100 and SIS300 and the high energy beam transport system. *HHH-2008 PROCEEDINGS*, 2008.

[6] K. Knie et al. Concept for the antiproton production target at FAIR. *Proceedings of IPAC2012*, WEPPD030, 2012.

[7] R. Maier for the HESR Consortium. The high-energy storage ring (HESR). *Proceedings of 2011 Particle Accelerator Conference*, THOCN2, 2011.

[8] $\overline{\text{P}}$ANDA Collaboration. Physics Performance Report for $\overline{\text{P}}$ANDA: Strong Interaction Studies with Antiprotons. 2009. arXiv:hep-ex/0903.3905.

[9] $\overline{\text{P}}$ANDA Collaboration. Technical Design Report for the $\overline{\text{P}}$ANDA Internal Targets: The Cluster-Jet Target and Developments for the Pellet Target. 2012. http://www.uni-muenster.de/Physik.KP/AGKhoukaz_Files/TechRep/Targets_TDR.pdf.

[10] $\overline{\text{P}}$ANDA Collaboration. Technical Design Report for the: $\overline{\text{P}}$ANDA Straw Tube Tracker. 2012. arXiv:1205.5441.

[11] B. Voss, J. Kunkel, R. Karabowicz. The GEM-Disks for the $\overline{\text{P}}$ANDA experiment. *GSI Annual Report 2009*. http://www-alt.gsi.de/informationen/wti/library/scientificreport2009/PAPERS/INSTRUMENTS-METHODS-58.pdf.

[12] C. Schwarz et al. The Barrel DIRC of PANDA. *JINST 7 C02008*, 2012. doi:10.1088/1748-0221/7/02/C02008.

[13] The India-$\overline{\text{P}}$ANDA Collaboration Team. Indian Participation in $\overline{\text{P}}$ANDA at FAIR: Detector Development and Physics Studies. http://www.veccal.ernet.in/∼pmd/FAIR/IFCC/Bangalore_physics_meet_dec_2011/panda.pdf.

[14] $\overline{\text{P}}$ANDA Collaboration. Technical Design Report for the: $\overline{\text{P}}$ANDA Electromagnetic Calorimeter. 2008. arXiv:0810.1216.

[15] The CMS Electromagnetic Calorimeter Group et al. Radiation hardness qualification of PbWO4 scintillation crystals for the CMS Electromagnetic Calorimeter. *JINST 5 P03010*, 2010. doi:10.1088/1748-0221/5/03/P03010.

[16] $\overline{\text{P}}$ANDA Collaboration. Technical Design Report for the: $\overline{\text{P}}$ANDA Muon System. 2012. http://panda-wiki.gsi.de/pub/Muon/TechnicalDesignReport/panda_tdr_muon_final.pdf.

[17] $\overline{\text{P}}$ANDA Collaboration. Technical Design Report for the $\overline{\text{P}}$ANDA Solenoid and Dipole Spectrometer Magnets. 2009. arXiv:0907.0169.

[18] $\overline{\text{P}}$ANDA Collaboration. Technical Design Report for: $\overline{\text{P}}$ANDA Forward Spectrometer Calorimeter. 2012. http://btev.ihep.su/∼paul/panda_tdr_FSC.pdf.

[19] Tsitohaina H. Randriamalala. *Conceptual Design of the $\overline{\text{P}}$ANDA Luminosity Monitor and Reconstruction Strategy to Measure the Width of the X(3872) State.* PhD thesis, Ruhr-Universität Bochum, 2011.

[20] G. Deptuch et al. Development of monolithic active pixel sensors for charged particle tracking. http://dx.doi.org/10.1016/j.bbr.2011.03.031.

[21] P. Achenbach, S. Bleser, J. Pochodzalla, A. Sanchez Lorente and M. Steinen. Hypernuclear Physics at $\overline{\text{P}}$ANDA. 2012. arXiv:1206.3149v1.

CHAPTER 3

The Micro-Vertex-Detector for the $\overline{\text{P}}$ANDA experiment

The Micro-Vertex-Detector is the innermost detector of $\overline{\text{P}}$ANDA and its main contributions to the measurements will consist in the determination of start vertices and the momentum of charged tracks. The physics program of the experiment includes the study of short-lived states, therefore the detectors must be able to reconstruct decay vertices, distinguishing them from the primary interaction point. In order to match the requirements settled by the physics program a vertex resolution better than 100 µm has to be achieved. Because of its position the MVD design was guided by several (sometimes competing) aims:

- high geometrical coverage: in order to avoid ambiguities and to reconstruct correctly the momentum also in case of scatterings of the particles within the detector volumes a high number of hit points per tracks is required. The target for the development of the MVD geometry was to achieve a coverage with four hit points per track in most of the acceptance;
- low material budget: introducing passive materials close to the interaction point would worsen the performance of all the surrounding detectors since due to multiple scattering and energy loss both the momentum and the track direction might be changed leading to a biased track reconstruction. The aim during the design of the detector was to keep the total equivalent material budget of the whole MVD below 10% of a radiation length in most of the regions;
- high rates capability: due to the small distances from the primary vertices, the portion of solid angle covered by each MVD sensor will be big, meaning that the sensors and the read out electronics will have to deal with high rates. This influenced the sensors design leading to a high granularity in order to achieve rates of a few kHz/channel. The front-end chips have been then designed to cope with this experimental conditions without compromising the performance due to pile-ups;
- high radiation hardness: since the flux of particles will be intense (especially in the first layers) both sensors and the electronics must be enough radiation hard to run adequately for the planned data taking period consisting of 10 years with a 50% duty cycle. Calculations and simulations showed that the sensors must be able to cope with a 10 Mrad total ionizing dose and a $10^{13} - 10^{14}$ n_{1MeVeq}/cm^2 non-ionizing irradiation.

3.1 Main concept

The MVD geometry foresees an onion shell-like barrel structure composed of four layers and a series of six forward disks positioned perpendicularly to the beam axis. In the forward direction a double wheel will cover bigger radii. A schematic view of the MVD geometry is shown in figure 3.1. The barrel part of the MVD will measure tracks with polar angle between approx-

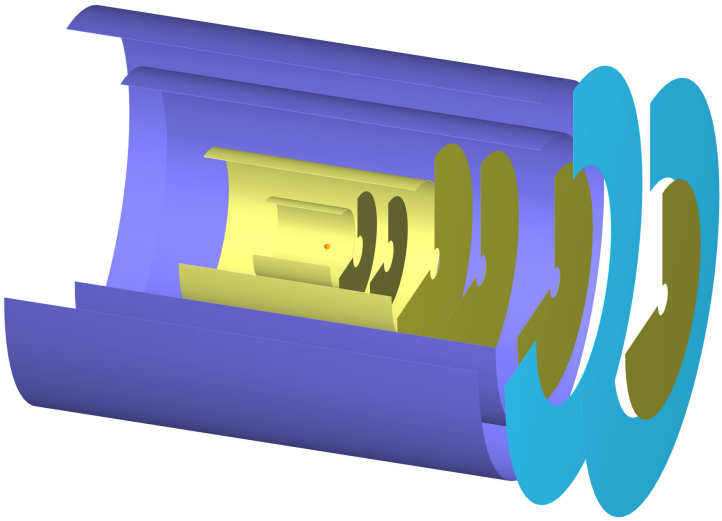

Figure 3.1: Schematic view of the elements composing the MVD geometry. In this figure the beam axis proceeds from left to right.

imately 35° and some 140° depending on the azimuthal angle, the forward elements will cover the smaller polar angles down to a minimum of 3°. Of course these numbers depend on the definition of coverage, the limits just quoted refer to the regions where at least one hit point can be measured. A detailed analysis of the coverage of the MVD can be found in the next chapter together with further characterizations of the detector geometry. Silicon pixel sensors [1]

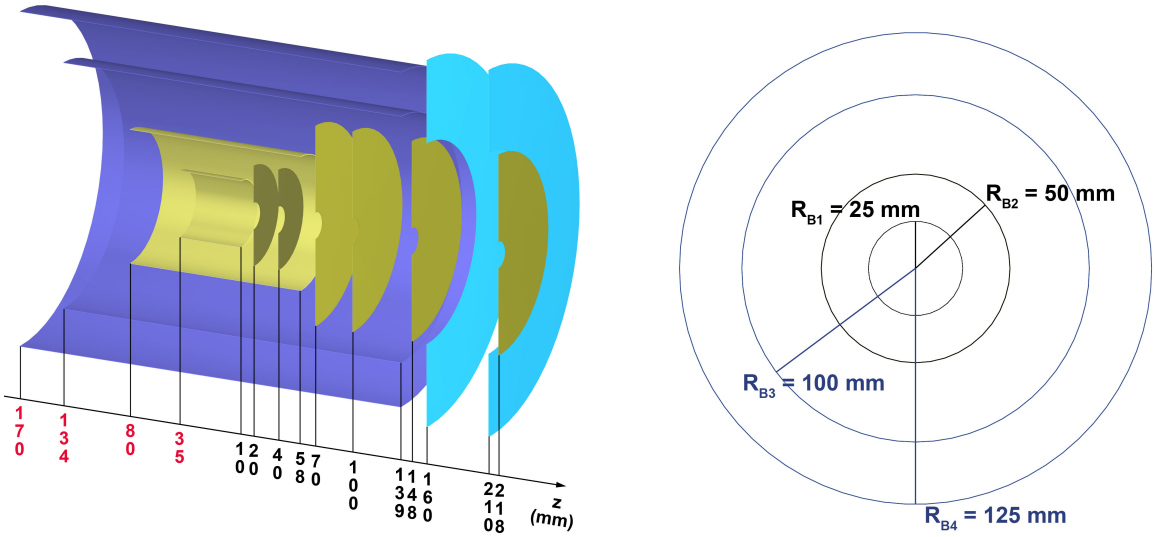

Figure 3.2: Sizes of the elements composing the MVD geometry, red numbers refer to negative coordinates.

are used to equip the most internal layers (the two innermost barrel layers and the six forward disks), while the outer ones (the two outermost barrel layers and the two forward wheels) will be realized with double sided silicon strip sensors [2]. The first pixel barrel layer will have a radius of 25 mm and a longitudinal length of 45 mm and it will be positioned just around the nominal interaction point (see figure 3.2). The second pixel barrel has a double radius and longitudinal extent of 138 mm, so that it includes the first two forward pixel disks whose external radius is 37.5 mm. All the pixel disks have an inner radius of 10 mm. The first two disks foresee an outer radius of 37.5 mm and they are therefore labelled as "small disks", while the last four disks, the so-called "large-disks" have a 75 mm outer radius. The six disks are positioned along the beam axis, downstream from the interaction point, covering the longitudinal range between $z = 20$ mm and $z = 218$ mm. The last two forward disks are nearly surrounded by the strip

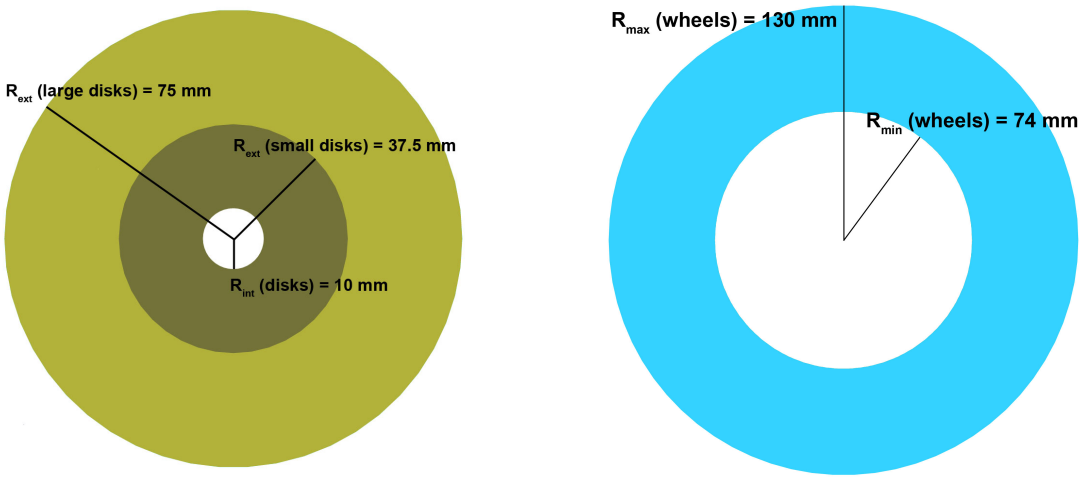

Figure 3.3: Sizes of the forward pixel disks and of the forward wheel.

forward wheels: the inner radius of these wheels is 74 mm, just 1 mm less than the outer radius of the large disks, while the external radius spans up to 130 mm (see figure 3.3). The strip wheels are positioned at a few mm of longitudinal distance from the last pixel disks, in order to have a small overlap and not to leave a gap in the coverage of the MVD. The numbers given here represent a simplification of the real geometry: each barrel will be realized with rectangular staves therefore it will not have a circular shape, the radius we refer to here is the average radial distance of the sensors composing a barrel layer from the nominal interaction point. The same consideration applies to the other components of the detector geometry, further details about each element can be found in the following.

3.2 The pixel part of the MVD

3.2.1 Sensors and front-end chips

Simulations were performed to determine the optimal granularity for the pixel part of the MVD able to deal with rates and track multiplicity of the $\overline{\text{P}}$ANDA experimental conditions. A final cell size of $100\,\mu\text{m} \times 100\,\mu\text{m}$ was chosen. A comprehensive comparison of the performance obtained with different pixel cell sizes can be found in appendix B. The sensors will be realized with epitaxial silicon [3] grown on a Czochralski (Cz) substrate [4] reaching a thickness of $100\,\mu\text{m}$. This technology allows to obtain the radiation hardness required for the innermost pixel sensors.

The Cz substrate has an initial thickness of some hundreds of µm, but can be thinned down to about 20 µm after the production in order to minimize the material budget of the sensors. A front-end chip named ToPix [5] was developed and implemented as an ASIC in a 130 nm CMOS technology. It consists of a self-triggered chip able to provide a time-overt-threshold (ToT) information about the charge collected in each channel and a time response based on a 155 MHz internal clock. Each pixel cell will be connected to its relative read out pad on a ToPix chip with a bump bond positioned in one of the corners of the cell (see figure 3.4a). The backside of the chip will be glued to a carbon foam structure with embedded cooling pipes acting both as a support and as a thermal contact for the modules. Sensors of different sizes will be produced

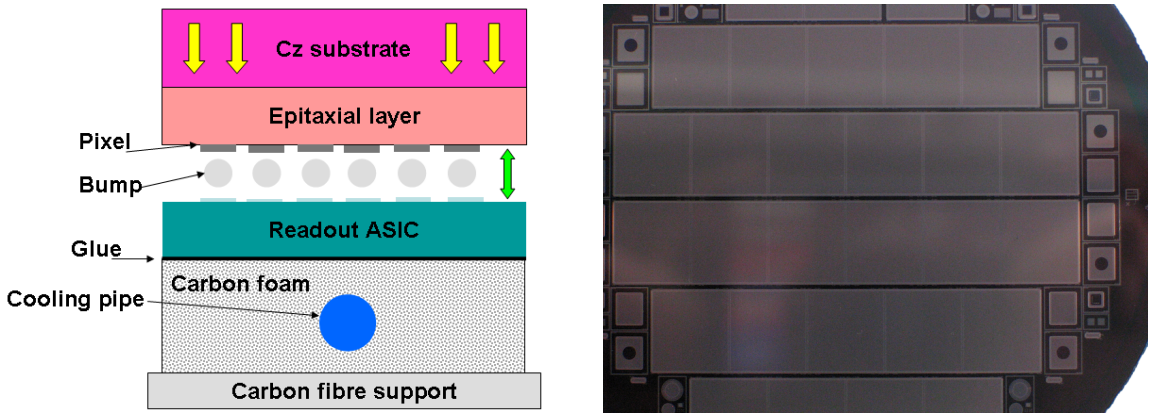

(a) Integration of a single pixel sensor with its front-end ToPix chip and with the services.

(b) Wafer showing the implementation of sensor with a different number of units.

Figure 3.4: Implementation and integration of the MVD pixel sensors [6].

to cope with the geometry of the various components of the MVD. Sensors including two, four, five and six units (the portion of a sensor read out by a single chip) will be realized. Each unit consists of a square with an active area of 1.14 cm × 1.16 cm. One unit will foresee 116 rows and 110 columns since the first and the last columns will have a 300 µm width. The reason of these larger columns consists in the fact that a small fraction of the area of the ToPix chip cannot be used to read out channels, since it is needed for internal services. The surface occupied by the first and the last two columns of each unit is used for such purpose. Using this method it is possible to position consecutive units without leaving gaps between each other. Figure 3.4b shows a portion of a wafer where the different sensor configurations were implemented.

3.2.2 The geometry

The two barrel layers of the MVD pixel part are composed of longitudinal staves featuring a different number of pixel sensor units. Each barrel consists of a double series of staves disposed in order not to leave open gaps along the azimuthal angle. The top and bottom regions around the interaction point are left free for the insertion of the target pipe. The staves of the innermost barrel layer are composed of single pixel sensors, while for the second layer two consecutive sensors are used. Figure 3.5 shows how the barrels are realized disposing longitudinal staves. The forward pixel disks are designed to use both of their sides to host detectors. In this way it is possible to avoid blind areas in the small gaps between adjacent sensors. The two small disks will be equipped with single sensors of different sizes in order to cover most of the surface with rectangular modules (see figure 3.6). The concept adopted for the large disks is the same: the

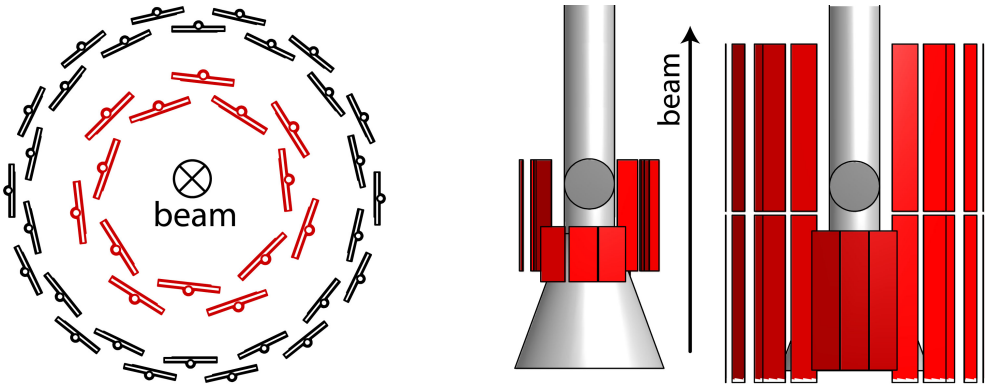

Figure 3.5: The figure on the left is a transverse (x-y) view of the two pixel barrel layers showing the disposition of the longitudinal staves along the two barrels; the innermost one is highlighted in red. The two pictures on the right are respectively a sketch of the longitudinal position of the pixel staves in barrel one and two.

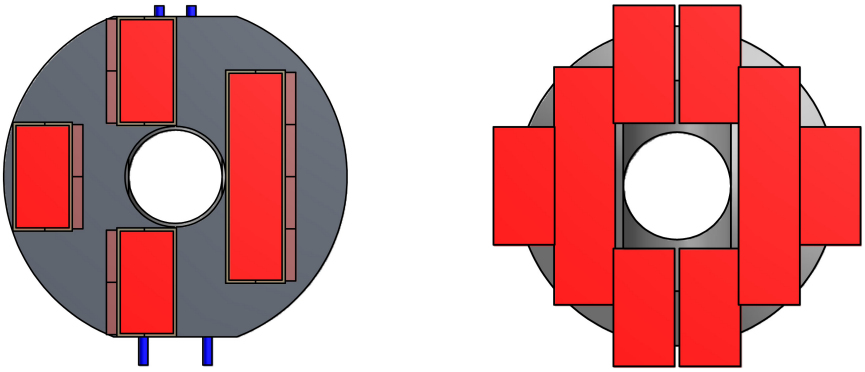

Figure 3.6: The figure on the left shows how one of the sides of a small disk is equipped with pixel sensors. The picture on the right plots the total coverage obtained considering both sides of the disk.

area to cover is just larger, therefore series of two consecutive sensors are used (see figure 3.7). Figure 3.6 and 3.7 show the integration of the sensors with the support carbon foam disks in which cooling pipes are embedded.

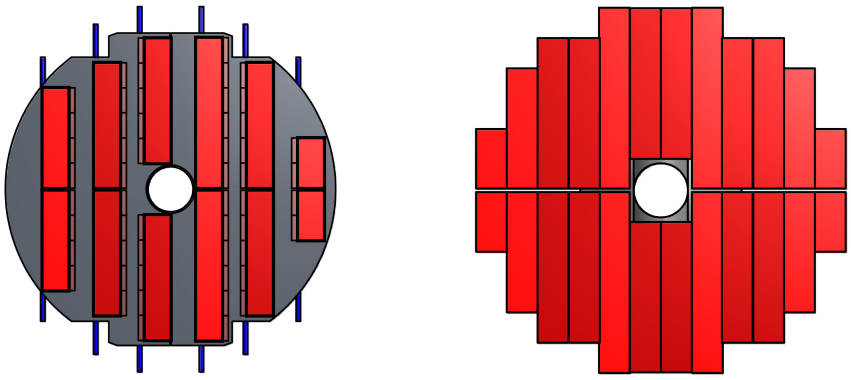

Figure 3.7: The large forward pixel disks: on the left the layout of a single side of a disk, on the right the total coverage achieved with the full disk.

Prototype sensors and front-end chips have been produced. Several tests were performed for the characterization of their performance. The prototypes were involved in the last MVD beam tests at the COSY synchrotron in Jülich [7] and at the T9 test area [8] of CERN. Results from the beam tests will be shown later in section 6.7.

3.3 The strip part of the MVD

3.3.1 Sensors and front-end chips

Double sided silicon strip sensors [2] will be used to equip the barrel part and the forward wheels. The strips on the two sides of the sensors will be realized respectively with p^+-in-n and n^+-in-n doped silicon. The n^+ strips will be insulated from each other with a p-spray deposition [9]. The sensors will be depleted with a punch through bias at typical voltages of about 60 V. The barrel sensors will be squared and rectangular depending on the position, foreseeing a 90° stereo angle. Trapezoidal sensors with 15° stereo angle will be used for the forward wheels. The strip sensors will be read out with trigger-less front-end chips. At the moment a custom solution based on the ToPix chip is under development [10]. Other options are available as backup solutions. In the barrel part a carbon foam structure with embedded cooling pipes houses the front-end chips. The sensors are positioned beside of the front-end chips. A small angle is foreseen between the sensor surface and the first part of the staves where the chips are positioned. Figure 3.8 shows the integration of the barrel strip sensors with all the services. The trapezoidal sensors composing the double forward wheel are kept together by a support

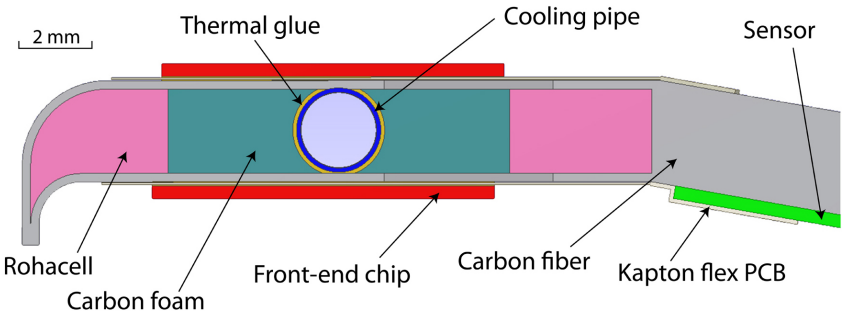

Figure 3.8: Integration of the strip barrel sensors with the support structure hosting the front-end chips and the cooling pipes [6].

structure holding two sensors one in front of the other, with space for the front-end chips on the portion of the support frame connecting the two layers of the double wheel. The front-end chips therefore sit on a plane with a 90° angle with respect to the sensor surfaces, this can be achieved using flex-pcb technologies [11] to realize the connector between the channels of each sensor and the corresponding pads of the front-end chips. The read-out chips will be cooled with a circular tube filled with chilled water in thermal contact with the support frame. Figure 3.9 shows the integration of two forward trapezoidal sensors with the necessary services.

Three different types of double sided silicon strip sensors will be used to equip the MVD (see figure 3.10):

- **rectangular sensors:** active area of 33.41 mm × 66.69 mm, 300 µm thick, 90° stereo angle and pitch of 65 µm (the possibility of reading out one every two strips is now under study

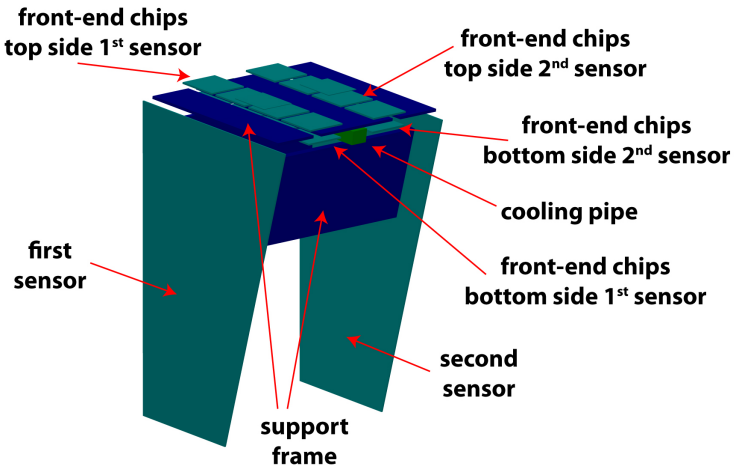

Figure 3.9: Integration of two forward trapezoidal sensors with the necessary services.

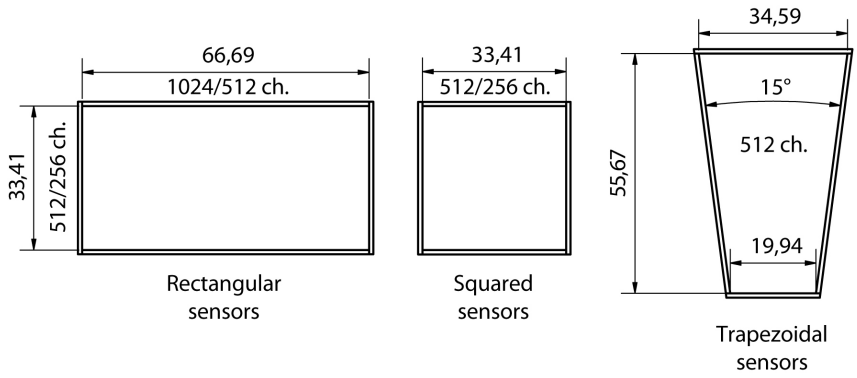

Figure 3.10: Sizes and features of the different silicon strip sensors adopted for the realization of the MVD.

since this would decrease the number of channels to be read out and therefore this would reduce the number of front-end chips, cables and cooling pipes which are required);

- **square sensors:** active area of 33.41 mm × 33.41 mm, same other properties as in the case of rectangular sensors;
- **trapezoidal sensors:** these sensors will have a height of 55.67 mm, major base of 34.59 mm and 19.94 mm minor base. The thickness will be of 300 µm as in the case of the barrel sensors (a backup plan consisting in the possibility of using two stacked single-sided trapezoidal sensors has been investigated). The stereo angle between strips on the two sides of one sensors was fixed to 15°, the pitch to 67.5 µm.

Prototype sensors have been used in several beam tests at different facilities and with various configurations. These studies will be described in chapter 6.

3.3.2 The geometry

The strip barrel layers follow a similar concept to the one of the pixel barrels. A series of longitudinal staves equipped with rectangular and squared sensors are disposed along each barrel

in a cylindrical configuration. Differently from the pixel case, the strip staves are not orthogonal to the radial directions. A small tilting angle is introduced to obtain a partial overlap between

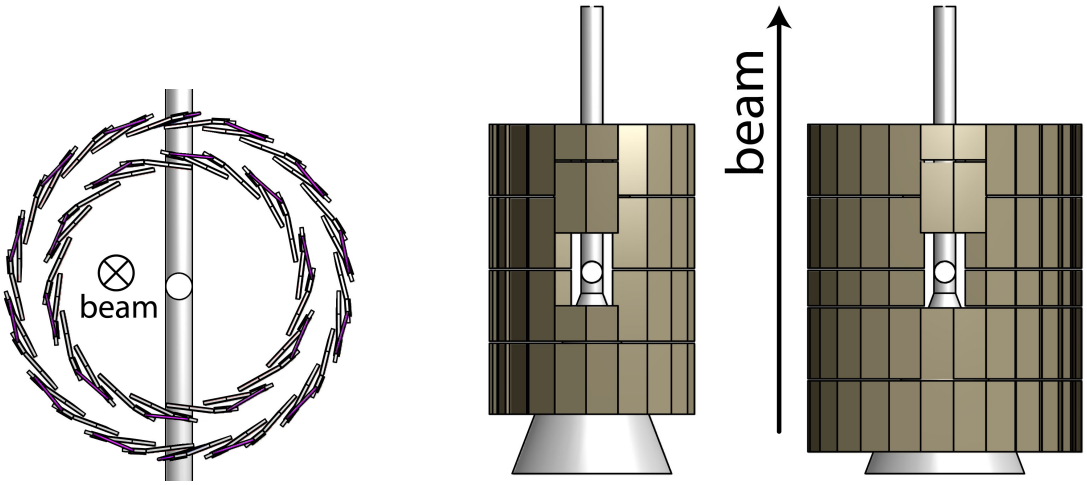

Figure 3.11: Position of the strip sensors used to equip barrel three and four. From left to right: an orthogonal view in the transverse plane of both barrels, a longitudinal view of barrel three and four.

consecutive staves: this allows to avoid gaps in the acceptance without needing a double layer of sensors to equip a barrel. The top and the bottom regions foresee a gap left free for the target pipe insertion. Four consecutive long rectangular sensors are used to realize the staves of barrel three (except for the region in correspondence with the target pipe cut-outs). Four long rectangular sensors and a squared one equip the longer staves of barrel four. Figure 3.11 shows the orthogonal and longitudinal positions of the strip sensors of barrel three and four. Twenty-four trapezoidal sensors are used to realize each of the forward wheels (see figure 3.12).

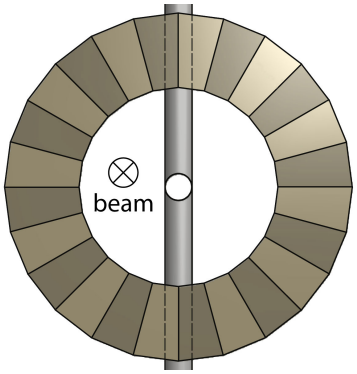

Figure 3.12: Trapezoidal sensors disposed to equip one of the two forward strip wheels. One every two sensors is positioned 5 mm downstream from the adjacent ones to maximize the coverage.

Adjacent sensors have a 5 mm gap along the longitudinal axis, this allows to have a small overlap of the sensors in the transverse plane and to maximize the coverage of the detector.

3.4 Radiation hardness and rates

The pixel layers being the closest to the interaction point will receive the most intense fluxes of particles. This means that the highest impact of both ionizing and non-ionizing damage will

be on the innermost barrel layers and on the central portions of the forward disks. Simulations were performed to estimate the total doses in a ten years data taking period. Both hydrogen and heavier targets were considered during this studies [6]. The pixel and strip sensor prototypes have been therefore irradiated at different facilities to test the radiation hardness: both neutrons and slow charged particles were used to irradiate the detectors and the effect on depletion voltages and p-n junction properties were monitored. These tests could assure a correct functionality of the sensors up to the experimental conditions. In the inner regions, due to the high particles density, single event upsets may occur in the digital part of the front-end chip, causing random variations of the content of bits from 1 to 0 or vice-versa. In order to prevent this problem a triple redundancy was implemented in the last ToPix generation [5]. Due to the bigger area corresponding to single read out channels, the strip sensors will have the highest rates in the MVD. In particular the channels fired more frequently will be those ones in the barrel sensors in their most forward regions: here the rates will reach about 10 kHz [6].

Bibliography

[1] N. Wermes. Pixel Detectors for Particle Detection and Imaging Applications. *Nucl. Instr. Meth. A*, 513:277–288, 2003. arXiv:hep-ex/0209014.

[2] O. Adriani et al. The new double sided silicon microvertex detector for the L3 experiment. *Nucl. Instr. Meth. A*, 348:431–435, 1994.

[3] D. Calvo et al. Thinned epitaxial silicon hybrid pixel sensors for the $\overline{\mathsf{P}}$ANDA experiment. *Nucl. Instr. Meth. A*, 594(29), 2008.

[4] L. Spiegel et al. Czochralski Silicon as a Detector Material for S-LHC Tracker Volumes. *Nucl. Instr. Meth. A*, 628:242–245, 2011. arXiv:1008.4107.

[5] G. Mazza et al. A CMOS 0.13m Silicon Pixel Detector Readout ASIC for the $\overline{\mathsf{P}}$ANDA experiment. *JINST 7 C02015*, 2012. doi:10.1088/1748-0221/7/02/C02015.

[6] $\overline{\mathsf{P}}$ANDA Collaboration. Technical Design Report for the: $\overline{\mathsf{P}}$ANDA Micro Vertex Detector. 2011. arXiv:1207.6581.

[7] COSY, Jülich, Germany. http://www2.fz-juelich.de/ikp/cosy/en/.

[8] L. Durieu, M. Martini and A.-S. Müller. Optics Studies for the T9 Beam Line in the CERN PS East Area Secondary Beam Facility. *Proceedings of the 2001 Particle Accelerator Conference, Chicago*, 2001.

[9] G. Pellegrini et al. Technology development of p-type microstrip detectors with radiation hard p-spray isolation. *Nucl. Instr. Meth.*, A566:360–365, 2006. 10.1016/j.nima.2006.07.005.

[10] A. Potenza. Design of a High Dynamic Range Front-End Electronics for Particle Detectors in a 0.13 µm CMOS technology. Master's thesis, Università degli Studi di Torino, Italy, 2009. https://wiki.to.infn.it/lib/exe/fetch.php?media=vlsi:alberto_potenza_master_thesis.pdf.

[11] R.Schnell, K.-Th. Brinkmann, S. Krah. Flex-PCB Pitch-Adapters for Silicon Micro-Strip Detectors. *GSI Scientific Report 2012 Input*, 2012.

CHAPTER 4

Implementation of the MVD geometry in the simulation framework

4.1 Development of the MVD geometry

The geometry of the MVD has been completely designed with computer-aided design (CAD [1]) tools, which allow to reach a high positioning precision, to manage complex sets of volumes and to perform mechanical simulations. The detector concept includes active sensors, electronics, cabling, cooling systems and support structures. Each of these components was designed taking into account the full complexity of the real detector realization [2]. In the model each sensor is provided with the required services, cables are disposed within the detector volume following a detailed routing scheme. The mechanical support structure consists of elements realized with different materials optimized to provide enough stiffness to hold the detector not compromising its performance. Cut outs and light sectors are present wherever this is possible with the aim of minimizing the amount of passive material crossed by particles flying through the detector. The strip barrel layers are hold by a cylindrical structure realized with carbon-foam and carbon-

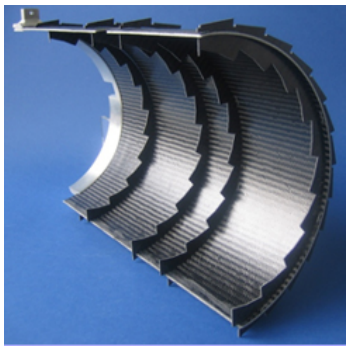

(a) Photo of a prototype realized with carbon foam and carbon fiber.

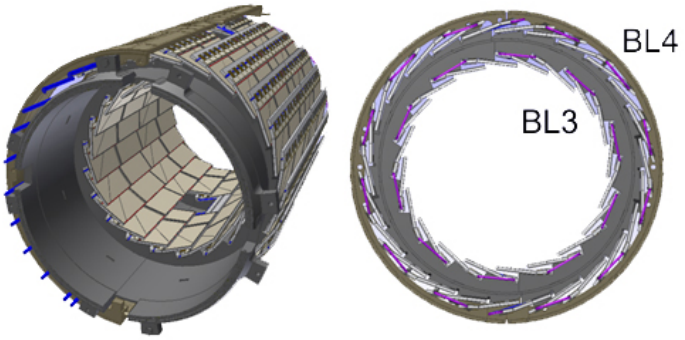

(b) CAD model of the support frame.

Figure 4.1: CAD model and prototype of the main support frame for the strip barrel sensors [3].

fiber. It foresees a saw tooth structure both on its internal and external surfaces to support

respectively the sensors of the third and fourth barrel layer. Single strip staves will be fixed to this main cylindrical support structure. Figure 4.1a and 4.1b show respectively the photo and the CAD drawing of a first prototype of such a support element. Each strip barrel stave includes a light frame hosting the sensors, the front-end chips and embedded cooling pipes (see figure 4.2a). The main MVD support structure will be used to attach the forward strip wheels as shown in figure 4.2b.

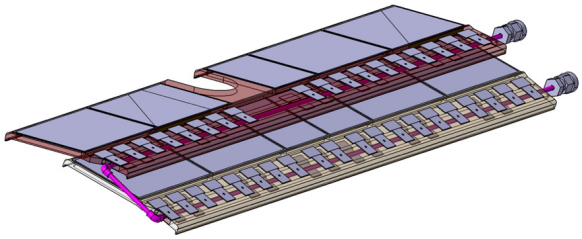

(a) Example of a barrel strip sensors stave from layer 4 including the support structure and the cooling pipes.

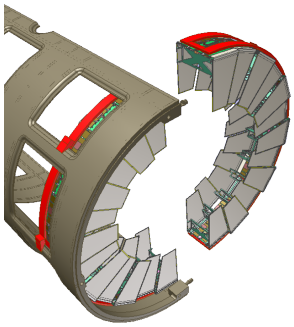

(b) Inclusion of the forward strip wheel in the main MVD support structure.

Figure 4.2: Support scheme for the strip sensors [3].

A similar concept is followed for the pixel barrel sensors: barrel staves include a Ω-shaped support structure, a cooling pipe and the detector assemblies consisting of sensors with bump-bonded front-end chips (see figure 4.3a). Each pixel barrel stave will be attached to the main pixel support structure in the backward region.

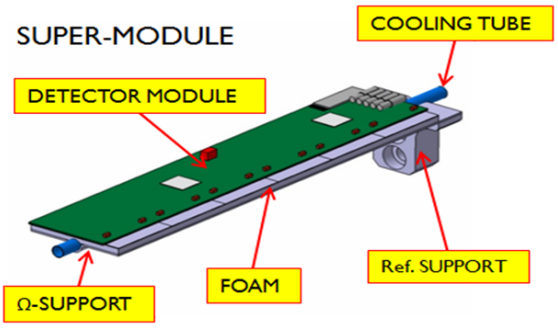

(a) Pixel barrel stave including sensors, front-end chips, support frame and cooling pipes.

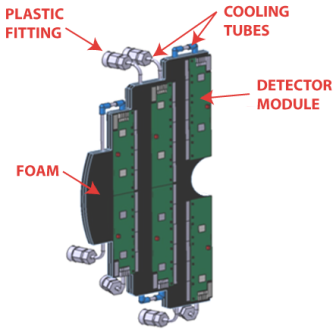

(b) Pixel forward sensors assembled with all the services on the forward support disks.

Figure 4.3: Support structures for the pixel sensors [3].

The forward pixel sensor assemblies are positioned on carbon-foam disks, which house a different number of cooling pipes depending on the size of the disks: each small half disk is equipped with one curling cooling pipe, while larger half disks are cooled with three pipes. Figure 4.3b shows as an example one of these larger forward disks. The six forward pixel disks are attached to each other by means of some cylindrical spacers. The overall forward structure is attached to the main MVD support frame with suspenders positioned in the most forward part of the MVD

volume. The whole support structure for the pixel part of the MVD is shown together with the sensors in the longitudinal section of figure 4.4.

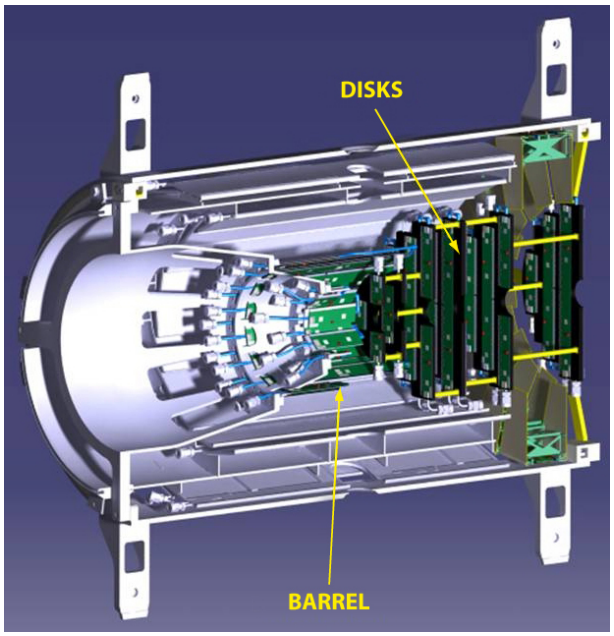

Figure 4.4: Half MVD support structure including all the pixel and strip sensors mounted on the support structures.

The entire MVD is divided longitudinally in two halves which are mechanically and statically independent. This is foreseen in order to minimize possible stresses on the sensors and to allow the installation of the detector clamping the beam pipe from the two sides. Each of the two halves is then attached to the common support structure which will hold the STT as well.

4.2 Detector models and geometries for particle propagation

The detector geometry has been designed with CAD softwares as described in the previous section. Most common CAD tools define shapes by means of boundary surfaces following the BREP scheme [4]. In this approach the basic components of a solid are defined as bounded portions of more general elements: for example a face is obtained out of a surface and edges as a limited part of a curve. The BREP definition of solids offers the advantage of a high flexibility, which is aimed when dealing with complex mechanical projects. An alternative approach in defining solids is known as Constructive Solid Geometry (CSG) [5]: here a set of basic solid is predefined and more complex objects are obtained combining these simple shapes with boolean operations such as union of volumes, intersection or difference. An example is shown in figure 4.5, where a parallelepiped with a cut-out is obtained subtracting a second parallelepiped from the first one. The software frameworks developed to propagate particles trough detector volumes initially supported only CSG definition of the geometry to be used for Monte-Carlo simulations. This is the case for example of Geant3 [6]. CSG geometries are easier to implement and faster to compute during the particle propagation. More recent developments allow Geant4 [7] to treat BREP geometry as well. The PandaRoot framework [8] uses VMC [9] as an interface with different transport codes: this allows to write a unique version of the code regarding for example the detector response, while VMC is taking care of correctly interfacing with the

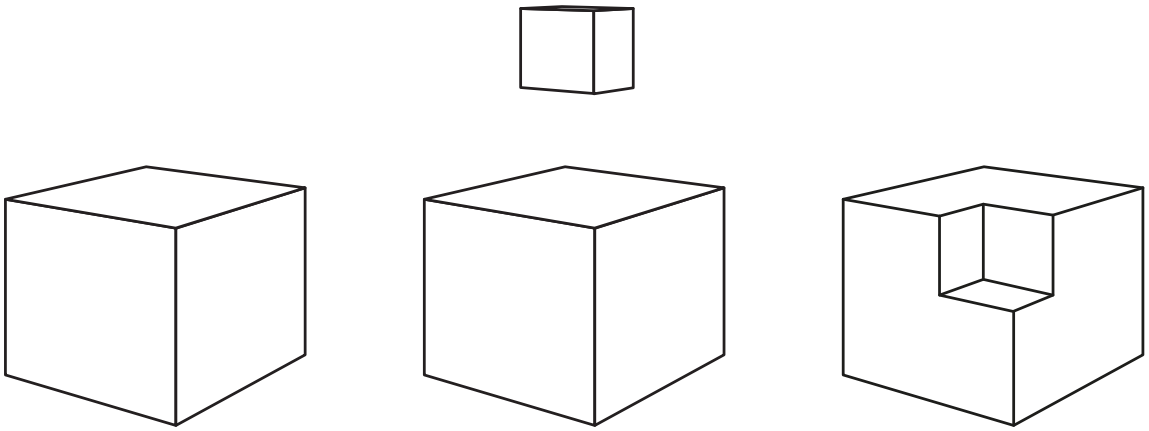

(a) Basic solid A. (b) Basic solid A and B. (c) Result of the difference A-B.

Figure 4.5: Example of CSG definition of a solid as a difference of two basic volumes.

selected transport code. Within the collaboration both Geant3 and Geant4 are widely used, so the detector geometry must be general enough to be working with both transport codes. Therefore the choice was taken to develop and tune a converter able to read a BREP model designed in CAD and transform it into a CGS VMC compatible geometry.

4.3 The geometry conversion

The CAD to ROOT converter [10] was developed and tuned within the PANDA MVD group. Figure 4.6 summarizes the procedure necessary to import the CAD model of a detector into the PandaRoot simulation framework. This converter can be provided with a CAD model by means of "STEP" files [11], which are a standard output of all the CAD design softwares. The OpenCascade 6.3 libraries [12] are used to access the information contained in the STEP files. Each volume is then converted from a BREP object to a CSG solid. This operation is crucial and can be difficult in case of complex shapes. The converter foresees the possibility of providing substitutional interpretations of critical volumes which cannot be correctly treated by the converter: in this case the user can provide a new definition of those volumes or specify the boolean operations to be used in order to combine the basic CSG solids necessary to describe the critical volume. The converter produces automatically a report about problems encountered during the conversion listing the name of all the volumes which cannot be correctly treated.

Every physical volume is filled with a certain material: during the conversion the converter must be provided with a text file where each volume is linked to a certain material name. General rules can be introduced: for example all the volumes whose names include a certain string can be linked to the same material with a single command. It is important to stress that at this point the converter does not know the properties of the different materials, each volume is simply labeled with the name of the material it has to be filled with. The PandaRoot framework contains a definition of the properties of all the materials used to create the geometry of the detectors. Therefore once the geometry has been converted it is still possible to change the property of the materials of its volumes acting within the framework. This is a useful feature when testing different options for some components: for example one can easily compare the effect of changing the material some cables are made of or test the consequences in terms of detector performance

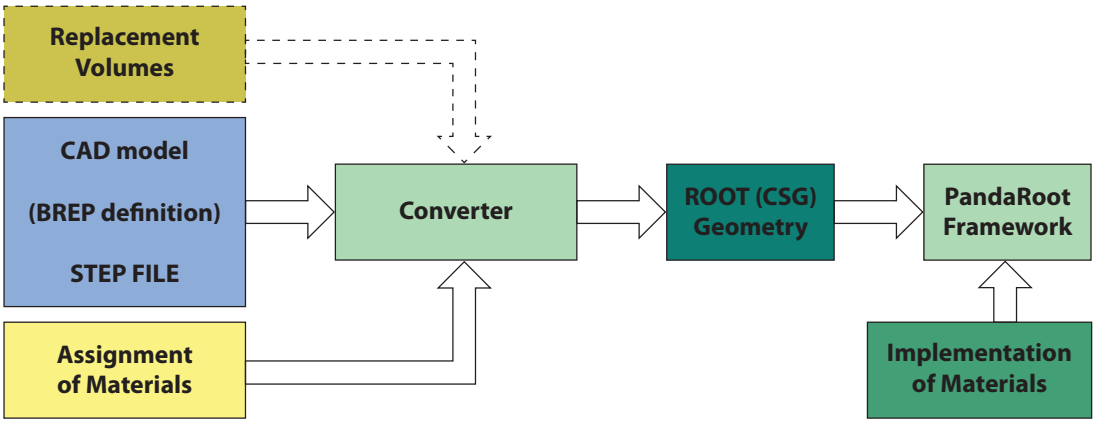

Figure 4.6: Flowchart showing the functioning of the CAD to ROOT converter.

of lightening the density of the carbon foams used for the support structures. Since the MVD model is really detailed and it contains several complex volumes, particularly for the support elements, the following approach has been followed: instead of providing substitutional volumes for each shape the converter could not handle with the standard methods, a division of the most complex solids has been realized at a CAD level. The idea was to split a complex volume into a set of simpler volumes which could immediately be properly treated by the converter. This procedure was for example adopted to import the pixel barrel support structures. The main structure holding the pixel staves is shown in figure 4.7a after the conversion. This element was realized as a composition of several basic solids as can be seen in figure 4.7b.

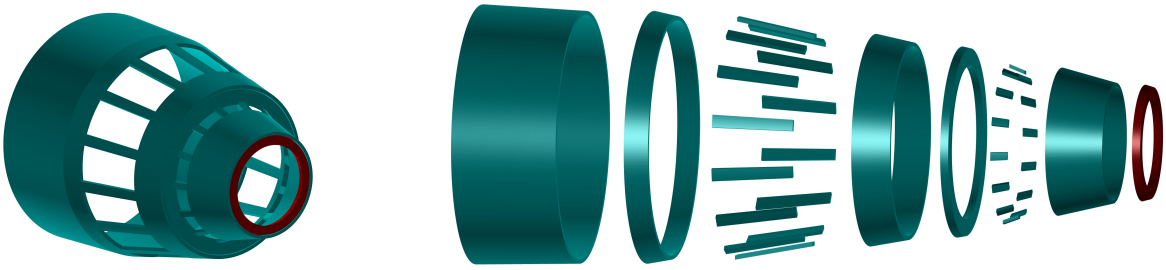

(a) Total support structure.

(b) Support structure divided into its sub-elements.

Figure 4.7: Example of complex volumes split into simpler solids. All the plots are produced in ROOT, therefore the geometry shown is the already converted one which is used for simulations.

The complete MVD geometry introduced in the simulation framework, including all the services and passive materials counts more than 110,000 nodes. Figure 4.8 shows details of the MVD geometry displayed with the ROOT [13] graphic tools: in particular figure 4.8a shows the silicon elements including active and passive parts of sensors and front-end electronics, figure 4.8b the overall MVD support structure, figure 4.8c exemplifies the routing scheme for the service cables and figure 4.8d displays electronic components such as capacitors and connectors [14]. A section of the converted full MVD geometry is shown in figure 4.9. A simplified version of the model, where only the silicon volumes are defined, was created to allow for fast simulations. This geometry can be useful for studies where the presence of passive materials close to the interaction point is not crucial and which require high statistics and therefore benefit from shorter computational times. All the plots shown in this and in the previous chapters refer to

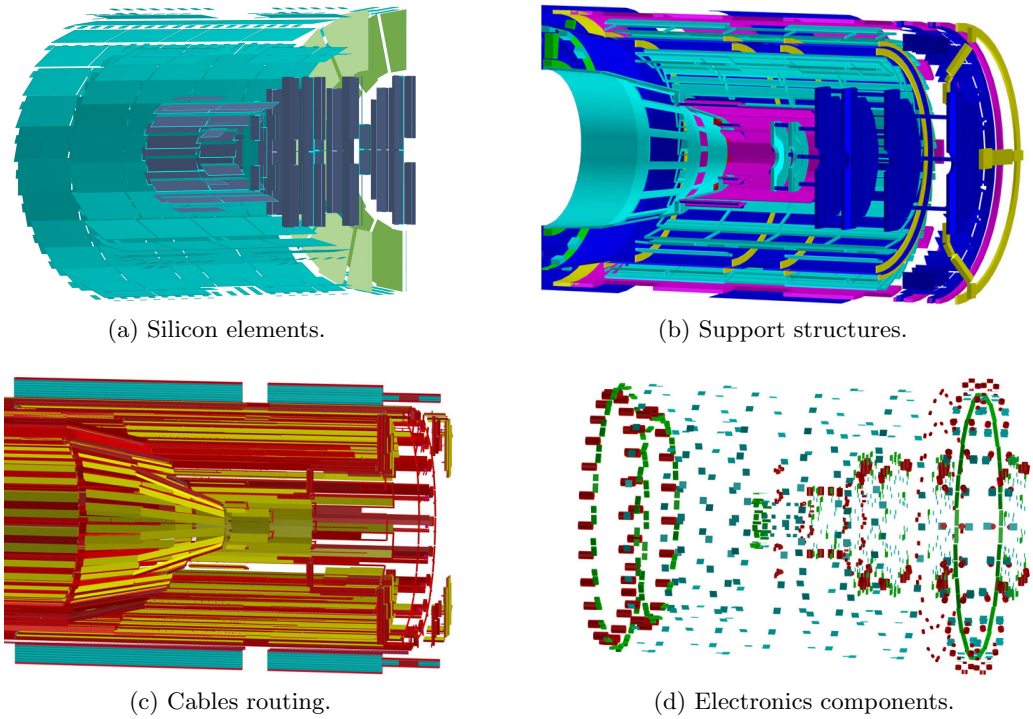

(a) Silicon elements.

(b) Support structures.

(c) Cables routing.

(d) Electronics components.

Figure 4.8: Elements of the MVD geometry introduced in the PandaRoot simulation framework.

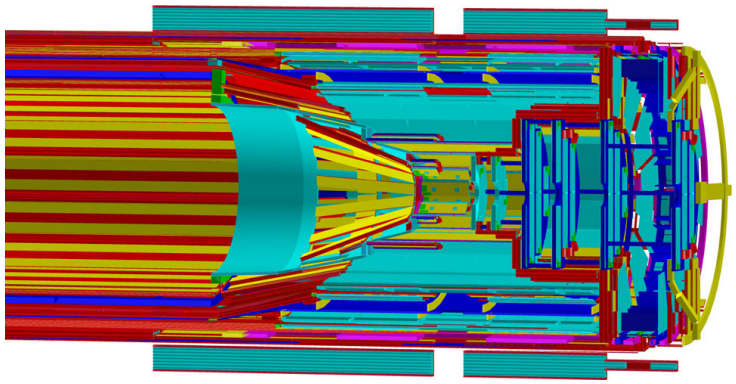

Figure 4.9: Section of the full geometry of the MVD used for simulations.

the MVD 2.1 model [15], which is the version of the MVD geometry used for all the studies compiled in this thesis.

4.4 Characterization of the MVD geometry

The introduction of the detailed geometry of the MVD within the PandaRoot simulation framework allowed to perform a precise characterization of the detector features and performance. Propagating particles from the nominal interaction point with different initial directions the geometrical coverage of the detector can be analyzed. Figure 4.10 shows the average number of hit points measured by the MVD when crossed by 1 GeV/c pions as a function of the two initial angles of such particles. This simulation was performed making use of the standard maps of the

magnetic field of the $\overline{\mathrm{P}}$ANDA experiment. Two holes in the acceptance appear at polar angles between 75° and 105° in opposite azimuthal regions: this is the effect of the space left uncovered to allow the insertion of the target pipe, which crosses the MVD breaking its azimuthal symmetry. The goal of having four hit points per track measured by the MVD is achieved in most

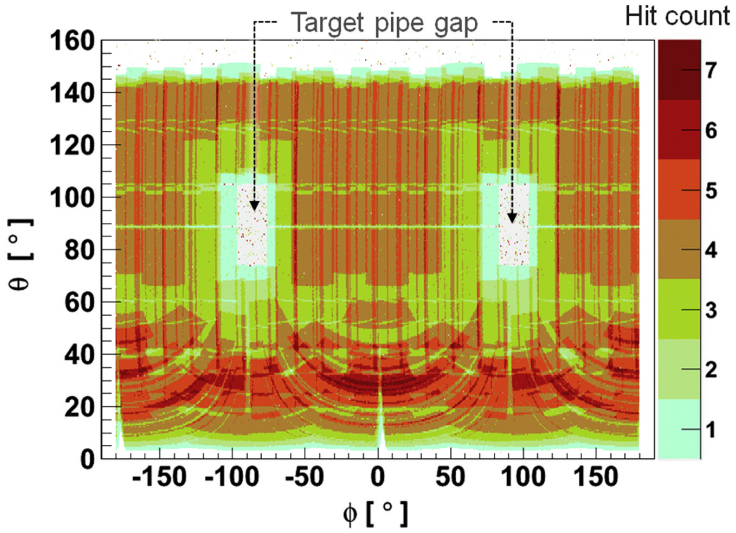

Figure 4.10: Map of the geometrical coverage of the MVD sensors [10]. The average number of hit points generated by 1 GeV/c pions is shown by the color code as a function of the initial direction of the particles. The standard 2T solenoidal magnetic field is included in the simulation.

of the covered solid angle. Small overlaps and gaps between sensors result respectively in the regions with higher (vertical darker bands) or lower (horizontal lighter segments) number of hit points. In the forward direction an average better coverage is achieved due to the presence of six forward pixel disks. The optimal number of 4 hit points per track was chosen since the pattern recognition will have to reconstruct the trajectories of particles which may scatter within the detector volume. In theory of course three points would be enough to reconstruct a helix, anyway in an experimental condition with overlap of events, considerable track multiplicities, multiple scattering and fake hit points generated by noise affecting the trajectories, having one more hit point in the MVD helps in the reconstruction phase. Coverage is not the only important feature of a vertex detector: the material budget is a crucial aspect when tracking charged particles with momenta in the range between hundreds of MeV/c and a few GeV/c. The design of the MVD was optimized as a compromise between the optimization of the coverage and the minimization of the amount of materials introduced. The material budget introduced by each component of the MVD was evaluated in the PandaRoot framework. Geant3 provides a probe particle (the so-called "geantino") which can be propagated through the volumes included in a geometry and which does not interact with matter. The trajectories of such particles are therefore straight tracks coming from their start vertex. This tool was used to determine the lengths of the trajectory portions inside each volume. Once the length of each segment is known it is possible to derive the equivalent number of radiation lengths. Moving along a track the single contributions in terms of radiation lengths can be summed up determining the total material load seen by that probe particle. According to figure 4.11 for example the total amount of material seen by that track can be described as:

$$\frac{\mathrm{X_{TOT}}}{\mathrm{X_0}} = \sum_{\mathrm{i=0}}^{\mathrm{N}} \frac{\mathrm{d_i}}{\mathrm{X_{0,i}}} = \frac{\mathrm{d_1}}{\mathrm{X_{0,1}}} + \frac{\mathrm{d_2}}{\mathrm{X_{0,2}}} + \frac{\mathrm{d_3}}{\mathrm{X_{0,3}}} + \frac{\mathrm{d_4}}{\mathrm{X_{0,4}}} + \frac{\mathrm{d_5}}{\mathrm{X_{0,5}}}$$

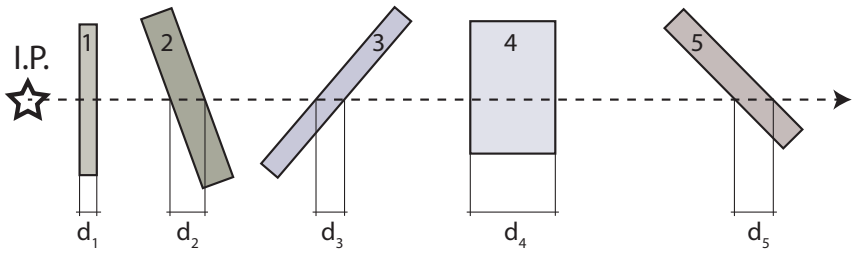

Figure 4.11: Exemplification of the method used to compute the amount of material budget along each track.

In this example the air filling the space between the volumes has been neglected, but it was taken into account when characterizing the detector geometry. Changing the initial direction of the geantinos a mapping of the whole MVD material can be obtained. Figure 4.12 shows the results

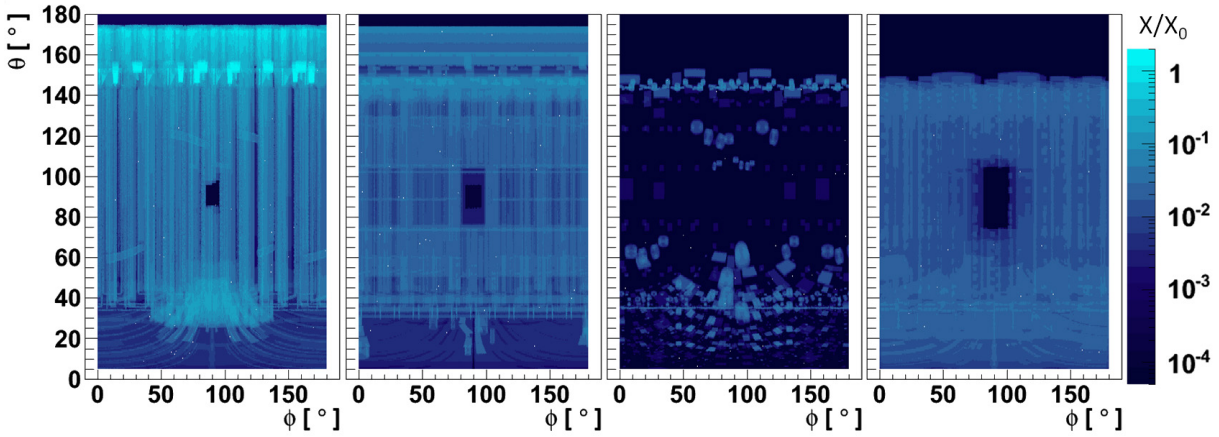

Figure 4.12: The maps show the equivalent radiation lengths introduced by different parts of the MVD: proceeding from left to right the contribution of the cable routing, of the support structure, of the electronic components and of the silicon elements are presented [10].

obtained for sets of elements of the MVD: the contribution to the material budget of cables, support structures, electronic components and silicon volumes (sensors and front-end chips) can be respectively distinguished from left to right. The stacked histogram of figure 4.13 allows to better distinguish the contribution of the different components at different polar angles. These values were obtained averaging along the azimuthal angular range. The design goal of having a total load of 10% of a radiation length is achieved in most of the acceptance. The peak at polar angles of about 40° is due to the routing scheme for the forward pixel disks which foresees, due to mechanical constraints, a double crossing of the service cables in this region. The backward region is not covered with sensors (see for example figure 4.10) due to the strong forward boost of the particles produced at $\overline{\mathrm{P}}$ANDA, which drastically reduces the number of particles flying at such high polar angles. Therefore this area has been selected to collect all the cables providing services to the sensors. Since the cables are routed around the backward cone of the beam pipe, the trajectories of particles coming from the interaction region will be nearly parallel to the cables. This results in a high amount of material visible from the interaction point at high polar angles and correspond to the peak at $\vartheta \sim 150°$ in figure 4.13.

Another important analysis possible with the detailed geometry of the detector is the determination of the distance from the interaction point of the first hit point measured by the MVD.

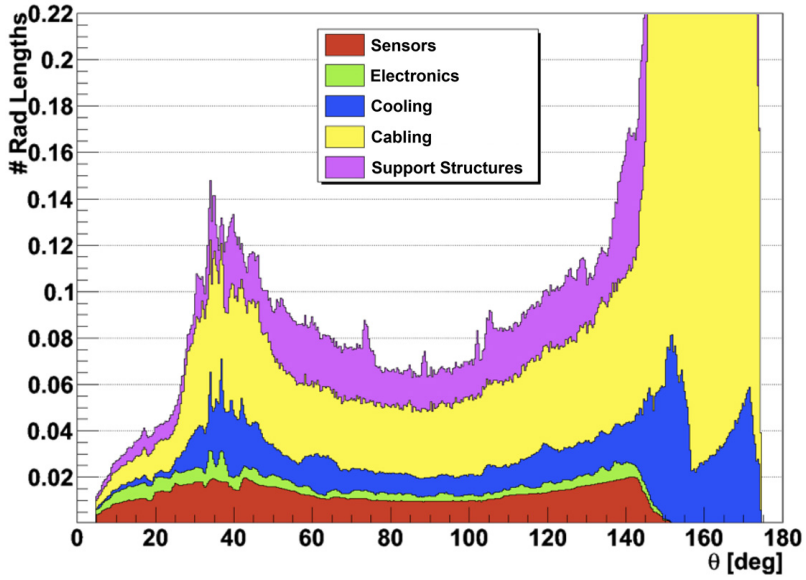

Figure 4.13: Stacked histogram showing the contribution in terms of equivalent radiation lengths of each group of elements in the MVD as a function of the polar angle.

Since the MVD aims to measure short-lived particles, it is crucial to measure a first hit point as close as possible to their start vertices. Since the sensors must be placed out of the vacuum, the minimum limit is imposed by the beam pipe, which has a radius of 20 mm. Figure 4.14 summarizes the values obtained mapping this distance as a function of the initial direction of the particles.

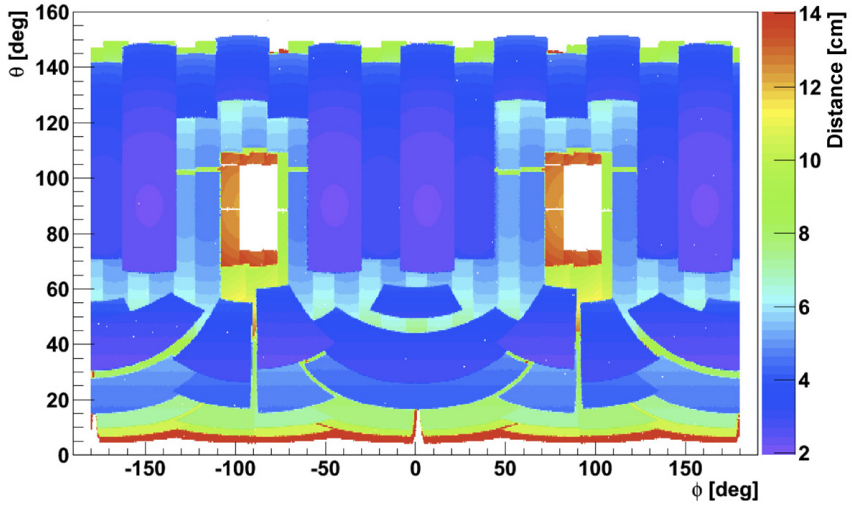

Figure 4.14: Map illustrating the distance between the nominal interaction point and the first hit point measured by the MVD as a function of the initial direction of a high momentum charged particle [3].

As in the case of the previous plots the map reflects the details of the geometry, therefore small gaps between the innermost sensors result in bigger distances as well as the holes in the acceptance due to the target pipe. Most of the tracks generate a hit point at distances of 4 cm or less from the interaction point, mostly on the first pixel barrel layer or on the first pixel forward disk. Figure 4.15 shows the average and minimum distance obtained at different polar

angles. Small polar angles correspond to bigger distances since the particles fly through the holes at the center of the first forward disks. Therefore the first hit point can be measured by the second, third, fourth, ... forward disk, depending on how small the initial polar angle is (see figure 4.16).

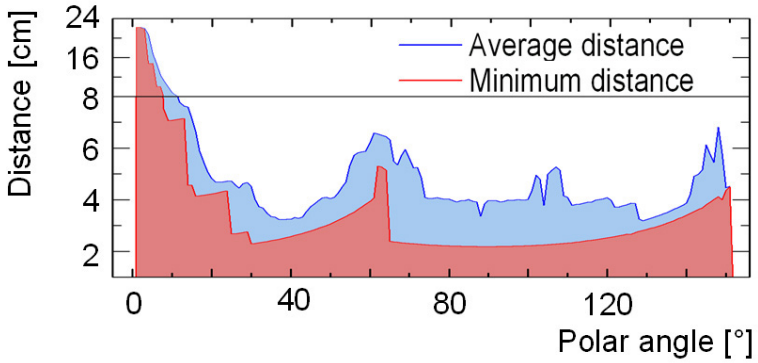

Figure 4.15: Average and minimum distance between the nominal interaction point and the first hit point along the azimuthal range as a function of the polar angle [3].

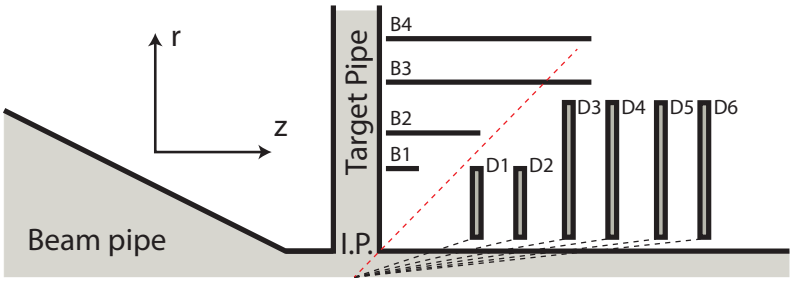

Figure 4.16: Scheme showing why for smaller polar angles the first hit point measured by the MVD is at a bigger distance from the nominal interaction point. The red line is an example of a particle flying through the gap between the innermost barrel layers and the first forward disks.

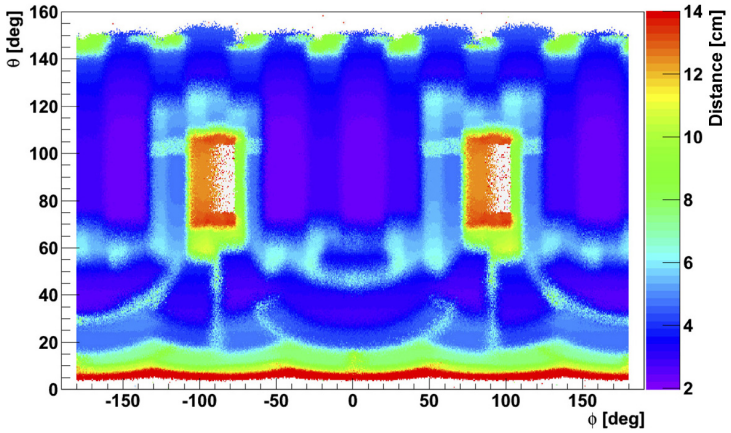

Figure 4.17: Distance between the interaction point and the first hit point in the MVD in a case were the interaction point is spread around the nominal one. The x and y coordinate of the interaction point follows here a Gaussian distribution with standard deviation $\sigma_{x,y} = 2$ mm, while its longitudinal position is distributed homogeneously in the range $x \in [-3, +3]$ mm.

The distance is increasing as well in the region around $\vartheta \sim 50°$: this is due to the gap between the end of the innermost barrel staves and the beginning of the first forward disks (see the red line in figure 4.16). The previous considerations were all made on the base of simulations propagating particles from the nominal interaction point. This was done to have a well defined situation in which to compare different geometries. Anyway in the experiment both the beam and the target will not be spot-like, therefore the crossing area will have a certain spread around the nominal interaction point. If we take into account for example a Gaussian distribution to describe the x/y position of the real interaction point with a standard deviation $\sigma_x = \sigma_y = 2$ mm and a flat distribution in the longitudinal range $z \in [-3, +3]$ mm we obtain results which are much less sharp than in the previous cases. The same gap will be seen differently by particles with the same initial direction, but with different start vertex. For example determining in this scenario the map showing the minimum distance between the start vertex of the particle and the first hit point leads to the distribution of figure 4.17. The distinction between regions is less precise, the structure appears blurred especially if compared with figure 4.14. It is important to notice that the effects of small gaps and overlaps will result in minor consequences when dealing with the realistic experimental conditions, therefore the optimization of the detector based on all the plots shown in this last section has been focused on the improvement of the average performances and of their homogeneity.

Bibliography

[1] Vijay Duggal. CADD Primer. *Mailmax Publishing*.

[2] Thomas Würschig. *Design optimization of the* $\overline{\text{P}}$ANDA *Micro-Vertex Detector for high performance spectroscopy in the charm quark sector*. PhD thesis, Universität Bonn, 2011.

[3] $\overline{\text{P}}$ANDA Collaboration. Technical Design Report for the: $\overline{\text{P}}$ANDA Micro Vertex Detector. 2011. arXiv:1207.6581.

[4] Boundary representation. http://cadd.web.cern.ch/cadd/cad_geant_int/thesis/node23.html.

[5] Constructive Solid Geometry. http://www.cs.mtu.edu/~shene/COURSES/cs3621/NOTES/model/csg.html.

[6] Geant3 manual. *CERN program library W5013*, 1993.

[7] GEANT4: An object oriented toolkit for simulation in HEP. http://geant4.cern.ch.

[8] Stefano Spataro. Event Reconstruction in the PandaRoot framework. *Journal of Physics: Conference Series*, 396(2):022048, 2012. http://stacks.iop.org/1742-6596/396/i=2/a=022048.

[9] I. Hřivnáčová et al. The Virtual Monte Carlo. 2003. arXiv:cs/0306005.

[10] S. Bianco, Th. Würschig, T. Stockmanns and K.-Th. Brinkmann. The CAD model of the $\overline{\text{P}}$ANDA Micro-Vertex-Detector in physics simulations. *Nucl. Instr. Meth.A*, 654:630–633, 2011. doi:10.1016/j.nima.2011.05.021.

[11] ISO 10303-1:1994. Industrial Automation Systems and Integration Product Data Representation and Exchange - Overview and Fundamental Principles. *International Standard*, ISOTC184/SC4, 1994.

[12] OpenCascade 6.3 documentation. http://www.opencascade.org/org/doc/.

[13] Rene Brun and Fons Rademakers. ROOT - An Object Oriented Data Analysis Framework. *Nucl. Instr. Meth. A*, 389:81–86, 1996. See also http://root.cern.ch/.

[14] S. Bianco on behalf of the $\overline{\mathsf{P}}$ANDA MVD group. Characterization of the $\overline{\mathsf{P}}$ANDA Micro-Vertex- Detector and Analysis of the First Data Measured with a Tracking Station. *IEEE Nuclear Science Symposium Conference Record*, N42(278):1149–1152, 2010.

[15] Documentation of the MVD 2.1 model. http://panda-wiki.gsi.de/pub/Mvd/ModelMvd2pt1/Mvd-2.1_Documentation.pdf.

CHAPTER 5

The vertex reconstruction performance of the $\overline{\text{P}}$ANDA spectrometer

The $\overline{\text{P}}$ANDA experiment will study the decay of several short-lived particles (see chapter 1). Therefore the Micro-Vertex-Detector is designed to be able to reconstruct primary and secondary vertices with a resolution in the order of 100 µm. These results are obtained complementing the measurements of the MVD with the information provided by other $\overline{\text{P}}$ANDA detectors. The MVD typically measures a number of hit points between three and six for each charged particle with its start vertex in the volume around the nominal interaction point. This number depends on the initial direction of such tracks since the geometry of the MVD foresees four barrel layers and six forward disks (see section 4.4). The information measured by the MVD in a standalone mode will be helpful for the determination of fast event selection criteria because it allows to provide an estimate about the number of charged tracks and their momenta in one event. Nevertheless when dealing with tracks close in the space the probability of assigning a hit point to the wrong track is significant and this can lead to a wrong determination of start vertex, momentum and even charge in the case of stiff particles (see figure 5.1a and 5.1b). This is the reason why

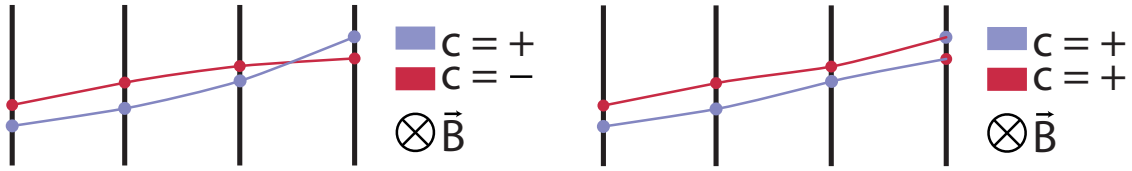

(a) Correct assignment. (b) Wrong assignment.

Figure 5.1: Example of a case where a incorrect assignment of hits to two tracks can lead to a wrong charge determination.

the track reconstruction is based on the combination of the information provided by different detectors. The STT measures a large number of hit points per track (typically between 20 and 30 per charged particle crossing the detector). Therefore the pattern recognition looks for correlations between the track-lets reconstructed by the two detectors. The high number of hit points measured by the STT allows for a better determination of the particles momentum and charge. Furthermore an important input comes from the combination of all the PID information from the $\overline{\text{P}}$ANDA detectors: only with the proper mass assumption it is possible to correctly

propagate the track candidates from the first hit point in the detectors back to their start vertices. Typically particles create their first hit at a distance between 2 and 10 cm from the interaction point (see figure 4.14), while often the particle decays under study take place at a few hundreds of µm far from the primary interaction point. In order to look for common vertices the track candidates need to be back propagated toward their closest point of approach to the incoming beam axis or to the nominal interaction point. Therefore the back-propagation has to take into account the energy loss inside the passive material (for example in the beam pipe) and the consequent change of bending radius. This results in a correction of the initial momentum and direction of the track, which both depend on the mass hypothesis for the track candidate. According to the Bethe formula (see [1]) (which has in this approximation a precision of a few percent in the kinematic range $0.1 < \beta\gamma < 1000$) the energy loss for ionization of a relativistic charged particle in an intermediate-Z material can be written as:

$$-\left\langle \frac{dE}{dx} \right\rangle = Kz^2 \frac{Z}{A} \frac{1}{\beta^2} \left[\frac{1}{2} \ln \left(\frac{2m_e c^2 \beta^2 \gamma^2 T_{max}}{I^2} - \beta^2 - \frac{\delta(\beta\gamma)}{2} \right) \right]$$

with $T_{max} = \frac{2m_e c^2 \beta^2 \gamma^2}{1+2\gamma m_e/M+(m_e/M)^2}$, where Z and A are respectively the atomic and the mass number of the material which is crossed by the particle, whose charge is written in terms of electron charge units ($z \cdot e^-$), $K/A = 4\pi N_A r_e^2 m_e c^2/A$ with N_A being the Avogadro's number and r_e the classic radius of the electron (2.817940325(28) fm), β and γ are the v/c ratio and the Lorentz factor of the incoming particle, m_e is the mass of the electron (0.510998918(44) MeV/c^2), I is the mean excitation energy of the material and M is the mass of the particle. Different particle species with the same momentum have different Bethe energy losses in the same passive material (see figure 5.2). Furthermore for light particles such as electrons the critical energy is at much lower values than for the other particle species, therefore Brehmsstrahlung is the dominant energy loss process for electrons of intermediate energies (see later figure 5.16). It is then crucial to apply the correct PID hypothesis when back-propagating the tracks.

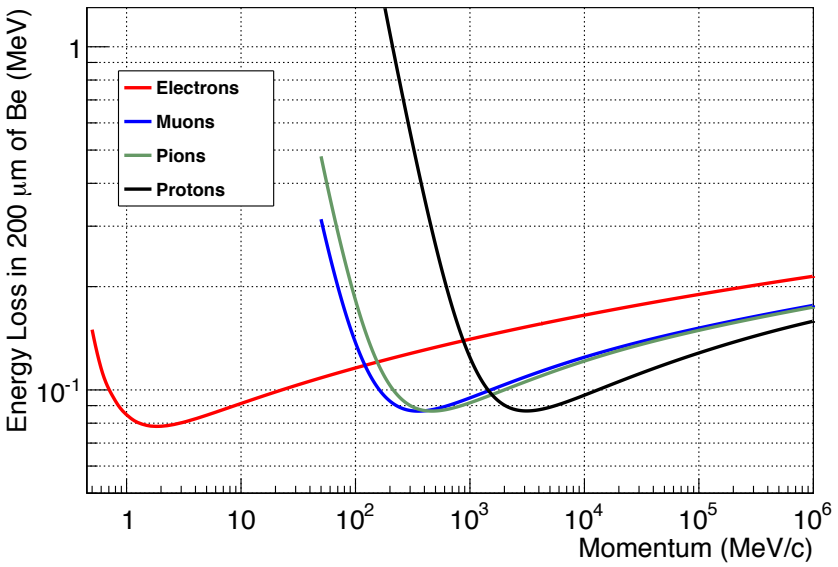

Figure 5.2: Energy loss for ionization as a function of the momentum for different particle species crossing 200 µm of beryllium (nominal value for the thickness of the beam pipe).

After this procedure has been performed it is possible to look for common vertices. The easiest strategy consists in applying a point of closest approach (POCA [2]) method between couples of tracks in the transverse x-y plane (see figure 5.3). The common vertex is determined averaging the POCA between couples of tracks. This average is weighted with an inverse function of the minimum distance between each couple of tracks: a POCA between tracks which are really close or even intersecting (like the two POCA highlighted in red in figure figure 5.3b) will have a bigger impact on the final vertex then the POCA between track with a bigger minimum distance (like the green one between tracks $\tilde{p}_1$ and $\tilde{p}_2$ again in figure 5.3b). For more details about different algorithms for the vertex reconstruction implemented within the PandaRoot framework see [3].

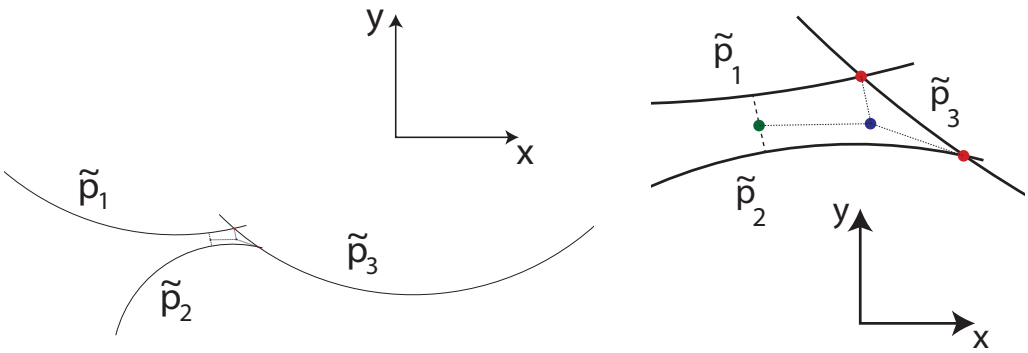

(a) Three tracks candidates for having a common vertex.

(b) Detail of how the POCA works in the transverse plane.

Figure 5.3: Example of one attempt to determine the common vertex between three tracks.

5.1 Characterization of the vertex reconstruction performance

The vertex reconstruction performance has to be characterized in order to understand what can be achieved in different kinematic conditions. A detailed study has been performed simulating different topologies and comparing the reconstructed vertices with what was given as input to the simulations [4]. In a first step four pions with a momentum of 1 GeV/c were propagated through the detectors starting from a common vertex. These particles were distributed homogeneously in the polar (ϑ) and azimuthal (φ) angle ranges: $\vartheta \in [10, 140]^\circ$, $\varphi \in [0, 360]^\circ$. Two of the pions were set to be positively charged, while the other two negatively charged. The simulation was performed including the MVD, the STT, the GEM and the FTS detectors. The whole procedure used for this study is shown in the flowchart of figure 5.4. Tracks were generated in the selected vertices and propagated through the detectors with Geant3 [5]. First Monte-Carlo hit points were generated in each detector, then the realistic response of each sensor was introduced digitizing the MC-true points and reconstructing realistic three-dimensional hit points. This last step introduces the granularity and the reconstruction strategy of the detectors under usage: both features influence resolutions and efficiencies. The next step consists in a pattern recognition and a complete track reconstruction combining the information coming from all the selected detectors. Tracks creating hits in the target spectrometer ("barrel tracks") and the ones measured with the forward tracker ("forward tracks") were treated differently. The reconstruction of the barrel tracks was performed in several steps: first an MVD-alone track finder was applied, which was then followed by a STT-alone track finder. Afterwards the track-

lets obtained in these last two steps were combined looking for new tracks in the set of not already used hits points. This information was complemented with the contribution of the GEM detector (when tracks were in its acceptance). When all the tracks had been identified a Kalman filter [6] looped forward and backward along all the hit points of each track performing a track fitting. Within the PandaRoot framework this operation is realized by the GENFIT package [7], which uses GEANE [8] as a propagator. When the track fitting has been performed a MC-match tool correlates the reconstructed tracks to their corresponding MC partners. This allows later comparisons which are helpful to characterize the whole reconstruction procedure. Differently, forward tracks do not undergo this procedure since the optimization of the pattern recognition and track fitting for tracks with small polar angles is still in progress. Forward tracks are identified with an ideal MC-driven pattern recognition. Then design resolution and efficiency of the forward tracker are used to smear the MC-truth relative to the forward tracks. A MC-match is performed for these tracks as for the barrel ones. When both types of tracks are reconstructed and fitted, the MC link is used to apply an ideal particle identification where each particle obtains the correct mass hypothesis. The optimization of a real particle identification, based on the information from all the detectors is in progress at the moment of writing this thesis. Afterwards tracks are back-propagated to their points of closest approach to the nominal interaction vertex. The last step consists in the analysis of the reconstruction results: here tracks can be combined obtaining vertex candidates and fitting their three-dimensional positions. The whole simulation campaign described in this chapter has been managed with custom graphic tools developed to interface the local computer cluster of the HISKP of Bonn. A description of such instruments can be found in appendix D. Details about the PandaRoot framework revision, the external packages and the geometry of the detectors used for the simulations are reported in appendix E.

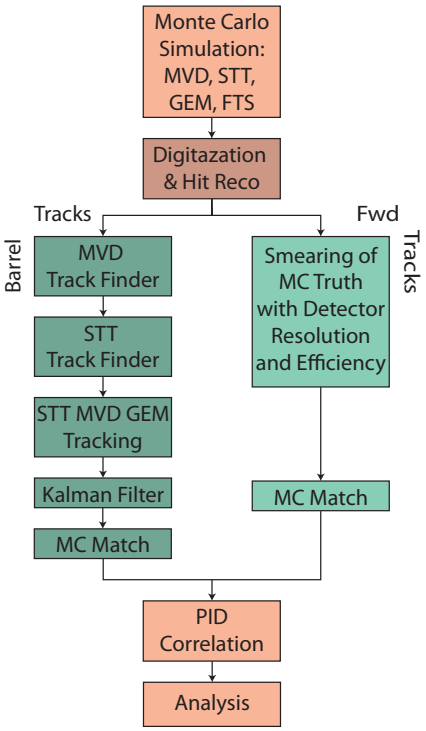

Figure 5.4: Scheme of the operations performed to simulate and reconstruct events.

5.1.1 Preliminary tests

The geometry of the MVD detector is quite symmetrical in the transverse (x-y) plane where the barrel sensors are disposed around cylinders and the forward ones in disks (see chapter 3). This is the overall layout of the MVD, but considering smaller portions of its volume this φ symmetry is not always maintained. The region around the target pipe is really difficult to provide with the services needed by the modules such as cooling and power supplies. Therefore the top and bottom staves of the innermost barrel pixel layers do not foresee sensor modules in the region just in front of the target pipe. This can be seen in figure 5.5a and 5.5b where sections of the first pixel barrel layers are shown. At specific polar angles this results in an inhomogeneous coverage along the azimuthal range: a different number of hit points are measured by the MVD for tracks with different initial φ angles. Tracks flying in the region close to the target pipe will have much bigger distances between their start vertex and the first measured hit point. This appears evidently in figure 4.14 where a rise in such distance appears at azimuthal angles

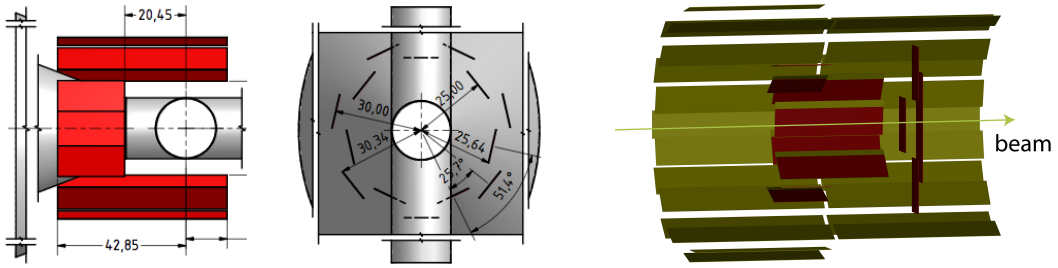

(a) Dimensions of the first pixel barrel layer: top (on the left) and front (on the right) view.

(b) Display of the innermost two barrel half-layers.

Figure 5.5: Dimensions and positions of the innermost barrel layers.

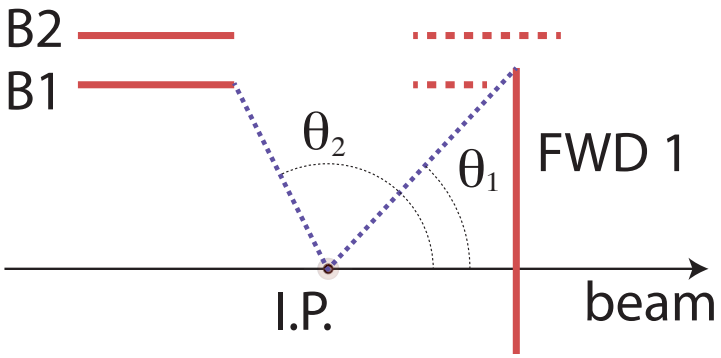

Figure 5.6: Scheme showing the polar angle region corresponding to the area not covered by barrel pixel sensors.

close to 90° and 270° and $\vartheta \in [\sim 50, \sim 125]^\circ$. This can be estimated as well starting from the geometry of the detector. Following the conventions of figure 5.6 and defining respectively ϑ_1 as the polar angle between the beam direction and the end of the first pixel disk and ϑ_2 as the one between the beam axis and the beginning of the backward barrel modules in the region around the target pipe, the obtained values depending on the φ angle are:

$$\vartheta_1 = \tan^{-1}\left(\frac{26.6\text{mm}}{14.4\text{mm}}\right) \sim 54^\circ$$

$$\vartheta_2, \text{min} = \tan^{-1}\left(\frac{20.45\text{mm}}{30.0\text{mm}}\right) \sim 125^\circ, \qquad \vartheta_2, \text{max} = \tan^{-1}\left(\frac{20.45\text{mm}}{25.0\text{mm}}\right) \sim 129^\circ$$

During the first analysis of the results of the simulations a clear difference between the vertex reconstruction performance for the x and y coordinates was found. For example shooting the four pions with a polar angle homogeneously distributed in $[10, 140]^\circ$ and smearing their azimuthal angles homogeneously in the range $[0, 360]^\circ$, the standard deviations of the reconstructed x and y vertex coordinate distributions were respectively $\sigma_x = 88.3$ µm and $\sigma_y = 69.4$ µm. This is not surprising due to the previous geometrical considerations: "vertical" tracks having azimuthal angles close to 90° or 270° are the most affected by the asymmetry in the detector coverage and they are measured less precisely in space than the other tracks. Since tracks orthogonal to the x axis are the ones providing the strongest constraint for the determination of the x coordinate of the common vertex, this φ-asymmetry of the disposition of the sensors will induce a worse vertex reconstruction performance along the x direction. Nevertheless some tests were performed to exclude other sources that could explain this behavior. An artificial rotation of 90° was applied

to the reconstructed tracks in the transverse plane before performing the vertex reconstruction (POCA method). This was done to check whether x and y were treated differently by the vertex reconstruction tools. The results are shown in table 5.1. Applying the artificial rotation there

σ	Default	90° Rot.
x	88.3 µm	69.4 µm
y	69.4 µm	88.3 µm

Table 5.1: Results obtained with and without an artificial 90° rotation in the transverse plane.

is an exact switch between the x and y performance, meaning that the vertex reconstruction does not bias the results treating differently the two variables. Another test was performed to ensure that the different resolutions achieved are really due to the φ-anisotropy of the sensors in the region in front of the target pipe. In this case the four pions were propagated from the nominal interaction point with well defined polar and azimuthal angles. A cross configuration in the transverse plane was chosen ($\varphi_2 = \varphi_1 + 90°$, $\varphi_3 = \varphi_1 + 180°$ and $\varphi_3 = \varphi_1 + 270°$) and the polar angle was fixed to $\vartheta = 75°$ for all the four pions. Two extreme cases were considered:

- **A:** $\varphi_1 = 45°$, in this situation the four tracks are not affected by the missing staves and they all have their first hit point on the innermost pixel barrel layer;
- **B:** $\varphi_1 = 0°$, two of the particles have initial azimuthal angle parallel to the target pipe, therefore they will not create hit points in the first barrel layers and they will have a bigger distance between the first measured point and the start vertex.

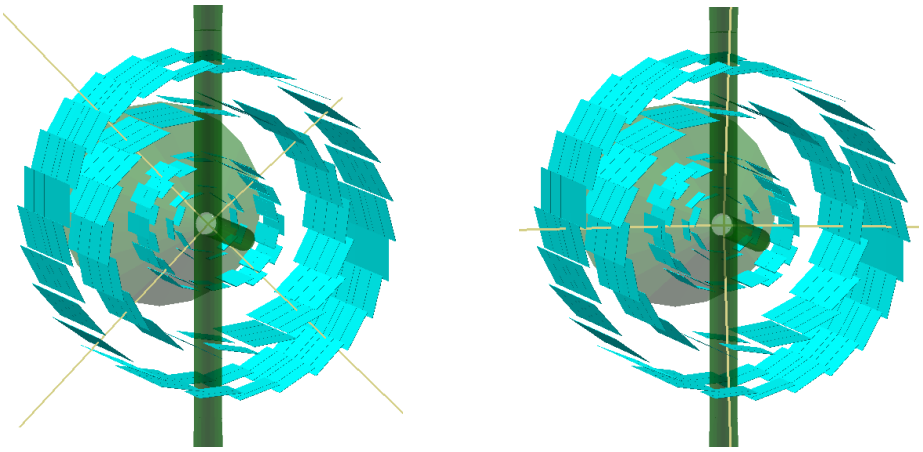

(a) Cross A layout. (b) Cross B layout.

Figure 5.7: The two layouts of the four pions initial directions used during the test.

The two cases are shown respectively in figure 5.7a and 5.7b. Table 5.2 summarizes the results obtained with this test. Using the cross A configuration, both with and without target and beam pipes, the achieved vertex resolutions for the x and y coordinates are equal. The presence of the passive material of the beam and target pipes increases slightly the standard deviations for both coordinates since particles scatter more before the first hit point can be measured. The situation is totally different when using the cross B setup: in this case the y coordinate is determined with a performance compatible with those of the cross A case, while the x coordinate suffers from the lack of hit points close to the start vertex, leading to a much worse standard deviation. In this case "vertical" tracks are reconstructed mostly using the information provided by the STT.

φ configuration	Beam/Target pipe	σ_x/µm	σ_y/µm
Cross A	No	30	30
Cross A	Yes	33	33
Cross B	No	103	29
Cross B	Yes	103	30
Uniform	Yes	67	47

Table 5.2: Results obtained with the different azimuthal configurations and fixing $\vartheta = 75°$ for all the particles.

If the four particles are distributed uniformly along the $[0, 360]^\circ$ range the results obtained are a compromise between the two extreme cases: $\sigma_x = 67$ µm and $\sigma_x = 47$ µm, where the two resolutions are much closer to each other than in the cross B case, but still the performance for the x coordinate is significantly worse than the y one. It is possible to scan the difference between these two resolutions as a function of the polar angle of the four pions setting $\vartheta_1 = \vartheta_2 = \vartheta_3 = \vartheta_4$ and distributing uniformly the azimuthal angle of each particle. Figure 5.8 shows the resolutions

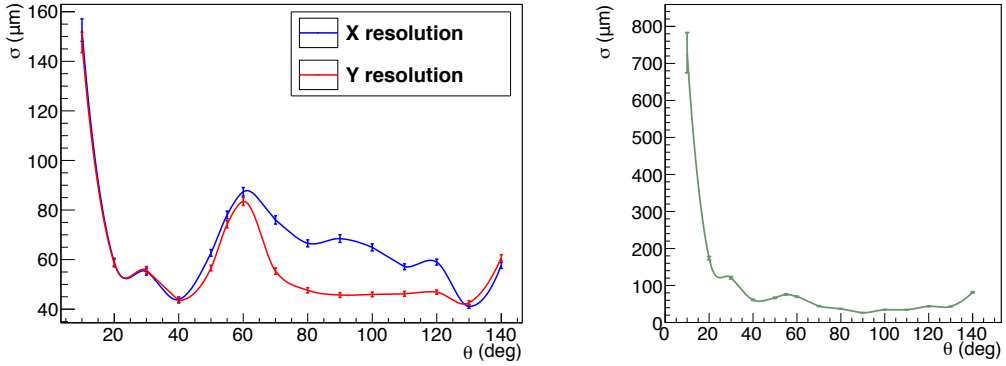

(a) Resolutions obtained for the x and y coordinates.

(b) Performance achieved determining the z coordinate of the vertices.

Figure 5.8: Results of the polar scan performed to study the differences between the performance in the three coordinates as a function of the initial polar angle of the pions.

obtained for the three coordinates. Each point in the plots correspond to a data set of 10.000 events. Here, as before, the term resolution is used to indicate the standard deviation of a gaussian fit performed on the obtained vertex distributions. The plot shows that the x and y resolutions are compatible for polar angles below $\sim 55°$ and above $\sim 125°$. In the intermediate region the x coordinate of the vertices is reconstructed with a worse performance than the y coordinate. This is in full agreement with what was estimated before on the base of the detector geometry. The z-resolution has a modulation in the polar range as well. The best performance is achieved for $\vartheta = 90°$ where all the four particles have an initial direction perpendicular to the z-axis, therefore the determination of the z coordinate of the common vertex maximally benefits from the disposition of barrel sensors. The z resolution becomes about 20% worse in the region $\vartheta \in [45, 65]^\circ$, where the passive material present in the MVD is higher due to the routing of the innermost pixel barrel layer (see figure 4.13). The same effect can be noticed in the x and y resolution plots. For small angles the FTS contribution is dominating the vertex determination, since there each track is smeared with a gaussian distribution with a 200 µm standard deviation.

5.1.2 The mapping of the vertex reconstruction performance

Three different scans have been realized in order to map the vertex reconstruction performance with four pions (two π^+ and two π^-) with a momentum of 1 GeV/c propagated from vertices positioned in different parts of the MVD inner volume:

- **Circular Scan -** the vertices were positioned along a circle of radius 1 cm, laying in the transverse x-y plane at z = 0 (see figure 5.9a);
- **Radial Scan -** the common vertices disposed along the vertical radius of the previously described circle (see figure 5.9b);
- **Longitudinal Scan -** the vertices were placed along the longitudinal (z) axis around the nominal interaction point (see figure 5.9c).

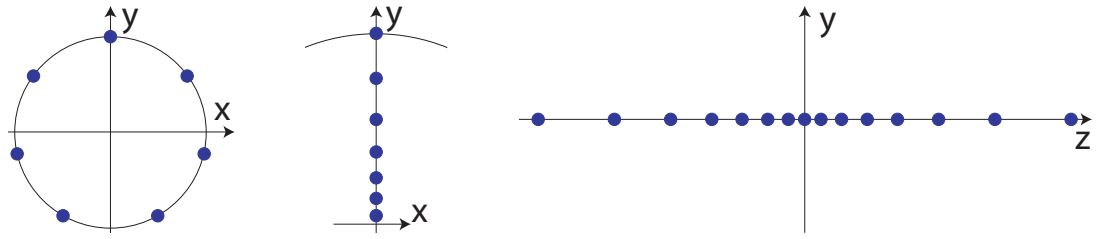

(a) Circular scan. (b) Radial scan. (c) Longitudinal scan.

Figure 5.9: Four pions scans.

Figure 5.10 shows the results of the longitudinal scan. All the three resolutions suffer a severe worsening when reaching along the z-axis distances of more than a few millimeters from the nominal interaction point. This is the expected behaviour since the pattern recognition used for these tests is initially assuming tracks to come from (0.,0.,0.) and it is efficient in the longitudinal range [–5, +5] mm. The obtained x-resolution is worse than the y one along all the

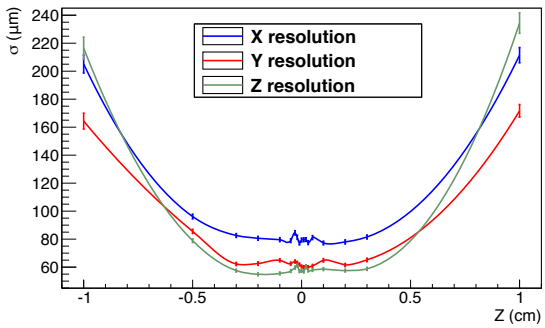

Figure 5.10: Results of the longitudinal scan of the vertex reconstruction performance.

scanned range, this is consistent with what was foreseen and studied in the previous section. In all the central part of the longitudinal range the obtained z-resolution is better than the x and y ones: this is due to the large polar angles of the tracks (ϑ is distributed homogeneously in the range $[10, 140]^\circ$) which allow for a better determination of the longitudinal coordinate (see also figure 5.8). Restricting the polar angle to small values the situation would be the opposite with better x and y resolutions. It is possible to notice small fluctuation in all the

three resolutions in the central longitudinal range [–2, +2] mm. These effects are produced by the small gaps between consecutive sensors (especially in the innermost barrel layers). When moving the common vertex to a position maximizing the number of tracks flying through one of these gaps the resolutions get locally worse. The momentum reconstruction performance was

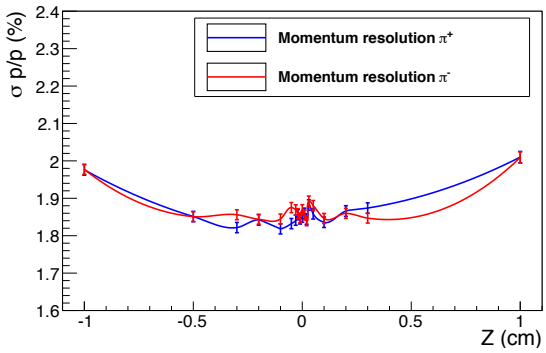

Figure 5.11: Results of the longitudinal scan of the momentum reconstruction performance for π^+ and π^- tracks.

monitored both for positively and negatively charged pions during the previous scan. The results are shown in figure 5.11: the momentum reconstruction is not too influenced by the position of the initial vertex, $\sigma p/p$ stays between 1.8 and 1.9% in the central part of the scanned range. This is due to the fact that for the momentum resolution it is more important to have several hit points measured with small multiple scattering (obtained with both the MVD and the STT) than to have hits as close as possible to the interaction point. The circular scan allowed to

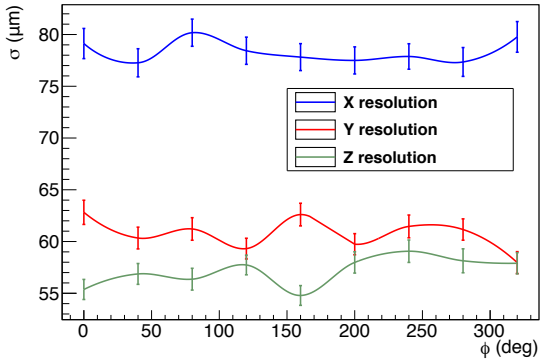

Figure 5.12: Results of the circular scan of the vertex reconstruction performance.

check the effect of moving the common vertex along a circle of radius 1 cm in the transverse plane. The results are shown in figure 5.12. Due to the φ-symmetry of the disposition of the barrel and forward sensors the performance is quite stable along the full circle, all the three resolutions have fluctuations of 2-3 μm. As before, the obtained x-resolution is significantly worse than the y one due to the top and bottom missing sensors (see the previous section) and the z performance is better due to the averagely bigger polar angles. Again the momentum resolution has small fluctuations within the range $1.8\% < \delta p/p < 1.9\%$, as shown in figure 5.13. The last scan performed (the radial scan) consisted in moving the common vertex along a radius of the circle in the transverse plane used for the circular scan. The results are summarized in figure 5.14. As in the previous cases the x-resolution is worse than the one obtained for the y coordinate. The performances are quite stable in the first 5 mm from the nominal interaction

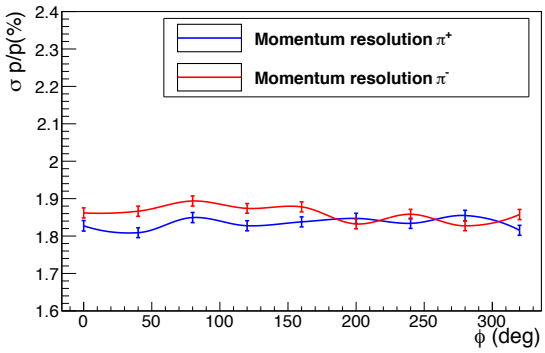

Figure 5.13: Results of the circular scan of the momentum reconstruction performance for π^+ and π^- tracks.

point. At bigger distances the efficiency of the pattern recognition drops down, due to the initial hypothesis of tracks coming form the nominal interaction point. For small radii the three resolutions have a small modulation due to the small gaps between consecutive sensors as in the case of the longitudinal scan. The momentum resolution is stable with small fluctuations in the range $1.8\% < \delta p/p < 1.9\%$ for both π^+ and π^- as in the two other scans (see figure 5.15).

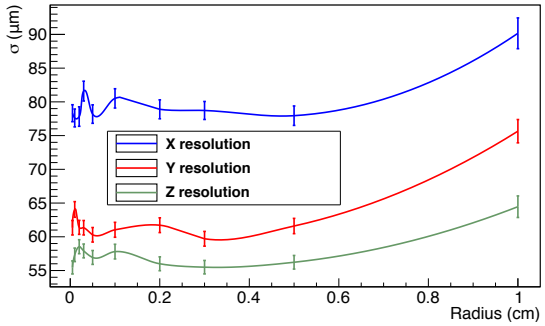

Figure 5.14: Results of the radial scan of the vertex reconstruction performance.

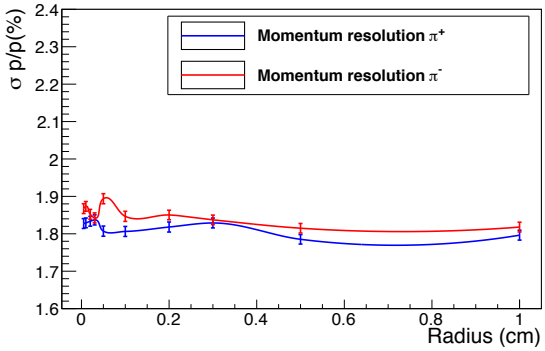

Figure 5.15: Results of the radial scan of the momentum reconstruction performance for π^+ and π^- tracks.

5.2 Primary vertex reconstruction

The determination of primary and secondary vertices is one of the most important tasks for the MVD. Therefore, after the characterization of the vertex reconstruction with the "four pions" scans, a real particle decay has been simulated and reconstructed in order to study a realistic kinematic scenario. Since $\overline{\text{P}}$ANDA is a fixed target experiment particles will be boosted forward along the beam axis in the laboratory reference frame, so most of the particles generated during a collision will be concentrated in the forward part of the target spectrometer and in the forward spectrometer acceptance. This is the reason why the different x and y resolutions noticed in the "four pions" scans does not emerge when trying to reconstruct most of the particle decays.

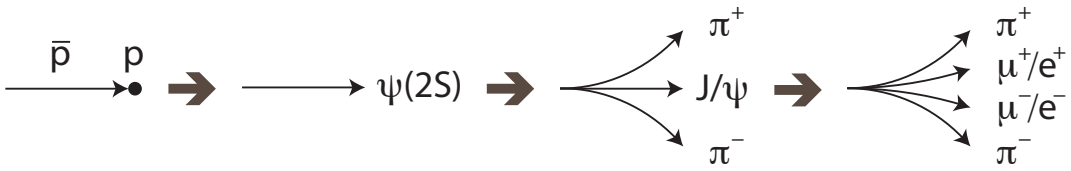

The benchmark channel chosen for this test is $\overline{\text{p}}\text{p} \to \psi(2\text{S}) \to \text{J}/\psi\pi^+\pi^-$ studying the J/ψ decays into $\mu^+\mu^-$ and into e^+e^-. This decay chain is convenient since the average lifetime of the $\psi(2\text{S})$ and of the J/ψ are both really short (respectively $1.95 \cdot 10^{-21}$ s and $7.05 \cdot 10^{-21}$ s [1]). This means that both the $\psi(2\text{S})$ and the J/ψ decay vertices can ben considered coincident with the interaction vertex taking into account the typical resolution achievable with a silicon vertex detector. Both the muonic and the electronic J/ψ decay were analyzed. The main difference between these two channels consists in the energy losses and multiple scatterings of the final state particles in the passive and active materials of the detectors. The critical energy for electrons is much lower than for muons. This energy corresponds to the point above which brehmsstrahlung becomes dominant over ionization as main energy loss mechanism. According to Jackson [10],

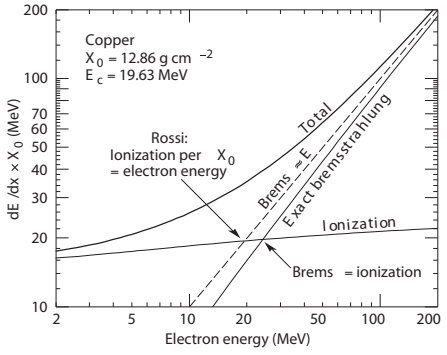

(a) Electron energy loss in copper per unit of radiation length [1].

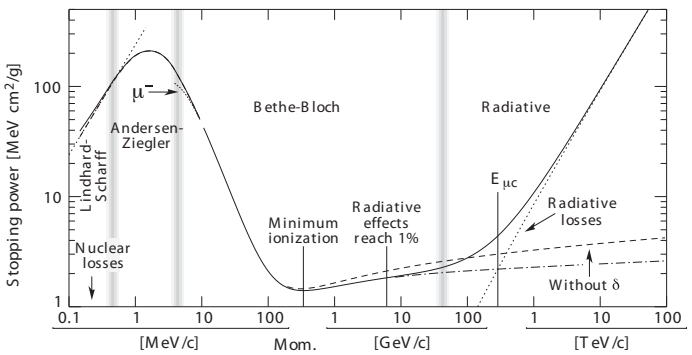

(b) Stopping power for positively charged muons in copper. $\text{E}_{\mu\text{c}}$ represents the critical for muons [9].

Figure 5.16: Critical energies for electrons and muons in copper.

the brehmsstrahlung cross section for relativistic particles with respectively initial (E) and final energy (E') satisfying the condition $\text{E}, \text{E}' >> \text{Mc}^2$, with Mc^2 being the invariant mass of the incident particle, can be written as:

$$\left(\frac{\mathrm{d}\chi_{\mathrm{R}}}{\mathrm{d}\omega}\right)_{\mathrm{Born}} \simeq \frac{16}{3}\frac{\mathrm{Z}^2\mathrm{e}^2}{\mathrm{c}}\left(\frac{\mathrm{z}^2\mathrm{e}^2}{\mathrm{Mc}^2}\right)^2\left(1-\frac{\hbar\omega}{\mathrm{E}}+\frac{3\hbar^2\omega^2}{4\mathrm{E}^2}\right)\left[\ln\left(\frac{2\mathrm{EE}'}{\mathrm{Mc}^2\hbar\omega}-\frac{1}{2}\right)\right]$$

The first factor of the differential cross section shows an explicit $1/M^2$ dependence which suppresses brehmsstrahlung for particles heavier then electrons. The power irradiated by brehmsstrahlung also drops rapidly with heavier masses ($\sim 1/M^4$). In the case of muons brehmsstrahlung still is the dominant energy loss mechanism at really high momenta (see figure 5.16b where the critical energy for muon in copper is marked with $E_{\mu c}$). For electrons the critical energy is much lower (see figure 5.16a), therefore brehmsstrahlung is the dominant process at the typical momenta of J/ψ decays. Since ionization is weak for both particle types due to the small masses, muons have a much smaller energy loss than electrons and can penetrate even thick materials. The muon decay of the J/ψ is therefore a cleaner channel where the final state particle are less affected by energy loss while flying through the detectors. When reconstructing the J/ψ electron decay more complex analysis strategies must be applied to deal with this scenario.

5.2.1 J/ψ muon decay

The J/ψ candidates are here determined combining reconstructed muons which are oppositely charged. Since the multiplicity of tracks is low (4 tracks only in the final state) and the muons are

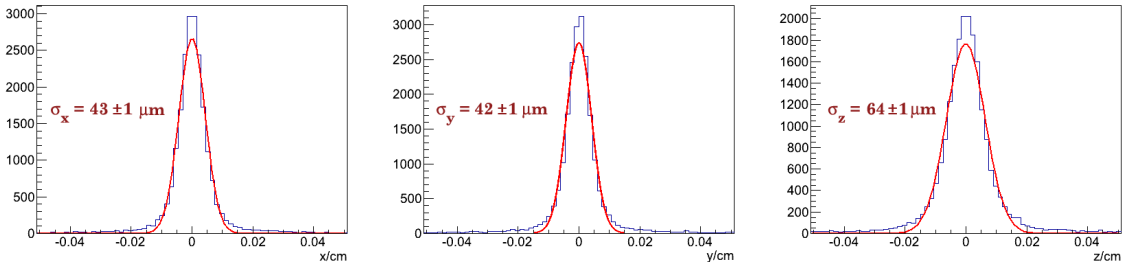

(a) x-coordinate. (b) y-coordinate. (c) z-coordinate.

Figure 5.17: Distribution of the reconstructed $J/\psi \to \mu^+\mu^-$ vertices.

a clean probe to study due to the small effect of multiple scattering, the preliminary reconstruction of this kind of decays does not require any selection on momentum or angular distribution. The plots of figure 5.17 show the distributions of the three reconstructed coordinates for such J/ψ vertex candidates. The x and y vertex resolutions are well compatible with each other. The z-coordinate is reconstructed slightly less precisely because of the forward boost of the J/ψ: the two muons are flying forward with small polar angle, therefore the relative polar angle between the two tracks is rather small, which makes it more difficult to determine the longitudinal position of their point of closest approach. These results were obtained within the PandaRoot framework using the "PndKinVtx" kinematic vertex fitter [11], which was used for all the vertex reconstructions performed during the studies shown in this sections. The J/ψ invariant mass distribution is shown in figure 5.18 and the position of its peak is in excellent agreement with the PDG values (see table 5.3). Of course the width of the distribution is dominated by the reconstruction resolution. A missing mass analysis was performed using the reconstructed pion candidates and the knowledge about the initial $\psi(2S)$ states. The J/ψ missing mass was obtained subtracting the four-momenta of the two π^+/π^- from the one of the initial $\psi(2S)$. The invariant mass distribution obtained with such technique is shown in figure 5.19. Using this analysis the mass value obtained is in excellent agreement with the PDG values (see table 5.3) and the width of the distribution improves of nearly one order of magnitude as compared with the direct J/ψ reconstruction.

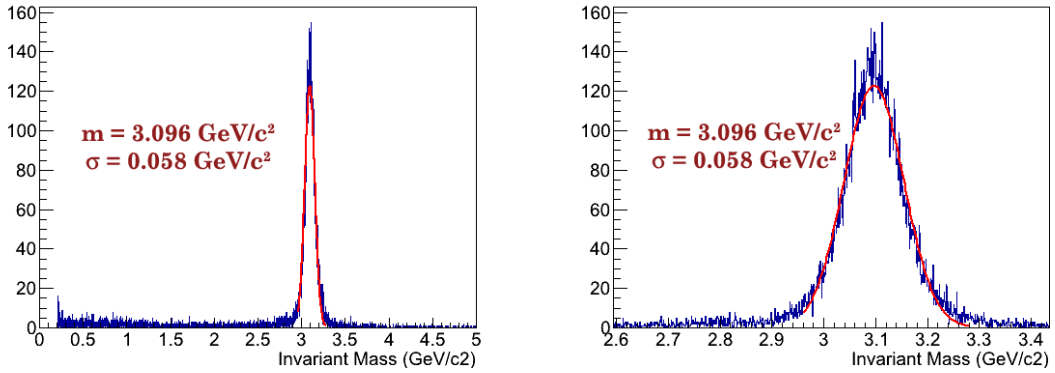

(a) Full distribution. (b) Zoom in the region of interest.

Figure 5.18: Distribution of the invariant mass of the J/ψ candidates.

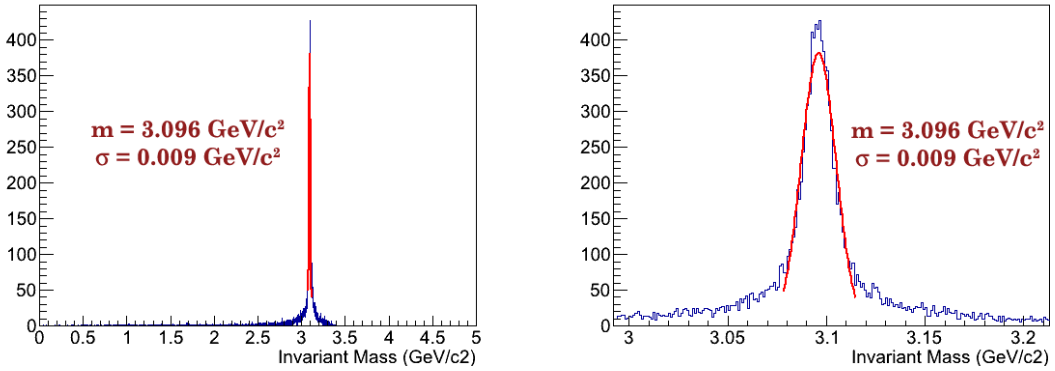

(a) Full distribution. (b) Zoom in the region of interest.

Figure 5.19: Distribution of the J/ψ missing mass obtained from the knowledge of the initial state and the four momenta of the reconstructed π^+ and π^-.

5.2.2 J/ψ electron decay

The $\overline{p}p \to \psi(2S) \to J/\psi\pi^+\pi^- \to e^+e^-\pi^+\pi^-$ decay was studied to test the reconstruction performance with particles more affected by scattering and energy loss than muons. A different analysis strategy was applied for this study: two dimensional plots showing the polar angle and the momentum of each reconstructed particle were considered. The Monte Carlo truth was used to tune a selection cut on the reconstructed electron/positron candidates (see figure 5.20). Only the tracks whose polar angle and momentum matched such an allowed region were used for the next steps of the analysis. The same procedure was followed for the π^+ and π^- candidates (see figure 5.21). The e^+/e^- candidates selected with these criteria were combined to reconstruct J/ψ vertices. The distributions of the reconstructed coordinates of the J/ψ vertices are shown in figure 5.22. The vertex reconstruction performance is well compatible with that one obtained in the previous subsection. The invariant mass distribution is shown in figure 5.23: the reconstructed peak mass is compatible within its error with the PDG value (see table 5.3). The width of the distribution is bigger than in the case of the muon J/ψ decay. This is due to the effect of the material of the detectors on electrons, which is more relevant than in the case of muons, as explained before. The missing mass analysis performed in the previous subsection was applied

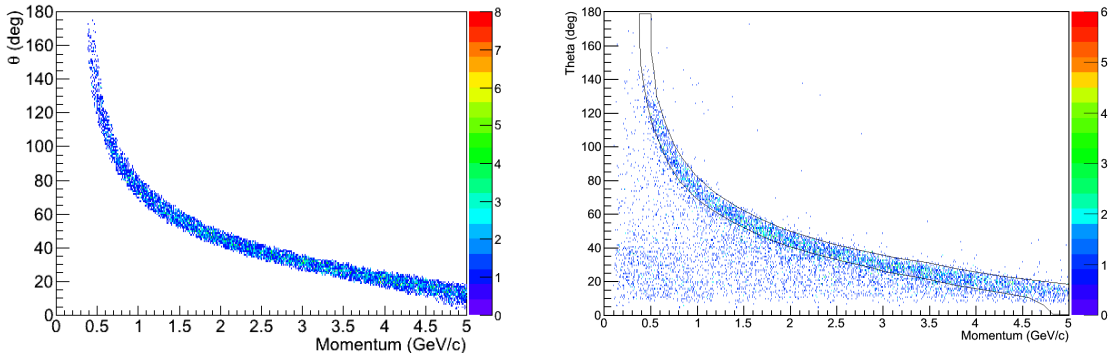

(a) Monte-Carlo truth.

(b) Reconstructed values with the superposed selection applied for the analysis.

Figure 5.20: Polar angle - momentum distribution relative to electrons and positrons.

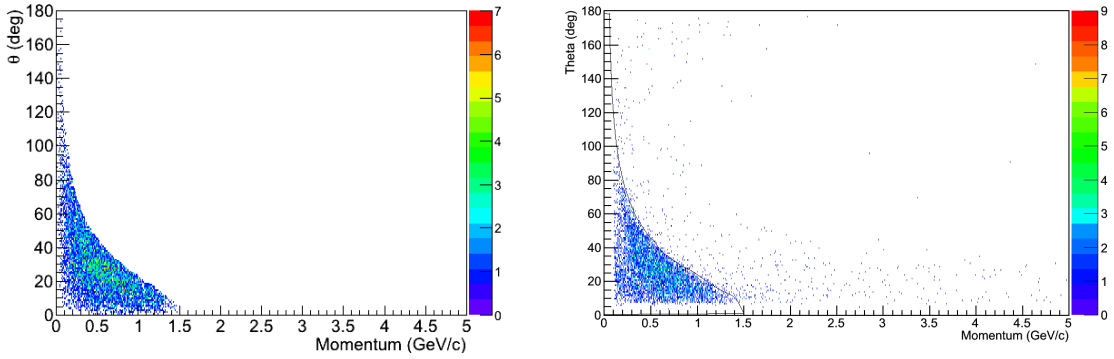

(a) Monte-Carlo truth.

(b) Reconstructed values with the superposed selection applied for the analysis.

Figure 5.21: Polar angle - momentum distribution relative to π^+ and π^-.

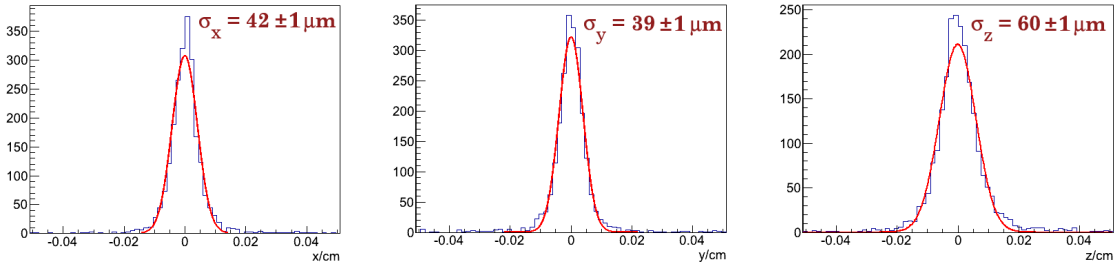

(a) x-coordinate.

(b) y-coordinate.

(c) z-coordinate.

Figure 5.22: Distribution of the reconstructed $J/\psi \to e^+e^-$ vertices after having applied the selection shown in figure 5.20.

to these decays as well. The results, which are shown in figure 5.24, are almost identical, since in this case the mass is mainly determined on the base of the reconstruction of the two pions, which have the same phase space range available in both the J/ψ decays. The main difference between the two cases consists in the fact that in the $J/\psi\pi^+\pi^- \to e^+e^-\pi^+\pi^-$ decay the pion candidates

were filtered according to what is shown in figure 5.21, while with $J/\psi\pi^+\pi^- \to \mu^+\mu^-\pi^+\pi^-$ all the pion tracks were used for the analysis. The $\psi(2S)$ vertices were reconstructed too, considering

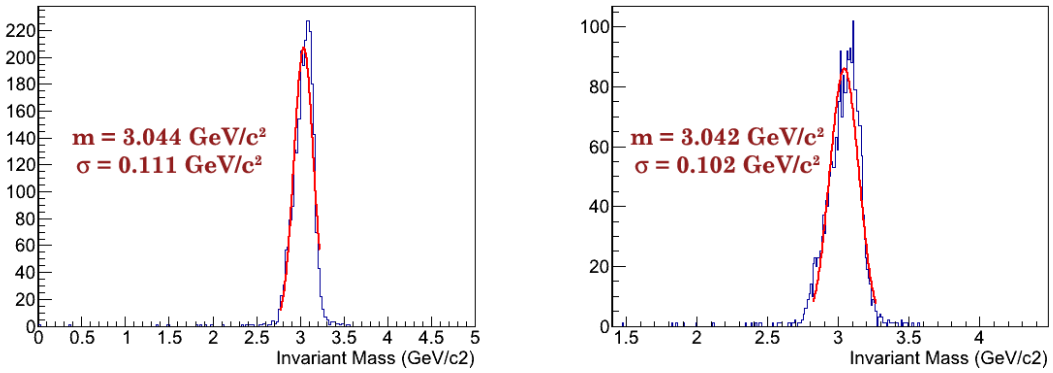

(a) Full distribution. (b) Zoom in the region of interest.

Figure 5.23: Distribution of the invariant mass of the J/ψ candidates.

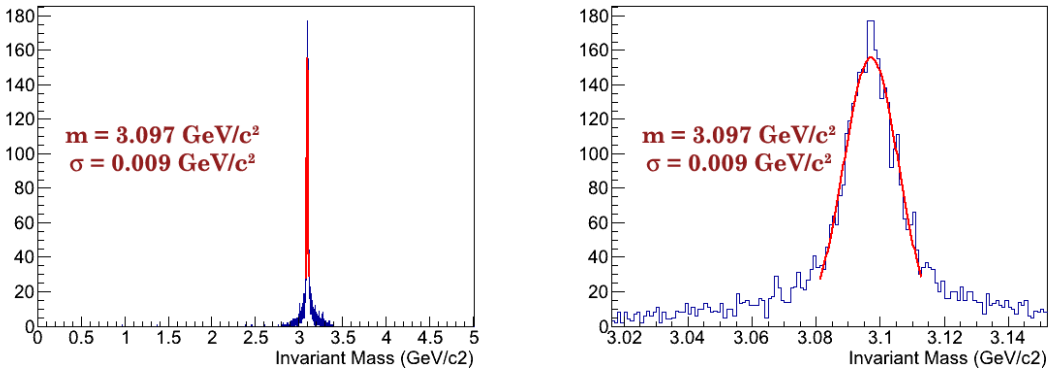

(a) Full distribution. (b) Zoom in the region of interest.

Figure 5.24: Distribution of the J/ψ missing mass obtained from the knowledge of the initial state and the four momenta of the reconstructed π^+ and π^-.

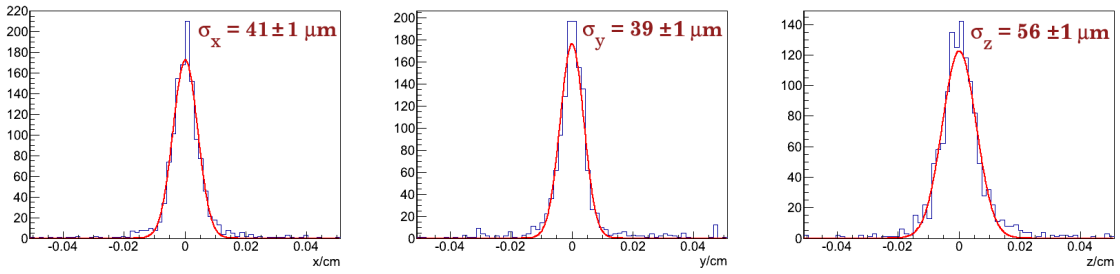

(a) x-coordinate. (b) y-coordinate. (c) z-coordinate.

Figure 5.25: Distribution of the reconstructed $\psi(2S) \to \pi^+\pi^-e^+e^-$ vertices after having applied the selection shown in figure 5.20 and 5.21.

for the fit four tracks (e^+,e^-,π^+,π^-) since the J/ψ decay can be considered instantaneous and its decay vertex as coincident with the primary vertex. The obtained results are shown in figure 5.25. The vertex reconstruction performances for the x and y coordinates are well compatible to what was obtained in figure 5.22. On the other hand the z coordinate of the $\psi(2S)$ vertices is determined more precisely than in the case of $J/\psi \to e^+e^-/\mu^+\mu^-$. Here four forwardly boosted

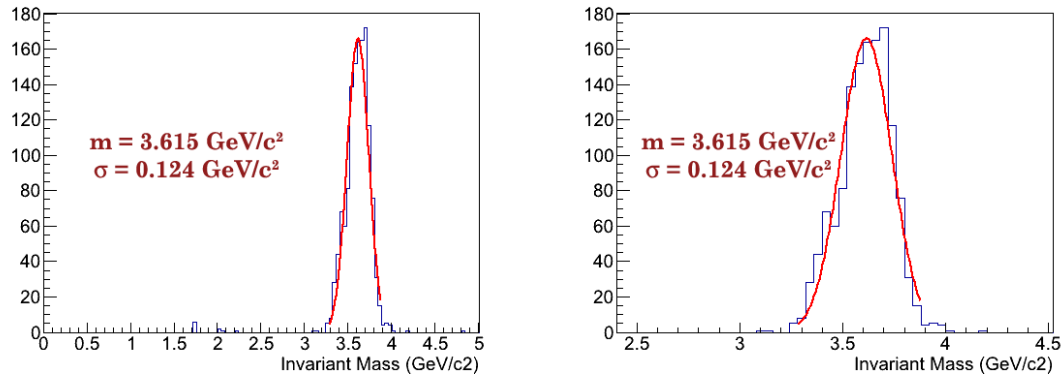

(a) Full distribution.

(b) Zoom in the region of interest.

Figure 5.26: Distribution of the invariant mass of the $\psi(2S)$ candidates.

PDG values for masses and widths		
State	Mass $\left(MeV/c^2\right)$	Width $\left(MeV/c^2\right)$
J/ψ	3096.916 ± 0.011	0.0929 ± 0.0028
$\psi(2S)$	$3686.109 + 0.012 - 0.014$	0.304 ± 0.009

Table 5.3: PDG values for mass and widths of different charmonium states (see [1]). These values were used as input for the Monte Carlo simulations.

particles are considered to reconstruct the vertex. Most of these tracks have polar angles of less than 45°, therefore the determination of the longitudinal coordinate of their vertices is less precise than the transverse ones. This is the reason why adding two more constraints (the two pion tracks) helps improving the z-vertex resolution. The invariant mass of each $\psi(2S)$ reconstructed candidate was determined obtaining the spectrum shown in figure 5.26. The peak values is compatible within its uncertainty with the mass of the $\psi(2S)$ reported in the PDG (see table 5.3), which was used as input for the Monte Carlo simulation.

Bibliography

[1] J. Beringer et al. (Particle Data Group). The Review of Particle Physics. *Phys. Rev. D86*, 010001, 2012.

[2] Implementation of the POCA alghoritm in the PndVtxPoca class. http://cbmroot.gsi.de/panda_doc/daily/html/classPndVtxPoca.html.

[3] Ralf Kliemt. *Simulations with the Panda Micro-Vertex-Detector*. PhD thesis, Universität Bonn.

[4] S. Bianco on behalf of the $\overline{\mathsf{P}}$ANDA MVD group. Beam tests and performance studies for the $\overline{\mathsf{P}}$ANDA Micro-Vertex-Detector. *IEEE Nuclear Science Symposium Conference Record*, N18(4):1503–1508, 2012.

[5] Geant3 manual. *CERN program library W5013*, 1993.

[6] R. Frühwirth. Application of Kalman filtering to track and vertex fitting. *Nucl. Instr. Meth. A*, 262(444), 1987.

[7] C. Höppner, S. Neubert, B. Ketzer, S. Paul. A Novel Generic Framework for Track Fitting in Complex Detector Systems. arXiv:0911.1008 [hep-ex].

[8] V. M. Maire, E. Nagy. GEANE: Average Tracking and Error Propagation Package. *CERN Program Library W5013-E.*

[9] Atomic Data and Nuclear Data Tables. *Vol. 76, No. 2, July 2001.*

[10] John David Jackson. Classical Electrodynamics. *3rd ed., Wiley, ISBN 0-471-30932-X.* p. 719.

[11] Documentation of the PndKinVtxFitter class. http://cbmroot.gsi.de/panda_doc/daily/html/classPndKinVtxFitter.html.

CHAPTER 6

A silicon strip tracking station

Building a tracking station composed of silicon strip sensors is a necessary and useful step during the development of a silicon detector for tracking of charged particles. The sensor technologies and the front-end electronics are first tested with a test station, where cosmic rays and sources can be used to compare different solutions and to understand the behavior of the systems. However, beam tests are required to verify the correct operation of the setup with high fluxes and rates, which the final sensors will have to deal with. Moreover beam tests allow to have high statistics in much shorter times and a more selected spectrum of particles, they are therefore suitable to study tracking algorithms and to investigate the performances of the sensors. These are the reasons why the Bonn group designed and built a silicon strip tracking station which has been tested at different particle accelerators.

6.1 The strip tracking station

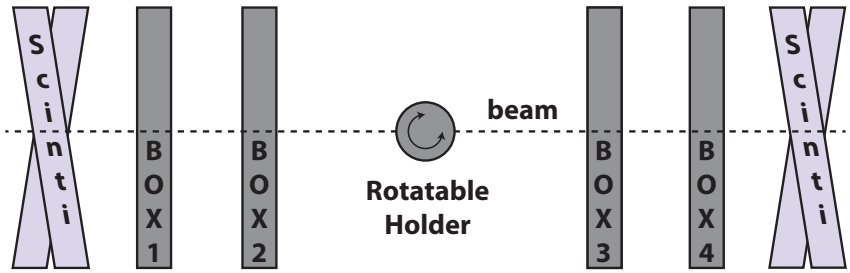

Figure 6.1: Scheme of the tracking station.

The tracking station set up by the Bonn group consists of four aluminum cases hosting silicon strip sensors [1] disposed along a longitudinal direction so that it can be used as a beam telescope (see figure 6.1). The four boxes can be moved along the longitudinal direction with step motors spanning a range of nearly 2 m and in the transverse plane with a positioning system which allows for a precise alignment of the sensors (see figure 6.2). A fifth holder is positioned at the

center of the tracking station. It is therefore possible to place volumes of materials in order to perform measurements of the scattering angle distributions. This fifth holder allows rotations around a vertical axis, so it can also be used to house one of the four sensors. The rotation of one sensor is interesting because one can study the effect of different incident angles of the beam with respect to the surface of the sensor on the cluster size of reconstructed hit points and on the total energy loss of the particles in the volume of the sensor. Each box is equipped either with a double sided module or with a couple of single sided ones arranged with a 90° stereo angle in order to be able to measure both transverse coordinates. The sensors are readout with three APV25S1 chips [2] per side. Every chip is bonded to 128 channels. The analog output of the APVs can be sampled with sampling ADC to determine the energy loss measured by each channel [3] [4]. The readout of the sensors is usually triggered by the coincidence of the signals generated in four scintillating slabs positioned at the beginning and at the end of the tracking station. More complex logics can be applied to trigger the data acquisition.

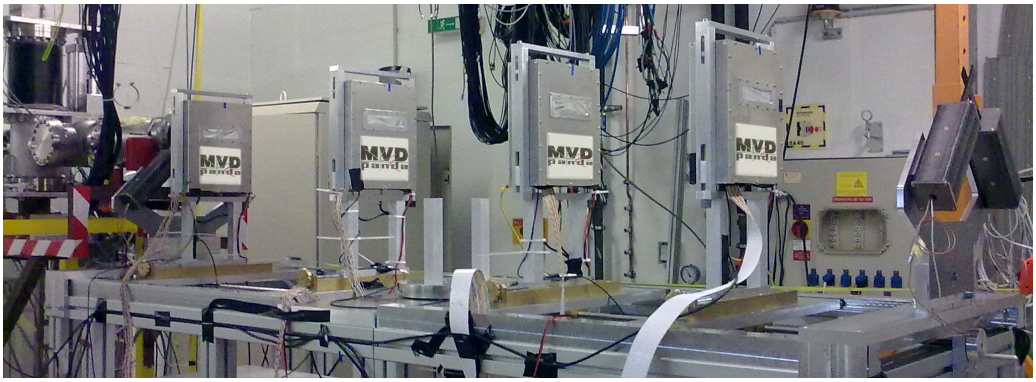

Figure 6.2: The tracking station setup at the COSY synchrotron [5].

6.2 The prototype silicon strip sensors

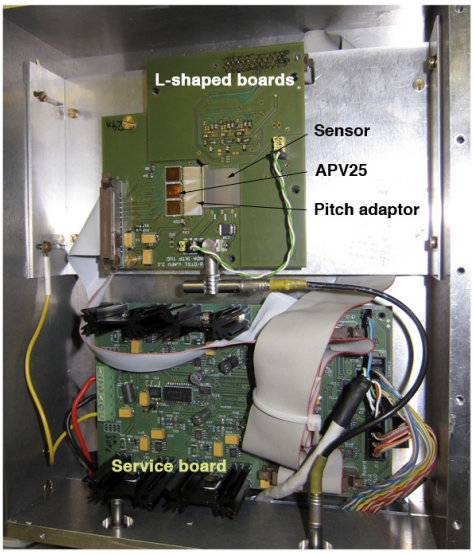

Figure 6.3: View of one box equipped with a sensor and service boards.

The square sensors used to equip the tracking station have an active area of 1.92×1.92 cm^2 and a thickness of 300 µm. The sensors have a 50 µm pitch and a stereo angle of 90°. The sensors were produced with p^+ and n^+ strips implemented in a n-bulk and usually punch through biased at typical voltages of about 60 V. As mentioned before each sensor side is read out with three APV25S1 front-end chips. Since the pitch of the sensors (50 µm) is different from the one of the front-end chips (44 µm) a ceramic pitch adaptor to connect each strip to the corresponding pad of the front-end chip is used (see figure 6.4). Figure 6.3 shows the typical setup of a sensor box. Two L-shaped PCB boards house the front-end chips and the pitch adaptor necessary to read out one side of the sensor. These boards also allow to provide the depletion voltage to the sensor. The second board inside the box (the one at the bottom) houses services for the previously described test board such as

voltage regulators and shapers. The whole box is realized with aluminium to shield the sensors from backgrounds and it features two cut-outs on the front and rear plates in correspondence of the active sensors. These cut-outs are covered with a 20 µm thick mylar layer which makes the internal part of the box light tight.

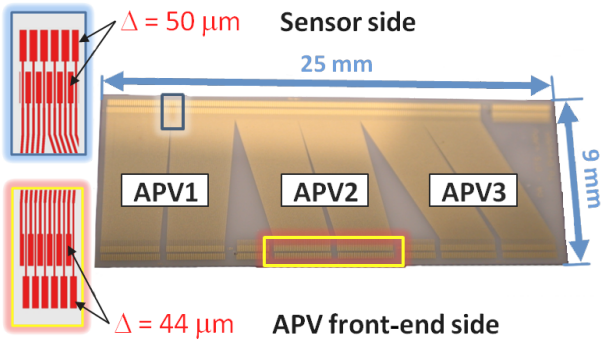

Figure 6.4: Pitch adaptor used to connect the front-end chips to the channels of the sensors [1].

6.3 The data acquisition system

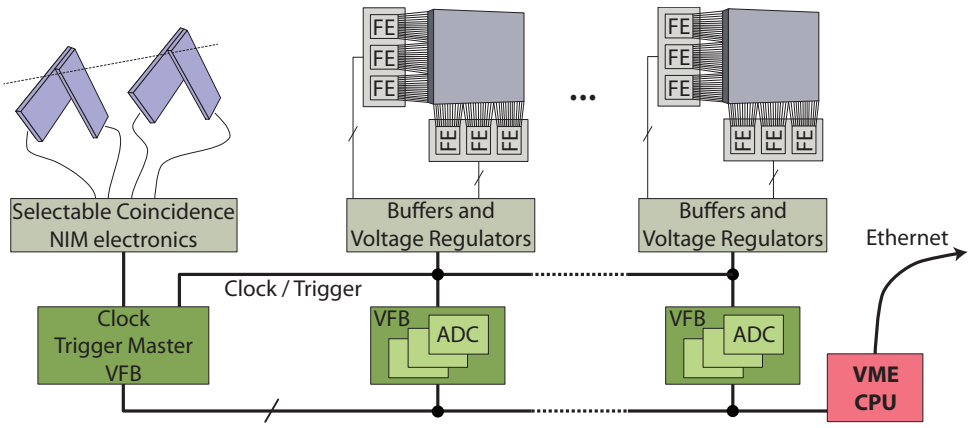

Figure 6.5: Scheme of the data acquisition system used to read out and store data from the sensors.

A selectable coincidence of the signals generated by the photomultipliers reading out each scintillating slab is processed by a clock/trigger master module, which redistributes a trigger pattern to all the front-end chips. In most of the cases a coincidence with a minimum of three hits in the four scintillators is required to trigger the acquisition. The analog output of each APV front-end chip is sampled by sampling ADC modules implemented on mezzanine boards, each of them plugged on a VME-FPGA-Board [3]. This last module can perform online operations such as baseline and pedestal correction. Even online clustering can be realized at this step. Data are transmitted then to the VME CPU via the VMEbus of the VME crate used to host the VME-FPGA-Boards. The DAQ software runs on the VME CPU and can be accessed from the counting room with an ethernet connection. Output data are stored in ASCII (American Standard Code for Information Interchange) and ROOT files [6] using custom containers collecting all the information about the response of all the front-end channels fired in a triggered event.

6.4 Conversion, alignment, energy calibration

The analysis of measured data has been performed within the PandaRoot framework [7] in order to use all the tools developed to treat simulated data. This is wanted in order to directly compare measurements and Monte-Carlo simulation, not being biased by different analysis instruments. A software infrastructure was developed for this purpose implementing a converter able to access the raw data and import them in a format compatible with the PandaRoot standards.

6.4.1 Conversion

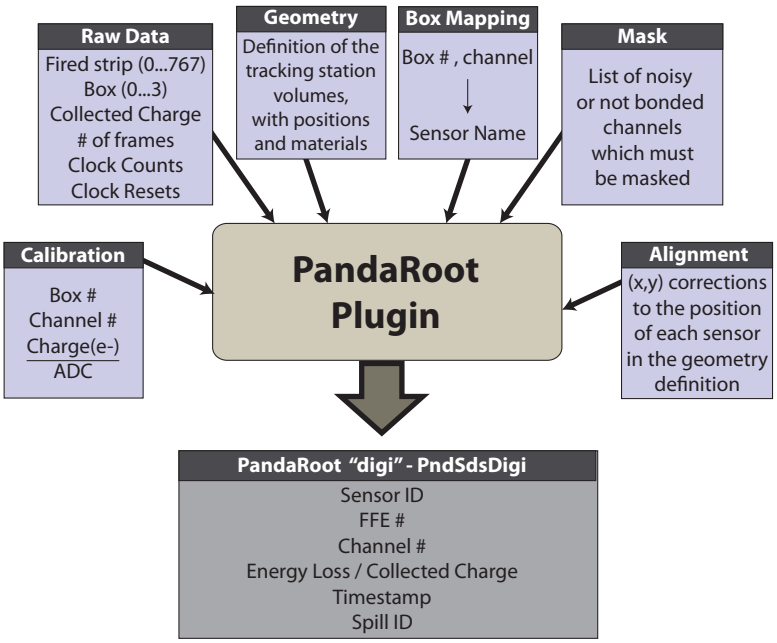

Figure 6.6: Scheme of the software infrastructure developed to import raw data into the analysis framework.

The structure of the developed converter is shown in figure 6.6. The converter classes include the class used to store the raw data, so that all the information can be accessed correctly. A geometry of the setup must be provided by mean of ROOT [6] geometrical volumes. This geometry can be tuned taking into account the results of an off-line alignment procedure (see section 6.4.2). An energy calibration can be applied to each channel of the sensors setting a ratio between the measured ADC counts and the corresponding collected charge / energy loss. The converter features the possibility of masking some channels. This is useful in the case of noisy channels, which are fired most of the times. Masking these channels at the converter level make all the following steps faster, avoiding unnecessary operations. A front-end map must be provided to the converter as well: in this file a link between the front-end numbering scheme used in the acquisition and the volume names defined in the geometry used for simulations can be introduced. The output of the conversion consists of `PndSdsDigiStrip` objects [8], which are the software implementation of the information collected by each channel of the MVD strip sensors.

6.4.1.1 Raw data and converted data

The raw data structure differs from the scheme used for the PandaRoot containers. For each fired channel an entry is saved in the raw data containing information about the channel number, the box to which it belongs, the number of ADC counts corresponding to the sampled amplitude of the analog output of the front-end chip, which is a function of the collected charge and the number of frames over threshold of the generated signal. Channels belonging to the same sensors

Info	**Raw data**	**Conv. Data**
Sensor	Box ID 0 ... 3	Sensor ID 0 ... 3
Front-end chip	implicit -	FE ID 0 ... 5
Channel	channel ID 0 ... 767	channel ID 0 ... 127
Collected charge	ADC counts	Charge
Timestamp	Clock	Timestamp
Spill	Reset ID	Spill ID
Frames	# frames	filtered

Table 6.1: Different conventions for raw and converted data containers.

are numbered from 0 to the total number of channels -1 (so for example channel 50 will be the 51^{th} channel of the first front-end chip, while channel 132 will be the 5^{th} of the second chip since every APV reads out 128 channels). There is no explicit information about the front-end chip which reads out that channel, since this can be derived from the absolute channel numbering. The converted data match the `PndSdsDigi` container layout featuring a sensor identification number, a front-end chip identifier (between 0 and 5 with the double-sided sensors), a channel number (in this case this number spans between 0 and 127 since the container has a front-end chip identifier) and an information about the collected charge (derived from the ADC counts of the raw data). In some cases an absolute timestamp and a reset counter can be added to allow the synchronization with other systems. The standard PandaRoot containers have been modified to include these two needed data members. Table 6.1 summarizes the values which can be assumed by the data members of the two different containers. Figure 6.7 shows the distribution of the fired channels along the six front-end chips of one sensor obtained during a beam test with 2.7 GeV/c protons at COSY [5]. The chips with an identifier between 0 and 2 refer to the front size of the sensor, while chips 3, 4 and 5 are used to read-out the the back side. Front-end chips 1 and 4 show the highest number of entries because they readout respectively the central region of the top and bottom sides of the sensor. The 2.7 GeV/c proton beam used during the test taken here as an example had a size of a few mm and the sensors were positioned so that they could see the most intense part of the beam at their centers. The same information can be obtained looking at the histogram shown on the left of figure 6.8, where the fired channel numbers (from the top side of the sensor) obtained from raw data are plotted. The histogram on the right of the same figure shows the distribution of the fired channels within the front-end chip number 1 derived from the converted data. In both plots the beam profile is evident and the channel pattern is well compatible. In both cases it can be noticed that channel 64 of the front-end chip 1 (in the raw data this corresponds to channel 192) is never fired, while the neighboring

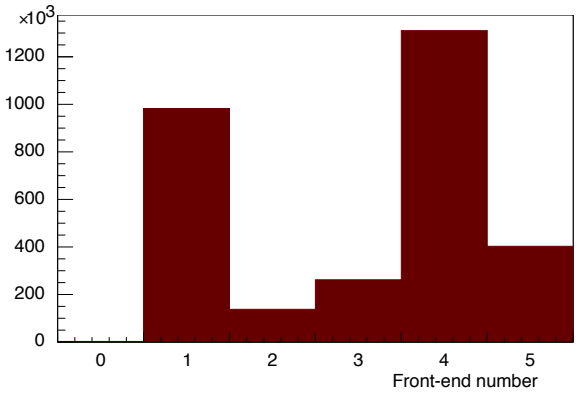

Figure 6.7: Distribution of the fired channels within the front-end chips used to read out the first sensor (converted data). These data were obtained during measurements performed at the COSY synchrotron [5] with 2.7 GeV/c protons.

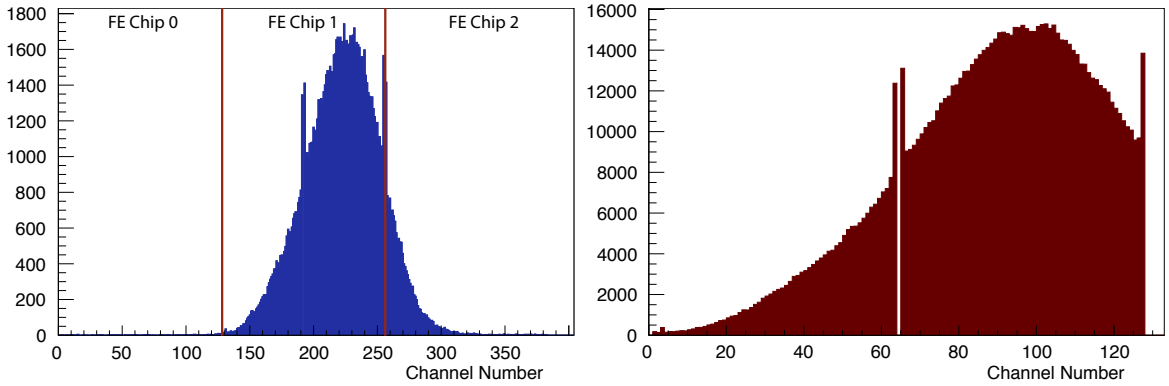

Figure 6.8: Comparison of the channel occupancy between the raw data (on the left) and the converter data from the front-end chip number 1 (on the right).

channels see an enhancement of events. The same phenomenon appears every 64 channels and it is determined by the structure of the pitch adaptor used for the beam tests: due to space limitations one every 64 channels could not be connected to the front-end chip; the previously described enhancement is explained considering that the charge generated in events in which one not bonded channel is hit by a particle is then shared between the two neighboring channels. Figure 6.9 shows the distributions of the ADC counts obtained sampling the analog output of the front-end chip (the plot on the left) and the corresponding collected charge obtained from the converted data (the histogram on the right). This plots shows the collected charge per channel (not the total energy loss per track), therefore it is possible to notice two peaks: the one corresponding to clusters composed by a single channel (the most prominent peak at some 22 ke^-, which is the expected peak energy loss of a minimum ionizing particle in 300 µm of silicon) and the one obtained from larger clusters.

6.4.2 Alignment

The setup is optically aligned during the installation sequence: a laser level is used to position all the boxes and the scintillating slabs along a straight line. An iterative procedure has been developed to perform a more precise offline alignment of the setup. Events in which each sensor

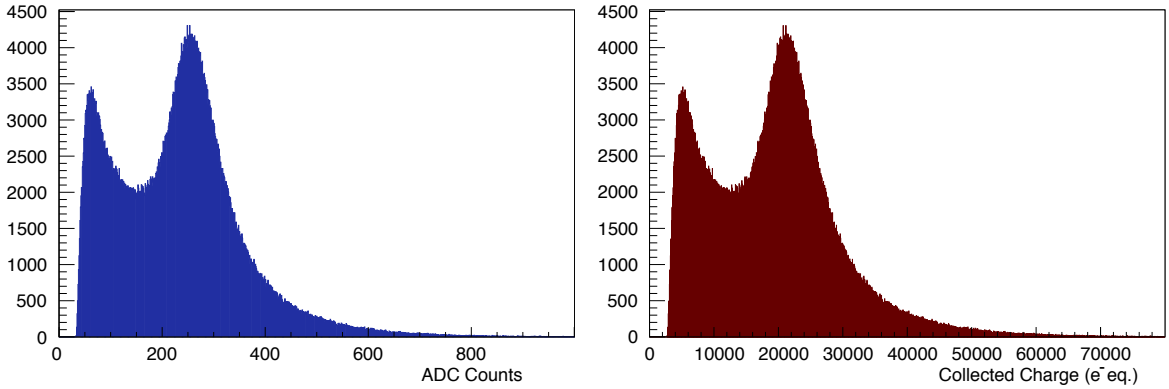

Figure 6.9: The left figure shows the distribution of the number of sampled ADC counts which is stored in the raw data, while the right histogram refers to the collected charge which is obtained from converted data.

measured one hit point are used to determine the residual distributions on the transverse plane of each sensor. In the case of a perfect alignment all the residual distributions would be centered around zero. The position of each sensor is corrected in the transverse x-y plane according to

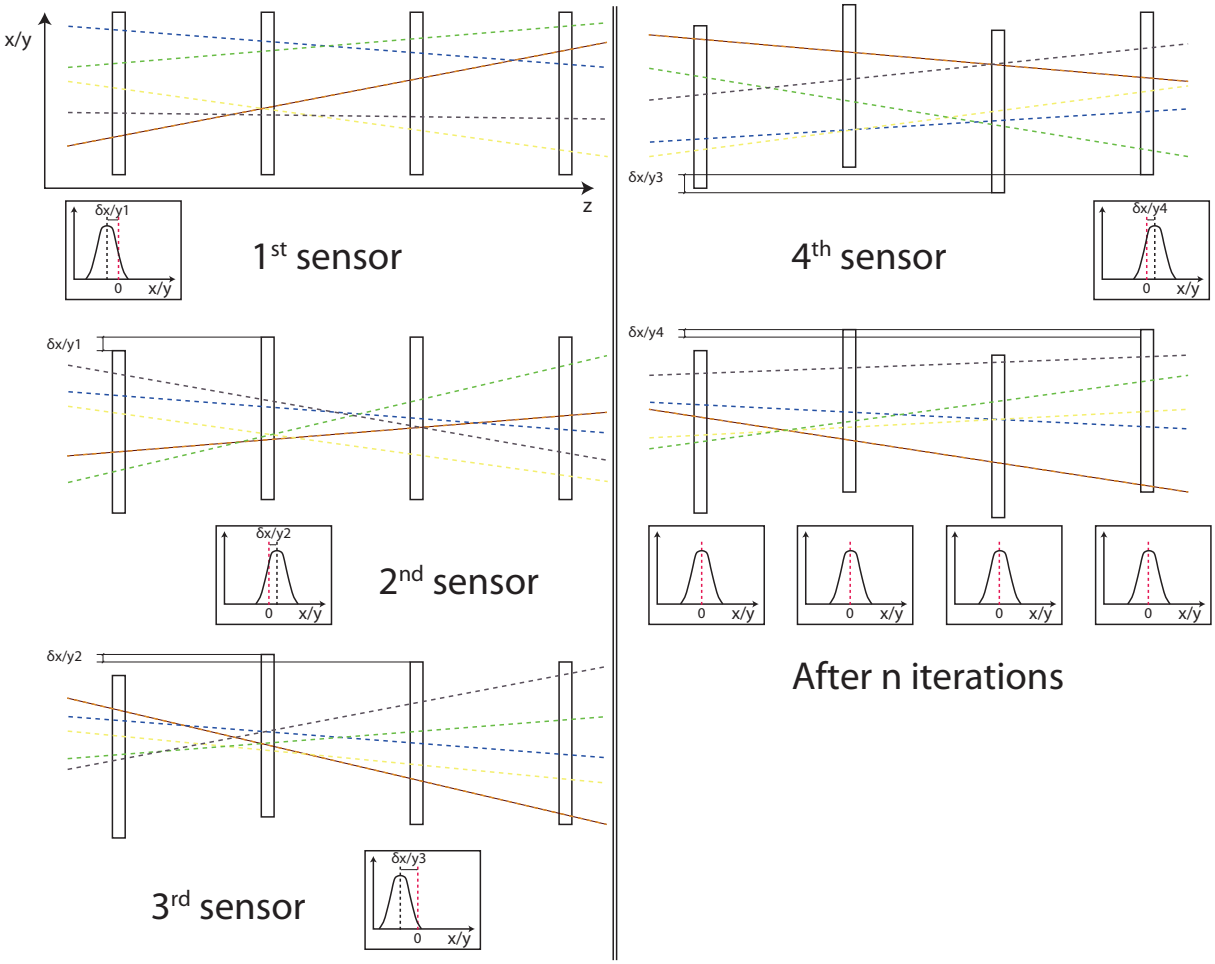

Figure 6.10: Description of the iterative alignment procedure.

the distance from zero of the mean of the corresponding residual distributions. The position of each sensor is corrected in different consequent steps: only after having moved the first sensor the residuals are calculated on the second plane, using the new position of the first sensor. After correcting the position of one sensor the residual distributions are determined on the next one. The whole procedure can be repeated several times until a certain desired precision is achieved. Figure 6.10 illustrates the steps followed during the alignment procedure. Figure 6.11 shows the y residual distribution on one sensor before the alignment and after five iterations of the offline alignment procedure.

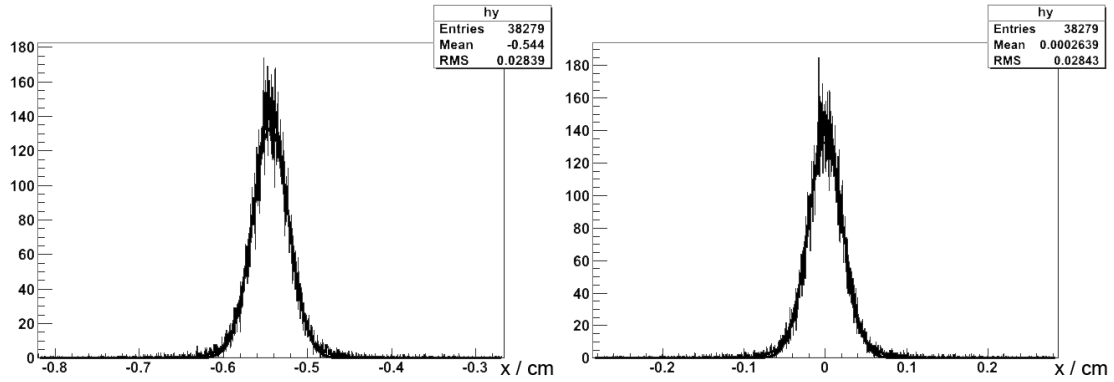

Figure 6.11: Residual distribution obtained before (left) and after five iterations of the alignment procedure.

6.4.3 Energy calibration

The energy calibration is performed in two steps. The APV-25S1 front-end chip foresees the possibility of injecting a nominal charge on all its channels. A scan in a typical range of collected charges can be performed obtaining a characterization of the response of the front-end chip to the injected charge. In this way it is possible to resolve the differences between the channels and to have a comparable response along the sensor. If needed a second calibration can be applied to the data, imposing a conversion factor between the absolute energy loss and the ADC counts of the APV output. As an example figure 6.12 shows the energy loss distributions obtained with beams of protons with different momenta, where the absolute calibration was performed fixing the energy loss / ADC counts ratio with the 2.95 GeV/c data: the mean energy loss was tuned according to the value available in the NIST database [9].

6.5 First beam tests

The first beam tests were performed with protons at the COSY synchrotron in Jülich and with electrons at DESY in Hamburg [10]. Several initial hardware characterizations of the sensors and the front-end chips were performed. Figure 6.13 shows some results from the first measurements at COSY. Figure 6.13a illustrates the map of hits obtained on a single sensor. The rhomboidal shape of the region with the highest number of hits is caused by the overlap of the scintillators used to trigger the acquisition, which was smaller than the active area of the sensors and had a 45° rotation with respect to the sides of the sensors (see figure 6.2). A comparison of the total energy loss in all the sensors crossed by a track is shown in figure 6.13b as a function of the number of stations in which a hit was measured. Figure 6.13c summarizes the results of a linear

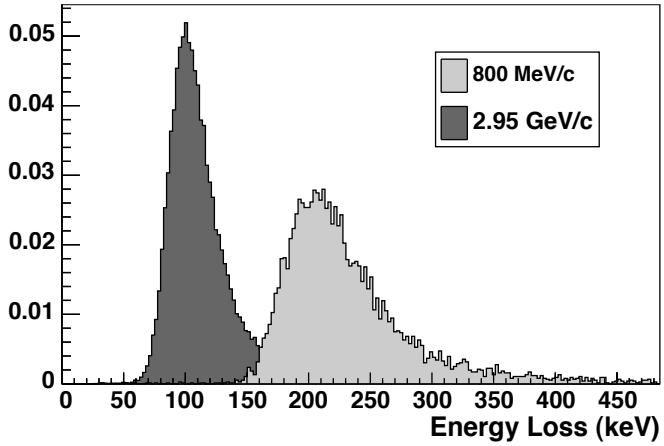

Figure 6.12: Energy loss distributions obtained with protons of different momenta at the COSY synchrotron.

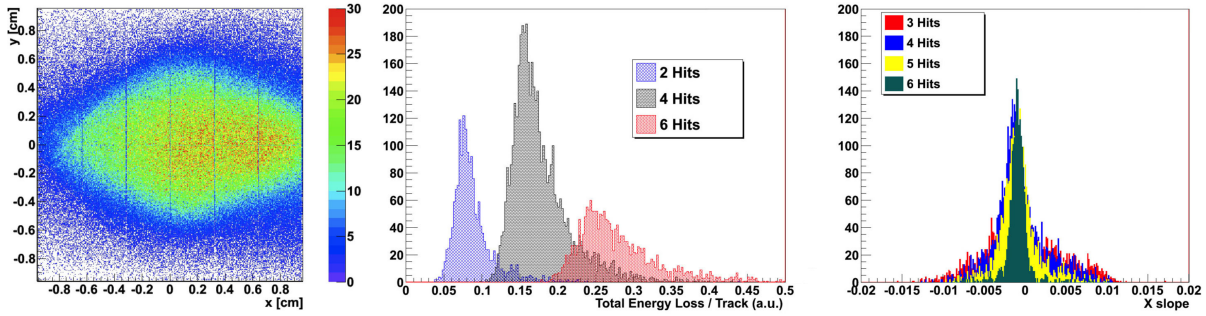

(a) Measured hit points. (b) Total energy loss per track. (c) Slopes of the fitted trajectories.

Figure 6.13: Results with the first beams of protons at the COSY synchrotron (Jülich) [5].

fit on the hit points measured by the tracking station. In particular the histogram shows the distributions of the angular coefficients obtained in events with different number of recorded hit points: the higher the number of included stations is, the narrower the distribution becomes due to the geometrical constraints.

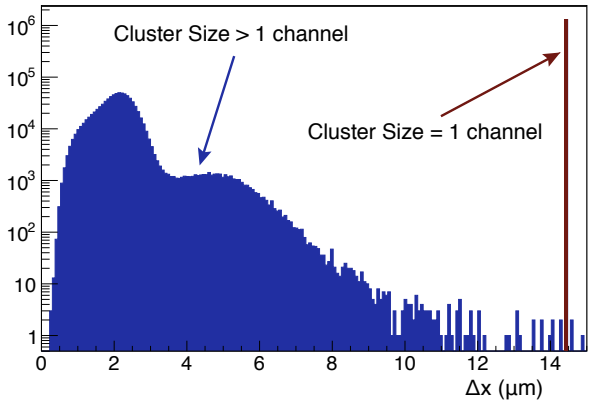

Figure 6.14: Distribution of the errors on the reconstructed coordinate measured with one sensor.

Figure 6.14 shows the distribution of the error on the reconstructed coordinate of single hit points measured with a sensor of the tracking station. A significant fraction of the clusters includes only one channel for the considered side of the sensor because the beam is orthogonal to the sensor surface. This is the reason of the prominent peak at 14.4 µm in figure 6.14. This value corresponds to $\Delta x = \text{pitch}/\sqrt{12} = 14.43\,\mu\text{m}$, which is the error assigned in the case of clusters composed of only one channel, without any charge shared between neighboring channels. The other structure at smaller errors corresponds to the case in which several channels contribute to the determination of the reconstructed coordinate and a charge weighted coordinate reconstruction method is applied. Different setups of the tracking station were tested, studying the effect of changes in the longitudinal position of the sensors and modifying the incident angle of the beam on the sensor plane.

6.5.1 Rotation of one sensor

The first test consisted in the rotation of one sensor positioned on the rotatable hold. The incident angle of the beam with respect to the sensor plane (see figure 6.15) was scanned analyzing the effect introduced on cluster size and energy loss. A 4 GeV electron beam at DESY was used to perform this study. The sensor was rotated scanning angles between 0° and 45°.

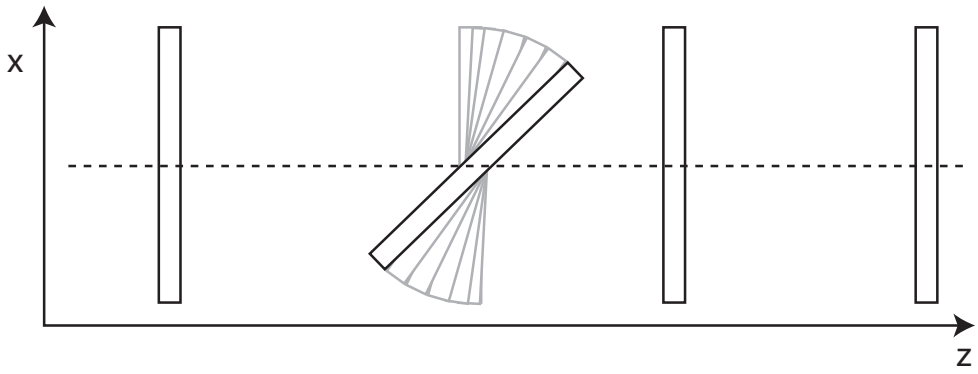

Figure 6.15: Setup used to study the effect of the rotation of one sensor changing the incident angle of the beam on the sensor plane.

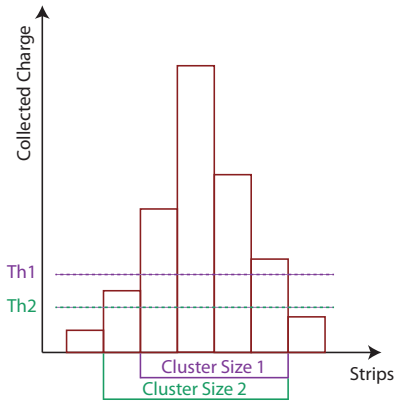

Figure 6.16: Effect of different minimum charge thresholds on the cluster size.

Figure 6.17 shows on the left the evolution of the energy loss in the sensor as a function of the rotation obtained from the measurements. Bigger crossing angles correspond to longer paths crossed by the beam within the sensor volume. Geometrically this path scales with $1/\cos(\alpha)$, where α is the rotation angle of the sensor. The energy loss is closely related to the effective length of the particle path inside the sensor volume since with minimum ionizing particles the energy loss per unit of radiation length can be considered constant in silicon volumes with a thickness of a few hundreds of µm. The total energy loss of the track was obtained performing a clustering procedure on the data, therefore the algorithm used in this phase, together with the setting of some thresholds (like the minimum collected charge per channel to be considered), generate small deviations from a pure $1/\cos(\alpha)$ trend. The plot on the right of figure 6.17 shows simulations of the experimental

setups. Since an absolute energy calibration was not performed (not necessary for the aims of the test) it is not possible to compare the absolute values shown in the two plots, however the scaling obtained in measurements and in simulations is compatible. An analysis of the obtained

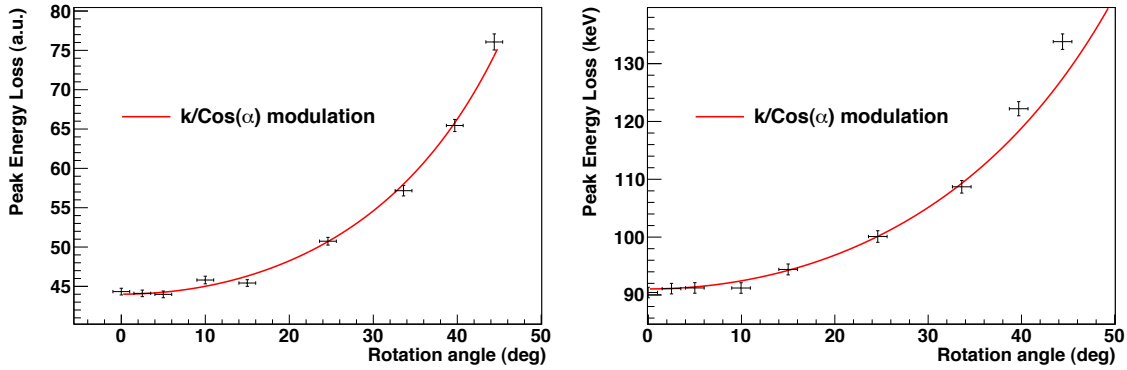

(a) Results of the measurements.

(b) Results of Monte-Carlo simulations.

Figure 6.17: Peak energy loss of 4 GeV electrons crossing a 300 µm thick sensor. Both measurement (left) and simulation (right) results are shown [11].

cluster size was performed and compared with simulations (see figure 6.18). The plots show a growing cluster size with bigger rotation angles: this is expected since geometrically a track has a higher probability of crossing more strips when the incident angle increases. In particular both plots show an enhancement at an angle of approximately 9.5°. This is the incident angle corresponding to a track spanning the whole width of a strip while crossing the thickness of the sensor: $\alpha_c = \arctan(\text{pitch/thickness})$ which substituting the features of the sensors used during this beam test results in $\alpha_c = \arctan(50\,\mu\text{m}/300\,\mu\text{m}) = 9.46°$.

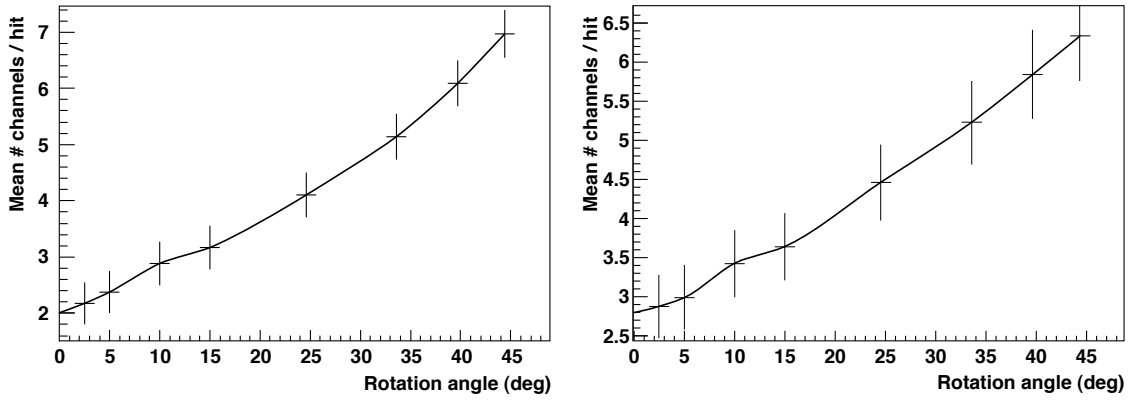

(a) Results of the measurements.

(b) Results of the Monte-Carlo simulations.

Figure 6.18: Distributions of the average number of channels contributing to the reconstruction of each hit point: results of measurements on the left and of simulations on the right.

The results of measurements and simulations show a similar behavior in the scanned angular range. The systematic offset between the two curves is due to the small differences in the settings used for clustering in the two cases. Since an absolute energy calibration was not performed the charge thresholds used to tune the clustering could not be adjusted to be perfectly equal in the two cases. In particular the value chosen as minimum charge/channel considered when

performing the cluster reconstruction is crucial for the determination of the cluster size (see figure 6.16) and can therefore influence the distributions shown in figure 6.18.

6.5.2 Translation of one sensor

Another interesting test was performed at the DESY accelerator with 3 GeV electrons changing the longitudinal position of one sensor. The second box of the tracking station was shifted along

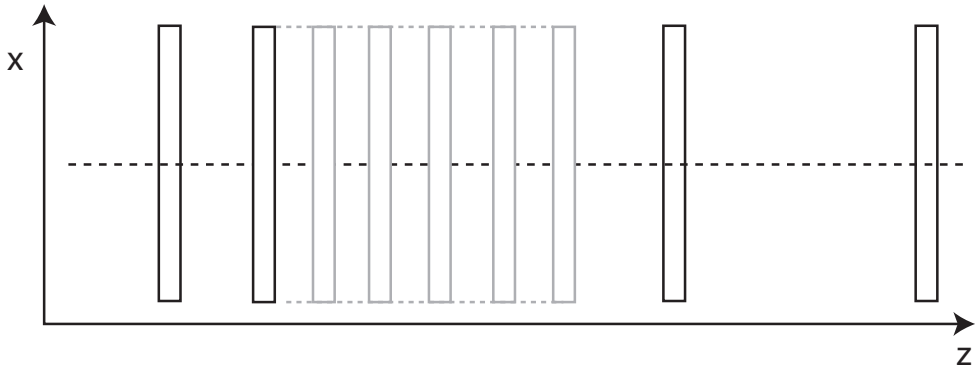

Figure 6.19: Layout of the setup used to characterize the effects of the translation of one sensor module.

the beam direction moving it from the closest possible position to the first sensor down to a nearly homogenous disposition of the four boxes along the tracking station span (see figure 6.19). Exclusive residual distributions (exclusive residuals are obtained not considering the hit point measured by the sensor plane under characterization while fitting the tracks as shown in figure 6.20) were determined for both transverse coordinates on each of the four sensor planes. Figure 6.21 shows the widths of the residual distributions obtained on each sensor when the

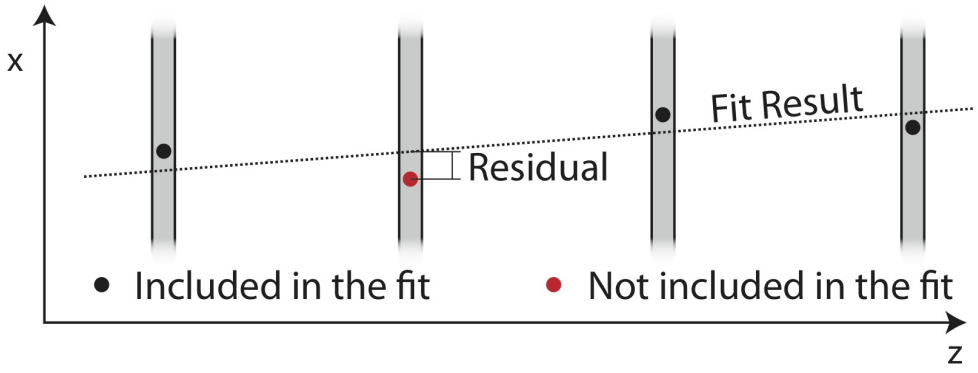

Figure 6.20: Exemplification of how the exclusive residuals were calculated.

second box is positioned at different longitudinal positions. Moving the second box forward the residuals become wider in all the sensors except for the third one, where the performance is improving of a few percent points. The residual distributions are narrower on the central planes (sensors 2 and 3) because the track is there constrained from both sides and at least one hit point upstream and one downstream are measured. The situation is similar both for the x and the y residuals. An estimator can be defined to take into account the combined effect of the shift of the second sensor box on all the sensors : $R_{x,y} = \sqrt[4]{1\sigma_{x,y} * 2\ \sigma_{x,y} * 3\ \sigma_{x,y} * 4\ \sigma_{x,y}}$, where ${}_i\sigma_{x,y}$ is the width of the x,y exclusive residual distribution determined on the i^{th} sensor. This does not

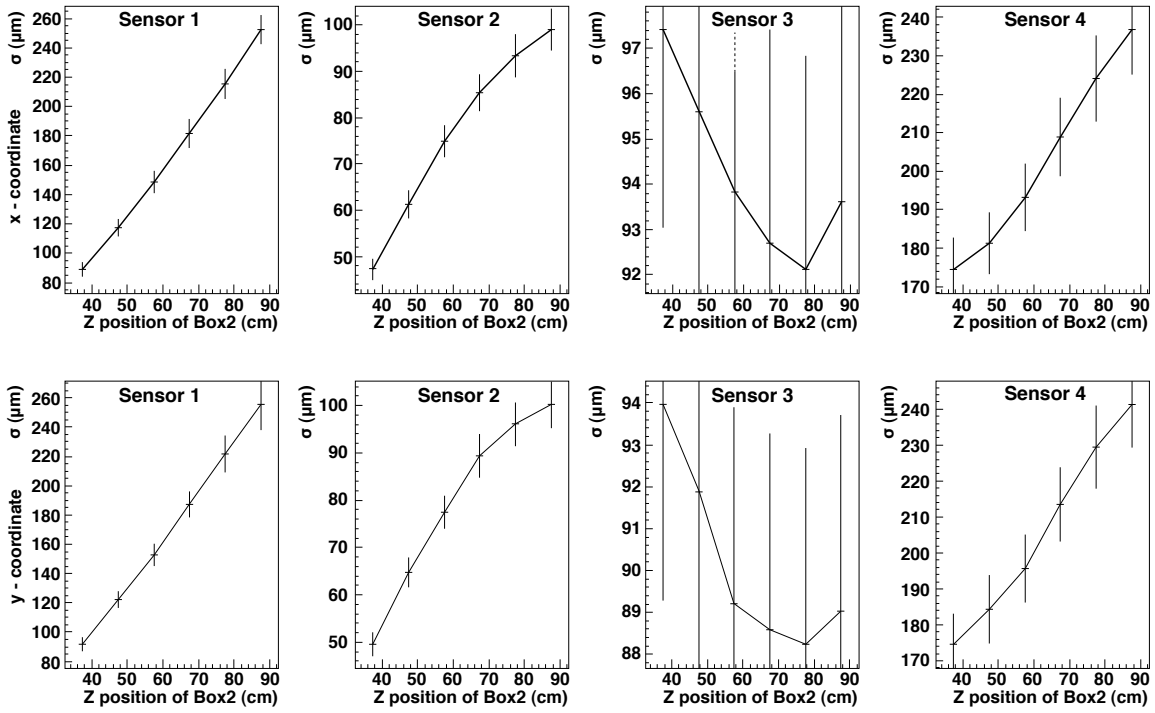

Figure 6.21: Widths of the residual distributions obtained on each sensor at the different longitudinal positions of the second box.

represent the track resolution of the tracking station, but just an estimator used to compare the different setups taking into account the information from all the sensors and it is influenced by the material budget of the setup. The results obtained with this estimator are shown in figure 6.22. Both for the x and y coordinate the estimator is minimal when the distance between the first and the second sensor plane is as small as possible.

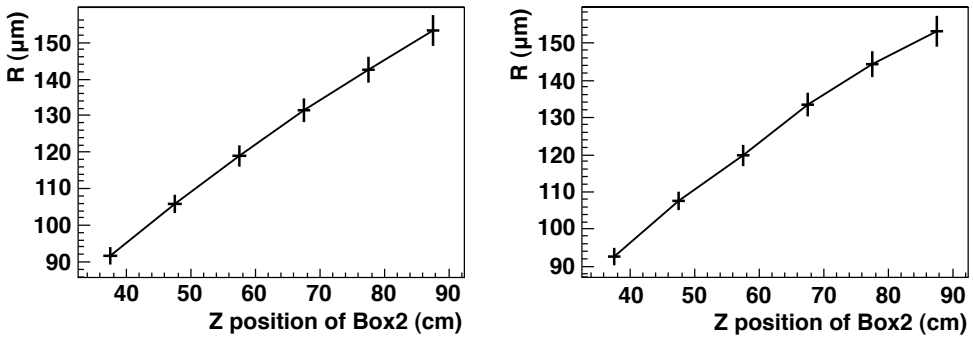

Figure 6.22: Values assumed respectively from left to right by the x and y estimator when moving the second sensor along the longitudinal axis.

6.6 Scattering measurements

The tracking station has been used to perform multiple scattering measurements. This studies had a double purpose. First the passive materials used to realize the services for the $\overline{\text{P}}$ANDA MVD needed a characterization in conditions similar to the experimental ones, so multiple

scattering measurements with different beams are a powerful tool to study their effect on charged particles. The second reason was the possible comparison between simulations performed within the PandaRoot framework and the results of measurements. This can be used to validate the simulation framework as a precise prediction tool to describe the effects of passive materials in a tracking detector. The method followed to measure the entity of the scattering in samples of different materials consisted in measuring two hit points before the scattering volume and two hit points downstream from it. In this way both the initial and the final direction of the particle trajectories are known and the deflection angles can be derived. Figure 6.23 summarizes the

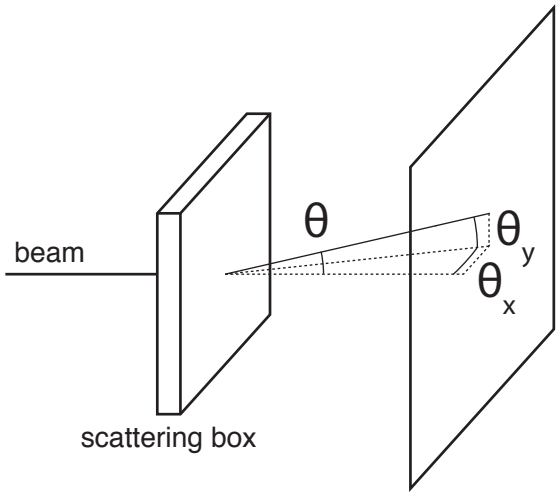

Figure 6.23: Definition of the scattering angles.

definitions used in the following: ϑ is the three-dimensional angle between the initial and the final track direction, while ϑ_x and ϑ_y are respectively the projected scattering angles along the x and y axis. ϑ and $\vartheta_{x,y}$ follow different distributions (see figure 6.24). The projected scattering angle distributions can be well described in their central part by Gaussian distributions centered around zero, whose widths measure the entity of the scattering. The ϑ angle, which represents an integration over the azimuthal angle of all the transverse projections, follows a distribution which can be described with the convolution of a Landau and a Gaussian distribution. In this case both the mean and the most probable value of the distributions are at a position which is different from zero, therefore the width and the peak position of such distributions can be considered as estimators of the relevance of the scattering. The projected scattering angle was chosen in this study since it allows to describe the scattering with one single value: the standard deviation of a Gaussian fit on the central part of its distributions. Applying this choice to the setup used during the experiment one can redefine the angles as shown in figure 6.25a. The histograms of figure 6.25b are the distributions obtained with this definition using electron and proton beams crossing volumes of different thicknesses and equivalent radiation lengths. The measurements and the simulations were performed using the same positions for the sensor boxes and the scattering volumes along the beam direction (see table 6.2) [11]. The simulations were realized using Geant3 to propagate the particles along the tracking station and trough the scattering volumes. A preliminary test was performed comparing Geant3 and Geant4: the results were really similar, therefore Geant3 was chosen because of the much faster required computational time. Different beam setups were used for this study: protons of 2.95 GeV/c at the COSY Synchrotron in Jülich and electrons with energies between 1 and 5 GeV at DESY in Hamburg.

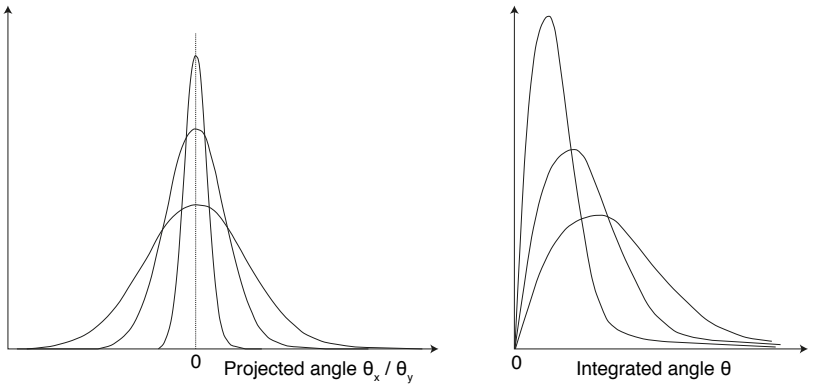

Figure 6.24: Integrated and projected scattering angle distributions. The different lines correspond to various thicknesses of the scattering volumes.

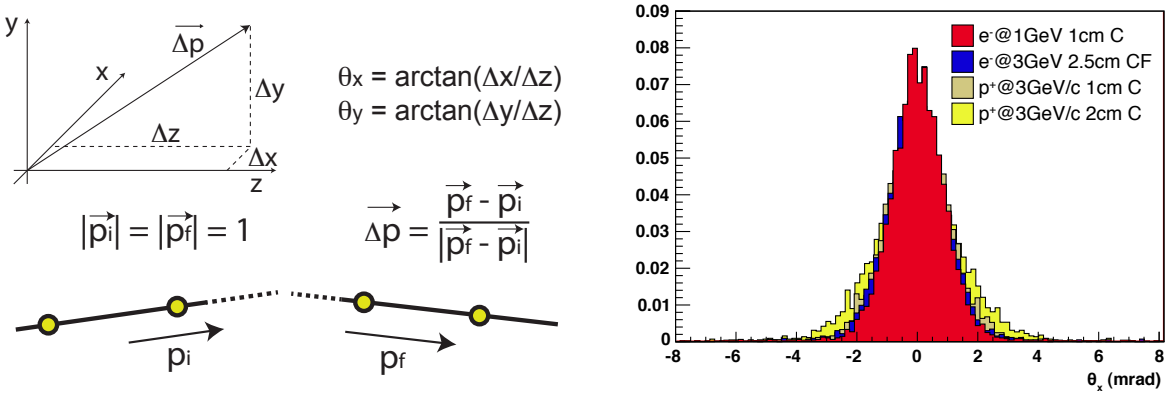

(a) Projected scattering angle definition in the experimental setup.

(b) Scattering angle distributions obtained in different beam conditions with several material samples.

Figure 6.25: Definition and measurements of the projected scattering angles [11].

Element	Long. Position (cm)
Box1	11.0
Box2	80.7
Scatt. Vol.	115.0
Box3	139.0
Box4	227.3

Table 6.2: Longitudinal position of the sensor boxes and of the scattering volumes used during the data taking and for the simulation of the setups.

The densities of the samples used during the measurements were determined measuring their volume and mass at the end of the beam tests. The determined values were used to define the materials used to fill the scattering volumes in the simulations.

A compilation of the obtained results is shown in table 6.3 where measurements are compared with simulations. In the case of protons the agreement between simulations and measurement is excellent with a discrepancy of less than 1%. The entity of the scattering scales compatibly with the increase of the equivalent radiation lengths. The scattering of electrons appears to be overestimated of a factor 10-20% in the Geant3 [12] simulations performed at energies of a

Ptc	**Mom.** GeV/c	**Volume**	**Thick.** cm	$\mathbf{X/X_0}$	$\boldsymbol{\sigma}_{\mathbf{meas}}$ mrad	$\boldsymbol{\sigma}_{\mathbf{sim}}$ mrad	**Var.** %
p^+	2.95	air	60	0.00197	0.532 ± 0.004	0.536 ± 0.002	0.75
p^+	2.95	1 cm C	1	0.042155	1.02 ± 0.01	1.01 ± 0.01	-0.98
p^+	2.95	2 cm C	2	0.079625	1.34 ± 0.01	1.33 ± 0.01	-0.74
e^-	1.	air	60	0.00197	1.24 ± 0.01	1.40 ± 0.01	12.9
e^-	2.	air	60	0.00197	0.622 ± 0.004	0.718 ± 0.003	15.4
e^-	3.	air	60	0.00197	0.423 ± 0.002	0.476 ± 0.002	12.5
e^-	4.	air	60	0.00197	0.325 ± 0.003	0.361 ± 0.002	11.1
e^-	5.4	air	60	0.00197	0.243 ± 0.003	0.284 ± 0.001	16.9
e^-	1	1 cm C	1	0.042155	2.48 ± 0.01	2.89 ± 0.01	16.5
e^-	5.4	1 cm C	1	0.042155	0.511 ± 0.004	0.599 ± 0.003	17.2
e^-	1	2 cm C	2	0.079625	3.15 ± 0.01	3.82 ± 0.02	21.3
e^-	5.4	2 cm C	2	0.079625	0.698 ± 0.002	0.807 ± 0.002	15.6
e^-	1	C-Foam	2.5	0.030445	2.18 ± 0.01	2.54 ± 0.01	16.5
e^-	3	C-Foam	2.5	0.030445	0.745 ± 0.003	0.887 ± 0.004	19.0
e^-	4	C-Foam	2.5	0.030445	0.588 ± 0.004	0.645 ± 0.003	9.7
e^-	1	Support Disk	0.4	∼0.0103	1.76 ± 0.01	1.87 ± 0.01	6.3
e^-	3	Support Disk	0.4	∼0.0103	0.600 ± 0.003	0.611 ± 0.002	1.8
e^-	4	Support Disk	0.4	∼0.0103	0.471 ± 0.004	0.483 ± 0.003	2.6
e^-	1	Carbon Foil	0.0650	∼0.00304	1.30 ± 0.01	1.56 ± 0.01	20.0
e^-	5	Carbon Foil	0.0650	∼0.00304	0.279 ± 0.002	0.334 ± 0.001	19.7

Table 6.3: Comparison of the results of measurements and simulations.

few GeV within the PandaRoot framework. The physics list selected for these studies was the default one for PandaRoot simulations since one of the purposes of this work was to validate the standard PandaRoot framework as a tool to predict the effect of materials inside the detectors and not to tune a standalone Geant3 simulation toolkit. The material samples characterized are compatible with those which will be used for the $\overline{\text{P}}$ANDA MVD. Full carbon elements will be present in the most stiff parts of the support structures. In order to minimize the material budget of the detector lighter materials will be used where possible: thin carbon foil and special carbon foams such as the ones involved in the scattering measurements here presented have been selected to realize for example the barrel staves of the strip part of the MVD. The support disk tested represents a specimen of more complex systems: it is realized with 4 mm thick carbon foam where steel cooling pipes have been embedded. In particular this disk is a prototype of the support structure holding the large forward pixel disks. The properties of the selected carbon foam assure the heat conductivity required to provide sufficient cooling power to the front-end chips. The beam momenta selected for these studies are compatible with those of the final state particles in the $\overline{\text{P}}$ANDA experimental conditions. Considered the large variety of scattering setups studied, the PandaRoot framework can be considered as a valid tool to estimate the order of magnitude of the entity of the multiple scattering induced by passive materials inside the $\overline{\text{P}}$ANDA detectors. Even if the in the case of electrons the scattering effects are overestimated by the simulations, the hierarchical scaling with the number of equivalent radiation lengths of the scattering volumes is respected.

6.7 First combined beam test: strip and pixel tracking stations

The strip tracking station has been tested in combination with other prototype detectors. A combined test with the beam telescope developed by the Torino $\overline{\text{P}}$ANDA MVD group with pixel sensors, was the occasion to test common event reconstruction strategies and analysis. This was the first time the two subsystems were taking data simultaneously. Different front-end chips, data acquisition systems and trigger logics were used in the two setups.

6.7.1 The pixel beam telescope

The pixel telescope is equipped with four silicon pixel sensors with an active area of $2.0 \times 3.2\,\text{mm}^2$. One sensor assembly is shown in figure 6.26: the pixel matrix (the silver box in the photo) covers most of the area of the ToPix3 readout chip [13], which is then connected to its test board. Each

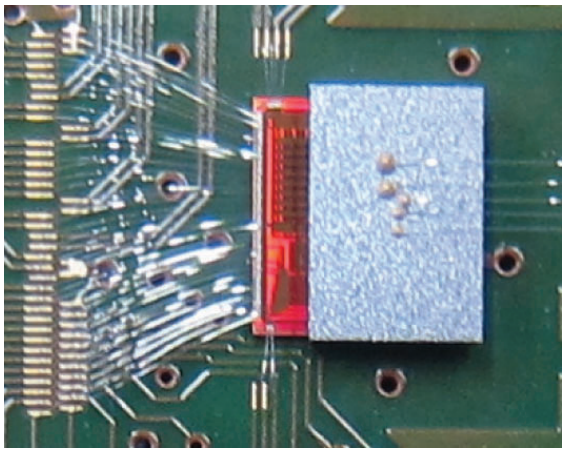

Figure 6.26: A pixel assembly with the sensor bump-bonded to the ToPix3 readout chip [14].

sensor assembly is connected on site to an FPGA board which is then linked with an ethernet connection to a PC in the counting room running the data acquisition software (see figure 6.27a). The read out scheme used for the pixel telescope is shown in figure 6.28. The four sensors are positioned along the longitudinal direction with a distance of 6 cm between consecutive sensor planes. The whole pixel sensors telescope is shown in figure 6.27b. The holding structure can host the sensor boards and the FPGA boards used to read out and process the data. The ToPix3 is a self-triggering read out chip, therefore it does not need an external signal to trigger the acquisition. A common clock is distributed to the four sensor assemblies. In order to synchronize the data measured by the strip tracking station and the pixel telescope the common clock can be distributed to the two systems together with a reset signal, which is activated every time a common clock is reset. Typically the reset signal has been used so far when resetting the common clock at the beginning of each new spill of particles cast by the accelerators.

A first generation of pixel sensor assemblies was produced and used in this combined beam test. The specimen includes the passive (not thinned) Cz-substrate, the epitaxial silicon layer, the bump bonds, the ToPix3 read out chip, a printed circuit board (PCB) for services. These assemblies have a significant material budget since the Cz-substrate was not thinned at the end of the production phase and the PCB did not foresee cutout windows in correspondence of the beam occupancy. Some capacitors were positioned on this PCB behind the active sensors area creating an asymmetric disposition of passive material in the sensor planes. New assemblies

Component	First Assemblies	Light Assemblies
Cz-substrate	525 µm	20 µm
Epi-silicon	100 µm	100 µm
ToPix3	300 µm	300 µm
PCB	1.1 mm	0 (cut out)
Capacitors	in	moved out

Table 6.4: Comparison of material of the first and updated pixel assemblies.

have been developed minimizing the impact of the passive materials and will be used in the upcoming beam tests. A comparison of the material load of the first and the updated assemblies is shown in table 6.4.

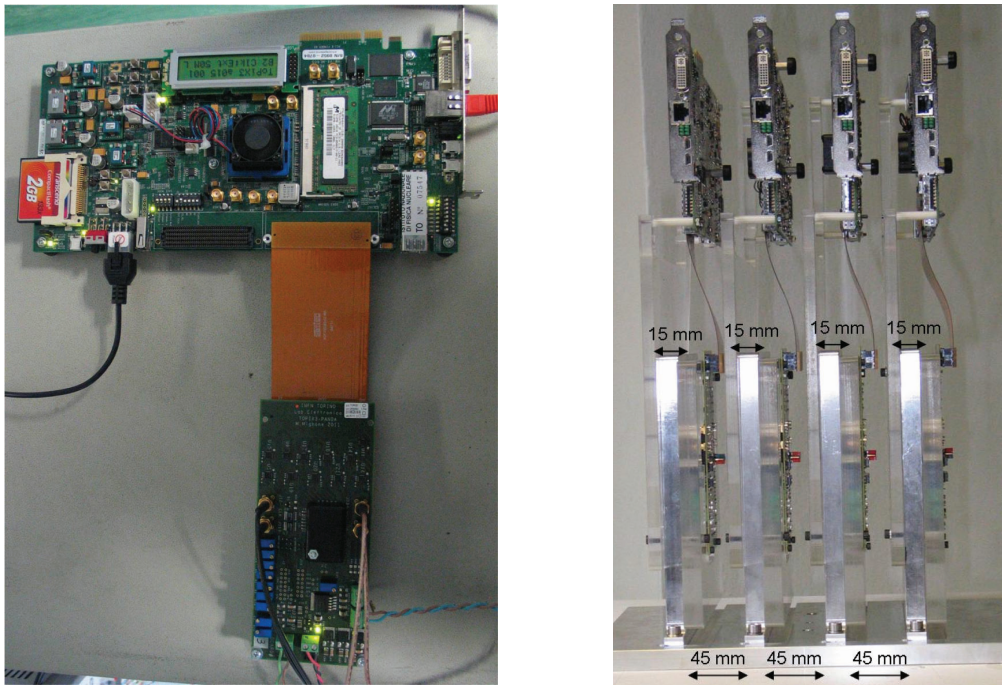

(a) A pixel sensor with its front-end chip, connected to their FPGA test board.

(b) The pixel beam telescope seen from the side.

Figure 6.27: A single sensor assembly and the whole telescope ready for data taking.

6.7.2 Event building

The two subsystems have different front-end chips: the APV25 used for reading out the strip sensors are triggered by the coincidence of the signals produced by four scintillators, while the acquisition of the pixel sensors is self-triggered. Therefore an event building is required since the output data of the two systems will show a different event structure. An event recorded by the strip tracking station consists of a set of fired channels from the four sensors, all of them recorded in correspondence of the same trigger signal.

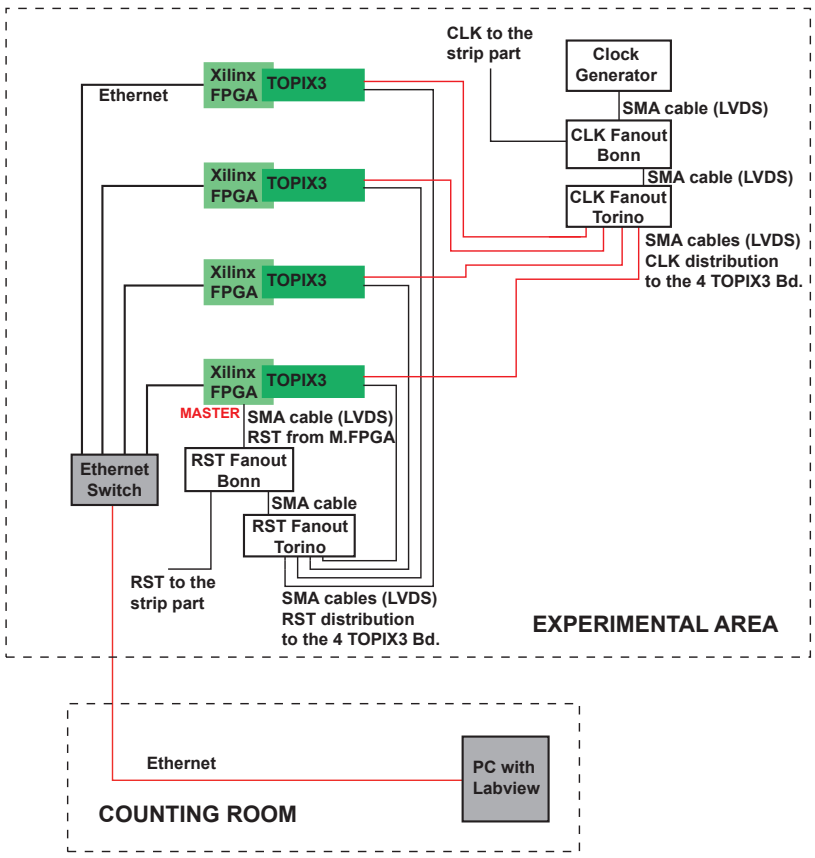

Figure 6.28: Scheme of the clock and reset signals distribution to the modules of the pixel beam telescope.

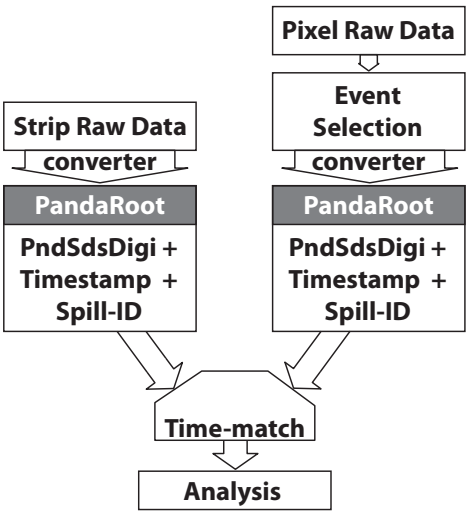

Figure 6.29: Flowchart of the operations needed to analyze the combination of strip and pixel hit points.

Since the events are triggered by the coincidence of small scintillators there is a high probability that events with one hit per sensor really correspond to a track going trough the whole station. In the case of the pixel telescope an event structure must be defined since the output data consists of a flow of fired channels with their corresponding timestamps. Channels can be fired by noise and by particles which are not belonging to the beam: for example secondary particles generated by the interaction of the beam with material positioned upstream from the considered sensor or deflected beam particles. In order to distinguish between genuine events and "background" it is useful to correlate the information provided by the two tracking systems. The first step is the definition of events in the data measured by the pixel telescope: sets of fired channels sharing the same timestamps are grouped together, those which have signals on all the four sensor planes are selected to be pixel events (see figure 6.30). The selection can be extended enlarging the timestamp coincidence

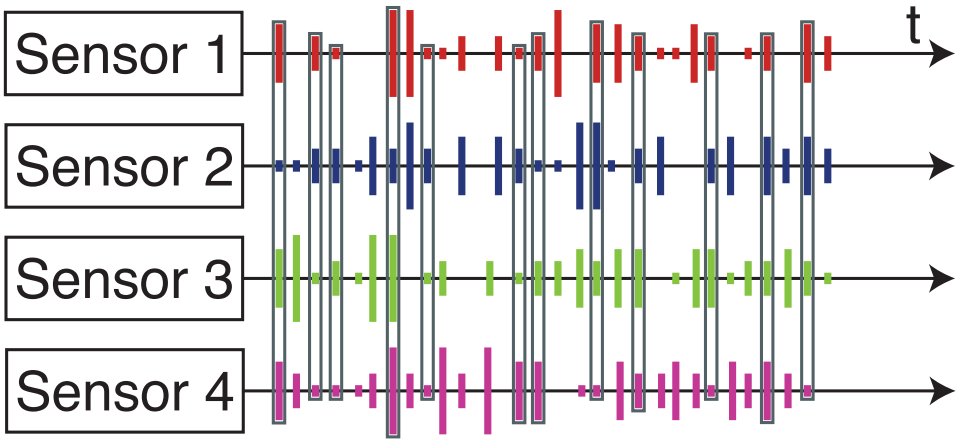

Figure 6.30: Exemplification of the procedure followed to select events on the base of the pixel signals. The height of the colored bar represent the number of fired channel, while the horizontal axis is the absolute time. Selected events are highlighted with a frame.

windows to a few clock cycles, therefore increasing the total number of events and taking into account possible timestamp fluctuations. In order to have the cleanest possible condition to match the pixel data with the strip ones, initially the selection has been limited to the case with all the signals sharing exactly the same timestamp. Figure 6.29 shows the flowchart followed to import raw data from both systems and to perform a combined analysis. The pixel data are pre-selected and divided into events before importing them into the PandaRoot framework. The two converted data sets are combined after the conversion looking at the timestamps of each event. An iterative procedure loops on the strip events, reads the corresponding timestamps and looks for compatible events in the pixel data set. In particular a combined event is defined as the correspondency of a strip and a pixel event whose timestamp falls in the same time window. In order to apply such a selection on the difference in timestamps between the two systems, the common clock distribution must be known in detail to characterize eventual latencies and take them into account. In order to measure the relative offset between the two DAQ systems a test was performed plotting the timestamp difference for all the events falling in a really large time window (for example 5 ms). The result obtained was a flat distribution due to random coincidences and a prominent narrow peak. Repeating this test on different spills and different days, the peak was monitored to be constantly positioned at -36.7 cycles of a 50 MHz clock (corresponding to 734 ns) during the whole beam test. For more details about this procedure see appendix A. After this preliminary test the real time match between the two data sets can be performed correcting for the determined offset. In this way the final set of combined events including hits from the strip tracking station and the pixel telescope is built.

6.7.3 The beam test

The first combined beam test involving the two tracking systems was performed at Jülich at the end of December 2011 [15]. A beam of 2.7 GeV/c protons was used to characterize different setups. Both a compact and a distributed configuration of the strip sensors along the beam around the pixel telescope were tested (see figure 6.31). The pixel telescope was used in different configurations: it was equipped with one or four sensors. Figure 6.33 shows the distribution of hit points on the first pixel and strip sensors crossed by the beam. A rectangle is drawn on the plot regarding the strip hit points and it delimits for comparison the size of the active area of

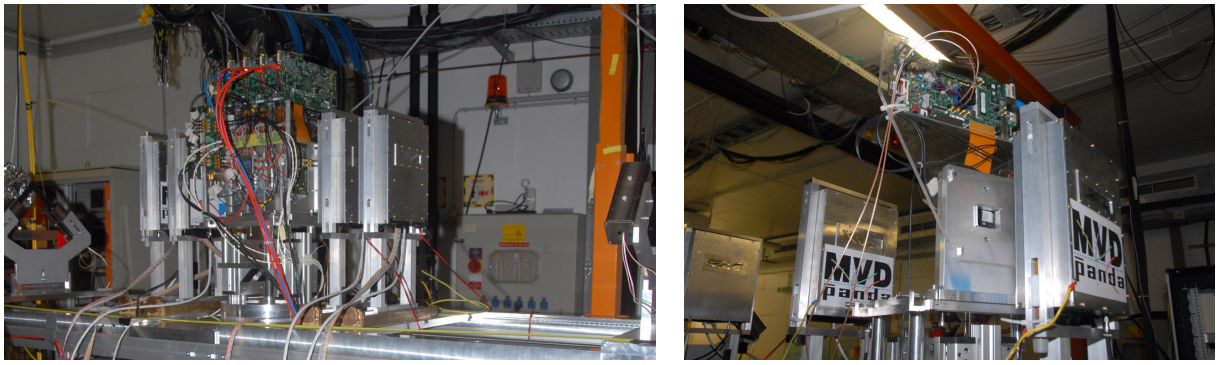

Figure 6.31: Different setups of the two tracking systems: on the left the compact disposition of the strip modules around the four pixel assemblies is shown, while the photo on the right describes the setup with a single pixel sensor rotated with respect to the beam direction [15].

pixel sensors. The pixel sensors sat in the central part of the beam and they were completely fluxed, while on the strip sensors it is possible to see the whole beam profile due to the bigger active area. A zoom on the distributions of the reconstructed x coordinate respectively on the first pixel and on the first strip sensor are shown in figure 6.33a and 6.33b. Both plots present a regular pattern with peaks corresponding to the position of the center of a channel: in the case of the pixel sensor the distance between two consecutive peaks is 100µm, while it is 50µm on the strip sensor.

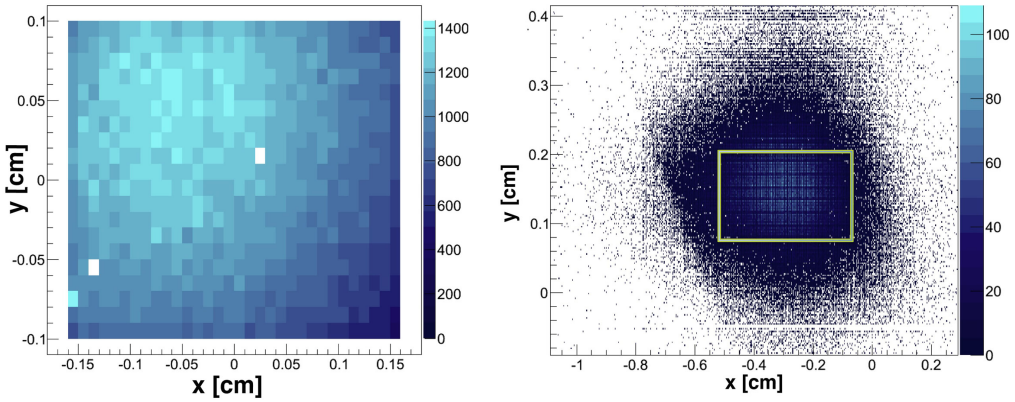

Figure 6.32: Maps of the hit points measured by the first pixel sensor (on the left) and by the first strip plane (on the right). A rectangle on the strip plane marks the corresponding pixel sensor active area [15].

This structure is the consequence of the cluster sizes expressed in term of channels contributing to the reconstruction of the position which are shown in figure 6.33c and 6.33d. Since the beam is orthogonal to the surface of the sensors, a consistent fraction of the hits are reconstructed with the information from a single channel in the case of the pixel sensor. Being the pixels larger than the strip pitch and much thinner, the probability of firing two neighboring channels is much lower. This explains why the average cluster size is bigger on the strip sensor and why the regular pattern of figure 6.33b is less dominant than that of figure 6.33a.

The pixel assemblies used for this test are the ones labeled as “first assemblies” in table 6.4, therefore the impact on protons with 2.7 GeV/c momenta was not negligible. Tracks were scattered by the material encountered in each detecting layer, therefore this beam test did not

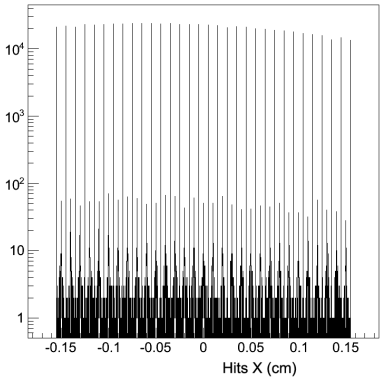

(a) Pixel sensor: reconstructed x coordinate.

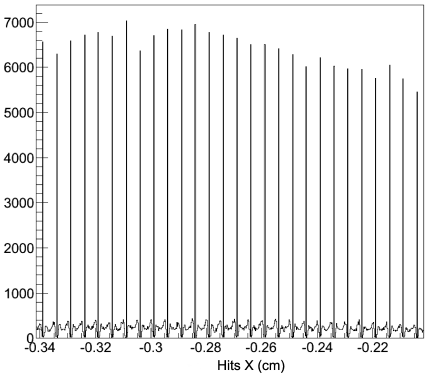

(b) Strip sensor: reconstructed x coordinate.

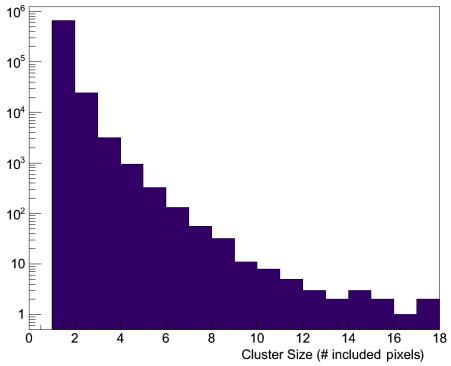

(c) Pixel sensor: cluster size.

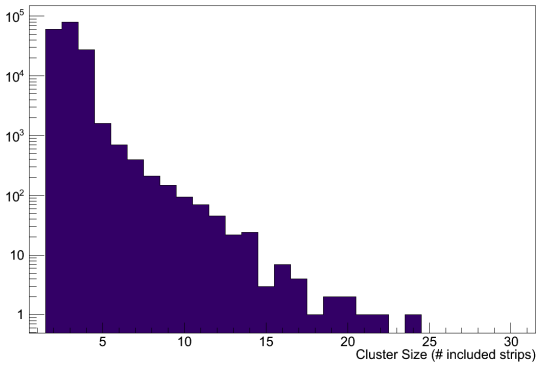

(d) Strip sensor: cluster size.

Figure 6.33: Top: reconstructed x coordinate respectively on the first pixel and strip sensor. Bottom: cluster size in terms of contributing channels on both sensors [15].

represent the ideal chance to characterize the intrinsic resolution of the sensor.

Nevertheless it was interesting not only to test the synchronous operation of the two systems but also to compare the tracking performaces achieved with different dispositions of the sensors, for example varying the lever arm between the pixel telescope and the strip tracking station.

Strip stand-alone analysis

The first analysis was realized using only the information provided by the strip tracking station. In this case the pixel assemblies were used just as scattering volumes and the aim was to compare the performance of the strip tracking station in different positioning configurations when dealing with an environment of particles affected by multiple scattering. The setups adopted for this test are listed in table 6.5. Setups A and B both foresee a distributed disposition of the strip sensors along the longitudinal span, with the maximum distance achievable respectively between sensors 1-2 and 3-4. In setup A a single pixel assembly was positioned on the fifth holder, nearly at the center of the strip tracking station, while setups B was equipped with four pixel assemblies (in this case table 6.5 reports the longitudinal position of the first pixel sensor). Setup C represents the most compact configuration achievable with the experimental apparatus.

Setup	**Strip B.1** cm	**Strip B.2** cm	**Pixel B.1** cm	**Strip B.3** cm	**Strip B.4** cm	**# Pixel Assemblies**
A	14	90	115	144	210	1
B	14	90	115	144	210	4
C	78	90	115	144	156	4

Table 6.5: Setups used for the strip stand-alone analysis.

The results of these studies are compiled in table 6.6, where the standard deviations of Gaussian fits on the exclusive residual distributions of each plane are reported. Only the first three sensors were considered for this analysis because the fourth plane is the most affected by scattering effects (since its longitudinal position is more downstream from the center of the station). Similarly to what was already shown in section 6.5.2, an estimator was defined as $\sqrt[3]{\sigma_{1,x/y} * \sigma_{2,x/y} * \sigma_{3,x/y}}/\sqrt{3}$ to compare the overall performance of the tracking station and not only the exclusive residual distributions obtained on each sensor. This estimator does not represent the tracking resolution, but just a tool to quantify the global effect of different positioning schemes. Setup A gave better results than setup B as expected because of the smaller

Setup A	$\boldsymbol{\sigma_x}$	$\boldsymbol{\sigma_y}$
1 Pixel Assembly	µm	µm
Strip Plane 1	598 ± 18	601 ± 17
Strip Plane 2	253 ± 8	255 ± 8
Strip Plane 3	427 ± 15	435 ± 14
Estimator (µm)	232 ± 4	234 ± 4
Setup B	$\boldsymbol{\sigma_x}$	$\boldsymbol{\sigma_y}$
4 Pixel Assemblies	µm	µm
Strip Plane 1	660 ± 21	654 ± 19
Strip Plane 2	288 ± 10	297 ± 9
Strip Plane 3	496 ± 16	494 ± 15
Estimator (µm)	263 ± 5	264 ± 5
Setup C	$\boldsymbol{\sigma_x}$	$\boldsymbol{\sigma_y}$
4 Pixel Assemblies	µm	µm
Strip Plane 1	114 ± 3	108 ± 3
Strip Plane 2	93 ± 3	89 ± 3
Strip Plane 3	500 ± 13	505 ± 15
Estimator (µm)	100 ± 2	98 ± 2
Estimator = $\sqrt[3]{\sigma_1 * \sigma_2 * \sigma_3}/\sqrt{3}$		

Table 6.6: Results of the strip stand-alone analysis.

amount of passive material interposed between the second and the third sensors. Setup C, with its compact disposition of the sensors, achieved the best results, even if it was equipped with four pixel assemblies. This is the expected behaviour at intermediate energies at which the effect of passive materials cannot be neglected [11].

6.7.4 Simulations

The experimental setup including both tracking stations was simulated within the PandaRoot framework [7] in order to estimate the expected performances of the combined tracking system. In particular exclusive residual distributions were determined on each of the pixel plane considering the MC-true hit points (i.e. assuming $\sigma_x = \sigma_y = 0$). This was done to estimate only the impact of the material present in the pixel assemblies and not its convolution with the intrinsic resolution of the pixel sensors.

Setup	**Strip 1** cm	**Strip 2** cm	**Pixel 1** cm	**Strip 3** cm	**Strip 4** cm
A	15	35	110	165	185
B	15	85	110	139	185
C	65	85	110	139	159

Table 6.7: Position of the modules along the longitudinal axis in the different simulated setups.

Three different dispositions of the strip sensors around the pixel tracking stations have been tested in order to find the optimal one to be used during the experimental test. Table 6.7 describes these three setups which represent respectively a "long lever arm" configuration (A), a homogenous disposition (B) and a compact distribution (C) of the strip sensors. The sensors were implemented in the simulations according to the values reported in table 6.8. This simulation campaign was realized before the beginning of the beam test, therefore the Cz-substrate thickness was fixed to the design values which is obtained with thinning techniques in the production procedure. The final prototypes used for the test did not undergo this procedure due to time limitations: the thickness of the tested assemblies is reported in the second column of table 6.4. The mylar foils used to close the boxes housing the strip sensors have not been taken into account for the simulations, since their contribution to the total material budget is negligible. Proton beams of three different momenta were simulated for each setup.

Element	**Thickness/Assembly**
Pixel Cz substrate	20 µm of silicon
Pixel Epi-Silicon	100 µm of silicon
Topix chip	300 µm of silicon
Pixel Pcb	1.1 mm
Strip Sensors	300 µm of silicon

Table 6.8: Material budget implemented in the preliminary simulations.

The results of the simulations are summarized in table 6.9. Setup C leads to the best results at all the three momentum values tested. Lower beam momenta correspond to an increasing effect of the scattering on the residual distributions, whose standard deviations grow of about a factor three decreasing the beam momentum from 2.95 GeV/c down to 1 GeV/c.

6.7.5 Results of the combined measurements

A double combined analysis has been performed on data measured with both tracking stations at COSY with 2.7 GeV/c protons. This momentum was selected since it was the last one used during the previous runs dedicated to the experiments taking data at COSY, therefore it was possible to focus the beam precisely and to have a small beam size at the extraction point

Setup	**Mom.** GeV/c	**Pixel Pl. 1** σ_x/σ_y (µm)	**Pixel Pl. 2** σ_x/σ_y (µm)	**Pixel Pl. 3** σ_x/σ_y (µm)	**Pixel Pl. 4** σ_x/σ_y (µm)	**Estimator** R_x/R_y (µm)
A	2.95	427 / 422	435 / 431	427 / 427	410 / 405	212 / 211
A	2.7	469 / 467	479 / 475	472 / 474	450 / 449	233 / 233
A	1.0	1690 / 1671	1767 / 1715	1751 / 1711	1646 / 1585	856 / 835
B	2.95	316 / 313	322 / 326	319 / 319	296 / 298	156 / 157
B	2.7	341 / 346	354 / 354	347 / 345	322 / 325	170 / 171
B	1.0	1225 / 1165	1247 / 1234	1245 / 1192	1149 / 1105	608 / 587
C	2.95	202 / 196	202 / 198	205 / 201	187 / 186	99 / 98
C	2.7	202 / 196	222 / 219	226 / 219	210 / 203	107 / 105
C	1.0	686 / 684	772 / 763	780 / 776	730 / 720	370 / 367
$R_{x,y} = \sqrt[4]{1\sigma_{x,y} *_2 \sigma_{x,y} *_3 \sigma_{x,y} *_4 \sigma_{x,y}}/\sqrt{4}$						

Table 6.9: Widths of the residual distributions on the pixel planes using different setups.

(a few mm). The data set considered was measured with the setup B described in table 6.5. Table 6.10 reports the standard deviations of the exclusive residual distributions obtained using the information provided by the the four strip planes and by the first pixel sensor.

	Strip Box1	**Strip Box2**	**Pixel Box1**	**Strip Box3**	**Strip Box4**
σ_x / µm	975 ± 37	267 ± 9	394 ± 15	179 ± 7	877 ± 32
σ_y / µm	908 ± 35	249 ± 8	368 ± 14	164 ± 6	811 ± 32

Table 6.10: Results of the combined analysis using the information provided by all the sensors.

The residual distributions become narrower when proceeding toward the center of the tracking station (strip box 2 and 3 obtain better results than the external sensors). This behavior will be described in section 6.7.7. The residuals on the first pixel plane are larger than on the neighboring strip sensors, even if this module has more constraints on both sides (two strip hit points upstream and two downstream). This is due to the pixel cell size ($100 \times 100\,\mu m^2$) which leads to a bigger position error than that obtained with the 50 µm pitch strip sensors in case of tracks perpendicular to the sensor planes, therefore generating mostly clusters composed of single fired channels.

A second analysis was performed on the same data, using only the first two strip sensors and the first pixel plane to calculate the residuals. The first two hit points were measured before tracks crossed the pixel assemblies, therefore this analysis strategy is less affected by the passive materials introduced by the pixel tracking station. The results are compiled in table 6.11 Using

	Strip Box1	**Strip Box2**	**Pixel Box1**
σ_x / µm	264 ± 8	51 ± 2	62 ± 2
σ_y / µm	272 ±10	53 ± 2	64 ± 2

Table 6.11: Results of the combined analysis taking into account the first two strip sensors and the first pixel assembly.

this second analysis technique the extrapolation of the track intersection with the pixel plane is much more precise and the residual distributions on the three considered detectors improves significantly.

6.7.6 Simulations for a new beam test

New pixel sensors assemblies were build, including the thinning procedure for the Cz-substrate. Several other solutions were adopted to minimize the material budget of the pixel tracking station: the PCBs holding the sensors and providing the required services were modified leaving free the region just in correspondence of the sensors active area and capacitors were moved away from the sensors as well. The properties of these lighter assemblies have been already summarized in table 6.4. Simulations were performed for a beam test at the T9 area of CERN [16]. A

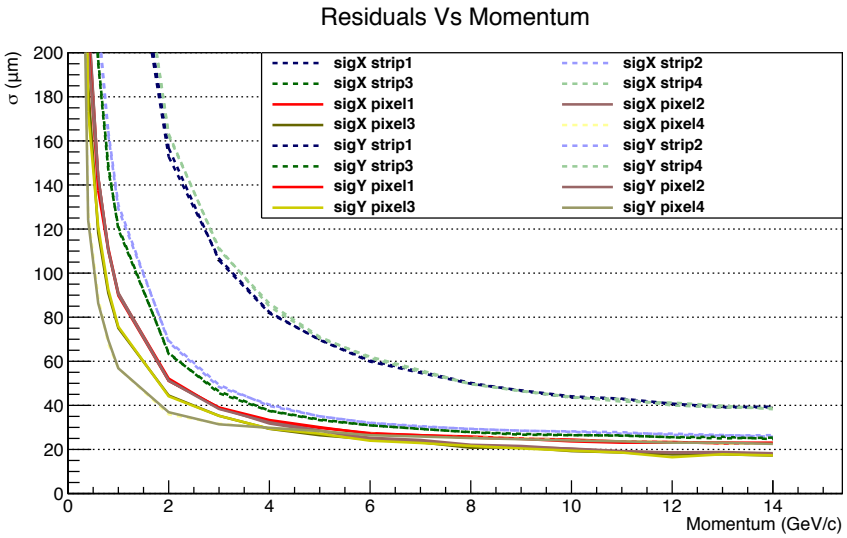

Figure 6.34: Results of the simulations performed including the new light pixel assemblies. The width of the residual distributions of each detector are plotted as a function of the pion beam momentum.

combined setup with both the strip and the pixel tracking stations in a compact configuration was implemented. Different beam settings are available at the T9 area: it is possible to select some particle species, their charge and their momentum. In order to obtain higher fluxes it is convenient to use all the hadrons with the same charge. Momenta up to 10 GeV/c can be achieved, at this regime the not selected beam is mainly composed by charged pions and protons. Simulations were realized propagating with Geant3 [12] positively charged pions through the setup and varying the initial beam momentum. Figure 6.34 shows the standard deviation of the exclusive residual distributions derived on each sensor plane as a function of the initial beam momentum. Due to the adoption of the light pixel assemblies multiple scattering is no longer dominating the residual distributions. The narrowest distributions were obtained on the central pixel planes because of the higher number of constraints available both upstream and downstream from the selected plane (see section 6.7.7). The performance improves rapidly increasing the momentum up to a few GeV/c. Above 8 GeV/c the performance starts to show an asymptotic trend on most planes. At 10 GeV/c the central pixel sensors can obtain standard deviations for their exclusive residual distributions below 20 µm.

6.7.7 Considerations about the residual distributions

In all the simulations and measurements shown before the same behavior can be observed: the width of the residual distributions is minimal at the center of the tracking stations and maximal at the longitudinal edges. This is due to the number of constraints applied upstream and

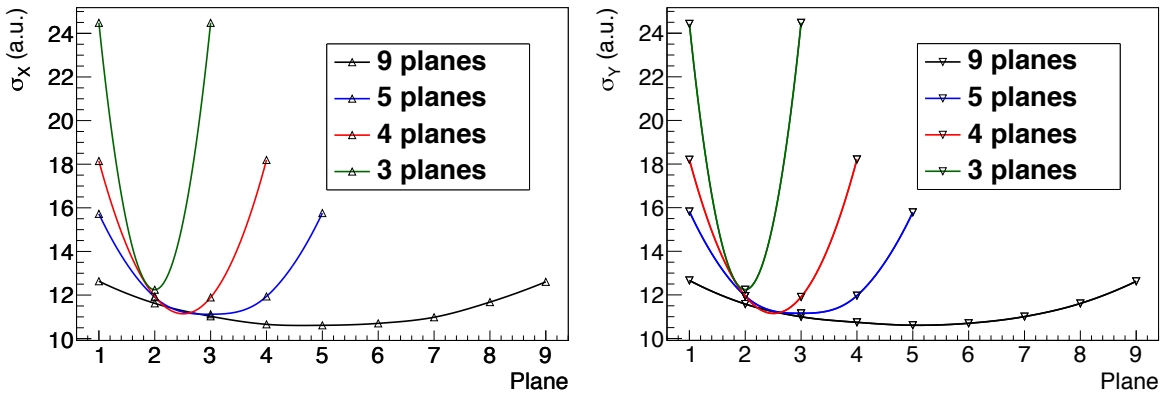

Figure 6.35: Width of the residual distributions as a function of the position of the considered plane within the tracking station. Different total numbers of sensors are considered and a resolution $\sigma_0 = 10$ a.u. is assumed.

downstream from the considered detector plane. An ideal test can be performed to understand this effect. If a tracking station if composed of a variable number of sensors with a resolution σ_0 on each of the transverse coordinate, it is possible to study the width of the residual distribution as a function of the position of a sensor within the station and of the total number of sensors involved. In order to avoid biases an ideal case is considered assuming no material budget and tracks being perfectly straight. The smearing of the measured hits is therefore only due to the instrinsic resolution of the sensors. Disposing a different number of sensors keeping constant the distance between consecutive planes (100,000 a.u.) and fixing $\sigma_0 = 10$ a.u., the standard deviations of the obtained residual distributions follow the behaviors shown in figure 6.35. In all the considered cases the narrowest residual distributions are obtained on the central modules, where the number of constraints on both sides is maximum. Increasing the total number of sensors the residuals on all planes become smaller and the distributions flatter. With a high number of sensors (i.e. the case with nine planes) the residual distribution widths approach the intrinsic resolution of the sensors (this can be seen quantitatively in table 6.12).

Plane	σ_x/σ_0 [%]	σ_y/σ_0 [%]
3 planes		
1/3	245	244
2/3	122	122
3/3	245	245
4 planes		
1/4	181	182
2/4	119	119
3/4	119	120
4/4	182	182
5 planes		
1/5	157	158
2/5	119	119
3/5	111	112

Plane	σ_x/σ_0 [%]	σ_y/σ_0 [%]
5 planes		
4/5	119	120
5/5	158	158
9 planes		
1/9	126	127
2/9	116	116
3/9	110	110
4/9	107	107
5/9	106	106
6/9	107	107
7/9	110	110
8/9	117	116
9/9	126	126

Table 6.12: Table showing the ratio between the widths of the residual distributions obtained in the different cases and the intrinsic resolution of the sensors σ_0.

Bibliography

[1] $\overline{\text{P}}$ANDA Collaboration. Technical Design Report for the: $\overline{\text{P}}$ANDA Micro Vertex Detector. Technical report, 2011. arXiv:1207.6581.

[2] M. Raymond et al. The CMS Tracker APV25 0.25 µm CMOS Readout Chip. *Paper presented at the 6th workshop on electronics for LHC experiments, Krakau, Poland*, Sept 2000.

[3] R. Schnell et al. FPGA-based readout for double-sided silicon strip detectors. *JINST 6 (2011)*, (C01008).

[4] R. Schnell, K.-Th. Brinkmann, H. Sohlbach, H.-G. Zaunick. The PANDA MVD Silicon Strip Detector. *JINST_081P_1112 [TWEPP 2012].*

[5] COSY, Jülich, Germany. http://www2.fz-juelich.de/ikp/cosy/en/.

[6] Rene Brun and Fons Rademakers. ROOT - An Object Oriented Data Analysis Framework. *Nucl. Instr. Meth.*, A389:81–86, 1996. See also http://root.cern.ch/.

[7] S. Spataro. Event Reconstruction in the PandaRoot framework. *Journal of Physics: Conference Series*, 396(2):022048, 2012. http://stacks.iop.org/1742-6596/396/i=2/a=022048.

[8] Reference for the PndSdsDigiStrip class. http://cbmroot.gsi.de/panda_doc/daily/html/classPndSdsDigiStrip.html.

[9] National Institute of Standards and Technology - PSTAR database. http://physics.nist.gov/PhysRefData/Star/Text/PSTAR.html.

[10] DESY, Hamburg, Germany. http://adweb.desy.de/∼testbeam/.

[11] S. Bianco, M. Becker, B. Kai-Thomas, R. Kliemt, K. Koop, R. Schnell, T. Würschig, H.G. Zaunick. Measurements with a Si-strip telescope. *PoS (RD11)*, (025), 2012.

[12] Geant3 manual. *CERN program library W5013*, 1993.

[13] G. Mazza et al. A CMOS 0.13m Silicon Pixel Detector Readout ASIC for the $\overline{\text{P}}$ANDA experiment. *JINST 7 C02015*, 2012. doi:10.1088/1748-0221/7/02/C02015.

[14] D. Calvo. The silicon Micro Vertex Detector of the $\overline{\text{P}}$ANDA experiment. *Nucl. Instr. Meth A*, (0), 2012. http://www.sciencedirect.com/science/article/pii/S0168900212009965.

[15] S. Bianco on behalf of the $\overline{\text{P}}$ANDA MVD group. Beam tests and performance studies for the $\overline{\text{P}}$ANDA Micro-Vertex-Detector. *IEEE Nuclear Science Symposium Conference Record*, N18(4):1503–1508, 2012.

[16] L. Durieu, M. Martini and A.-S. Müller. Optics Studies for the T9 Beam Line in the CERN PS East Area Secondary Beam Facility. *Proceedings of the 2001 Particle Accelerator Conference, Chicago*, 2001.

CHAPTER 7

Reconstruction of the $\Lambda_c - \overline{\Lambda}_c$ decays

7.1 Considerations about the input to the simulations

The $\overline{\text{P}}$ANDA experiment will allow to study a large variety of physics topics as already discussed in chapter 1. In particular in section 1.2 the capabilities of the experiment in the heavy baryons sector were described.
In this chapter the $\overline{p}p \rightarrow {\Lambda_c}^+(2286)\,{\overline{\Lambda}_c}^-(2286)$ reaction will be analyzed to understand the potential performance of the setup with such short-lived heavy baryons.
Different theoretical predictions have produced estimates for the $\overline{p}p \rightarrow {\Lambda_c}^+{\overline{\Lambda}_c}^-$ cross section at the $\overline{\text{P}}$ANDA energies: depending on the study considered the value ranges between some tens of nb [1] [2] and 200 nb [3].
Within the many decay channels of the ${\Lambda_c}^+$, the one into $pK^-\pi^+$ was selected for this study due to the optimization of the reconstruction strategies adopted within this thesis for vertices with small distances (a few mm) from the nominal interaction point (see section 5.1.2). Many other decay channels of the Λ_c include a Λ^0 in the final state (the branching ratio for $\Lambda_c \rightarrow \Lambda^0 + \textit{anything}$ is 35% [4]) and therefore require dedicated reconstruction tools to study secondary vertices with distances of several cm from the primary vertex, which would add the possibility of applying vertex selections in order to tag the Λ^0 candidates. Furthermore the selected decay only includes charged particles and involves three different particle species, thus limiting the combinatorial ambiguities in the final state. This decay has a measured branching ratio of $(5.0 \pm 1.3)\,\%$ [4]. The decay pattern selected for this analysis is therefore $\overline{p}p \rightarrow {\Lambda_c}^+(2286)\,{\overline{\Lambda}_c}^-(2286) \rightarrow pK^-\pi^+\overline{p}K^+\pi^-$.
The maximum beam momentum available at $\overline{\text{P}}$ANDA has been selected in order to maximize the opening angle between the ${\Lambda_c}^+$ and the ${\overline{\Lambda}_c}^-$ in the laboratory frame. This allows to better distinguish the two secondary vertices. More details about the kinematics of the $\overline{p}p \rightarrow \Lambda_c\overline{\Lambda}_c$ decay are discussed in appendix C.
Measurements of the same final state in $p\overline{p}$ annihilations at similar energies were performed in the seventies with the Mirabelle bubble chamber at the Serpukhov accelerator (see [5]). These experiments provided a measurement of the total cross section for the non resonant reaction: $\sigma_{\overline{p}\,p \rightarrow \overline{p}\,p\,\pi^+\,\pi^-\,K^+\,K^-} = (0.023 \pm 0.012)$ mb.

Inv. Mass	(2286.46 ± 0.14) MeV/c^2
Mean Life	(2.00 ± 0.06)·10^{-13} s
cτ	59.9 µm

Table 7.1: Invariant mass and other parameters of the $\Lambda_c{}^+$ (2286) [4].

7.2 Reconstruction of the pure signal

7.2.1 Input to the simulations

The reaction $\overline{p}p \rightarrow \Lambda_c\overline{\Lambda}_c$ at a fixed beam momentum defines an univocal relation between the kinematic parameters of the Λ_c and those of the $\overline{\Lambda}_c$. A derivation of the values assumed by the transverse and longitudinal momenta, as well as by the polar angle of the two tracks is shown in appendix C. Figure 7.1a and 7.1b show respectively the polar angle of the Λ_c tracks as a function of their momentum and the their transverse momentum as a function of the longitudinal momentum. This represents the input from the event generator provided to the simulations. In particular it is important to notice that there is an elliptical relation between the transverse and the longitudinal momentum of a particle from a two-body decay at a fixed energy. For a better understanding figure C.1a and C.1b show the longitudinal and transverse momenta of the Λ_c and $\overline{\Lambda}_c$ tracks as a function of their longitudinal momenta in the $\overline{p}p$ rest frame. At a fixed beam momentum the maximum transverse momentum is obtained when there is no longitudinal momentum in the $\overline{p}p$ rest frame, which corresponds to a symmetric decay in the laboratory frame, while there is no transverse momentum in the case in which the two particles are aligned to the beam axis in the $\overline{p}p$ rest frame. The values assumed by both the momenta and the polar angles in figure 7.1 are in agreement with the estimates shown in appendix C.

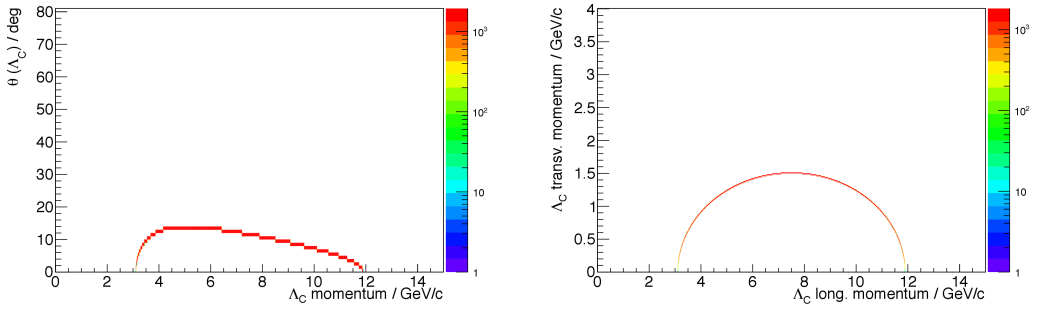

(a) Momentum and polar angle.

(b) Transverse and longitudinal momentum.

Figure 7.1: Momenta and polar angles of the Λ_c as defined by the event generator.

The selected decay pattern for the Λ_c and c.c. foresees three daughter particles, therefore the kinematics of these tracks is much less restricted than in the case of the mother particle. Figure 7.2 shows the momenta and the polar angles of the protons, the negatively charged kaons and the positively charged pions into which the Λ_c decays. The charge conjugates ($\overline{\Lambda}_c \rightarrow \overline{p}K^+\pi^-$) are not shown here since the distributions show analogous trends (the $\overline{p}p \rightarrow \Lambda_c\overline{\Lambda}_c$ decay is in these simulations homogeneously distributed in the phase space).

Figure 7.3 shows the transverse and longitudinal momenta assumed by the three daughter particles. Here again since it is a three-particles decay, the kinematics is less constrained and there is no univocal relation between the components of the momenta.

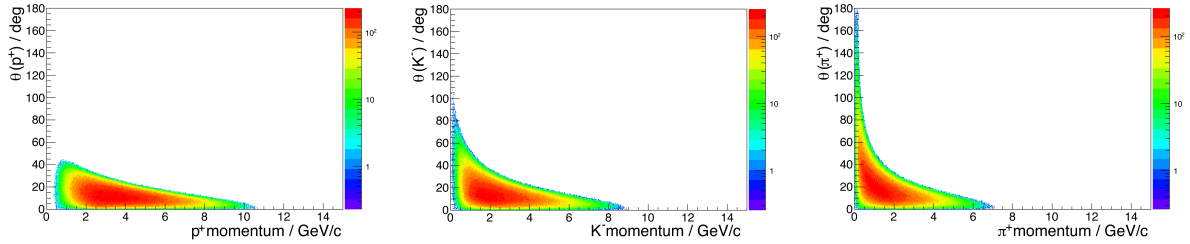

(a) Protons (b) Kaons (K^-) (c) Pions (π^+)

Figure 7.2: Distributions of the polar angles and momenta of the final state particles in the MC input provided to the simulation.

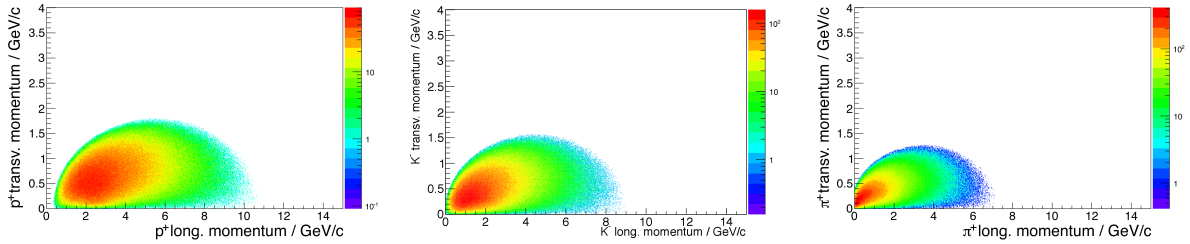

(a) Protons (b) Kaons (K^-) (c) Pions (π^+)

Figure 7.3: Distributions of the longitudinal and transverse momenta of the final state particles in the MC input provided to the simulation.

7.2.2 Reconstructed tracks

The simulation of the detector performance for the reconstruction of the selected channel has been performed within the PandaRoot framework. The six final state particles produced by the event generator (EvtGen [6]), have been propagated through the experiment simulating the response of the detectors. Afterwards a full track reconstruction was performed following the scheme shown in figure 5.4. The same experimental setup and the same PandaRoot revision adopted for the studies of chapter 5 were used here (see appendix E). A first selection on the reconstructed tracks was based on the results of the track fitting and their back-propagation toward the nominal interaction point. If these procedures generated an error, then the corresponding track was removed from the lists of particles on which the analysis is performed.

Figure 7.4 shows the polar angles and the momenta of the final state reconstructed tracks. In this case both charge conjugates are shown since there are small differences in the efficiencies and resolutions which depend on the charge of the particles. Together with a general smearing of the Monte-Carlo input coming from the resolution of the detectors, it is possible to notice that more soft protons and c.c. are reconstructed with low momenta (below 200 MeV/c), while they are not present in the Monte-Carlo input.

The distributions of the transverse and longitudinal momenta of the reconstructed tracks is shown in figure 7.5 for all the final state particles.

Λ_c and $\overline{\Lambda}_c$ candidates can be respectively obtained combining (p, K^-, π^+) and $(\overline{p}, K^+, \pi^-)$ triplets of reconstructed tracks. The plots of figure 7.6 were obtained taking into account all such candidates and plotting the values of their longitudinal and transverse momenta. The elliptical band observed in the Monte-Carlo input of figure 7.1 is here still dominant. Nevertheless the plots are populated by entries in the surrounding regions. This is due to the absence of selections

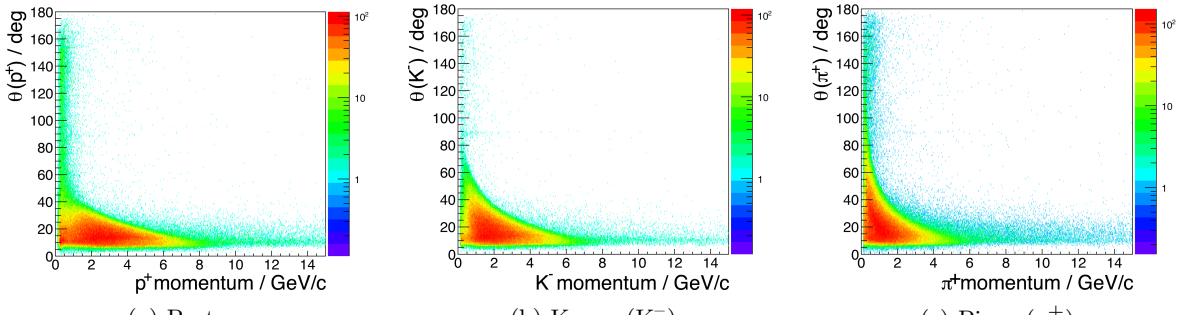

(a) Protons (b) Kaons (K^-) (c) Pions (π^+)

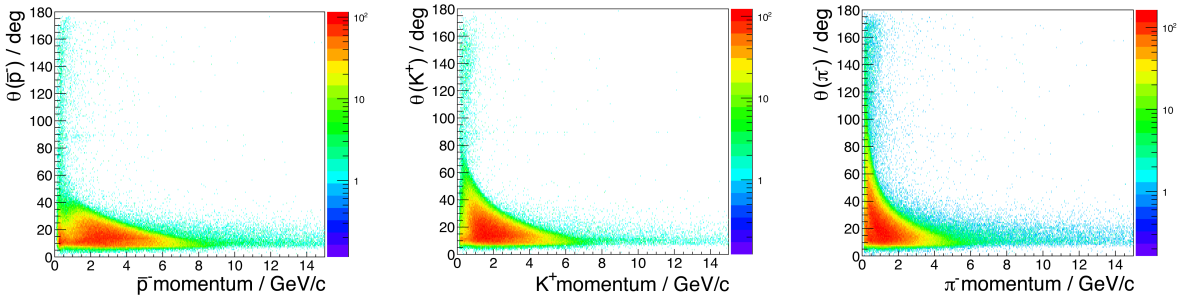

(d) Antiprotons (e) Kaons (K^+) (f) Pions (π^-)

Figure 7.4: Distributions of the reconstructed momentum and polar angle of the final state particles.

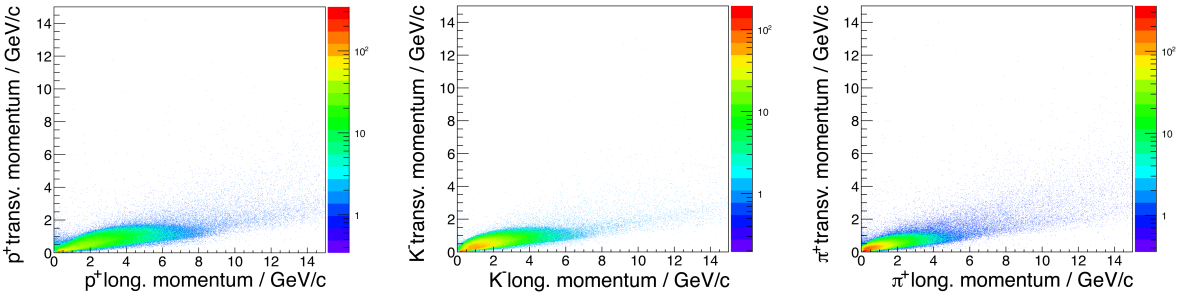

(a) Protons (b) Kaons (K^-) (c) Pions (π^+)

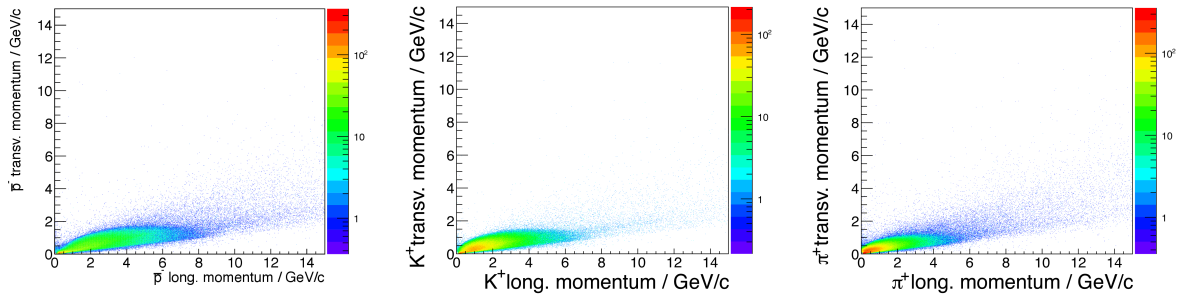

(d) Antiprotons (e) Kaons (K^+) (f) Pions (π^-)

Figure 7.5: Distributions of the reconstructed longitudinal and transverse momentum of the final state particles.

on the Λ_c candidates, all the combinations are used so far. Secondary particles (for example pions), generated during the propagation of the final state particles through the experimental

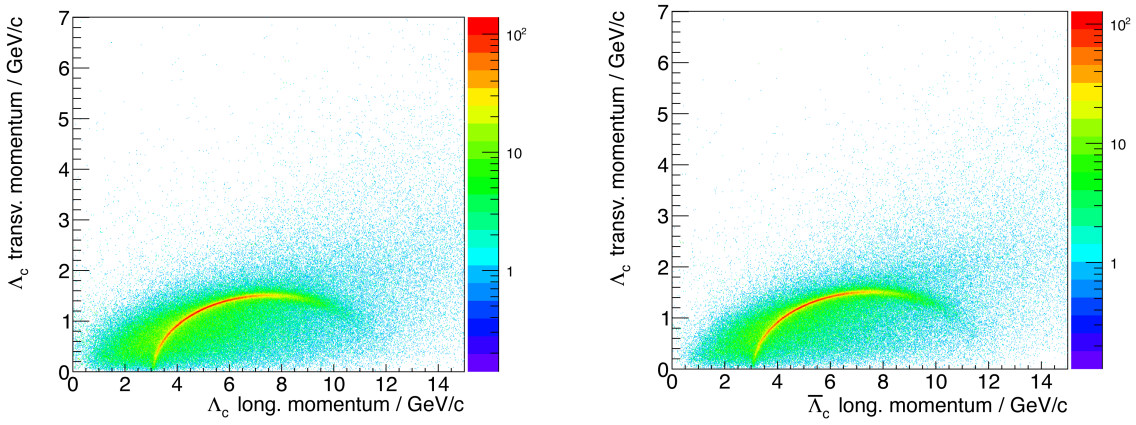

(a) Λ_c (b) $\overline{\Lambda}_c$

Figure 7.6: Reconstructed transverse and longitudinal momentum of Λ_c and $\overline{\Lambda}_c$ candidates before the kinematic selection is applied.

setup, can lead to a wrong reconstruction of the Λ_cs if they are not distinguished from the proper particles forming the decay vertex under study. The same considerations apply both to the reconstructed Λ_c (see figure 7.6a) and $\overline{\Lambda}_c$ vertices (see figure 7.6b). Figure 7.7 shows

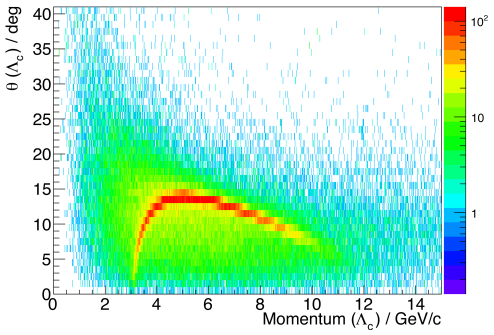

Figure 7.7: Polar angle - momentum distribution for the reconstructed Λ_c candidates.

the distribution of the momentum and polar angle of the reconstructed Λ_c candidates. The most populated band of the plot is well compatible with the Monte-Carlo input provided to the simulation (see figure 7.1a).

Figure 7.8a and 7.8b show invariant mass spectrum obtained for such candidates. Both plots show a prominent peak in correspondence of the nominal Λ_c invariant mass (see table 7.1).

In order to distinguish true Λ_c vertices from wrong association of particle triplets, selections on the kinematics can be performed. In particular it is useful to cut in the transverse - longitudinal momentum plane, discarding particles outside of the elliptical region (see figure 7.9a). It is possible to improve the selection of true Λ_c candidates considering also the polar angle - momentum distribution shown in figure 7.7 and filtering only the tracks with values compatible with the Monte-Carlo input (see the implemented selection in figure 7.9b).
Applying these selections the invariant mass spectra appear much cleaner as shown in figure 7.10 and 7.11: the tails around the nominal invariant mass value are much lower than in the previous case.

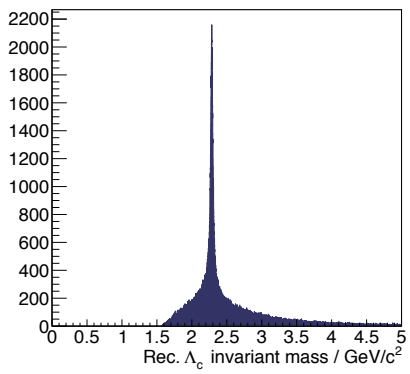

(a) Λ_c

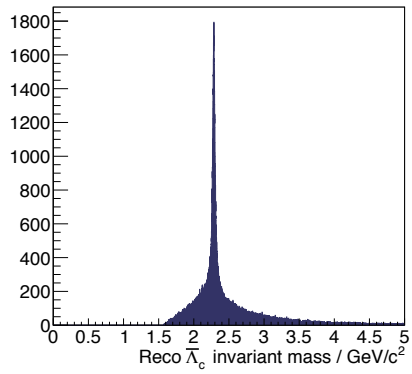

(b) $\overline{\Lambda}_c$

Figure 7.8: Invariant mass of Λ_c and $\overline{\Lambda}_c$ candidates without any selection.

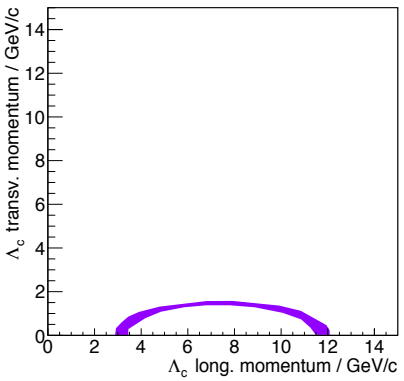

(a) Cut in tranverse-longitudinal momentum plane.

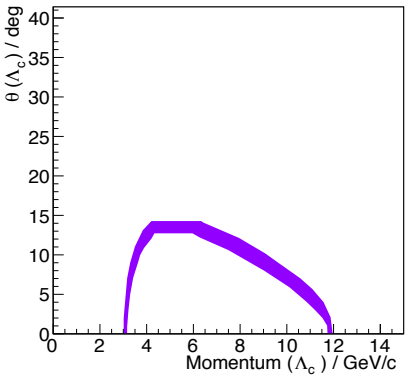

(b) Cut in the momentum-polar angle plane.

Figure 7.9: Kinematical selections applied during the analysis.

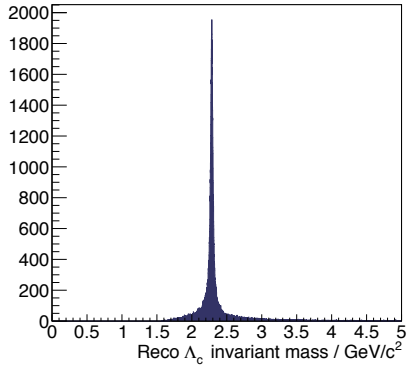

(a) The whole spectrum.

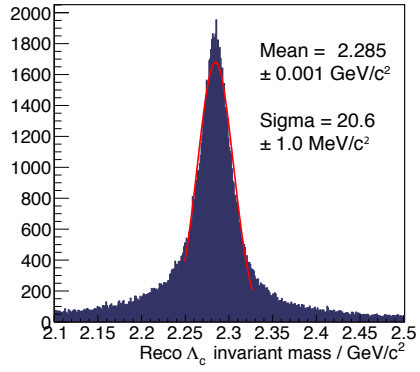

(b) Zoom on the region of interest.

Figure 7.10: Invariant mass of Λ_c candidates satisfying the cut shown in figure 7.9a.

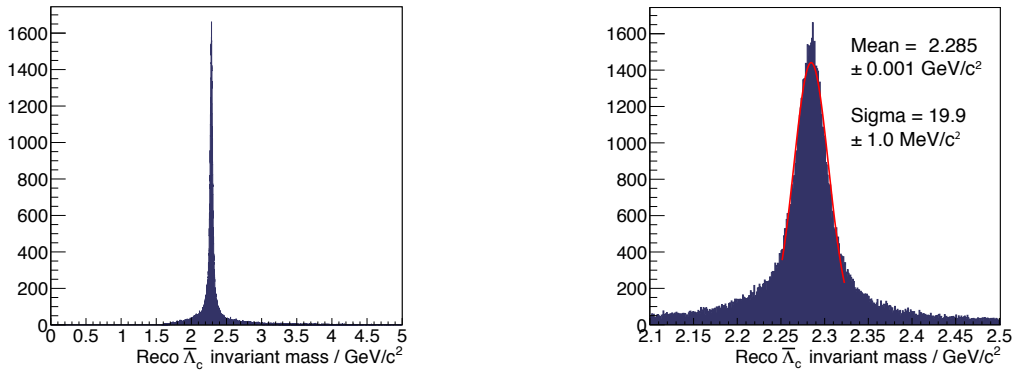

(a) The whole spectrum.

(b) Zoom on the region of interest.

Figure 7.11: Invariant mass of $\overline{\Lambda}_c$ candidates satisfying the cut shown in figure 7.9a

Fitting with a Gaussian distribution the peak of the two invariant mass spectra the following results were obtained (see figure 7.10b and 7.11b):

$$\begin{aligned} m(\Lambda_c) &= (2.285 \pm 0.001)\,\mathrm{GeV/c^2},\ \sigma(\Lambda_c) = (20.6 \pm 1.0)\,\mathrm{MeV/c^2} \\ m(\overline{\Lambda}_c) &= (2.285 \pm 0.001)\,\mathrm{GeV/c^2},\ \sigma(\overline{\Lambda}_c) = (19.9 \pm 1.0)\,\mathrm{MeV/c^2} \end{aligned}$$

All the invariant mass plots shown in this section feature a prominent peak corresponding to the Λ_c nominal invariant mass sitting on larger non-symmetric tails. This influences the results of Gaussian fits performed on the peaks, since the selected range for the fit can vary the standard deviation obtained. An estimate of the fluctuation of the standard deviations obtained with small changes in the fitted range led to an error of 1 MeV/c^2.

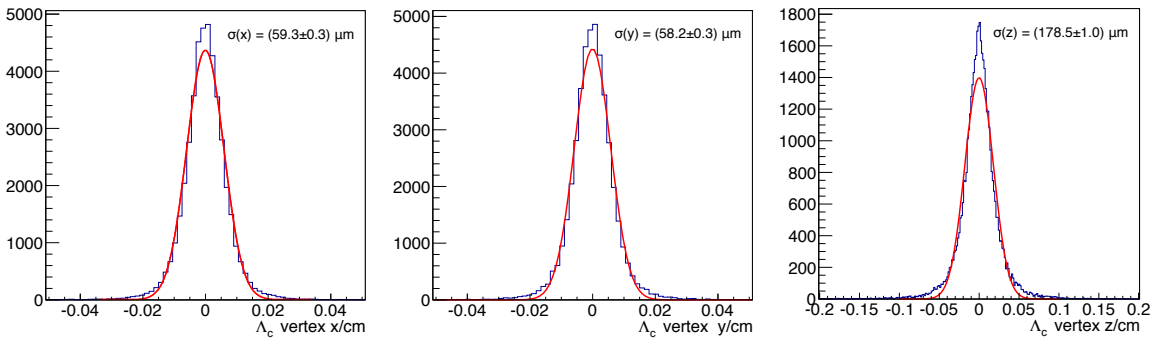

(a) x coordinate.

(b) y coordinate.

(c) z coordinate.

Figure 7.12: Distributions of the coordinates of the reconstructed Λ_c vertices satisfying the cut show in figure 7.9a.

Fitting the decay vertices of the $\Lambda_c/\overline{\Lambda}_c$ candidates and comparing the reconstructed position with the Monte-Carlo true decay vertices, the vertex resolution can be determined. In this study the "PndKinVtx" kinematic vertex fitter [7] implemented in the PandaRoot framework was used to fit the decay vertices. The results obtained for the Λ_c and $\overline{\Lambda}_c$ are reported respectively in figure 7.12 and 7.13. Due to the strong forward boost of the final state particles the transverse coordinates of the vertices are determined more precisely than the longitudinal position.

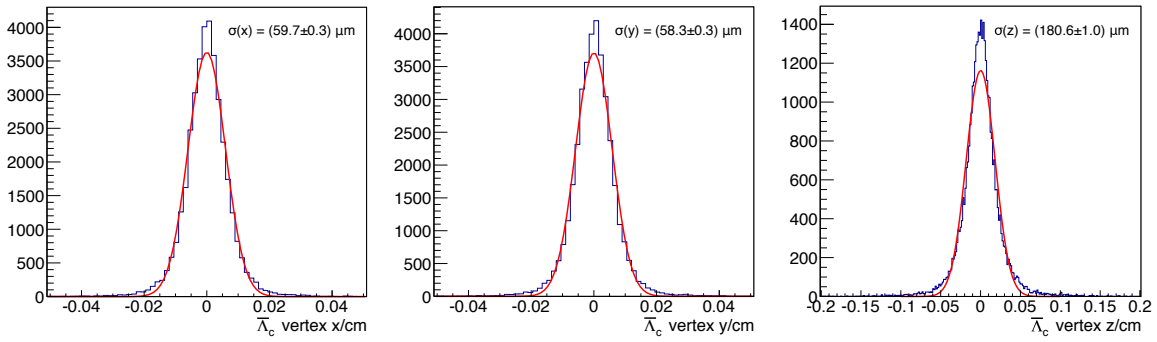

(a) x coordinate. (b) y coordinate. (c) z coordinate.

Figure 7.13: Distributions of the coordinates of the reconstructed $\overline{\Lambda}_c$ vertices satisfying the cut show in figure 7.9a.

The standard deviation of Gaussian fits performed on the distributions of the reconstructed vertex coordinates are respectively:

$$\begin{aligned} \sigma_x(\Lambda_c) &= (59.3 \pm 0.3)\,\mu m, \quad \sigma_y(\Lambda_c) = (58.2 \pm 0.3)\,\mu m, \quad \sigma_z(\Lambda_c) = (178.2 \pm 1.0)\,\mu m \\ \sigma_x(\overline{\Lambda}_c) &= (59.7 \pm 0.3)\,\mu m, \quad \sigma_y(\overline{\Lambda}_c) = (58.3 \pm 0.3)\,\mu m, \quad \sigma_z(\overline{\Lambda}_c) = (180.6 \pm 1.0)\,\mu m \end{aligned}$$

Taking advantage of the knowledge about the initial $\overline{p}p$ state it is possible to perform a four constraints fit (with its implementation in the PandaRoot framework [8]) on the $\Lambda_c\overline{\Lambda}_c$ system.

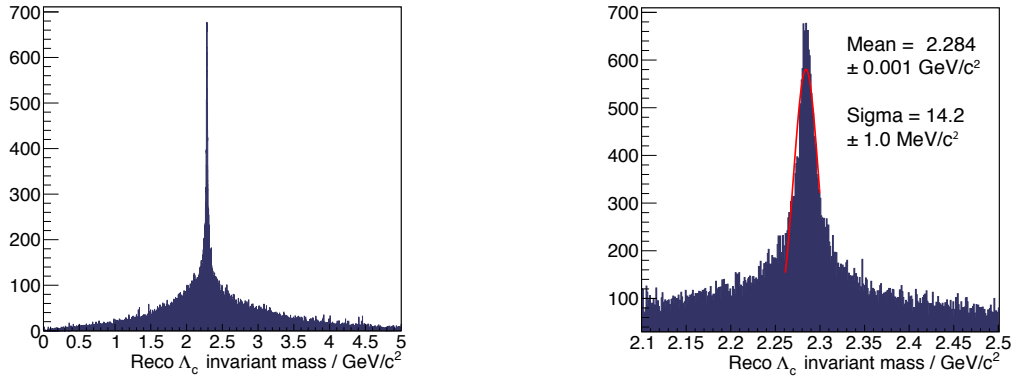

(a) The entire invariant mass spectrum. (b) Zoom on the region of interest.

Figure 7.14: Invariant mass of the Λ_c candidates reconstructed with a four constraints fit on the initial state.

This allows to derive the properties of the daughter particles of such system, therefore accessing the invariant mass of the fitted Λ_c and $\overline{\Lambda}_c$ candidates. The spectra obtained with the four constraints fits are shown in figure 7.14 and 7.15: the peak corresponding to the nominal mass appears narrower than in the previous distributions, the standard deviation of Gaussian fits on the region of the spectra around the peak lead to $\sigma(\Lambda_c) = (14.2 \pm 1.0)\,\mathrm{MeV/c^2}$ and $\sigma(\overline{\Lambda}_c) = (15.1 \pm 1.0)\,\mathrm{MeV/c^2}$.

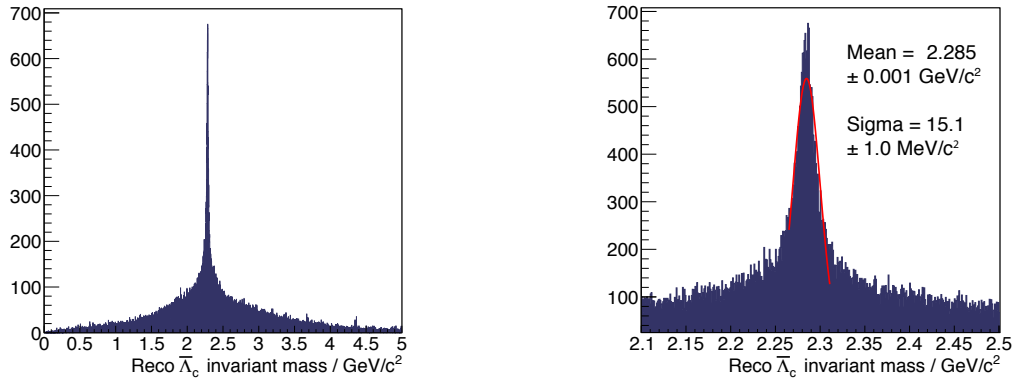

(a) The entire invariant mass spectrum.

(b) Zoom on the region of interest.

Figure 7.15: Invariant mass of the $\overline{\Lambda}_c$ candidates reconstructed with a four constraints fit on the initial state.

7.3 Non-resonant background

The final state is composed of six particles with different charge and type. Ambiguities in the Λ_c candidates reconstruction might emerge from the association of secondary tracks to the proper vertices, as described before, but the final state itself does not have two identical particles which could be ambiguously assigned. The decay length of both the Λ_c and the $\overline{\Lambda}_c$ is comparable

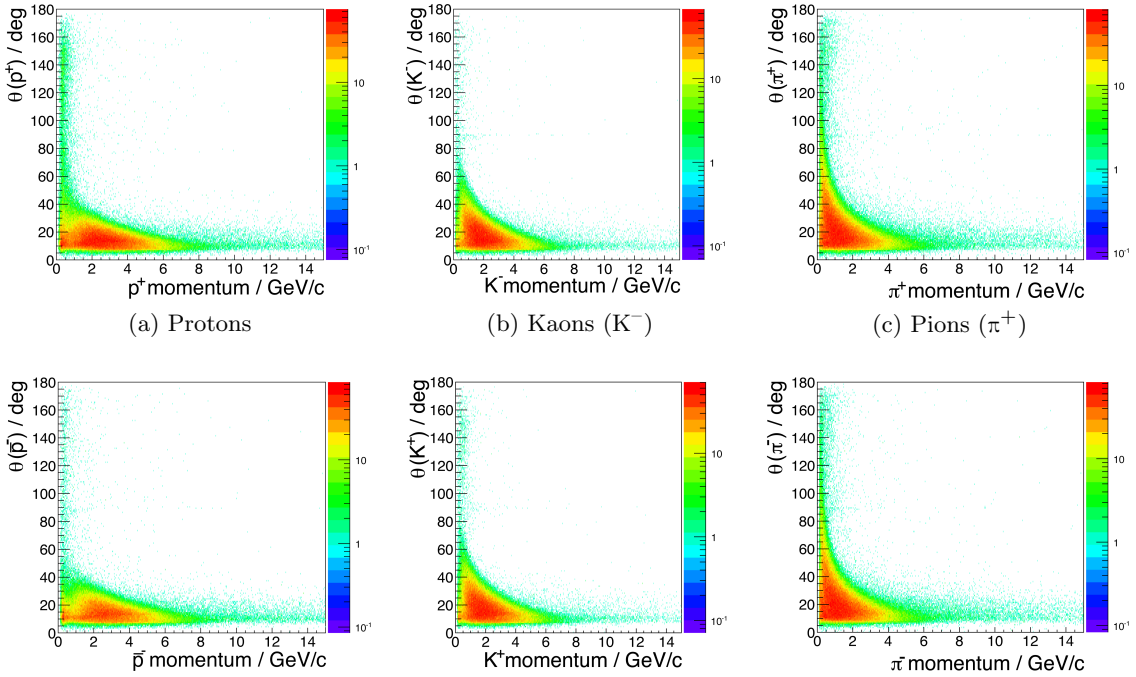

(a) Protons

(b) Kaons (K^-)

(c) Pions (π^+)

(d) Antiprotons

(e) Kaons (K^+)

(f) Pions (π^-)

Figure 7.16: Distributions of the reconstructed momentum and polar angle of the final state particles in the non resonant case.

with the vertex resolution of the setup in the transverse plane (see table 7.1). It is therefore difficult to distinguish the proper Λ_c vertex from a primary interaction just on the base of the

reconstructed position. It is therefore worth to compare the results found in the previous section with what is obtained with the same analysis strategies applied to the same final state, but in a non resonant $\overline{p}p \to \overline{p}\,p\,\pi^+\,\pi^-\,K^+\,K^-$ reaction.
This will be the most challenging source of background since it features the same final state signature of the pure signal and it cannot be distinguished with a vertex tagging (like for example one can do with the $\overline{P}$ANDA MVD for the D mesons) due to the extremely short lifetime of the Λ_c. Figure 7.16 and 7.17 show respectively the distributions of the polar angle, the momentum, its transverse and longitudinal components for all the reconstructed final state particles. These distributions are quite similar to those relative to the resonant case (see figure 7.4 and 7.5), since there the Λ_c decay is phase space distributed and the total energy available in the initial state is the same. Combining $pK^-\pi^+$ vertices it is possible to study the properties of such fake

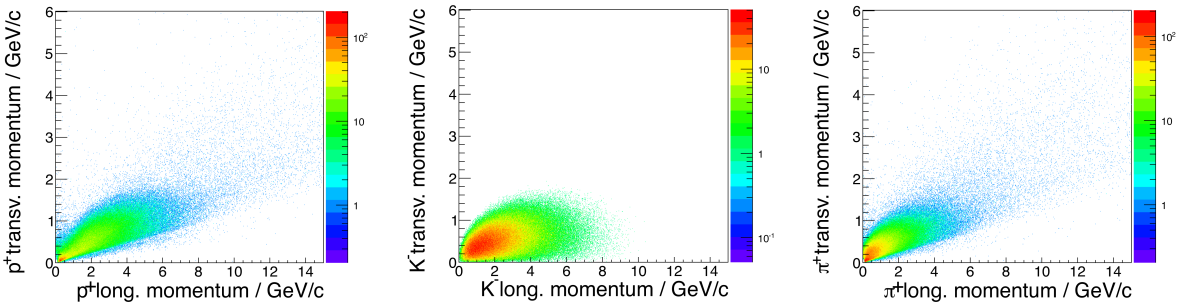

(a) Protons (b) Kaons (K^-) (c) Pions (π^+)

(d) Antiprotons (e) Kaons (K^+) (f) Pions (π^-)

Figure 7.17: Distributions of the reconstructed longitudinal and transverse momentum of the final state particles in the non resonant case.

Λ_c candidates and to evaluate strategies to distinguish them from the real Λ_c analyzed in the previous section. Figure 7.18 shows in a combined plot the transverse and the longitudinal momentum of the fake Λ_c and $\overline{\Lambda}_c$ candidates. Differently from the resonant case of figure 7.6, here no elliptical band corresponding to the decaying particle is present. The distribution appears spread with a higher density of particles with intermidiate longitudinal (3-7 GeV/c) and transverse (0.5-1.5 GeV/c) momenta. The distribution of the momentum and polar angle of the reconstructed fake Λ_c candidates obtained in the non resonant case is shown in figure 7.19. Also these plots show a wider spread than the histogram related to the pure signal case (figure 7.7) and a maximum density for particles with intermediate momenta (4-8 GeV/c) and polar angles ($\sim$3-15°). The Λ_c and $\overline{\Lambda}_c$ invariant mass spectra obtained considering all the possible $pK^-\pi^+$ and $\overline{p}K^+\pi^-$ triplets are respectively shown if figure 7.20a and 7.20b. The distributions show a broad structure with no evident peak corresponding to the invariant mass of the Λ_c. Applying the selections shown in figure 7.9a and 7.9b it is possible to filter out a consistent fraction of the

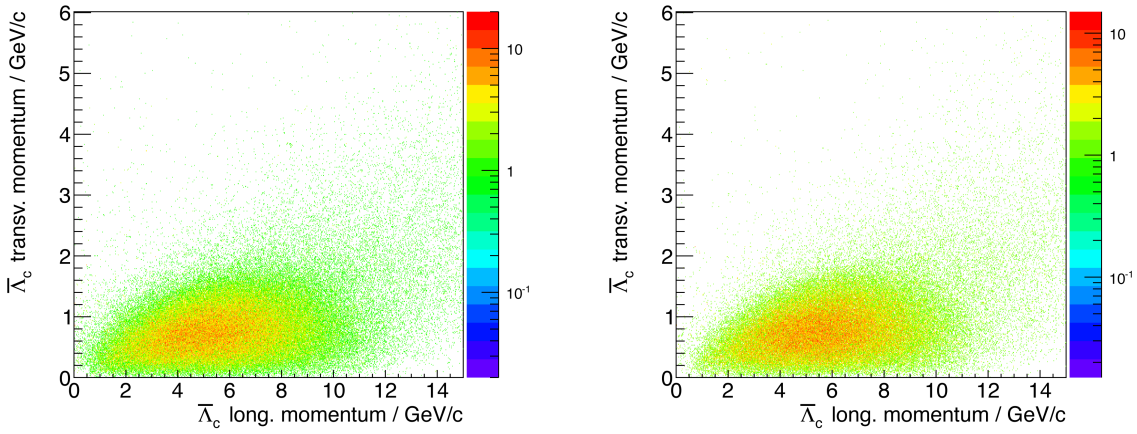

(a) Λ_c (b) $\overline{\Lambda}_c$

Figure 7.18: Reconstructed transverse and longitudinal momentum of Λ_c and $\overline{\Lambda}_c$ candidates in the non resonant case before the kinematic selection is applied.

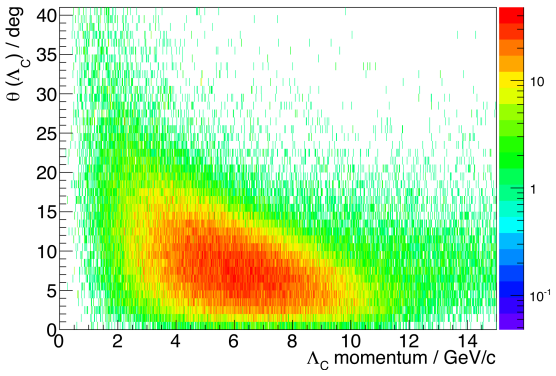

Figure 7.19: Distribution of the momentum and polar angle of the reconstructed fake Λ_c candidates obtained in the non resonant case.

the fake Λ_cs. The invariant mass plots obtained with these cuts are shown in figure 7.21a and 7.21b. The distribution does not show a different trend from the previous plots, but the number of events satisfying the selection is considerably smaller. In particular the suppression factors obtained applying the two kinematic cuts of figure 7.9 are summarized in table 7.2: the total number of entries of the invariant mass spectra is significantly decreased in both the resonant and the non-resonant case, while the suppression on the amplitude of the peak of the distribution is much stronger for the non-resonant reaction. Figure 7.22a and 7.22b show the invariant mass

	Resonant	Non-resonant
Inv. Mass Entries	33.05 %	7.99 %
Peak amplitude	88.0 %	11.4 %

Table 7.2: Fraction of the entries still populating the invariant mass spectra after the application of the kinematic cuts and ratio between the peak amplitude in the two different reactions.

spectra obtained performing a four-constraints fit on the initial state. Here again the plots do not show a peak but a broad distribution with a width of a few GeV/c^2.

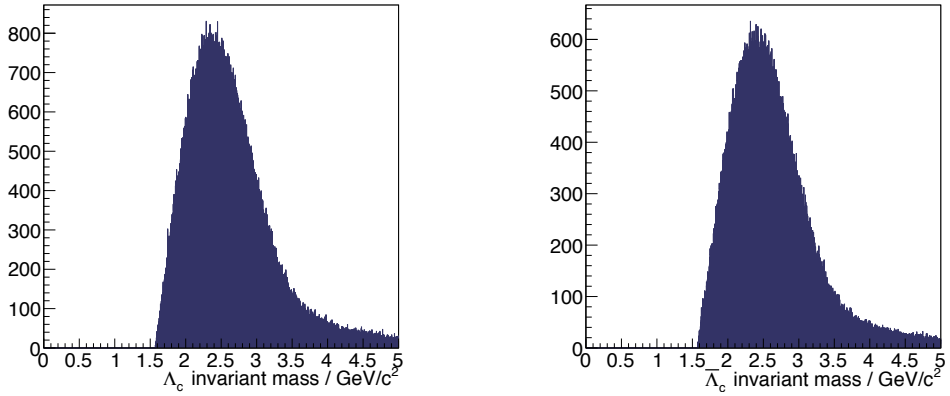

(a) Λ_c (b) $\overline{\Lambda}_c$

Figure 7.20: Invariant mass of all the reconstructed Λ_c and $\overline{\Lambda}_c$ candidates in the non resonant case.

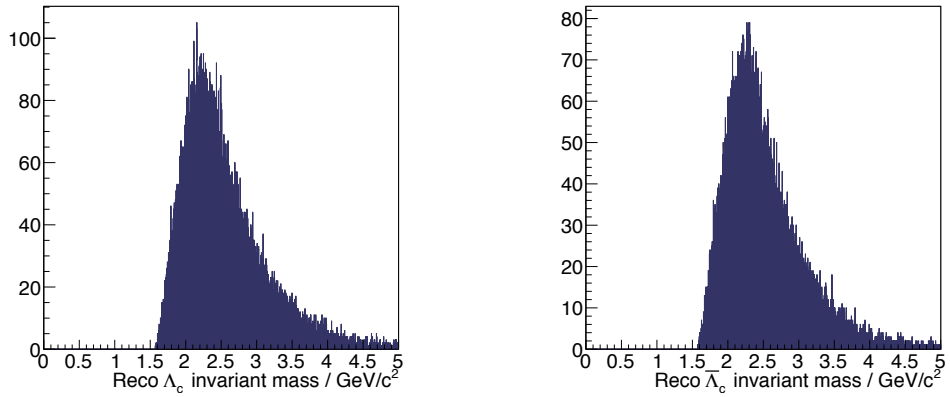

(a) Λ_c candidates. (b) $\overline{\Lambda}_c$ candidates.

Figure 7.21: Invariant mass of the reconstructed Λ_c and $\overline{\Lambda}_c$ candidates after the kinematic cut.

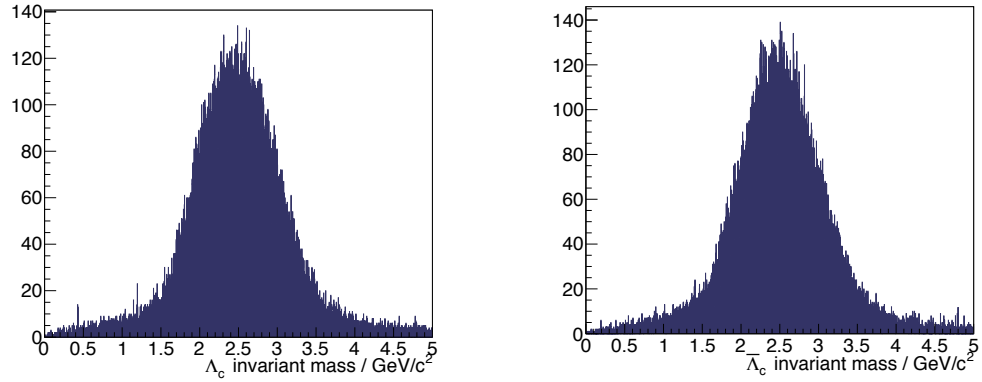

(a) Λ_c candidates. (b) $\overline{\Lambda}_c$ candidates.

Figure 7.22: Invariant mass of Λ_c and $\overline{\Lambda}_c$ candidates reconstructed with four constraints fits.

7.4 Final results

In order to evaluate the significance of the resonant signal over the non-resonant background some considerations about the cross sections of the two processes must be done. The cross section of the non-resonant reaction $\overline{p}p \to pK^-\pi + \overline{p}K^+\pi^-$ was measured to be (0.023 ± 0.012) mb at the Sepukhov facility with an energy $\sqrt{s} = 7.862$ GeV. In order to extrapolate the cross section of the non-resonant process at the maximum energy available at $\overline{\text{P}}$ANDA ($p_{beam} = 15$ GeV/c, $\sqrt{s} = 5.474$ GeV), a scaling with respect to the available energy $\sqrt{s}$ analogous to the one of the $\overline{p}p \to 6$ prongs process was assumed.

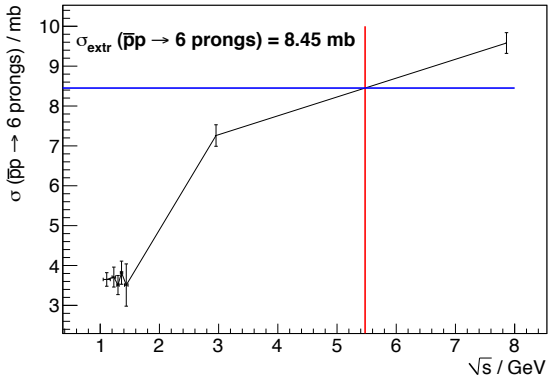

Figure 7.23: Extrapolation of the $\overline{p}p \to 6$ prongs cross section at the maximum $\overline{\text{P}}$ANDA energy from existing measurements [5] [9] [10].

Figure 7.23 summarizes the 6 prongs cross section measurements performed in the energy region close to the $\overline{\text{P}}$ANDA regime. Interpolating the data point the following cross section can be determined: $\sigma(\sqrt{s} = 5.474 \text{ GeV})_{\overline{p}p \to 6 \text{ prongs}} = 8.45$ mb. Scaling the $\overline{p}p \to pK^-\pi^+\overline{p}K^+\pi^-$ cross section with the same factor obtained in the 6 prongs case the following can be derived:

$$\sigma(\sqrt{s} = 5.474 \text{ GeV})_{\overline{p}p \to pK^-\pi^+\overline{p}K^+\pi^-} = 0.020 \text{ mb}$$

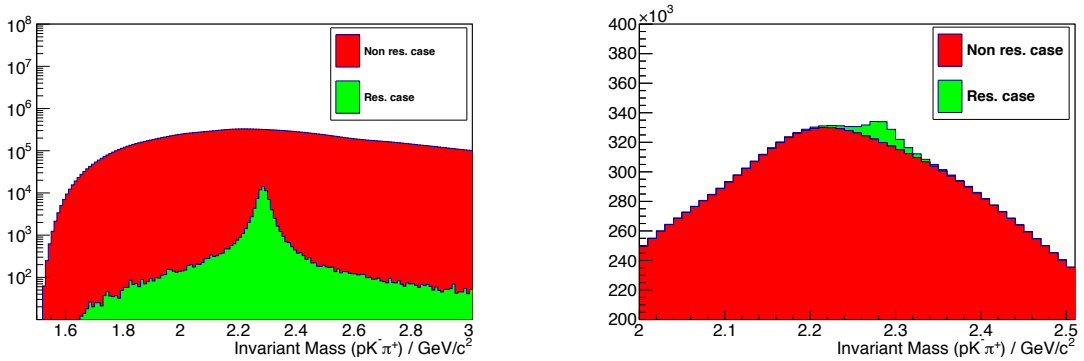

(a) Superposed invariant mass spectra.

(b) Stacked invariant mass spectra.

Figure 7.24: Invariant mass of the kinetically selected Λ_c candidates in the resonant and in the non resonant reaction.

Considering the estimated $\bar{p}p \to \Lambda_c\overline{\Lambda}_c$ cross section of 200 nb [3] and the 5% branching ratio of the selected Λ_c decay a scaling of a factor 2000 between the non-resonant and the resonant signal can be deduced.
Figure 7.24 shows the invariant mass spectra obtained in the resonant and in the non-resonant case assuming the previous scaling between the number of events considered for the two reactions. Both the kinematic cuts shown in figure 7.9 were applied to the Λ_c candidates. In particular figure 7.24a is the logarithmic superposition of the two spectra, while in figure 7.24b the contribution of the signal is stacked over the non-resonant distribution. The contribution of the Λ_c signal is discernible from the non-resonance spectrum due to the kinematic selections applied to both data sets. For comparison the superposed and stacked spectra obtained without kinematic cuts are shown in respectively in figure 7.25a and 7.25b. In these plots the signal contribution is not anymore statistically significant and it is fully dominated by the non-resonant distribution.

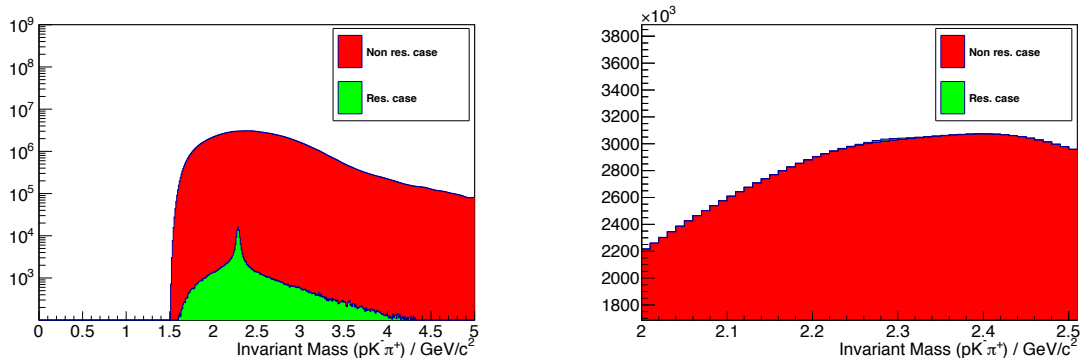

(a) Superposed invariant mass spectra.

(b) Stacked invariant mass spectra.

Figure 7.25: Invariant mass spectra obtained without kinematic selections on the Λ_c candidates.

Bibliography

[1] A.T. Goritschnig, P. Kroll, W. Schweiger. $p\bar{p} \to \Lambda_c\overline{\Lambda}_c$ within the generalized parton picture - first results. *PoS LC2008:021,2008.* arXiv:0811.2661 [hep-ph].

[2] A. Khodjamirian, Ch. Klein, Th. Mannel, Y.-M. Wang. How much charm can $\overline{\text{P}}$ANDA produce? *Eur. Phys. J. A*, 48:1–12, 2012. http://dx.doi.org/10.1140/epja/i2012-12031-8.

[3] A. B. Kaidalov, P. E. Volkovitsky. Binary reactions in $\bar{p}p$ collisions at intermediate energies. *Zeitschrift für Physik C Particles and Fields*, 63:517–524, 1994. http://dx.doi.org/10.1007/BF01580332.

[4] J. Beringer et al. (Particle Data Group). PR D86, 010001 (2012). *http://pdg.lbl.gov.*

[5] M.A. Jabiol et al. General features of pp interactions at 32 GeV/c. *Nucl. Phys. B*, 127(3):365 – 383, 1977. http://dx.doi.org/10.1016/0550-3213(77)90445-X.

[6] D. J. Lange. The EvtGen particle decay simulation package. *Nucl. Instr. Meth. A*, (462):152–155, 2001. http://www.slac.stanford.edu/∼lange/EvtGen/evtgen.pdf.

[7] Documentation of the PndKinVtxFitter class. http://cbmroot.gsi.de/panda_doc/daily/html/classPndKinVtxFitter.html.

[8] Documentation of the Pnd4CFitter class. http://cbmroot.gsi.de/panda_doc/daily/html/classPnd4CFitter.html.

[9] J. B. Gay et al. The Reaction $\overline{p}p \rightarrow 3\pi^{-}3\pi^{+}$ Between 1.09-GeV/c and 1.44-GeV/c and the Effect of π π Phase Shifts. *Nuovo Cim.*, A31(593), 1976. http://dx.doi.org/10.1007/BF02734652.

[10] H.W. Atherton et al. General characteristics of the annihilation reaction $\overline{p}p \rightarrow 3\pi^{+}3\pi^{-}(\pi^{0})$ at 3.6 GeV/c. *Nucl. Phys. B*, 18(1):221 – 245, 1970. http://www.sciencedirect.com/science/article/pii/0550321370902890.

Appendices

APPENDIX A

Time match of the pixel and strip DAQ systems

The strip tracking station and the pixel telescope involved in the combined beam tests have two different data acquisition (DAQ) systems. The strip sensors are triggered by the coincidence of scintillating slabs put in front and at the end of the station. On the contrary the pixel assembly is composed of a silicon pixel sensor bump bonded to a trigger-less chip provided with a 50 MHz clock. Therefore the two subsystems record different subsets of events and it is necessary to perform an event building, finding overlapping events in which both trackers have recorded hits. The event building is performed in two steps. First a selection is applied to the strip hits looking for events where the four strip planes were recording a hit, this is done to select real tracks going through the whole tracking station and therefore crossing the pixel telescope as well. In a second phase for each selected strip event a procedure loops on the pixel events looking for hit timestamps compatible with the strip ones.

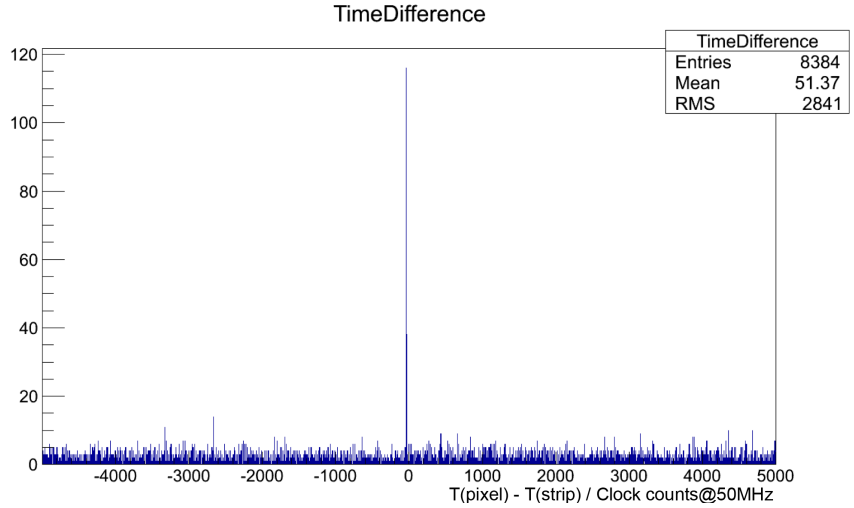

Figure A.1: Difference between the timestamps of the hits recorded by the two subsystems combining events in a wide absolute event time range.

The developed software task loops on the list of strip events. For each of them a portion of

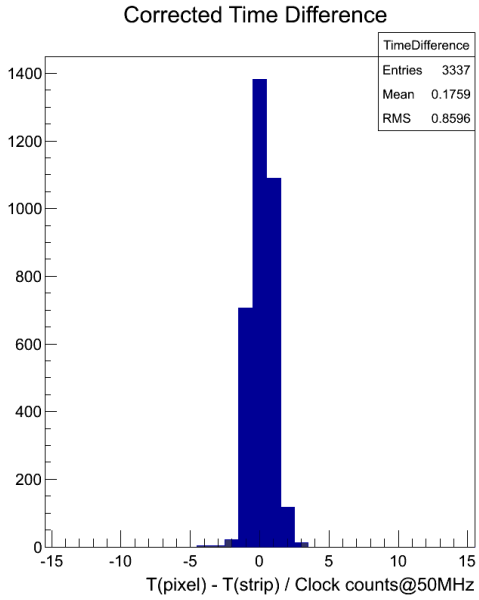

Figure A.2: Zoom of the timestamp difference after the offset correction.

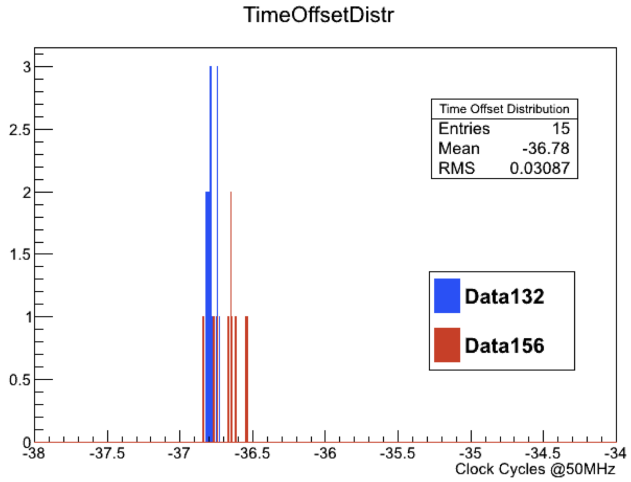

Figure A.3: Average systematic offsets obtained in different spills. The two colors refers to two different runs during the data taking. Total mean value and RMS are displayed on the figure.

the pixel data having timestamps falling in a symmetric window around the strip timestamp is considered. A systematic offset between the two DAQ systems can be easily measured and corrected. The user can set the width of the compatibility window depending on the purpose of the study. For example when determining the time offset between the two DAQ systems one wants to have a really wide window (see figure A.1). In this case a peaked structure emerges from a flat distribution when the offset between the DAQs is constant in the analyzed data sample. On the contrary, once the offset is corrected, the window will be reduced in order to select only events with a satisfactory time coincidence (see for example the compatible events of figure A.2). During the combined beam test at COSY (Jülich) the offset was monitored to be constant during the data taking. Figure A.3 shows the offset values obtained in different spills of two runs corresponding to different days of the test.

APPENDIX B

Tests with different setups of the MVD

In order to characterize the effects of different parameters of the MVD design on its performance, two different benchmark studies were selected:

- the propagation and reconstruction of the reaction $\overline{p}p \rightarrow \psi(2S) \rightarrow J/\psi\pi^+\pi^- \rightarrow \mu^+\mu^-\pi^+\pi^-$;
- the propagation and reconstruction of four 500 MeV/c pions (two π^+ and two π^-) coming from a common vertex (0,0,0) distributed homogeneously in the polar range $[10°, 140°]$.

Different geometries were adopted varying the thickness of the pixel sensors (100 and 200 µm), the pixel cell size (50×50, 100×100, 150×150 and 200×200 µm) and removing the first or the second pixel barrel layer. The results are compiled in table B.1. In each case a full reconstruction was performed determining the vertex resolutions in the two considered channels, which are labelled respectively as ResX, ResY and ResZ in the table. Furthermore the three-dimensional distance of the reconstructed vertices from the nominal interaction point (0,0,0) was studied, determining the position of the most frequent value in each configuration (see figure B.1). These values are reported in the previous table in the D column.

One last check was realized to quantify the effect of adding passive materials to the innermost layers of the detector. One millimeter of full carbon was positioned in front of barrel one, barrel two, the first and the second forward pixel disks. The results obtained from events with four 500 MeV/c pions are summarized in table B.2.

Vertex resolution as a function of the momentum

It is also interesting to study the effect of the pixel cell size on the vertex resolution as a function of the momentum of the final state particles. Two different channels were considered:

- $\overline{p}p \rightarrow \psi(2S) \rightarrow J/\psi\pi^+\pi^- \rightarrow \mu^+\mu^-\pi^+\pi^-$
- $\overline{p}p \rightarrow \pi^+\pi^-$, with p_{beam}=15 GeV/c

Channel	Sens. Thick.	# Barrel layers	Pixel cell size	Res X	Res Y	Res Z	D
	µm		µm × µm	µm	µm	µm	µm
J/ψ	100	4	50×50	26	26	45	46.2
J/ψ	100	4	100×100	38	36	57	61.7
J/ψ	100	4	150×150	50	48	75	80.4
J/ψ	100	4	200×200	60	57	89	95.1
J/ψ	200	4	50×50	31	29	52	52.6
J/ψ	200	4	100×100	45	42	62	70.2
J/ψ	200	4	150×150	54	52	76	85
J/ψ	200	4	200×200	63	60	84	96.1
Four π	100	4	50×50	81	62	55	92.6
Four π	100	4	100×100	93	77	60	107.5
Four π	100	4	200×200	118	98	87	141.3
Four π	200	4	50×50	94	77	64	110
Four π	200	4	100×100	94	81	68	114.7
Four π	200	4	200×200	121	107	87	146.8
J/ψ	200	3 (1^{st} removed)	100×100	44	42	68	71.6
Four π	200	3 (1^{st} removed)	100×100	127	117	96	157.1
J/ψ	200	3 (2^{nd} removed)	100×100	44	42	67	71.2
Four π	200	3 (2^{nd} removed)	100×100	119	85	76	129

Table B.1: Comparison of the results obtained with the different setups.

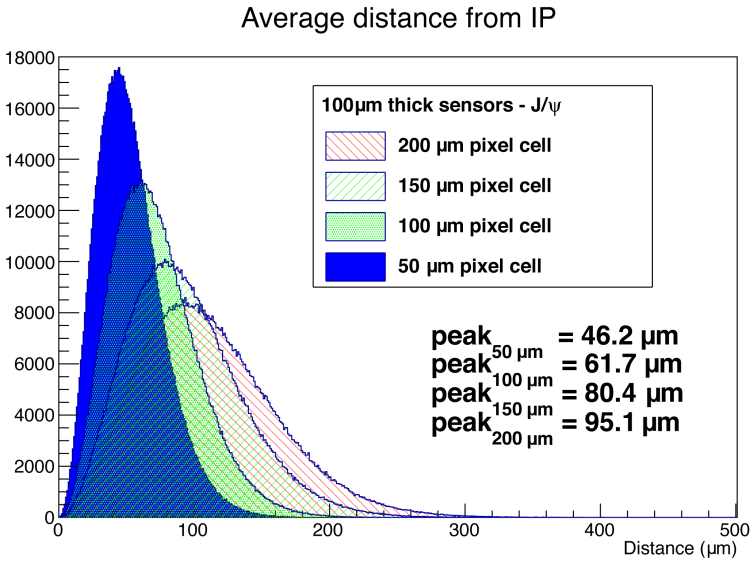

Figure B.1: Distributions of the distance between the reconstructed vertices and the origin obtained with 100 µm thick sensors in the J/ψ channel.

B.0.1 $\overline{p}p \to \psi(2S) \to J/\psi\pi^+\pi^- \to \mu^+\mu^-\pi^+\pi^-$

This channel was used to characterize the reconstruction performance for $J/\psi \to \mu^+\mu^-$ vertices as a function of the momentum of one of the two final state muons. Since the decaying J/ψ comes from primary decays into three particles, its momentum is not fixed neither in module

Channel	Sens. Thick.	# Barrel layers	Pixel cell size	Res X	Res Y	Res Z	D
	µm		µm × µm	µm	µm	µm	µm
Four π	200	4	100×100	100	84	69	117.9

Table B.2: Analysis of the effect of additional passive materials close to the interaction point.

nor in direction, but follows a distribution. This influences the kinematics of the two final state muons. Figure B.2a and B.2b show respectively the relation between the polar angles and the momenta of such two muons. Figure B.2c and B.2d show respectively the dependency of the

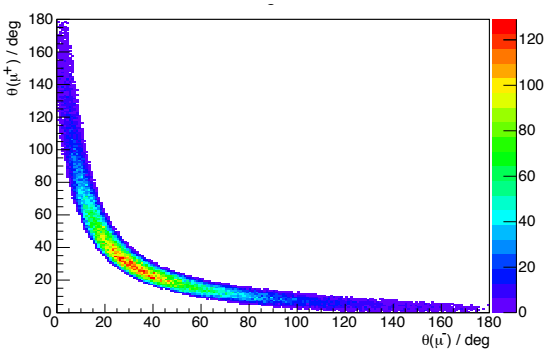

(a) Distribution of the polar angles of the two muons.

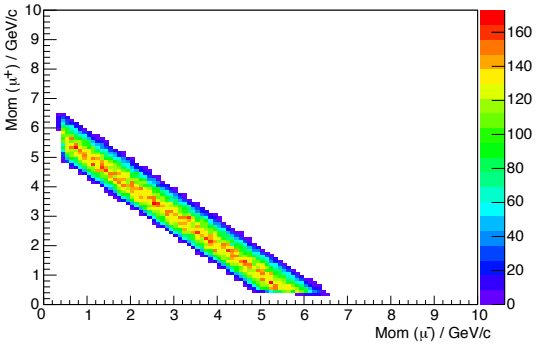

(b) Distribution of the momenta of the two muons.

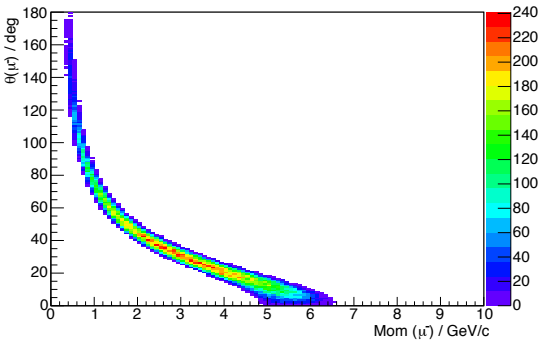

(c) Polar angle of one muon as a function of its momentum.

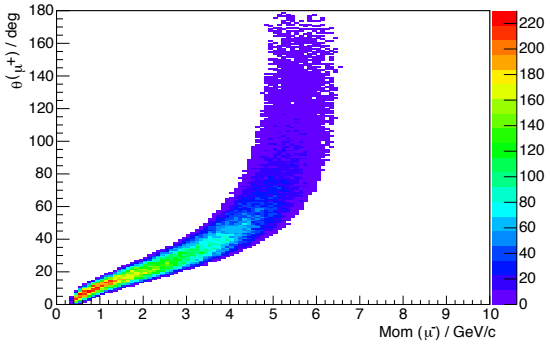

(d) Polar angle of one muon as a function of the momentum of the other muon.

Figure B.2: Kinematics of the Monte-Carlo input provided to PandaRoot for propagation and reconstruction.

polar angle of the μ^- and of the μ^+ with respect to the momentum of the final state μ^-. All the plots of figure B.2 refer to the Monte-Carlo input provived to the simulation, therefore not including acceptance and efficiency effects. Reconstructing the decays within the PandaRoot framework the vertex resolutions can be plotted as a function of the reconstructed μ^- momentum as shown in figure B.3. These plots compare the performance of designs with different pixel cell sizes in a wide kinematical range: different momenta of the muons correspond to different polar angles and therefore to different incident angles of the tracks on the surface of the sensors and to different average cluster size. In order to disentangle the vertex resolution from the momentum resolution, the previous plots can be modified showing on the x-axis the MC-true momentum of the muon. The results obtained following this method are shown in figure B.4.

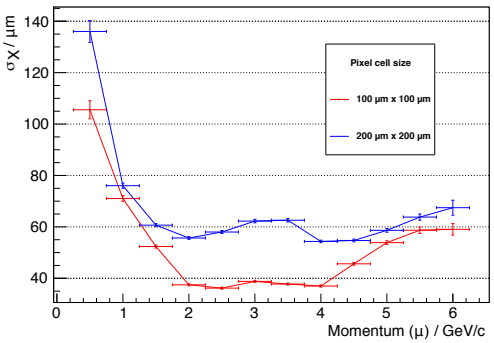

(a) X vertex resolution.

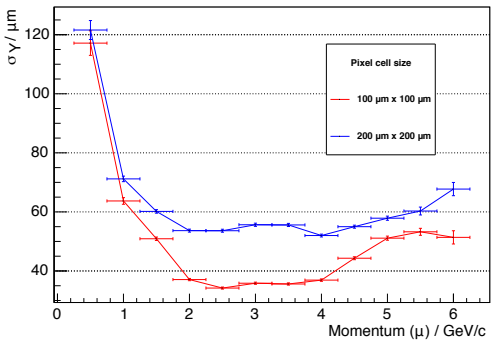

(b) Y vertex resolution.

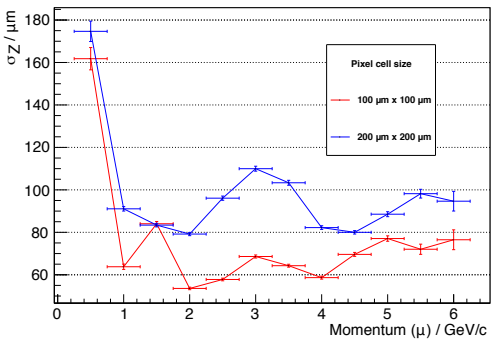

(c) Z vertex resolution.

Figure B.3: Resolution for $J/\psi \to \mu^+\mu^-$ vertices as a function of the μ^+ momentum with different pixel cell sizes.

In all the considered cases the pixel cell with 100 µm size produces better results. The modulation which can be observed for example in figure B.4b is due to the corresponding polar angles of those tracks.

Starting from the symmetrical solution in which both muons have the same momentum and therefore identical polar angle (even if with opposite direction), the coordinate resolutions improve moving toward higher and lower momenta. This is due to the fact that in the symmetrical solution the two tracks have polar angles of some 30°, therefore crossing the region of the MVD where the cables of the innermost pixel layers are routed outside of the innermost region (see figure 4.13).

Smaller μ^- momenta correspond to bigger μ^- polar angles, while the μ^+ will fly closer to the longitudinal axis. This results in a bigger relative angle between the two tracks and in a smaller amount of material crossed by the two tracks, leading to a better determination of the vertex position. Proceeding to even lower μ^- (or symmetrically μ^+) momenta, the track flying forward gets a small polar angle, therefore missing the first forward pixel disks. This results in a worsening of the vertex reconstruction performance.

B.0.2 $\overline{p}p \to \pi^+\pi^-$

The second channel considered to compare the performance of two different pixel cell sizes is $\overline{p}p \to \pi^+\pi^-$ studied at the maximum $\overline{\text{PANDA}}$ beam momentum (p_{beam}=15GeV/c). In this

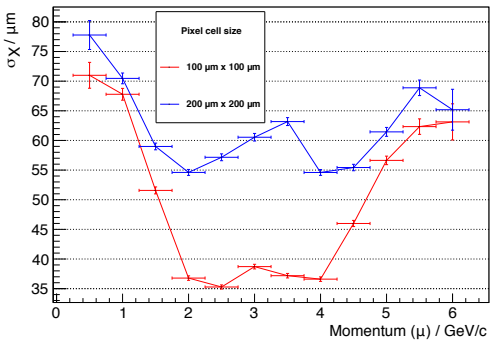

(a) X vertex resolution.

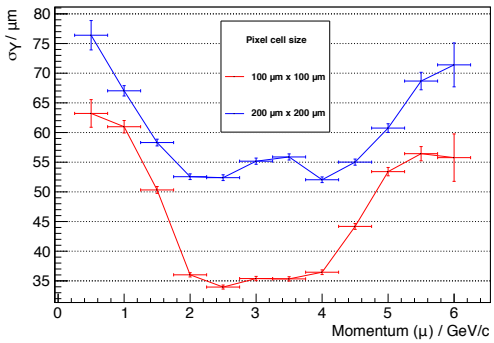

(b) Y vertex resolution.

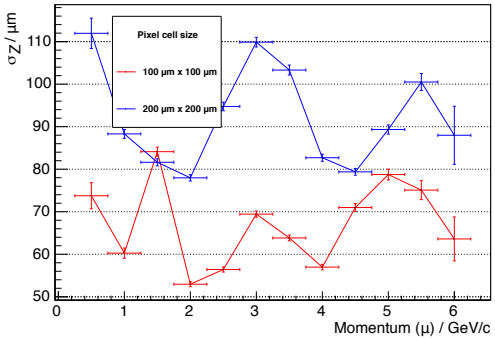

(c) Z vertex resolution.

Figure B.4: Resolution for $J/\psi \to \mu^+\mu^-$ vertices as a function of the μ^+ MC-true momentum with different pixel cell sizes.

case the two pions are the only two particles in the final state, therefore the relation between the momenta and the polar angles of the two pions is univocal. Figure B.5a and B.5b show respectively the relation between the polar angles and the momenta of the pions.

Figure B.5c plots the polar angle of the π^- as a function of its momentum, while figure B.5d shows the polar angle of the positively charged pion again as a function of the momentum of the π^-. As in the previous case all the plots in figure B.5 illustrate the Monte-Carlo input provided to the simulations and do not take into account any implementation of the detector response.

Figure B.6a, B.6b and B.6c show respectively the reconstructed x, y and z vertex resolutions as a function of the π^- momentum. As in the J/ψ case, the design foreseeing $100\,\mu m \times 100\,\mu m$ pixel cells leads to the best results, with a more homogeneous performance. The behavior for high and low π^- momenta appears not symmetric: low reconstructed momenta correspond here to a worse performance than that one obtained with high momenta. This is particularly evident in figure B.6c. The reason of such trends is that what is plotted there is the convolution of the vertex and the momentum resolutions. Figure B.7 summarizes a comparison between the input and the reconstructed momentum of the π^+ candidates: in a fraction of the reconstructed tracks the determined momentum is lower than the input one. In particular comparing figures B.7b and B.7c it is possible to notice the discrepancy between the input and the measured momenta at the two edges of the momentum range.

As in the J/ψ case it is worth to plot the vertex resolutions as a function of the Monte-Carlo momentum of the pion candidates in order to disentangle the effect on the vertex resolution

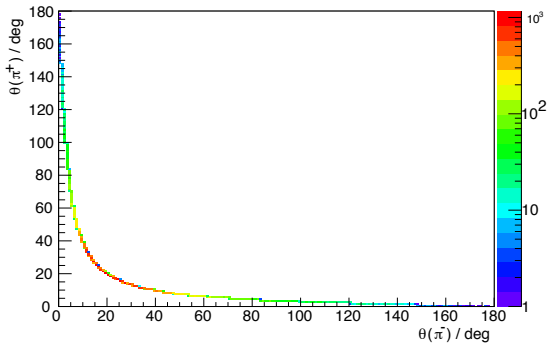

(a) Distribution of the polar angles of the two pions.

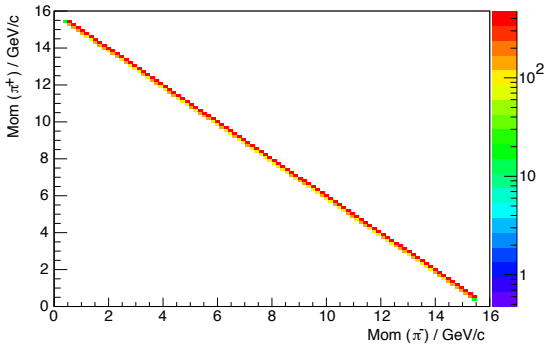

(b) Distribution of the momenta of the two pions.

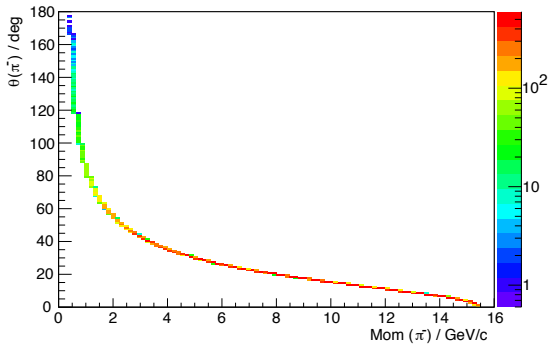

(c) Polar angle of one pion as a function of its momentum.

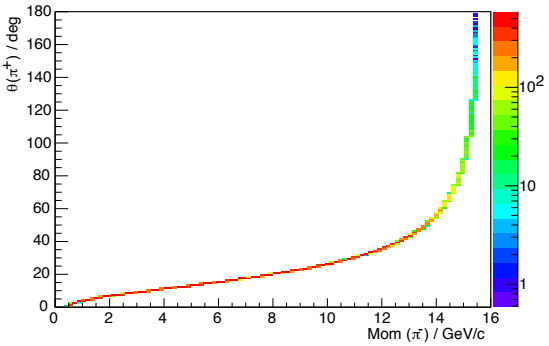

(d) Polar angle of one pion as a function of the momentum of the other pion.

Figure B.5: Kinematics of the MC input provided to PandaRoot for propagation and reconstruction to study the vertex reconstruction performance in the reaction $\bar{p}p \to \pi^+\pi^-$ with $p_{beam} = 15$ GeV/c.

from the one on the momentum resolution. Figure B.8 shows these last results: as before the smaller pixel cell provides a better and more homogeneous performance. Figure B.8c looks nicely symmetric for high and low momenta. The structure with two prominent peaks can be explained with the geometry of the detector. Tracks (π^-) with polar angles below 17° do not hit the first forward pixel disks, this is the reason of the rising of the z-resolution when the momentum is going from 7 to 6 GeV/c. The other pion of the final state (π^+) reaches a polar angle of about 25° when its momentum goes below 6 GeV/c. This polar angle is the limit of the acceptance of the forward strip wheels (it represents the minimum angle required to create 2 hit points), therefore tracks with bigger ϑ benefit from two more hit points contributing to the track reconstruction. This is the justification of the the improving z-resolution for momenta decreasing from 6 GeV/c. The same argumentations can be used symmetrically to explain the peak at p_{π^+} =10GeV/c.

Conclusions

The option of a 50 µm × 50 µm pixel cell was excluded, since it is not possible to implement both the analog and the digital part of a front-end chip with the required specifications in such a small area. The simulations described in this channel show clearly that the 100µm × 100µm cells lead to better and more homogenous performances in different physics cases.

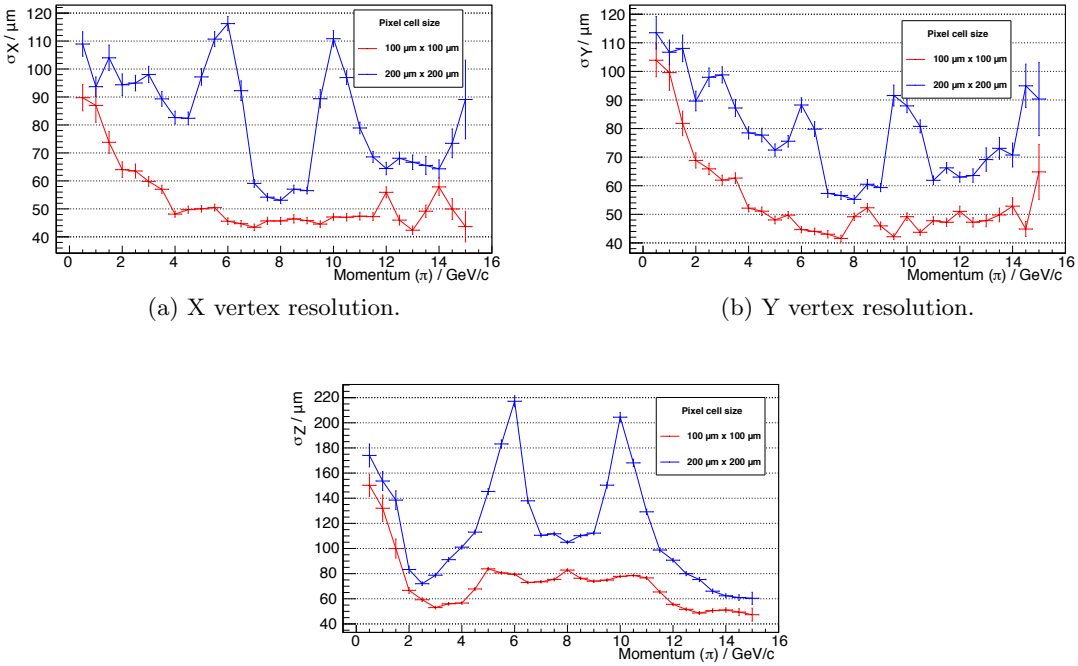

(a) X vertex resolution.

(b) Y vertex resolution.

(c) Z vertex resolution.

Figure B.6: Resolutions for $\overline{\mathrm{p}}\mathrm{p} \to \pi^+\pi^-$ vertices as a function of the π^+ momentum with different pixel cell sizes.

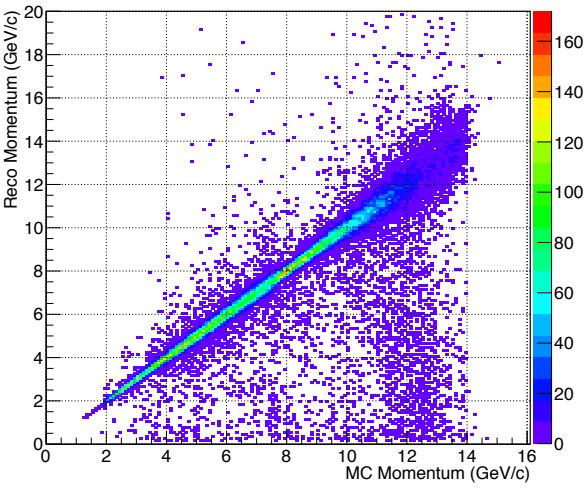

(a) Reconstructed π^+ momentum as a function of the MC-true values.

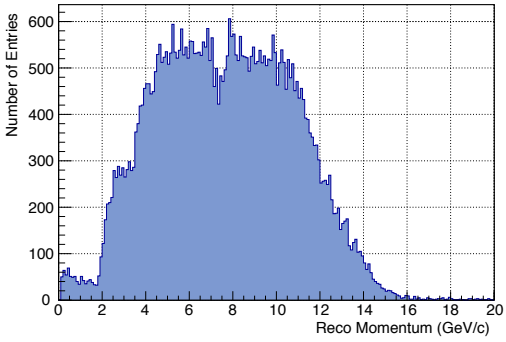

(b) Reconstructed π^+ momenta spectrum.

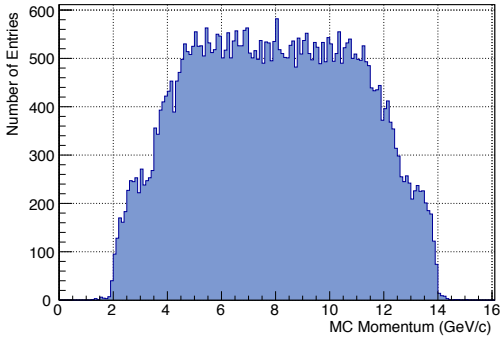

(c) MC π^+ momenta spectrum.

Figure B.7: Comparison between reconstructed and MC-true π^+ momentum values.

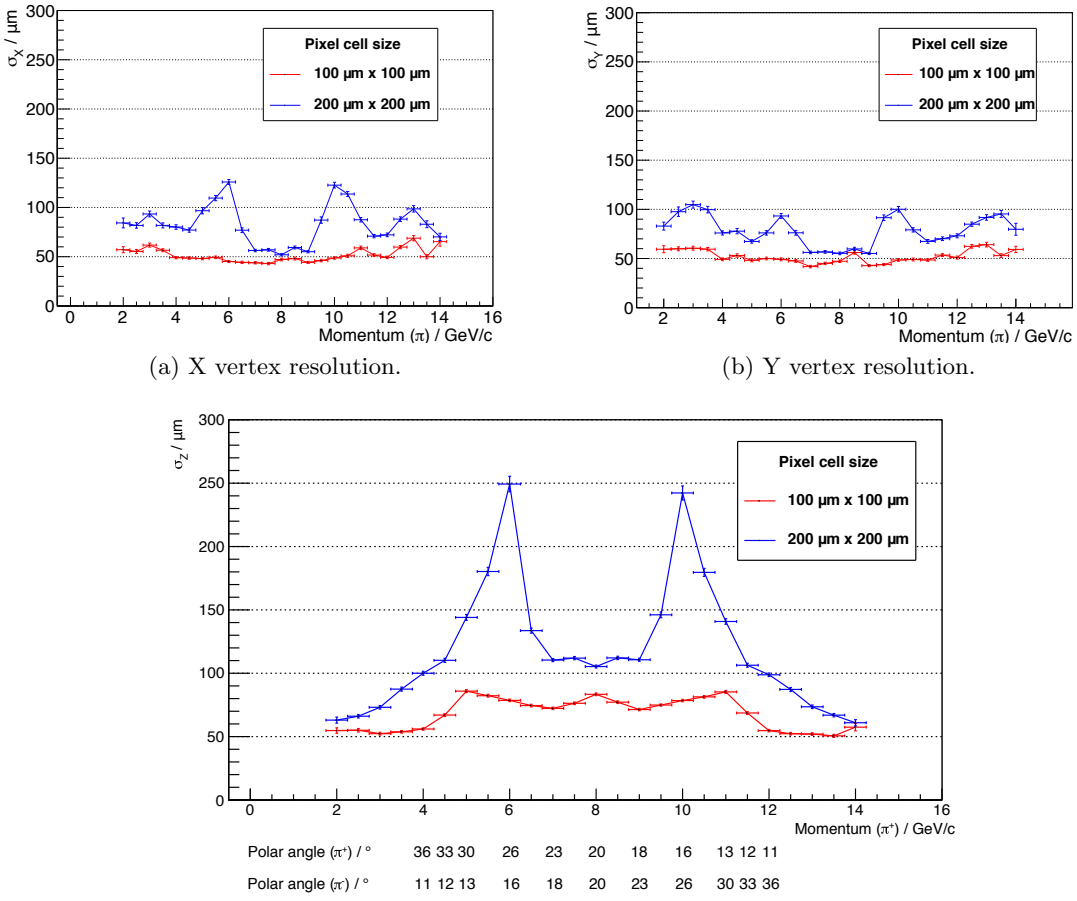

(a) X vertex resolution.

(b) Y vertex resolution.

(c) Z vertex resolution.

Figure B.8: Resolutions for $\overline{p}p \rightarrow \pi^+\pi^-$ vertices as a function of the π^+ MC-true momentum with different pixel cell sizes.

APPENDIX C

Kinematics of the reaction $\overline{\mathrm{p}}\mathrm{p} \rightarrow {\Lambda_\mathrm{c}}^{+}(2286)\,\overline{\Lambda}_\mathrm{c}^{-}(2286)$

Two different approaches can be followed to study the $\overline{\mathrm{p}}\mathrm{p} \rightarrow {\Lambda_\mathrm{c}}^{+}(2286)\,\overline{\Lambda}_\mathrm{c}^{-}(2286)$ reaction: the first one consisting in the production of the Λ_c and $\overline{\Lambda}_\mathrm{c}$ at threshold, the second one in the maximization of the beam momentum in order to increase the transverse momentum in the final state. In this appendix the following notation will be used to indicate four-momenta and their components:

$$\tilde{\mathrm{p}} = \begin{bmatrix} \mathrm{E} \\ \mathrm{p_z}\cdot\mathrm{c} \\ \mathrm{p_y}\cdot\mathrm{c} \\ \mathrm{p_x}\cdot\mathrm{c} \end{bmatrix} \qquad \tilde{\mathrm{p}}/\mathrm{GeV} = \begin{bmatrix} \mathrm{E} \\ \vec{\mathrm{p}}\cdot\mathrm{c} \end{bmatrix}$$

For the production at threshold a beam momentum of 10.147 GeV/c has to be chosen so that the energy available in the rest frame is sufficient to create a ${\Lambda_\mathrm{c}}^{+}(2286)\,\overline{\Lambda}_\mathrm{c}^{-}(2286)$ system at rest. In the laboratory frame we have:

$$\tilde{\mathrm{p}}_{\overline{\mathrm{p}}} = \begin{bmatrix} \mathrm{E}_{\overline{\mathrm{p}}} \\ \mathrm{p}_{\overline{\mathrm{p}}}\cdot\mathrm{c} \\ 0 \\ 0 \end{bmatrix}, \tilde{\mathrm{p}_\mathrm{p}} = \begin{bmatrix} \mathrm{M_p} \\ 0 \\ 0 \\ 0 \end{bmatrix}, \frac{\tilde{\mathrm{p}}_{\mathrm{L,TOT}}}{\mathrm{GeV}} = \begin{bmatrix} 10.190 \\ 10.147 \\ 0 \\ 0 \end{bmatrix} + \begin{bmatrix} 0.938 \\ 0 \\ 0 \\ 0 \end{bmatrix} = \begin{bmatrix} 11.128 \\ 10.147 \\ 0 \\ 0 \end{bmatrix}$$

since $\mathrm{E}_{\overline{\mathrm{p}}} = \sqrt{\left(\mathrm{M}_{\overline{\mathrm{p}}}\cdot\mathrm{c}^2\right)^2 + \left(\mathrm{p}_{\overline{\mathrm{p}}}\cdot\mathrm{c}\right)^2} = \sqrt{(0.938\,\mathrm{GeV})^2 + (10.147\,\mathrm{GeV})^2} = 10.190\,\mathrm{GeV}$ and $\tilde{\mathrm{p}}_{\mathrm{L,TOT}} = \tilde{\mathrm{p}}_{\overline{\mathrm{p}}} + \tilde{\mathrm{p}}_\mathrm{p}$. Now in the $\overline{\mathrm{p}}\mathrm{p}$ rest frame (center of momentum frame):

$$\tilde{\mathrm{p}}^*_{\overline{\mathrm{p}}} = \begin{bmatrix} \mathrm{E}^*_{\overline{\mathrm{p}}} \\ \mathrm{p}^*_{\overline{\mathrm{p}}}\cdot\mathrm{c} \\ 0 \\ 0 \end{bmatrix}, \tilde{\mathrm{p}}^*_\mathrm{p} = \begin{bmatrix} \mathrm{E}^*_\mathrm{p} \\ \mathrm{p}^*_\mathrm{p}\cdot\mathrm{c} \\ 0 \\ 0 \end{bmatrix}, \tilde{\mathrm{p}}_{\mathrm{R,TOT}} = \tilde{\mathrm{p}}^*_{\overline{\mathrm{p}}} + \tilde{\mathrm{p}}^*_\mathrm{p} = \begin{bmatrix} \mathrm{E}^*_{\overline{\mathrm{p}}} + \mathrm{E}^*_\mathrm{p} \\ 0 \\ 0 \\ 0 \end{bmatrix} \text{ because } \mathrm{p}^*_{\overline{\mathrm{p}}} = -\mathrm{p}^*_\mathrm{p}.$$

The module of a four-momentum is Lorentz-invariant. Therefore it must be that: $\left|\tilde{\mathrm{p}}_{\mathrm{L,TOT}}\right| = \left|\tilde{\mathrm{p}}_{\mathrm{R,TOT}}\right|$

$$\left|\tilde{p}_{L,TOT}\right| = \sqrt{\left(E_L \cdot c^2\right)^2 - \left(p_L \cdot c\right)^2} = \sqrt{\left(11.128\,\text{GeV}\right)^2 - \left(10.147\,\text{GeV}\right)^2} = 4.569\,\text{GeV}$$
$$E^*_{\overline{p}} = \sqrt{\left(M_p \cdot c^2\right)^2 + \left(p^* \cdot c\right)^2} = E^*_p, \text{ with } M_{\overline{p}} = M_p \text{ and } \left|p^*_{\overline{p}}\right| = \left|p^*_p\right| = p^*$$
$$\left|\tilde{p}_{R,TOT}\right| = \sqrt{\left(E^*_{\overline{p}} + E^*_p\right)^2} = \sqrt{\left(E^*_{\overline{p}}\right)^2 + \left(E^*_p\right)^2 + 2 \cdot E^*_{\overline{p}} \cdot E^*_p} =$$
$$= \sqrt{\left(M_p \cdot c^2\right)^2 + \left(p^* \cdot c\right)^2 + \left(M_p \cdot c^2\right)^2 + \left(p^* \cdot c\right)^2 + 2 \cdot \left(\left(M_p \cdot c^2\right)^2 + \left(p^* \cdot c\right)^2\right)} =$$
$$= 2 \cdot \sqrt{\left(M_p \cdot c^2\right)^2 + \left(p^* \cdot c\right)^2}$$

Imposing the Lorentz-invariance:

$$2 \cdot \sqrt{\left(M_p \cdot c^2\right)^2 + \left(p^* \cdot c\right)^2} = \left|\tilde{p}_{L,TOT}\right|$$
$$\rightarrow \left(M_p \cdot c^2\right)^2 + \left(p^* \cdot c\right)^2 = \left|\tilde{p}_{L,TOT}\right|^2 / 4 \rightarrow \left(p^* \cdot c\right)^2 = \left|\tilde{p}_{L,TOT}\right|^2 / 4 - \left(M_p \cdot c^2\right)^2$$
$$\rightarrow p^* \cdot c = \sqrt{\left|\tilde{p}_{L,TOT}\right|^2 / 4 - \left(M_p \cdot c^2\right)^2} = \sqrt{\left(4.5685\,\text{GeV}\right)^2 / 4 - \left(0.938\,\text{GeV}\right)^2}$$
$$\rightarrow p^* = 2.083\,\text{GeV/c}$$
$$E^*_{\overline{p}} = E^*_p = \sqrt{\left(M_p \cdot c^2\right)^2 + \left(p^* \cdot c\right)^2} = 2.284\,\text{GeV}$$

The boost along the z-axis which transforms the four-momenta from the laboratory frame to the rest frame can be written as:

$$\Gamma \cdot \tilde{p}_{L,TOT} = \tilde{p}_{R,TOT}$$

$$\begin{bmatrix} E_{R,TOT} \\ 0 \\ 0 \\ 0 \end{bmatrix} = \begin{bmatrix} \gamma & -\beta\gamma & 0 & 0 \\ -\beta\gamma & \gamma & 0 & 0 \\ 0 & 0 & 1 & 0 \\ 0 & 0 & 0 & 1 \end{bmatrix} \cdot \begin{bmatrix} E_{L,TOT} \\ p_{L,TOT} \cdot c \\ 0 \\ 0 \end{bmatrix} = \begin{bmatrix} \gamma \cdot E_{L,TOT} - \beta\gamma \cdot p_{L,TOT} \cdot c \\ -\beta\gamma \cdot E_{L,TOT} + \gamma \cdot p_{L,TOT} \cdot c \\ 0 \\ 0 \end{bmatrix}$$

Substituting the values one obtains: $\begin{bmatrix} 4.569 \\ 0 \\ 0 \\ 0 \end{bmatrix} = \begin{bmatrix} \gamma \cdot 11.128 - \beta\gamma \cdot 10.147 \cdot c \\ -\beta\gamma \cdot 11.128 + \gamma \cdot 10.147 \\ 0 \\ 0 \end{bmatrix} \text{GeV}$

$$\begin{cases} 4.569\,\text{GeV} = \gamma \cdot 11.128\,\text{GeV} - \beta\gamma \cdot 10.147\,\text{GeV} \\ 0 = \gamma \cdot 10.147\,\text{GeV} - \beta\gamma \cdot 11.128\,\text{GeV} \end{cases}$$
$$\begin{cases} \gamma \cdot 10.147 = \beta\gamma \cdot 11.128 \rightarrow \beta = 10.147/11.128 = 0.912 \\ \gamma = 2.436 \end{cases}$$

Now if $\tilde{p}^*_3$ and $\tilde{p}^*_4$ are respectively the four-momenta of the ${\Lambda_c}^+$ and of the ${\overline{\Lambda}_c}^-$ in the rest frame, and $\tilde{p}_3$ and $\tilde{p}_4$ are the ones in the laboratory frame, since the two particles are at rest in the center of momentum frame one can write:

$$\frac{\tilde{p}^*_3}{\text{GeV}} = \begin{bmatrix} M_{\Lambda_c^+} \cdot c^2 \\ 0 \\ 0 \\ 0 \end{bmatrix} = \begin{bmatrix} 2.286 \\ 0 \\ 0 \\ 0 \end{bmatrix}$$

$$\frac{\tilde{p}_3}{\mathrm{GeV}} = \begin{bmatrix} \gamma & +\beta\gamma & 0 & 0 \\ +\beta\gamma & \gamma & 0 & 0 \\ 0 & 0 & 1 & 0 \\ 0 & 0 & 0 & 1 \end{bmatrix} \cdot \begin{bmatrix} M_{\Lambda_c^+} \cdot c^2 \\ 0 \\ 0 \\ 0 \end{bmatrix} = \begin{bmatrix} \gamma \cdot M_{\Lambda_c^+} \cdot c^2 \\ \beta\gamma \cdot M_{\Lambda_c^+} \cdot c^2 \\ 0 \\ 0 \end{bmatrix} = \begin{bmatrix} 5.568 \\ 5.077 \\ 0 \\ 0 \end{bmatrix}$$

$E_3 = E_4$

$\vec{p}_3 + \vec{p}_4 = 0$

When the $\Lambda_c{}^+$ and the $\overline{\Lambda}_c{}^-$ are created at rest in the center of momentum frame, the momentum in the laboratory frame is fully determined by the boost between the two systems. Since the two particle do not have any transverse momentum, they will have the same four-momenta in the lab frame. Therefore their decays both come from a point along the z axis and it is difficult to distinguish the two decay vertices. We will now change the initial beam momentum, thus giving some extra transverse momentum in the laboratory frame to the two Λ_cs. This will produce a separation of the two decaying particles in both reference frames (in the rest frame they will be flying back-to-back). Setting the maximum beam momentum available at $\overline{\mathsf{P}}\mathsf{ANDA}$ $p_{\overline{p}} = 15\,\mathrm{GeV/c}$ the total four-momentum of the initial state becomes:

$$\frac{\tilde{p}_{L,TOT}}{\mathrm{GeV}} = \begin{bmatrix} 15.029 \\ 15 \\ 0 \\ 0 \end{bmatrix} + \begin{bmatrix} 0.938 \\ 0 \\ 0 \\ 0 \end{bmatrix} = \begin{bmatrix} 15.967 \\ 15 \\ 0 \\ 0 \end{bmatrix}$$

The module of the total four-momentum in the laboratory frame is:

$$\left|\tilde{p}_{L,TOT}\right| = \sqrt{\left(E_{L,TOT} \cdot c^2\right)^2 - \left(p_{L,TOT} \cdot c\right)^2} = \sqrt{\left(15.967\,\mathrm{GeV}\right)^2 - \left(15\,\mathrm{GeV}\right)^2} = 5.473\,\mathrm{GeV}$$
$$\left|\tilde{p}_{R,TOT}\right| = 2 \cdot \sqrt{\left(M_p \cdot c^2\right)^2 + \left(p^* \cdot c\right)^2}$$
$$\rightarrow p^* \cdot c = \sqrt{\left|\tilde{p}_{L,TOT}\right|^2/4 - \left(M_p \cdot c^2\right)^2} = \sqrt{\left(5.473\,\mathrm{GeV}\right)^2/4 - \left(0.938\,\mathrm{GeV}\right)^2}$$
$$\rightarrow p^* = 2.571\,\mathrm{GeV/c}$$
$$E_p^* = \sqrt{\left(M_p \cdot c^2\right)^2 + \left(p^* \cdot c\right)^2} = 2.737\,\mathrm{GeV} \rightarrow E_{R,TOT} = 2 \cdot E_p^* = 5.473\,\mathrm{GeV}$$

Therefore we now have:

$$\frac{\tilde{p}_{L,TOT}}{\mathrm{GeV}} = \begin{bmatrix} 15.967 \\ 15 \\ 0 \\ 0 \end{bmatrix} \text{ and } \frac{\tilde{p}_{R,TOT}}{\mathrm{GeV}} = \begin{bmatrix} 5.473 \\ 0 \\ 0 \\ 0 \end{bmatrix}$$

which leads to:

$$\frac{\tilde{p}_{R,TOT}}{\mathrm{GeV}} = \begin{bmatrix} 5.473 \\ 0 \\ 0 \\ 0 \end{bmatrix} = \begin{bmatrix} \gamma \cdot E_{L,TOT} - \beta\gamma \cdot p_{L,TOT} \cdot c \\ -\beta\gamma \cdot E_{L,TOT} + \gamma \cdot p_{L,TOT} \cdot c \\ 0 \\ 0 \end{bmatrix} = \begin{bmatrix} \gamma \cdot 15.967 - \beta\gamma \cdot 15 \cdot c \\ -\beta\gamma \cdot 15.967 + \gamma \cdot 15 \cdot c \\ 0 \\ 0 \end{bmatrix}$$

$$\begin{cases} \gamma \cdot 15 = \beta\gamma \cdot 15.967 \rightarrow \beta = 15/15.967 = 0.939 \\ \gamma = 2.917 \end{cases}$$

In the center of momentum frame the $\Lambda_c{}^+$ and the $\overline{\Lambda}_c{}^-$ fly back-to-back and their direction is isotropically distributed. Since the boost only influences the z-coordinate, in the transverse x-y plane the distribution of the two particles will be isotropic in the laboratory frame as well. In the following the $p_{3,y} = p_{4,y} = 0$ case will be considered. Four different specific configurations in the center of momentum reference frame will be discussed:

- A $p_{3,z} = p_{4,z} = 0$;
- B $p_{3,x} = p_{4,x} = 0$;
- C $p_{3,x} = p_{3,z} = p_{4,x} = p_{4,z} = p_3/\sqrt{2}$;
- D general case.

A

$$\frac{\tilde{p}_{R,TOT}}{GeV} = \begin{bmatrix} 5.473 \\ 0 \\ 0 \\ 0 \end{bmatrix} = \tilde{p}_3^* + \tilde{p}_4^*$$

$$\tilde{p}_3^* + \tilde{p}_4^* = \begin{bmatrix} 2E_3^* \\ 0 \\ 0 \\ 0 \end{bmatrix} \rightarrow E_3^* = 2.737 \text{ GeV} \rightarrow p_3^* = \sqrt{2.737^2 - 2.286^2} \text{ GeV/c} = 1.504 \text{ GeV/c}$$

$$\vec{p}_3^* = \begin{bmatrix} 0 \\ 0 \\ p_3^* \end{bmatrix}, \vec{p}_4^* = \begin{bmatrix} 0 \\ 0 \\ -p_3^* \end{bmatrix}$$

$$\frac{\tilde{p}_3}{GeV} = \begin{bmatrix} \gamma & +\beta\gamma & 0 & 0 \\ +\beta\gamma & \gamma & 0 & 0 \\ 0 & 0 & 1 & 0 \\ 0 & 0 & 0 & 1 \end{bmatrix} \cdot \begin{bmatrix} E_3^* \\ 0 \\ 0 \\ p_3^* \cdot c \end{bmatrix} = \begin{bmatrix} \gamma \cdot E_3^* \\ \beta\gamma \cdot E_3^* \\ 0 \\ p_3^* \end{bmatrix} = \begin{bmatrix} 7.984 \\ 7.500 \\ 0 \\ 1.504 \end{bmatrix}$$

$$\frac{\tilde{p}_4}{GeV} = \begin{bmatrix} 7.984 \\ 7.500 \\ 0 \\ -1.504 \end{bmatrix}$$

B

$$\vec{p}_3^* = \begin{bmatrix} p_3^* \\ 0 \\ 0 \end{bmatrix}, \vec{p}_4^* = \begin{bmatrix} -p_3^* \\ 0 \\ 0 \end{bmatrix}$$

$$\frac{\tilde{p}_3}{\mathrm{GeV}} = \begin{bmatrix} \gamma & +\beta\gamma & 0 & 0 \\ +\beta\gamma & \gamma & 0 & 0 \\ 0 & 0 & 1 & 0 \\ 0 & 0 & 0 & 1 \end{bmatrix} \cdot \begin{bmatrix} E_3^* \\ p_3^* \cdot c \\ 0 \\ 0 \end{bmatrix} = \begin{bmatrix} \gamma \cdot E_3^* + \beta\gamma \cdot p_3^* \cdot c \\ \beta\gamma \cdot E_3^* + \gamma \cdot p_3^* \cdot c \\ 0 \\ 0 \end{bmatrix} = \begin{bmatrix} 12.106 \\ 11.889 \\ 0 \\ 0 \end{bmatrix}$$

$$\frac{\tilde{p}_4}{\mathrm{GeV}} = \begin{bmatrix} \gamma & +\beta\gamma & 0 & 0 \\ +\beta\gamma & \gamma & 0 & 0 \\ 0 & 0 & 1 & 0 \\ 0 & 0 & 0 & 1 \end{bmatrix} \cdot \begin{bmatrix} E_3^* \\ -p_3^* \cdot c \\ 0 \\ 0 \end{bmatrix} = \begin{bmatrix} \gamma \cdot E_3^* - \beta\gamma \cdot p_3^* \cdot c \\ \beta\gamma \cdot E_3^* - \gamma \cdot p_3^* \cdot c \\ 0 \\ 0 \end{bmatrix} = \begin{bmatrix} 3.861 \\ 3.111 \\ 0 \\ 0 \end{bmatrix}$$

C

$$\vec{p_3^*} = \begin{bmatrix} p_3^*/\sqrt{2} \\ 0 \\ p_3^*/\sqrt{2} \end{bmatrix}, \vec{p_4^*} = \begin{bmatrix} -p_3^*/\sqrt{2} \\ 0 \\ -p_3^*/\sqrt{2} \end{bmatrix}$$

$$\frac{\tilde{p}_3}{\mathrm{GeV}} = \begin{bmatrix} \gamma & +\beta\gamma & 0 & 0 \\ +\beta\gamma & \gamma & 0 & 0 \\ 0 & 0 & 1 & 0 \\ 0 & 0 & 0 & 1 \end{bmatrix} \cdot \begin{bmatrix} E_3^* \\ p_3^* \cdot c/\sqrt{2} \\ 0 \\ p_3^* \cdot c/\sqrt{2} \end{bmatrix} = \begin{bmatrix} \gamma \cdot E_3^* + \beta\gamma \cdot p_3^* \cdot c/\sqrt{2} \\ \beta\gamma \cdot E_3^* + \gamma \cdot p_3^* \cdot c/\sqrt{2} \\ 0 \\ p_3^* \cdot c/\sqrt{2} \end{bmatrix} = \begin{bmatrix} 10.899 \\ 10.603 \\ 0 \\ 1.064 \end{bmatrix}$$

$$\frac{\tilde{p}_4}{\mathrm{GeV}} = \begin{bmatrix} \gamma & +\beta\gamma & 0 & 0 \\ +\beta\gamma & \gamma & 0 & 0 \\ 0 & 0 & 1 & 0 \\ 0 & 0 & 0 & 1 \end{bmatrix} \cdot \begin{bmatrix} E_3^* \\ -p_3^* \cdot c/\sqrt{2} \\ 0 \\ -p_3^* \cdot c/\sqrt{2} \end{bmatrix} = \begin{bmatrix} \gamma \cdot E_3^* - \beta\gamma \cdot p_3^* \cdot c/\sqrt{2} \\ \beta\gamma \cdot E_3^* - \gamma \cdot p_3^* \cdot c/\sqrt{2} \\ 0 \\ -p_3^* \cdot c/\sqrt{2} \end{bmatrix} = \begin{bmatrix} 5.068 \\ 4.397 \\ 0 \\ -1.064 \end{bmatrix}$$

D

In the general case, always with the assumption $p_3^*, y = p_4^*, y = 0$, one can write:

$$\vec{p_3^*} = \begin{bmatrix} \alpha \\ 0 \\ \sqrt{(p_3^*)^2 - \alpha^2} \end{bmatrix}, \vec{p_4^*} = \begin{bmatrix} -\alpha \\ 0 \\ -\sqrt{(p_3^*)^2 - \alpha^2} \end{bmatrix}, E_3^* = E_4^* = E_R/2$$

Then applying the inverse boost transformation:

$$\frac{\tilde{p}_3}{\mathrm{GeV}} = \begin{bmatrix} \gamma & +\beta\gamma & 0 & 0 \\ +\beta\gamma & \gamma & 0 & 0 \\ 0 & 0 & 1 & 0 \\ 0 & 0 & 0 & 1 \end{bmatrix} \cdot \begin{bmatrix} E_3^* \\ \alpha \cdot c \\ 0 \\ \sqrt{(p_3^*)^2 - \alpha^2} \cdot c \end{bmatrix} =$$

$$= \begin{bmatrix} \gamma \cdot E_3^* + \beta\gamma \cdot \alpha \cdot c \\ \beta\gamma \cdot E_3^* + \gamma \cdot \alpha \cdot c \\ 0 \\ \sqrt{(p_3^*)^2 - \alpha^2} \cdot c \end{bmatrix} = \begin{bmatrix} 7.984 + 2.741 \cdot \alpha \cdot c \\ 7.500 + 2.917 \cdot \alpha \cdot c \\ 0 \\ \sqrt{2.263 - \alpha^2 \cdot c^2} \end{bmatrix}$$

$$\frac{\tilde{p}_4}{\mathrm{GeV}} = \begin{bmatrix} \gamma & +\beta\gamma & 0 & 0 \\ +\beta\gamma & \gamma & 0 & 0 \\ 0 & 0 & 1 & 0 \\ 0 & 0 & 0 & 1 \end{bmatrix} \cdot \begin{bmatrix} E_3^* \\ -\alpha \cdot c \\ 0 \\ -\sqrt{\left(p_3^*\right)^2 - \alpha^2 c} \end{bmatrix} =$$

$$\begin{bmatrix} \gamma \cdot E_3^* - \beta\gamma \cdot \alpha \cdot c \\ \beta\gamma \cdot E_3^* - \gamma \cdot \alpha \cdot c \\ 0 \\ -\sqrt{\left(p_3^*\right)^2 - \alpha^2} \cdot c \end{bmatrix} = \begin{bmatrix} 7.984 - 2.741 \cdot \alpha \cdot c \\ 7.500 - 2.917 \cdot \alpha \cdot c \\ 0 \\ -\sqrt{2.263 - \alpha^2 \cdot c^2} \end{bmatrix}$$

The results obtained for the case D are shows in figure C.1a, C.1b and C.2 where the energy, the components of the momentum and the polar angle of the Λ_c and $\overline{\Lambda}_c$ are plotted as a function of the α parameter. Figure C.2 shows also the angle between the two tracks which is obtained summing the polar angles of the two tracks, since these have opposite azimuthal direction.

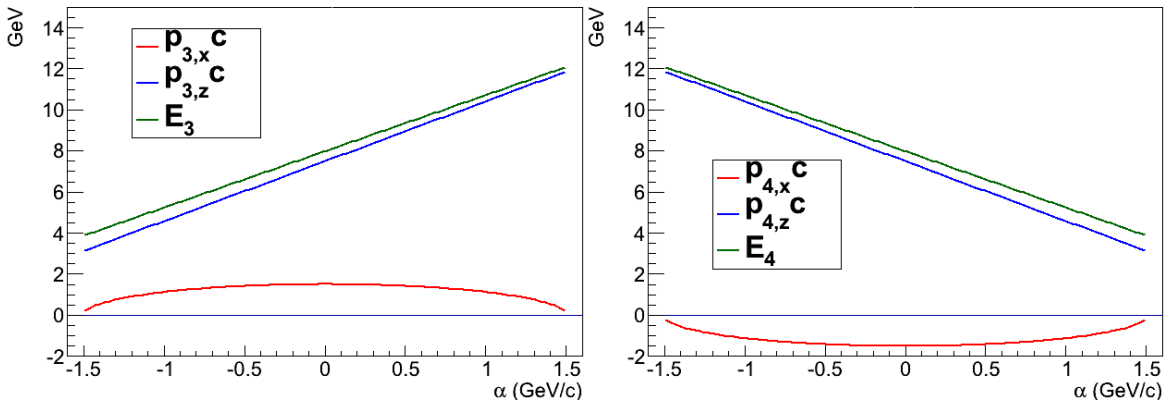

(a) Λ_c. (b) $\overline{\Lambda}_c$.

Figure C.1: Energy, transverse and longitudinal momentum of the Λ_c and $\overline{\Lambda}_c$ as a function of the α parameter with a beam momentum of 15 GeV/c.

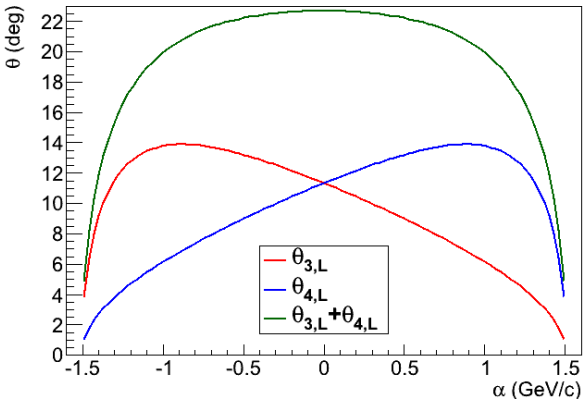

Figure C.2: Polar angles of the two tracks as a function of α with a beam momentum of 15 GeV/c.

APPENDIX D

GUI tools to control mass simulations

Two graphical tools were developed to facilitate the submission and the control of mass scale simulations on the 64 bit linux cluster available at Helmholtz-Institut für Strahlen- und Kernphysik in Bonn. Both applications were developed in Java (see [1]) to improve the portability between different systems. The Java graphic interface generates a bash script calling all the macros necessary to simulate and perform a full event reconstruction according to the input settings provided by the user. Afterward a condor script is created, which submits sets of jobs to the cluster.

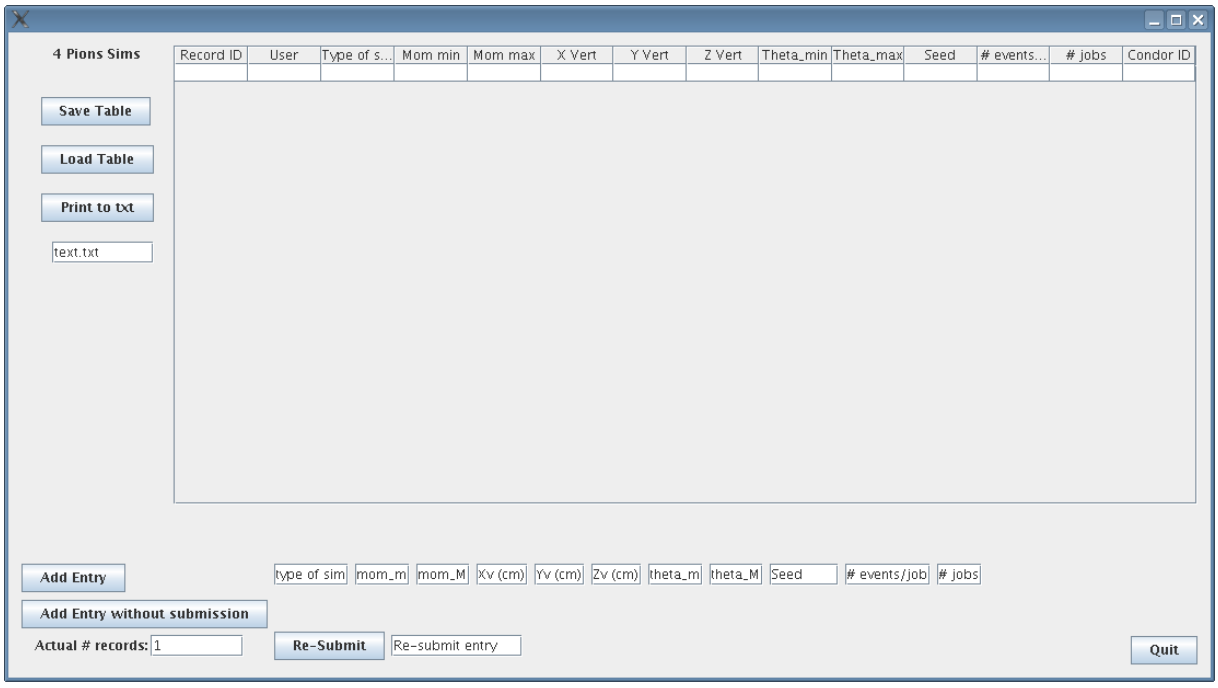

Figure D.1: Appearence of the GUI used to control the "4-π" scans.

4-π studies

The first application shown in figure D.1 is designed to commit the simulations where four pions were propagated from a common vertex (see section 5.1.2). The user can set the momentum and the polar angle range of the four particles (the simulation will be started smearing homogeneously the parameters in the selected range). Furthermore the vertex position can be set, as well as the initial seed to be provided to initialize the random generator, the number of events per job and the total number of jobs. After the commission, a log containing all the details is added to a summary table which can be saved and printed to text.

Physics channels

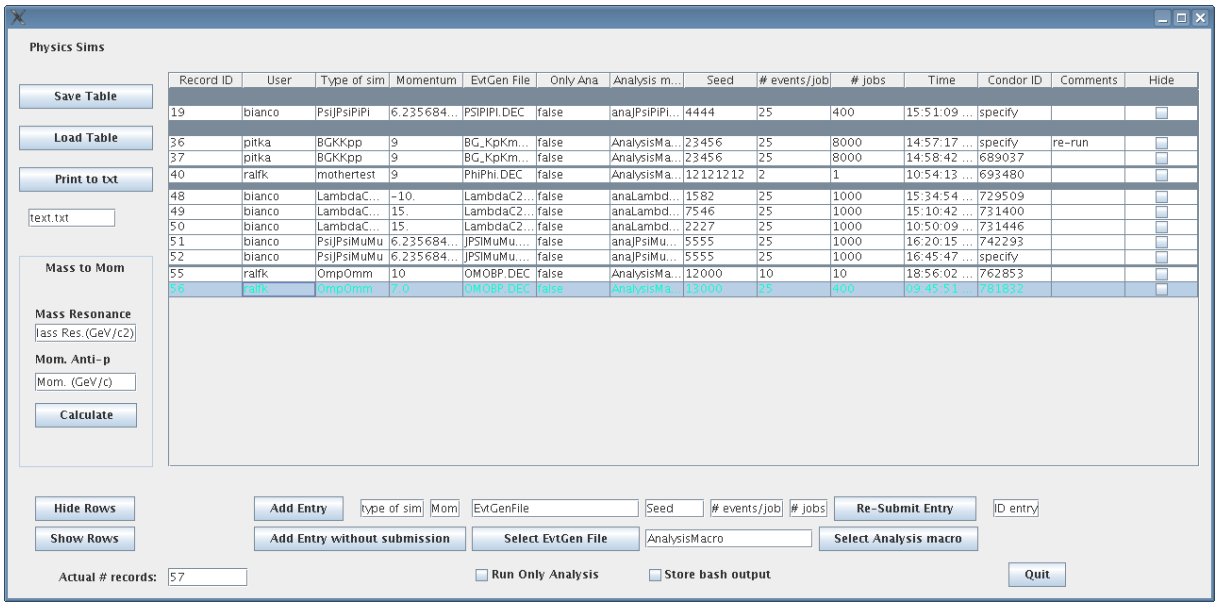

Figure D.2: Appearence of the GUI used to control the simulation and reconstruction of physics channels.

The second tool (see figure D.2) was designed to manage simulation and analysis of different physics channels. The user can specify the initial $\overline{\mathrm{p}}$ beam momentum or the center of mass energy. The GUI lets the user choose a decay model and the analysis macro to be used. Simple check boxes allow to re-run the analysis without repeating the simulation and the track reconstruction, to pipe the output and logs to specific files, to hide some entries in the final summary table.

Bibliography

[1] Java SE 6 Documentation, http://docs.oracle.com/javase/6/docs/.

APPENDIX E

Settings and setups used for the Monte-Carlo simulations

All the simulations showed in this thesis were performed within the PandaRoot framework. The framework revision number 12729 together with the "may11" version of the external packages was adopted for all these studies.

The following geometries have been used to implement the elements of the $\overline{\text{P}}$ANDA experiment during these studies.

All these components were physically placed in the cave used for the simulations, even if their answer was not always considered for the analysis.

- **Solenoidal Magnet:** FullSuperconductingSolenoid_v831.root
- **Dipole:** dipole.geo
- **Beam Pipe:** hard-coded implementation in the "PndPipe" class
- **MVD:** Mvd-2.1_FullVersion.root

  Mvd-2.2_FullVersion_Prelim.root
- **STT:** straws_skewed_blocks_35cm_pipe.geo
- **EMC:** Geometry version 19
- **Muon Detectors:** hard-coded in the "PndMdt" class
- **GEM:** gem_3Stations.root
- **Forward DIRC:** dsk.root
- **Barrel DIRC:** hard-coded in the "PndDrc" class
- **FTS:** fts.geo

PandaRoot repository:
https://subversion.gsi.de/trac/fairroot/browser/pandaroot/trunk?rev=12729

External packages:
https://subversion.gsi.de/fairroot/fairsoft/release/may11

3D	3-Dimensional
ADC	Analog to Digital Converter
APV	Analog Pipeline Voltage mode
ASIC	Application Specific Integrated Circuit
AU	Arbitrary Units
C.C.	Charge Conjugate
CERN	Conseil Européen pour la Recherche Nucléaire
COSY	COoler SYnchrotron
CT	Central Tracker
Cz	Czochralski
DAFNE	Double Annular ring For Nice Experiments
DAQ	Data Acquisition
DESY	Deutsches ElektronenSYnchrotron
DIRC	Detector for Internally Reflected Cherenkov Light
DPM	Dual Parton Model
EMC	Electromagnetic Calorimeter
FAIR	Facility for Antiproton and Ion Research
FE	Front-End
FEE	Front-End Electronics
FINUDA	FIsica NUcleare a DAFNE
FPGA	Field Programmable Gate Array
FS	Forward Spectrometer
FTS	Forward Tracking System
GEM	Gas Electron Multiplier
GSI	Gesellschaft für Schwerionenforschnung
GUI	Graphical User Interface
HESR	High Energy Storage Ring
HL	High Luminosity (HESR operation mode)
HR	High Resolution (HESR operation mode)
HV	High Voltage

IP	Interaction Point
MC	Monte-Carlo
MCP PMT	Multi-Channel Plate PMT
MDT	Mini Drift Tubes
MIP	Minimum Ionizing Particle
MPV	Most Probable Value
MVD	Micro Vertex Detector
PANDA	antiProton ANnihilation at DArmstadt
PCB	Printed Circuit Board
PDG	Particle Data Group
PID	Particle Identification
PMT	Photomultiplier
POCA	Point of Closest Approach
QCD	Quantum Chromo Dynamics
RICH	Ring Imaging Cherenkov Counter
RMS	Root Mean Square
SDS	Silicon Detector Software
STT	Straw Tube Tracker
TOF	Time-of-Flight
ToPix	Torino Pixel
ToT	Time-over-Threshold
TS	Target Spectrometer
VMC	Virtual Monte-Carlo
VME	Versa Module Eurocard

List of Figures

List of Tables

Acknowledgments

I want to thank Prof. Dr. Kai-Thomas Brinkmann for the continuous support, the useful advises and the trust he has always put on me.

I am grateful to Prof. Dr. Ulrike Thoma who accepted to be the second referee for this thesis and has been part of my BCGS supervising committee during the last years. I want to thank all the professors who accepted to be referees of my dissertation.

I also want to acknowledge the support of the Bonn Cologne Graduate School of Physics and Astronomy, which gave me the opportunity to attend several conferences and to join the interesting lectures and workshops organized in the last three years.

I am beholden to my colleagues and to all the people of the HISKP who shared with me some time, the office, working hours, coffees or jokes. I am especially grateful to all the guys who happened to sit in the same office with me, in particular to Christian who has been there for the whole period and to Philipp who helped me with the translations into German!

Thanks to the "good old guys" Thomas, Hans-Georg and Ralf for having helped and guided me since the beginning through this great experience. Working and spending time with you has been a pleasure.

Thanks to Max, Karsten, Andreas and Robert. The discussions with all of you were fruitful and helpful, whether they were about physics or not! Thanks to Bob again for having always carefully reminded us about every single deadline.

Thanks to Tommaso and Laura for their careful reading of this thesis and for the useful suggestions. I am indebted with Tommaso for his editing tips.

I am grateful to all the $\overline{\text{P}}$ANDA MVD collaborators from Bonn, Giessen, Torino and Jülich, as well as to many other people within the $\overline{\text{P}}$ANDA collaboration.

Grazie to Francesco, Valentina, Azzurra and the other guys I have been spending time with here in Bonn. It has been a great time together and I always felt at home with you.

Thanks to my family for having kept on supporting me along this adventure, for all the help in the difficult periods and for having made me feel constantly in touch with home.

Thanks to Eli for everything.